Peering into the Darkness: Quantum Chemistry Shines a Light on Reaction Mechanisms in the Gas-phase and in Solution

Nina Leeb

Doctor of Philosophy

University of York

Chemistry

September 2021

Abstract

Computational chemistry has continued to advance allowing for more complex investigations into larger systems. A challenge remains the way that solvent should be accounted for in a system. Implicit solvent corrections are quick and can easily be added to a computational method when needed. However, solvents can play a more direct role in a reaction through hydrogen-bonding or by acting as a solvent catalyst. This involvement requires including the bulk solvent in calculations, which is not possible with standard QM methodologies. Addition of explicit solvent molecules requires careful consideration of the position and number of solvent molecules. Three mechanistic investigations are presented here, all involving a different treatment to model the system accurately.

First, the barriers for the abstraction of hydrogen atoms on 1-butyl-3-methylimidazolium by an F atom were determined. The reactions were carried out *in vacuuo*, and as such, a gas-phase DFT model was enough to accurately describe the system.

Secondly, a phosphoramidate reaction of $[Cp^*Ir(\kappa^2\text{-N,O-Xyl(N)P(O)(OMe)}_2)][BAr^F{}_4]$ with propyne was modelled in dichloromethane. No direct solvent involvement was identified during the experiment and robust experimental data confirmed that implicit solvent corrections accounting for dichloromethane were needed.

Finally, two Diels-Alder reactions were modelled that were involved in the synthesis of methoxatin. The experimental results indicated a strong solvent effect, showing only significant yields in HFIP and TFE. Implicit solvent corrections did not determine the origin of this solvent effect. The inclusion of at least one explicit solvent molecule was needed to understand the effect of HFIP and TFE on the reactions.

Access to reliable experimental data ensured the chosen methodology was sufficient for modelling each system well. Confidence in the insights from these studies is thus gained and enables feedback to be provided about the choice of substrate and solvent.

Table of Contents

Table of Tables

Table of Figures

Table of Schemes

Table of Equations

Acknowledgements

"You must never give into despair. Allow yourself to slip down that road, and you surrender to your lowest instincts. In the darkest times, hope is something you give yourself. That is the meaning of inner strength."

- Uncle Iroh, Avatar: The Last Airbender, Episode 5: Avatar Day, Book: Earth

Something that I heard all the time, and even said myself multiple times, during my studies was that a PhD is isolating. I knew this and tried to prepare for this as best as possible. It's important to add to that though, that you don't get through your PhD alone – not just because of your supervisor(s) but also the people who you surround yourself with end up having such an impact on your PhD experience.

I know that typically this is the space reserved for thanking these people, but I have tried to always let those people know how much they mean to me at every stage of the PhD. So, I hope that you all know who you are, and you know that I wouldn't have been able to do this without you. If I haven't done that as well as I had hoped, then I plan to do a better job at that from now on.

When I thought about what to write here, I knew it needed to reflect me and my experience during my PhD. Acknowledgements – it feels like another way to say, "tell me how you made it through your PhD". For me it was the injustice that I see every day in the world around us. The blatant racism, sexism, ableism, classism, ageism, heterosexism, gender binarism etc. but also the small forms of it that add up very quickly and can hurt just as much. When things got tough for me during my PhD it was those awful moments that showed me that things could be worse. They made me appreciate the life I have and how fortunate I am to be blessed with the struggle of an education.

So, as unconventional as it is, I want to acknowledge the sexist remarks I've heard all my life, the ableism that I experienced after my diagnosis. I want to acknowledge the racism that I see on the news, hear about from my friends, the classism that is so strong in this country, and the heterosexism that exists in our governments. I want to acknowledge all the awful things that we humans do because it was those horrendous moments during my PhD that kept me fighting. Those moments of pain and injustice fuelled the fire in me to finish, knowing that with it comes more power and more opportunities to make a change in this world.

While I wish we lived in a kind and understanding world I have had to learn, during my time as a PhD student, that this is not reality and not under my control. But I also learnt that I could control my actions and that I will continue to fight as hard as I can to bring that world into reality.

Author's Declaration

I declare that the research presented in this thesis is, to the best of my knowledge, original. The work was carried out under the supervision of Dr John Slattery in the Department of Chemistry of the University of York between October 2016 and September 2021.

The results presented in Chapter 3 were published in:

Nina M. Leeb, Marcus W. Drover, Jennifer A. Love, Laurel L. Schafer, and John M. Slattery, *Organometallics* 2018, 37, 4630-4638.

This thesis has not been submitted for any other degree at this or any other University.

Thesis Numbering Scheme

1) In Chapter 2 the different abstraction sites are referred to as **C***, where the * refers to the numbers given in Figure 2.8
2) In Chapter 2 the two steps of the stepwise hydrogen abstraction are differentiated by the bond that is formed. **ring_TS_CF** and **ring_min_CF** refer to the TS and minimum where the C-F bond is formed respectively, while **ring_TS_HF** and **ring_min_HF** refers to the TS and minimum where the H-F bond is formed respectively
3) *E* and *Z* are used to indicate the stereochemistry of the alkenyl group in the isomers of complexes **5a** and **5b** in Chapter 3
4) When more than one regioisomer was determined, these are differentiated by **a**, **b**, **c**
5) When more than one conformational isomer of the same complex was determined, these are differentiated by **i**, **ii**, **iii**, **iv**, **v**
6) *endo* and *exo* are used to differentiate the two ways that the diene and dienophile can react in a Diels-Alder reaction

1. Introduction to Computational Chemistry

1.1. Quantum Chemistry

1.1.1. Schrödinger Equation

Modelling chemical systems requires accurately determining how particles interact and behave. Classical mechanics is unable to describe atomic and subatomic particles accurately and quantum mechanics (QM) is needed instead. The time-independent Schrödinger equation (Equation 1.1) gives the energy of a system in a particular stationary state.

$$\mathbf{H}\Psi = \mathrm{E}\Psi$$

Equation 1.1 - Time-Independent Schrödinger equation. **H** is the time-independent Hamiltonian operator, Ψ is the wave function, and E is the total energy of the system.[1]

This is an eigenvalue equation, as an operator acts on a function producing a value and the same function again. The time-independent equation can only be used to calculate the energy of stationary states, while the time dependent Schrödinger equation needs to be used when dealing with dynamic phenomena. The wave function, Ψ, describes the system fully and becomes increasingly complex as the system grows. The Schrödinger equation can only be solved exactly for one or two particle systems such as H or H_2^+ and methods have been developed to approximate the wave function and solve this equation.

Computational methods that use the Schrödinger equation to determine the position of nuclei and thus the energy of the system, are known as *ab initio* methods. The term "*ab initio*", meaning "from first principles", refers to the use of the underlying physics at work within a system.

The Hamiltonian operator, **H**, gives the total energy of the system, E, when it acts on the wave function. Different operators can act on the wave function to give different observables such as position, momentum, spin, etc. Since **H** gives the total energy of the system everything that contributes to the energy of the system must be represented in the operator. For example, the molecular or Coulomb Hamiltonian (Equation 1.2) considers the repulsion between nuclei, electron-electron repulsion, nucleus-electron attraction, the kinetic energy of the nuclei, and the kinetic energy of the electrons.

$$\boldsymbol{H = V_{ee} + V_{nn} - V_{en} - T_n - T_e}$$

Equation 1.2 – Molecular/Coulomb Hamilton operator, **H**, where **V** represents the potential energy operator, **T** the kinetic energy operator, n the nuclei, and e the electrons.[1]

The two repulsion terms increase the energy of the system and are therefore added to the total energy. The attraction term and the two kinetic terms both stabilise the system and therefore lower the total energy.

1.1.2. Born-Oppenheimer Approximation

The Hamiltonian operator can be simplified by applying the Born-Oppenheimer approximation. The first step is known as the clamped nuclei approximation, where the kinetic energy of the nuclei is set to zero and the repulsion between the nuclei is constant. This is possible due to the assumption that because the nuclei are much larger than the electrons, they move much slower. From the perspective of the electrons the nuclei can therefore be considered stationary, hence the kinetic energy is zero and the repulsion that is experienced is fixed. Through this approximation the coordinates of the system are now no longer variables but parameters.

The Hamiltonian operator can therefore be simplified and is now referred to as the electronic Hamiltonian operator, **H_{elec}** (Equation 1.3). Next the kinetic energy of the nuclei is reintroduced, and the motion of the nuclei can be determined through a similar approximation. Since the electrons are much smaller and move much quicker than the nuclei, an average field can be used for them, and the motion of the nuclei are determined in this field. The nuclei now move on a potential energy surface (PES), which is a solution of the electronic Schrödinger equation. The PES that is generated is the same for different isotopes, since the PES is independent of mass.

$$\mathbf{H_{elec} = V_{ee} - V_{ne} - T_e}$$

Equation 1.3 – Electronic Hamilton operator, **H**, where **V** represents the potential energy operator, **T** the kinetic energy operator, n the nuclei, and e the electrons.[1]

The Born-Oppenheimer approximation works well, but issues arise at very long bond distances during bond breaking. Here a small change in the nuclear coordinates can cause a dramatic change in the electronic wave function.

1.1.3. Self-Consistent Field Theory

Solving the electronic Schrödinger equation, however, still poses some issues. The electronic coordinates cannot be separated as atoms are bonded to each other and a change in one atom results in a change in neighbouring atoms. Approximations therefore need to be used giving an approximate wave function. The variational principle states that the energy of an approximate wave function will always be either higher in energy or equal in energy to the exact wave function.

The first approximation involves considering each electron individually and determining how it will move with respect to the mean field created by the other electrons. An electron's position is then adjusted to lower the energy, followed by the next, and so on, until no further electrons need to be moved and the field has reached consistency. This process is called the self-consistent field (SCF) procedure.

1.1.4. Slater Determinants

The total energy is therefore given by the summation of the individual energies. This however is not an accurate description as electrons are indistinguishable and are not completely independent. Assigning an electron to a specific orbital makes them distinguishable and moving electrons uncorrelated ignores that electrons repel each other and therefore the probability of finding an electron is dependent on the location of another electron. The Pauli exclusion principle states that no two electrons can have identical quantum numbers. In terms of the wave function this can be stated as the electronic wave function must be antisymmetric with respect to the exchange of coordinates (space and spin) of two electrons. If two electrons are exchanged the sign of the wave function changes and if two electrons are identical the wave function vanishes.

$$\Phi_{\mathrm{SD}} = \frac{1}{\sqrt{\mathrm{N}!}} \begin{vmatrix} \phi_1(1) & \phi_2(1) & \cdots & \phi_{\mathrm{N}}(1) \\ \phi_1(2) & \phi_2(2) & \cdots & \phi_{\mathrm{N}}(2) \\ \vdots & \vdots & \ddots & \vdots \\ \phi_1(\mathrm{N}) & \phi_2(\mathrm{N}) & \cdots & \phi_{\mathrm{N}}(\mathrm{N}) \end{vmatrix}$$

Equation 1.4 – Normalised Slater determinant for an N electron system.[2]

Equation 1.4 shows the general structure of a Slater determinant for an N electron system. The wave function is constructed using such Slater determinants. The columns correspond to orbitals and the rows are the coordinates of the electrons. Using such a determinant obeys the Pauli exclusion principle and makes the wave function antisymmetric as the exchange of two electrons (interchanging two rows) changes the sign of the determinant. The use of a determinant also means that if two electrons have the same spin (two columns are identical) the determinant will be zero.

1.2. Hartree Fock Method

The Hartree Fock method uses the idea of a self-consistent field with a single slater determinant as the wave function. N coupled differential equations are then created for the N orbitals, which are then solved iteratively. These equations are known as the Hartree Fock equations (Equation 1.5).

$$\mathbf{F_i}\phi_i' = \epsilon_i\phi_i'$$

Equation 1.5 – The Hartree Fock equations where $\mathbf{F_i}$ is the Fock operator, a one-electron energy operator, ϕ_i' the canonical MOs, and ε_i the energy.[2]

The Hartree Fock equations are pseudo-eigenvalue equations that must be solved iteratively. The result is the variation of the total energy and not the actual total energy. The total energy is obtained from the wave function. The canonical molecular orbitals (MOs) are used for carrying out the variational calculation. Changing the order of the orbitals does not impact the wave function since rows and columns are just added and subtracted, which does not change the determinant.

Expanding the MOs using a basis set (see 1.4 Basis Sets) gives the Roothaan-Hall matrix equation (see Equation 1.6). These are also pseudo-eigenvalue equations and must be solved iteratively in an SCF procedure.

$$\mathrm{FC} = \mathrm{SC}\varepsilon$$

Equation 1.6 – Roothaan-Hall equation where F is the Fock matrix, C the coefficient matrix, S the overlap matrix, and ε the diagonal matrix of the orbital energies.[2]

The SCF procedure here involves forming a guess matrix of the coefficients, C, and then forming the F matrix. This is then diagonalised and the new coefficients are then used to form a new F matrix. This process is repeated until the coefficients generated from the diagonalisation of F are the same (within a given threshold) to those that are used to generate F.

The computational cost of Hartree Fock calculations typically scales by M^4, where M is the number of basis functions used. Since the accuracy of the results improves with larger basis sets this method can become quite demanding for large systems with a large basis set. If an infinite basis set is used the Hartree Fock limit is reached but is still not the exact solution to the Schrödinger equation due to the missing correlation energy.

1.3. Post-Hartree Fock Methods

In the Hartree Fock method the interaction between electrons is replaced by the interaction of individual electrons with a mean-field. This, however, introduces an error where only approximately 99% of the total energy is obtained. Unfortunately, this remaining 1% is typically needed to describe chemical phenomena. The difference between the Hartree Fock energy and the lowest possible energy using the same basis set is called the correlation energy. If the Hartree Fock limit is reached and the correlation energy with an infinite basis set is obtained the true solution to the electronic Schrödinger equation is obtained.

The addition of a Slater determinant to adhere to the Pauli exclusion principle does introduce some correlation energy into the system. The electrons now avoid each other to not violate the Pauli exclusion principle. This form of correlation is called Fermi correlation where the spin of the electrons is the same. Coulomb correlation is due to the interaction between electrons not being correlated that have the opposite spin.

$$\Psi = \mathrm{a}_0 \Phi_{\mathrm{HF}} + \sum_{\mathrm{i}=1} \mathrm{a}_{\mathrm{i}}\, \Phi_{\mathrm{i}}$$

Equation 1.7 – Post-Hartree Fock methods use the Hartree Fock single Slater determinant wave function, Φ_{HF}, and add excited Slater determinants, Φ_i, to recover more correlation energy. The methods differ in how they calculate the coefficients of these new excited Slater determinants.[2]

Post-Hartree Fock methods seek to recover as much of the correlation energy as possible where the first possibility is to use more than one Slater determinant. The addition of one Slater determinant introduced some correlation energy into the system and further Slater determinants will recover more correlation energy (see Equation 1.7). A basis set that is larger than the minimal basis set produces occupied and unoccupied orbitals. The unoccupied orbitals do not contribute to the energy of the Slater determinant.

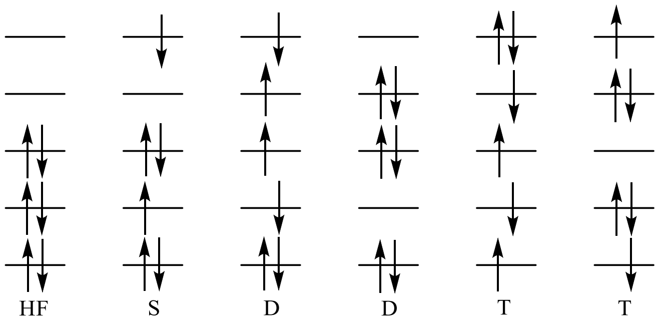

Figure 1.1 – Excited Slater determinants formed from the Hartree Fock determinant. Single (S), Double (D), and Triple (T) Slater determinants are shown as examples of how electrons can be excited to form a many-body wave function.

Excited Slater determinants are formed by occupying these previously unoccupied orbitals but still only describe the ground state of the system. Slater determinants can therefore be singly, doubly, or triply excited by exciting one, two, or three, electrons (see Figure 1.1). These determinants are then referred to as Singles, Doubles, Triples, etc. depending on the number of excited electrons. The number of determinants that can be formed depends on the size of the basis set that is used. The larger the basis set the more excited determinants can be formed and therefore the better the resulting many-body wave function becomes.

Using more Slater determinants recovers more correlation energy but also increases how computationally demanding the calculation is. Using all the possible excited determinants that can be formed with a given basis set recovers all the correlation energy, for that given basis set. Only small systems can be studied accurately whereas much of the correlation energy is recovered as possible. Approximations can be made to speed up the calculation. Since the core electrons are not involved in the chemical transformations that are studied these can be excluded from being excited. This frozen-core approximation therefore only produces excited Slater determinants where the valence electrons have been excited.

The three main methods that include excited Slater determinates are Configuration Interaction (CI), Coupled Cluster (CC), and Many-Body Perturbation Theory (MBPT). These will be discussed briefly in turn.

1.3.1. Configuration Interaction

In Configuration Interaction linear combinations of excited Slater determinants are formed and the coefficients are determined such that the energy is minimised. The determinants are sorted by their level of excitation, starting with the Hartree Fock determinant, then single, double, or triple excited Slater determinants (see Equation 1.8). Full-CI is when every possible excited determinant is included. However, the number of excited determinants grows exponentially, and the expansion must therefore be truncated at some point.

$$\Psi_{CI} = a_o\Phi_{HF} + \sum_{S} a_S\,\Phi_S + \sum_{D} a_D\,\Phi_D + \sum_{T} a_T\,\Phi_T + \cdots = \sum_{i=0} a_i\Phi_i$$

Equation 1.8 – A wave function in CI is formed by starting with the Hartree Fock Slater determinant, Φ_{HF}, and adding linear combination of Single (S), Double (D), Triple (T), etc. excited Slater determinants.[2]

CI singles (CIS) is when the expansion is truncated after the singly excited determinants. Brillouin's theorem however shows that this does not improve upon the HF determinant. CI doubles (CID) is the first method where the wave function is improved upon, followed by CI singles doubles (CISD) as this includes the S/D cross terms.

Truncation is necessary to be able to carry out calculations, however, even with this the equations are still difficult and time consuming to solve. Truncated CI, however, is not size consistent or size extensive. When two identical molecules are brought together, a variety of different doubly excited slater determinants can be formed. It is possible for there to be a double excitation on one molecule, a double excitation on the other, or a single excitation in each. All three examples would be a doubly excited determinant. When the two molecules are separated, eventually the energy should equal twice the energy of the individual CISD energy. However, the double excitation where a single electron is excited in each molecule is now no longer present. This size consistency issue makes it impossible to calculate dissociation energies.

Truncated CI is also not size extensive because the method does not scale with the number of particles. Truncated CI recovered less and less correlation energy as the size of the system is increased. Full-CI is both size consistent and size extensive but can only be used on small systems.

1.3.2. Coupled Cluster

Coupled Cluster uses an exponential ansatz instead of a linear one for the wave function (see Equation 1.9). The cluster operator, **T**, generates all excited Slater determinants of a given type e.g., single, double, triple, etc.

$$\Psi_{\mathrm{CC}} = \mathrm{e}^{\mathbf{T}}\Phi_0$$

$$\mathbf{T} = \mathbf{T}_1 + \mathbf{T}_2 + \mathbf{T}_3 + \cdots + \mathbf{T}_{\mathrm{N_{elec}}}$$

Equation 1.9 – Coupled Cluster wave function where **T** is the cluster operator and Φ_0 the Hartree Fock reference wave function.[1]

If **T** is not truncated, then all possible excitations are included and the wave function will be the same as that produced through full-CI. The strength of CC is the way that truncation works. Coupled Cluster Doubles (CCD) is the first truncation that recovers some of the correlation energy. Coupled Cluster Single Doubles (CCSD) contains both the single and double excitations and greatly improves upon the energy without significantly increasing the demand compared to CCD.

The way that the truncation works means that not only are single and double excitations included but some triple excitations too. Truncated CC methods are size consistent and size extensive because of this. CCSD(T) is most commonly used in the literature where single and double excitations are included explicitly, and the contribution of the triple excitations is estimated through perturbation.

1.3.3. Many-Body Perturbation Theory

Many-Body Perturbation Theory relies on the correlation energy being quite small compared to the total energy and therefore the Hartree Fock energy is a good starting point that is already close. A Hamiltonian operator can therefore be described which is composed of the reference Hamiltonian obtained from Hartree Fock and a perturbation Hamiltonian operator (see Equation 1.10).

$$\mathbf{H} = \mathbf{H_0} + \lambda\mathbf{H}'$$

Equation 1.10 – Hamiltonian operator, **H**, for MBPT using the Hamiltonian obtained from Hartree Fock as a reference Hamiltonian, $\mathbf{H_0}$, and adding a perturbation Hamiltonian, $\mathbf{H'}$. λ is a parameter that determines the strength of the perturbation.[1]

The perturbation parameter, λ, determines the strength of the perturbation and is included as powers in a Taylor expansion of the perturbed wave function and the energy. If λ is zero then the result is just the reference Hamiltonian, $\mathbf{H_0}$, and is known as the zeroth-order wave function and energy. The corrections are referred to as first-order, second order, etc. depending on the number of terms that are included from the Taylor expansion. As with CI, MBPT methods are truncated as an infinite basis set and infinite excited Slater determinants cannot be calculated.

Møller-Plesset (MP) perturbation theory is one of the most used perturbation theory methods. This is because MP methods recover a large amount of correlation energy in a shorter amount of time, when compared to CI.[3–5] MP sums over the Fock operators, but since this counts the electron-electron repulsion twice, the perturbation operator is larger than the reference operator. This method is, however, size extensive, which makes it such a commonly used method. With MP, the order of the method determines the correction that is added. The zeroth-order wave function is the Hartree Fock determinant and so is the first-order wave function.

MP2, where the second-order corrections are included, is the first method to recover correlation energy and typically recovers 80-90 % of the correlation energy. The time needed to calculate the energy using MP2 increases by M^4, where M is the number of basis functions used, and is comparable to the time needed for a Hartree Fock calculation. For MP3 the time increases by M^6 and recovers about 90-95 % of the correlation energy.[6]

CI is the simplest post-Hartree Fock method but unfortunately without full-CI no meaningful results can be obtained. MP perturbation theory, while not as accurate as CC, does a great job at recovering a good amount of correlation energy in a short period of time. The issue can be that if the reference wave function is not a great description of the system the number of corrections terms that are needed to describe the system accurately could be quite high and, in some cases, convergence will not be reached. Errors for perturbation methods can be high since there is no upper bound for the energy but by using relative energies error cancellation leads to decent results.

1.4. Basis Sets

Ab initio methods make use of basis sets to describe the orbitals in the system. Using an infinite basis set means that the Schrödinger equation is solved exactly but this is impossible in actual calculations. The larger the number of basis functions the more accurately the system is described but this increases the computational effort required. Different types of basis functions will describe the atomic orbitals better meaning fewer functions need to be used. It is therefore key to use the smallest number of basis functions while not compromising the accuracy.

1.4.1. Slater and Gaussian Type Orbitals

Slater (STO) and Gaussian (GTO) type orbitals are typically used as basis functions in computational chemistry. Slater orbitals (see Equation 1.11) describe the s orbital for hydrogen very well but as they do not contain any radial nodes p, d, etc. orbitals can only be formed by taking linear combinations of STOs. The exponential dependence results in relatively rapid convergence as more functions are used. STOs naturally have a cusp at the nucleus, where no electrons are located.

$$\phi_{abc}^{STO}(x, y, z) = Nx^a y^b z^c e^{-\zeta r}$$

Equation 1.11 – Slater type orbital functional form where N is a normalization constant and ζ, zeta, determines the width of the orbital where a large ζ gives narrow orbitals and a small ζ gives diffuse orbitals. a, b, and c control the angular moment where a+b+c = L.[2]

GTOs can be expressed in terms of Cartesian coordinates (see Equation 1.12) but also using polar coordinates. Using the polar coordinates can greatly reduce the number of components and thereby speed up calculations. The lack of a cusp for GTOs causes problems as behaviour near the nucleus is not accurately modelled. The shape of an STO is a better model for an orbital as it does not fall off as quickly near the nucleus like a GTO and the tail-end is also not as well described with a GTO. STOs are typically more accurate but linear combinations of GTOs can improve the accuracy. Typically, three times as many GTOs are needed as STOs to achieve the same accuracy. Even though a larger number of GTOs are needed, compared to STOs, they are easier to calculate and are therefore the most common orbital types used.

$$\phi_{abc}^{GTO}(x, y, z) = Nx^a y^b z^c e^{-\zeta r^2}$$

Equation 1.12 – Gaussian type orbital functional form where N is a normalization constant, ζ, zeta, determines the width of the orbital and a, b, and c control the angular moment where a+b+c = L.[2]

1.4.2. Classification of Basis Sets

As the number of basis functions is increased the system is described more accurately. Using an infinite basis set would be ideal but is impossible to calculate. A minimal basis set is one that contains the smallest number of functions to be able to describe the system. For hydrogen and helium this would be a single s-function. A larger basis set can be used where double the number of required functions is used. For hydrogen and helium this would be two s-functions and is referred to as a Double Zeta (DZ) basis set.

Triple (TZ), Quadruple Zeta (QZ), and Quintuple (5Z) basis sets contain three, four, and five times as many functions respectively. Since valence electrons are key for reactivity these are typically described with more basis functions while the core electrons are described by just a single function. These split valence basis sets allow for larger, more accurate, basis sets to be used without needing to use as many resources on the core electrons.

Using a larger basis set than the minimal basis set allows for greater flexibility in the description of the orbitals. This improved flexibility means that systems where the electron distribution is not the same in all directions is better described. Polarization functions can also be added, where higher angular momentum functions are added for certain atoms. For example, giving hydrogen p-functions allows for an asymmetric description of the electron distribution in a bond.

Diffuse functions can also be added where larger functions with the same angular momentum are added to atoms. Diffuse functions have a small zeta exponent in the orbital functional, therefore they are very broad. Addition of these functions is important for anions, electronegative atoms, and for long range effects.

1.4.3. Pople Style Basis Sets

Pople basis sets are split valance basis sets that take the form k-nlmG. The numbers k, n, l, and m indicate how many GTOs have been used to represent an STO. Here k represents the core orbitals and n, l, and m the valence electrons. Two or three numbers in front of the G can indicate a double zeta valence or triple zeta valence basis set. For example, 6-31G is a split valence double zeta basis set, where the core orbitals are described through a contraction of six GTOs. The valence orbitals are split in two, where the inner valence orbitals are described by a contraction of three GTOs, and the outer valence orbitals by just a single GTO. 6-311G is a triple zeta split valence basis set, where the valence orbitals are split into three and described by three, one, and one GTO basis functions.

Polarization and diffuse functions can be added and are indicated by the type of function (p, d, or f) and + respectively. For polarization functions in a Pople basis set the functions added to hydrogen are kept separate from other atoms. A '+' indicates that a set of *s*- and *p*-functions are added for heavier atoms, while a '++' means that a diffuse *s*-function is also added for hydrogen. The 6-311++G(2*d*,2*p*) basis set therefore contains diffuse *s*- and *p*-functions for the heavy atoms and diffuse *s*-functions for the hydrogen atoms. The polarization functions are added both to the heavy atoms and the hydrogen atoms with 2 *d*-functions added for the heavier atoms and 2 *p*-functions for hydrogen atoms.

1.4.4. Correlation Consistent Basis Sets

Correlation consistent (cc) basis sets try to recover the correlation energy of the valence electrons. These basis sets are designed so that addition of further functions of the same type results in a similar contribution as higher angular momentum functions. A second *d*-function therefore provides the same energy stabilisation as the first f-function that is used. The general form of these basis sets is cc-pV*Z where * is either D, T, Q, 5, etc. to indicate a double, triple, quadruple, quintuple, etc. basis set.

The cc-pVDZ basis set consists of 2 *s*- and 1 *p*-functions for the valence orbitals of hydrogen, and 3 *s*-, 2 *p*-, and 1 *d*-functions for the valence orbitals of the first-row elements. Diffuse functions can be added, where one extra diffuse function is added for each angular momentum. For examples the basis set aug-cc-pVDZ contains an extra 1 *s*-, 1 *p*-, and 1 *d*-function.

1.4.5. Karlsruhe Basis Sets

The Karlsruhe basis sets, also referred to as the Ahlrichs basis sets, were developed by Florian Weigend and Reinhart Ahlrichs in Karlsruhe, Germany. The most commonly used of these split valence basis sets are def2-SV(P), def2-SVP, def2-TZVP, def2-TZVPP, def2-QZVP, and def2-QZVPP, where SV stands for split valance (a double zeta basis set), TZV for triple zeta valence, QZV for quadruple zeta valence, (P) indicates partial polarization where polarization functions are not present on hydrogen, P indicates polarization functions are present on all atoms, and PP denotes heavy polarization.[7] For DFT, def2-SV(P) has shown to produce great results especially for geometry optimizations, while the def2-TZVP basis set gives results close to the DFT basis set limit and reduces the errors seen in the bond length and bond angles.[8]

1.4.6. Effective Core Potentials

Atoms lower in the periodic table contain many core electrons. While split valence basis sets mean that only a single GTO can be used to describe the core electrons, this can start to cause issues with describing the valence electrons accurately. Including more functions to describe the core electrons, however, can greatly increase the computational cost and time needed for a calculation. Relativistic effects also need to be considered for heavier atoms.

Using an Effective Core Potential (ECP) or Pseudopotential (PP) replaces the core electrons by a suitable function and only the valence electrons are then treated explicitly. Replacing the core electrons greatly speeds up calculations, takes part of the relativistic effects into consideration, and still describes systems well. While all the core electrons can be replaced by an ECP, results are typically better if the last shell of the core electrons is included explicitly.

1.4.7. Basis Set Superposition Error

Since an infinite basis set cannot be used for calculations, the errors in the absolute energy are typically quite large, and in the region of thousands of kJ mol^{-1}.[6] Relative energies are commonly used in chemistry, the subsequent error cancellation leads to quite accurate and meaningful results. When calculating relative energies only values that have been calculated with the same basis set can be compared. Even if a double zeta basis set is used for two systems, if these do not include the same basis functions the relative energy will be meaningless.

One of the most common errors encountered when using a method that needs a basis set is an effect known as Basis Set Superposition Error (BSSE). This error arises when basis functions on one atom are close enough to also describe the orbitals on other atoms. This addition of more basis functions compensates for the lack of an infinite basis set and, therefore, stabilises sections of a system to a greater extent, when compared to the isolated system. This is particularly a problem for systems where small energy changes are being modelled, such as in van der Waals complexes and hydrogen-bonding.

An example of this is determining the strength of a hydrogen-bond between two formic acid molecules. Since the two monomers are quite close together the atoms that are part of the two hydrogen-bonds are described better in the dimer than in the monomer. The energy of the dimer is, therefore, determined to be lower than it should be and consequently the strength of the hydrogen-bond is overestimated. With an infinite basis set the BSSE is zero and, therefore, including more basis functions reduces the size of the error. However, a large number of basis functions are needed for the error to become negligible, which is not feasible for most calculations.

1.5. Density Functional Theory

Ab initio methods are greatly hindered by the dimensionality of the wave function. So much so that typically only very small systems can be studied at very high levels of theory. An alternative approach is Density Functional Theory (DFT) which utilises the electron density for determining the energy of the system and other related properties. This was made possible by Hohenberg and Kohn who were able to show that the electron density of a system can be used to fully describe the ground state energy. Using a functional, the energy produced would be unique for every electron density.

The scaling issue of *ab initio* methods is solved due to the fixed dimensionality of the electron density, no matter the size of the system being studied. Electrons have three spatial coordinates and one spin coordinates, meaning the wave function for an N-electron system has 4N variables that need to be considered. The electron density, however, is only 3 dimensional no matter the size of the system.

1.5.1. Orbital-Free DFT

The electron density fully describes the system as the number of electrons is determined by integrating the density, the position of the nuclei is determined by the location of cusps in the density, and the charge of these nuclei is given by the height of these cusps. The issue, however, is that the functional that relates the electron density to the energy of the system is not known. Approximate functionals are therefore used to relate these two quantities.

A DFT functional is made up of three parts (see Equation 1.13):

1) The kinetic energy, T
2) The electron/nucleus attraction, E_{ne}
3) The electron/electron repulsion, E_{ee}

$$\mathrm{E_{DFT}} = \mathrm{E_{ne}}[\rho] + \mathrm{T}[\rho] + \mathrm{E_{ee}}[\rho]$$
$$\mathrm{E_{ee}}[\rho] = \mathrm{J}[\rho] + \mathrm{K}[\rho]$$

Equation 1.13 – Standard form of a DFT functional where E_{ne} is the attraction between nuclei and electrons, T is the kinetic energy, E_{ee} is electron-electron repulsion. E_{ee} can be further split into J, the Coulomb term, and K, the exchange term.[1]

As before, the Born-Oppenheimer approximations can be applied so that the nucleus/nucleus repulsion is a constant (and the kinetic energy of the nuclei is zero). The electron/electron repulsion can be further divided into the coulomb and exchange contributions from Hartree Fock, which would include electron correlation. The earliest functionals considered a uniform electron gas where the coulomb and exchange contributions are calculated analytically. The aim was to find a uniform gas where the density is the same as the molecule being studied, which is known as Thomas-Fermi theory. The Hohenberg-Kohn theorem states that the energy of these two systems would be identical since the density is identical.

While the uniform electron gas was found to work in some situations, especially for metallic systems, it did not work for atoms and molecules, so much so that atoms were shown to not be able to form molecules. The Thomas-Fermi theory is improved by adding correction terms, describing now a non-uniform gas instead. However, this is not as accurate as *ab initio* methods.

1.5.2. Kohn-Sham Theory

Kohn and Sham realised that it was the kinetic energy term that was causing issues and re-formulated the expression. This involved reintroducing orbitals through a Slater determinant. Only a single Slater determinant needs to be used since DFT already described the energy. The kinetic energy is split into two terms, where one can be calculated exactly, and the other is a small correction term. The re-introduction of orbitals does increase the complexity of the wave function from 3 to 3N variables. Along with this, electron correlation once again emerges as a problem.

Kohn-Sham DFT (KS-DFT) is now the most widely used method for calculations on large systems. The computational cost can often be comparable to that for Hartree Fock calculations, but correlation energy is now included. The orbitals that are used in KS-DFT and Hartree Fock are, however, very different. The key part in Kohn-Sham functionals (see Equation 1.14) is the exchange-correlation functional, E_{XC}, as this is the only unknown part and the way that it is tackled is what differentiates all the KS-DFT functionals.

$$\mathrm{E_{DFT}}[\rho] = \mathrm{T_S}[\rho] + \mathrm{E_{ne}}[\rho] + \mathrm{J}[\rho] + \mathrm{E_{XC}}[\rho]$$

Equation 1.14 – General Kohn-Sham DFT functional expression where T_S is the kinetic energy term, E_{ne} is the attraction between the nuclei and electrons, J is the Coulomb term, and E_{XC} is the exchange-correlation term.[1]

The exchange-correlation functional can be approximated or parametrised. However, this starts to cause issues as DFT may begin to be considered as a semi-empirical method. Local Density Approximation (LDA) functionals assume that the electron density only depends on the position in space. This approximation typically works well in the solid state but not for molecules. General Gradient Approximation (GGA) functionals include the first derivative of the density, which greatly improves the performance, e.g. BP86, PW91. Hybrid functionals use Hartree Fock exchange and mix it with the exchange-correlation functions since Hartree Fock calculates the exchange exactly. B3LYP is the most commonly used hybrid functional.

DFT struggles to describe weak interactions well and is best suited for systems where molecules are strongly bound. Large, weak anions are difficult to calculate along with excited states. Another issue with DFT is that there is no systematic way to improve upon this method. Using a larger basis set does not give more accurate energies if the functional being used is not suited for the system being studied.

1.6. Empirical and Semi-Empirical Methods

Ab initio methods produce accurate results, but the use of the underlying physics does make these methods time demanding. Empirical methods, such as Molecular Mechanics (MM), use parameters that are generated from experiment and do not utilise the underlying physics. This makes these methods much faster, but the accuracy depends on the force field containing the parameters.

$$\mathrm{E_{FF}} = \mathrm{E_{str}} + \mathrm{E_{bend}} + \mathrm{E_{tors}} + \mathrm{E_{non-bond}}(+\mathrm{E_{cross}})$$

Equation 1.15 – Total energy of a system using a force field where E_{str} is the energy of stretching of a bond, E_{bend} is the energy of bending a bond, E_{tors} is the torsional energy of rotating a bond, $E_{non\text{-}bond}$ is the energy of non-bonding interactions, and E_{cross} is the energy of coupling of the stretch, bend, and torsion term but are not always included in a force field.[1]

Different parameters must be generated for not just each element but also atom type since an oxygen in an alcohol will have very different parameters to an oxygen in a ketone. A force field is generated by considering all possible unique interaction. The total energy of the system is then calculated by summing the interactions (see Equation 1.15).

1.6.1. Stretching term

The energy needed to stretch the bond between two atoms A and B is modelled by a spring. This can be expressed using a Taylor expansion terminated at second order (see Equation 1.16). This expression is known as the harmonic oscillator, where k^{AB} is the force constant for the A-B bond.

$$\mathrm{E_{str}}\left(\mathrm{R^{AB}} - \mathrm{R_0^{AB}}\right) = k^{AB}(\mathrm{R^{AB}} - \mathrm{R_0^{AB}})^2$$

Equation 1.16 – Taylor expansion terminated at second order to describe the energy as a bond between atom A and atom B is stretched from an equilibrium bond length, R_0.[1]

Terminating the Taylor series here works well for many systems, but it does not describe vibrational frequencies well or strained ring systems. Expanding further introduces more force constants that need to be fitted. Using a Morse potential (see Equation 1.17) provides a better description for a typical energy curve as this allows for the energy to converge towards the dissociation energy, D.

$$\mathrm{E}\left(\mathrm{R}^{\mathrm{AB}}-\mathrm{R}_0^{\mathrm{AB}}\right)=\mathrm{D}\left(1-\mathrm{e}^{-\sqrt{\frac{k}{2D}}\left(\mathrm{R}^{\mathrm{AB}}-\mathrm{R}_0^{\mathrm{AB}}\right)}\right)^2$$

Equation 1.17 – Morse potential to describe the energy as a bond between atom A and atom B is stretched from an equilibrium bond length, R_0. D is the dissociation energy.[1]

This model is close to an actual potential for a diatomic. For each atom in the system being modelled a different set of parameters needs to be used to describe a single, double, and triple bond.

1.6.2. Bending term

To describe the energy needed to change the bond angle between atom A, atom B and atom C from its equilibrium bond angle, θ_0, a Taylor expansion is used and terminated at second order (see Equation 1.18).

$$\mathrm{E}_{\mathrm{bend}}\left(\theta^{\mathrm{ABC}}-\theta_0^{\mathrm{ABC}}\right)=\mathrm{k}^{\mathrm{ABC}}\left(\theta^{\mathrm{ABC}}-\theta_0^{\mathrm{ABC}}\right)^2$$

Equation 1.18 – Taylor expansion at second order to describe the energy as a bond angle is bent between atom A, atom B, and atom C from its equilibrium bond angle, θ_0.[1]

Terminating at the second term describes most systems well but if higher accuracy is required a third order term can be added without issues.

1.6.3. Torsional term

A change in dihedral angle is modelled by a periodic function. A change in energy is seen when a dihedral angle is altered due to the difference in attractive and repulsive forces in different conformations. A rotation of 360° brings the molecule into the same position making a periodic function is ideal for describing a change in the dihedral angle. A Fourier series (see Equation 1.19) is used and expanded as a series of cosine functions.

$$E_{tors}(\omega) = \sum_{n=1} V_n \cos(n\omega)$$

Equation 1.19 – A Fourier series to describe the energy as a dihedral angle, ω, between atom A, atom B, atom C, and atom D is altered in a system, where n determines the periodicity and V_n describes the size of the barrier for rotation around the B-C bond.[1]

1.6.4. Non-bonding term

The last term encompasses all interactions that are non-bonding that are present in the system. It is important to not double count interactions. The Lennard-Jones potential (see Equation 1.20) is used to describe van der Waals interactions as it correctly shows that at large distances the energy is zero but at close distances very quickly becomes repulsive.

$$E_{LJ} = \varepsilon\left[\left(\frac{R_0}{R}\right)^{12} - 2\left(\frac{R_0}{R}\right)^{6}\right]$$

Equation 1.20 – Lennard-Jones potential to describe the van der Waals interactions where R_0 is the minimum energy distance and ε is the depth of the minimum.[1]

Charge and dipole dependent terms can also be added, which are typically described by the Coulomb potential (see Equation 1.21).

$$E_{el}\left(R^{AB}\right) = \frac{Q^A Q^B}{\varepsilon R^{AB}}$$

Equation 1.21 – Coulomb potential to describe the interaction of two point charges, A and B, where ε is the dielectric constant.[1]

For dipole/dipole interactions the directionality of the dipole is important. The interaction between two dipoles can be seen in Equation 1.22.

$$E_{el}\left(R^{AB}\right) = \frac{\mu^A \mu^B}{\varepsilon (R^{AB})^3}(\cos\chi - 3\cos\alpha_A \cos\alpha_B)$$

Equation 1.22 – Interaction between two dipoles, A and B, where χ, α_A, and α_B describe specific angles between the interaction dipoles.[1]

Since double counting of interactions leads to not modelling the system accurately often either charge or dipole terms are included and not both since dipole terms can be represented by charge distributions.

1.6.5. Cross-coupling terms

Cross-coupling terms are sometimes added and greatly improve the performance of MM. These terms describe how the other terms impact each other and are typically expressed as products of first-order Taylor expansions (see Equation 1.23).

$$\mathrm{E}_{\mathrm{str/bend}} = \mathrm{k}^{\mathrm{ABC}}\left(\theta^{\mathrm{ABC}} - \theta_0^{\mathrm{ABC}}\right)[\left(\mathrm{R}^{\mathrm{AB}} - \mathrm{R}_0^{\mathrm{AB}}\right) - ((\mathrm{R}^{\mathrm{BC}} - \mathrm{R}_0^{\mathrm{BC}})]$$

Equation 1.23 – An example of a stretch/bend cross-coupling term for A-B-C formed through the product of first-order Taylor expansions.[1]

A variety of cross-coupling terms can be included to account for the impact that stretching one bond has on another, a bend has on a dihedral angle, and even a cross-coupling term that considers how three terms impact each other. Typically this cross-coupling term is only added to one of the atoms in the bond, angle, dihedral angle instead of all of them.

1.6.6. Semi-Empirical Methods

Semi-empirical methods are combination of *ab initio* and empirical methods. Hartree Fock is used as a starting point and simplified by reducing the number of two-electron integrals needed to construct the Fock matrix. The number of integrals needed can be reduced by only considering the valence electrons explicitly and the core electrons are accounted for by reducing the nuclear charge or using a function to model the nuclear charge and the core electrons together. Along with this a minimal basis set is used, which also greatly speeds up the calculations. Semi-empirical methods such as Modified Neglect of Diatomic Overlap (MNDO), Austin Model 1 (AM1) and Parametric Method number 3 (PM3) are some of the most used methods and can be useful as a starting point to generate structures that can then be used for further *ab initio* calculations.

1.7. Geometry Optimizations

Computational methods try to optimise geometries by finding stationary points on a potential energy surface. These points are where the gradient, the first derivative, is zero. Minima correspond to a position on the PES where the second derivative is positive in all directions. Saddle points are where the second derivative is negative in one direction but positive in all others and in mechanistic studies are referred to as transition states (TS).

1.7.1. Finding Minima

A PES can be composed of many minima and saddle points. The lowest energy minimum on a surface is referred to as the global minimum while all others are local minima. Finding minima involves determining the first derivative, the gradient, and for some methods the second derivative. Two of the most common methods are described below.

1.7.1.1. Steepest Decent

The steepest descent method of finding a minimum evaluates the gradient and follows it downhill. This method will always find a minimum because even when a minimum has been passed and the function increases again the method will step into the opposite direction towards the minimum. One of major issues with steepest descent is for very shallow PESs where the desired minimum can be overstepped. The true minimum is never located with this method as it only slowly approaches it at an ever-decreasing speed. Convergence is reached when the change in the gradient reaches a certain threshold where the change becomes very small.

1.7.1.2. Newton-Raphson

Newton-Raphson uses the second derivative of the function known as the Hessian, **H**, and is not limited to just finding minima. Near a minimum all the values in the Hessian will be positive and a step in the opposite direction, as with steepest decent, is taken. If one of the values, however, is negative the direction of the step will be uphill, and a first-order saddle point can be found instead of a minimum. Newton-Raphson will converge to the nearest stationary point, so the chosen input structure needs to be close to the final structure of the chosen stationary point.

The step size for this method can reach infinity if one of the values in the Hessian is close to zero. This can lead to incorrect structures and potentially the method will not converge. By introducing a shift parameter, the step length can be controlled along with ensuring that the method only takes steps downhill when a minimum is desired. The advantage with Newton-Raphson is that structures that are close to the desired stationary point will converge very quickly. Calculating, storing, and inverting the Hessian can be very demanding for some calculations. This can be overcome by using an approximate Hessian, which is updated as the optimization proceeds.

1.7.2. Finding First-Order Saddle Points

While there are a variety of methods for finding minima and the steepest descent method is guaranteed to lead to a minimum there is no such method for finding first-order saddle points. Two general categories exist for finding transition states, which either rely on knowing two minima (interpolation methods) or by directly determining the structure (local methods).

1.7.2.1. Interpolation Methods

Interpolation methods require that the geometries of the starting minimum and the product minimum, which are connected by the transition state, are known. The transition state structure can be determined by determining the reaction coordinates that are changing from the starting material to the product. These changing variables are optimized while the rest are kept fixed. Methods such as this are referred to as “coordinate driving” and work for systems where only one or two variables are changing significantly. With these methods only one structure is optimized to locate the transition state.

The Saddle algorithm is a two structure interpolation method, where the geometry of the starting minimum is displaced slightly towards that of the product geometry. This structure is then optimized, and the process repeated until convergence is reached. There are also methods that use more than two structures such as the Self-Penalty Walk and the Chain method, which calculate energies along a reaction coordinate to find the maximum.

Interpolation methods struggle when there either is no transition state or multiple transition states between two points.

1.7.2.2. Local Methods

Local methods rely on having a good idea of the geometry of the transition state and using this as a starting point. Newton-Raphson, as mentioned in 1.7.1.2, can locate a transition state if the starting structure is close to the desired stationary point. The limitations of this method are that convergence is only reached, and reached quickly, when a guess structure is used that is close to the transition state. The method also requires calculating the Hessian, which is computationally expensive.

The dimer method works the same as Newton-Raphson but instead of calculating the Hessian, to determine the direction of the next step, two close-lying structures are used. The two structures, the dimer, on the potential energy surface have almost identical coordinates but are slightly displaced by a small distance. The method reaches a saddle point by moving the dimer uphill on the PES by rotating and translating the dimer.

Local methods converge rapidly when a starting geometry close to the desired saddle point is known. Without a good starting structure, the wrong transition state, or even a minimum, can be located if the calculation does converge.

1.7.2.3. Piecing Everything Together

Once a transition state has been located confirmation is needed that it connects to the desired two minima either side of it. Intrinsic Reaction Coordinate (IRC) and Dynamic Reaction Coordinate (DRC) calculations can be used for this. IRC calculations follow the PES downhill by methods such as steepest decent. The points located by an IRC calculation are not guaranteed to be minima and should be optimized to confirm that the transition state does lead to the desired minima.

DRC calculations are slightly different in that the system is either slightly deflected along the reaction coordinate or some initial momentum is supplied. The motion of the atoms is determined similar to molecular mechanics. As with IRC calculations the two end points are not necessarily minima on the PES and should be optimized to locate the minima that the transition state leads to.

1.8. Transition-State Theory

Geometry optimizations of both minima and first-order saddle points along with IRC or DRC calculations result in a PES of the reaction. Transition-State Theory (TST) is used to understand how reactions occur where the dynamics along the reaction coordinate are treated classically while the vibrational and rotational energy states are quantized to account for their quantum nature. The probability of finding a molecule in a given quantum state is calculated by the Boltzmann distribution. The rate constant can be expressed in terms of the Gibbs free energy difference between the transition state and the reactant, given as they are in equilibrium (see Equation 1.24).

$$\mathrm{k_{rate}} = \frac{k_B \mathrm{T}}{\mathrm{h}} \mathrm{e}^{\frac{-(\Delta \mathrm{G_{TS}} - \Delta \mathrm{G_{reactant}})}{\mathrm{RT}}}$$

Equation 1.24 – Macroscopic rate constant, k_{rate}, given by the difference between the Gibbs free energy of the TS, ΔG_{TS}, and the reactant, $\Delta G_{reactant}$. This equation is only accurate when the TS is in equilibrium with the reactants and that all molecules that pass over the TS become products.[1]

This macroscopic rate constant, k_{rate}, is an upper limit to the true rate constant since it is assumed that all molecules that pass through the TS become products. No re-crossing is therefore allowed. A transmission coefficient, κ, can be used to allow for re-crossing and to account for tunnelling, which can be important for hydrogen transfers. TST assumes that the internal energy redistribution *via* vibrations is much faster than the time for bond forming or bond breaking. The rate of reaction, therefore, depends on the amount of internal energy and not the type of internal energy i.e. bending and stretching vibrations are treated the same.

Calculations are typically carried out on a small number of particles, which form a microscopic system, while experiments are performed on macroscopic samples. Statistical mechanics connects the properties of a microscopic system to the properties of a macroscopic system.

If a PES of a reaction can be obtained the Gibbs free energy changes can be used to determine an idea of the rate of the reaction. The rate of a reaction can then be used to infer details about the yield of a reaction. The faster the rate of a reaction, the higher the yield of a reaction should be. This assumes, like the rate constant, that all of the molecules that proceed through the TS become product i.e. no side reactions are occurring.

1.8.1. Statistical Mechanics

Statistical mechanics uses partition functions, q, to calculate macroscopic functions. For a single particle the partition function is a sum over all energy levels, ε_i (see Equation 1.25).

$$\mathrm{q} = \sum_{\mathrm{i=levels}}^{\infty} \mathrm{g_i} \mathrm{e}^{-\frac{\varepsilon_i}{\mathrm{k_B T}}}$$

Equation 1.25 – Partition function, q, for a single particle where ε_i is the energy of the level, k_B is the Boltzmann constant, and g_i is the degeneracy factor showing the number of levels with the same energy.[1]

For a collection of particles the partition function, Q, is determined differently depending on whether the particles are interacting or not. For identical non-interacting particles, such as for an ideal gas, the partition function is given by Equation 1.26.

$$Q = \frac{q^N}{N!}$$

Equation 1.26 – Partition function, Q, for N identical non-interacting particles, where q is the partition function of a single particle.[1]

For interacting particles, such as in the liquid or solid state, the partition function is determined by summing over all energy states, E_i, for all particles, N (see Equation 1.27).

$$Q = \sum_{i=\text{states}}^{\infty} e^{-\frac{E_i}{k_B T}}$$

Equation 1.27 – Partition function, Q, for interacting particles where E_i is the energy state for all particles.[1]

The total partition function for a polyatomic molecule can be determined by taking the product of the translational, rotational, vibrational, and electronic partition functions (see Equation 1.28). This separation of the partition function is possible because of the rigid-rotor harmonic-oscillator approximation when dealing with an ideal gas.

$$q_{tot} = q_{trans} q_{rot} q_{vib} q_{elec}$$

Equation 1.28 – Total partition function, q_{tot}, given by the product of the translational (q_{trans}), rotational (q_{rot}), vibrational (q_{vib}), and electronic (q_{elec}) partition functions.[1]

1.8.1.1. Translational Partition Function

The translational energy can be determined by using a 'particle in a box', where the potential energy inside the box is zero and infinite outside. This box results in standing waves, cosine and sine functions, as solutions to the Schrödinger equation. The total energy levels are given by Equation 1.29.

$$\varepsilon_n = \frac{n^2 h^2}{8\pi^2 M}$$

Equation 1.29 – Particle in a box. The total energy levels is dependent on the mass, M, and is associated with the quantum number n.[1]

The energy of the levels is quantized but the energy difference is very small and can therefore be treated as continuous. Summing over the energy levels using the partition function allows the use of an integral as seen in Equation 1.30.

$$q_{trans} = \sum_{n=0}^{\infty} e^{-\frac{\varepsilon_n}{k_B T}} \approx \int_{n=0}^{\infty} e^{-\frac{\varepsilon_n}{k_B T}} dn$$

Equation 1.30 – Translational partition function, q_{trans}, can be determined using an integral due to the summation of energy levels with small energy differences.[1]

Combining Equation 1.29 and Equation 1.30 gives an expression where the only molecular parameter that determines the translational partition function is the molecular mass M (see Equation 1.31).

$$q_{trans} = \left(\frac{2\pi MkT}{h^2}\right)V$$

Equation 1.31 – Expression for the translational partition function, which is dependent on the molecular mass, M, and the volume, V.[1]

1.8.1.2. Rotational Partition Function

Using the rigid-rotor approximation, where the rotation of a molecule is assumed to occur without any change in geometry, the energy levels for a diatomic are given by Equation 1.32.

$$\epsilon_J = J(J+1)\frac{h^2}{8\pi^2 I}$$
$$I = m_1 r_1^2 + m_2 r_2^2$$

Equation 1.32 – Rotational energy levels shown in terms of the quantum number J. The moment of inertia, I, is given by the atomic masses of the two atoms, m, and the distance of the nuclei to the centre of mass, r.[1]

As with the translational partition function the spacing between the energy levels is very small so an integral can therefore be used to replace the summation and give the expression for the rotational partition function shown in Equation 1.33.

$$q_{rot} = \frac{8\pi^2 IkT}{h^2\sigma}$$

Equation 1.33 – Rotational partition function, q_{rot}, is dependent on the moment of inertia, I, and the symmetry index, σ, which is 2 for a homonuclear diatomic and 1 for a heteronuclear diatomic.[1]

For a non-liner polyatomic system the expression becomes much more complex, and an approximation is used to give the rotational partition function (see Equation 1.34). The rotational partition function for a polyatomic therefore depends on the mass of the atoms and their geometry.

$$q_{\mathrm{rot}} = \frac{\sqrt{\pi}}{\sigma}\left(\frac{8\pi^2 kT}{h^2}\right)^{3/2} \sqrt{I_1 I_2 I_3}$$

Equation 1.34 – Rotational partition function for a non-linear polyatomic system. The symmetry index, σ, is now given by the number of proper symmetry operations for the molecule. The inertia is now given by a 3x3 matrix.[1]

1.8.1.3. Vibrational Partition Function

A harmonic oscillator is the simplest approximation that can be used to describe molecular vibrations and leads to the energy expression shown in Equation 1.35. Unlike the translational and rotational partition function the spacing between the energy levels for vibrations is much larger and an integral can no longer be used to replace the summation.

$$\varepsilon_n = \left(n + \frac{1}{2}\right) h\nu$$

$$\upsilon = \frac{1}{2\pi}\sqrt{\frac{k}{\mu}}$$

$$\mu = \frac{m_1 m_2}{m_1 + m_2}$$

Equation 1.35 – Vibrational energy levels, where ν is the vibrational frequency, k the force constant, and μ the reduced mass.[1]

The vibrational partition function can be simplified due to the regular spacing between the vibrational states. Both the summation and the simplified form can be seen in Equation 1.36.

$$q_{\mathrm{vib}} = \sum_{n=0}^{\infty} e^{-\frac{\varepsilon_n}{2kT}}$$

$$q_{\mathrm{vib}} = \frac{e^{-\frac{h\nu}{2kT}}}{1 - e^{-\frac{h\nu}{2kT}}}$$

Equation 1.36 – Vibrational partition function, q_{vib}, can be simplified due to the regular spacing between the energy levels, ε_n.[1]

For a polyatomic molecule a new set of coordinates are formed called vibrational normal coordinates where the vibrational modes can be considered independent of each other. The vibrational energy levels are then expressed as a sum over all vibrational modes in the molecule (see Equation 1.37). The number of vibrational modes, n_{vib}, is 3N-6 (3N-5 for a linear molecule). For a transition state one of the vibrational modes will be negative and is therefore an imaginary mode which is not considered. The number of vibrational modes for a transition state is therefore 3N-7.

$$E_{vib} = \sum_{i=1}^{n_{vib}} \left(n_i + \frac{1}{2}\right) h\nu_i$$

Equation 1.37 – Vibrational energy levels in a polyatomic atom where n_{vib} is the number of vibrational modes in the molecule and ν_i is the vibrational frequency of the i^{th} vibrational mode.[1]

The vibrational partition function from these vibrational energy level using the normal coordinates is then a product as seen in Equation 1.38.

$$q_{vib} = \prod_{i=1}^{n_{vib}} \frac{e^{-\frac{h\nu_i}{2kT}}}{1 - e^{-\frac{h\nu_i}{2kT}}}$$

Equation 1.38 – Vibrational partition function for a polyatomic molecule.[1]

1.8.1.4. Electronic Partition Function

The electronic partition function is a sum over all electronic quantum states and like the vibrational partition function an integral cannot be used due to the large spacing between energy levels. The spacing is now so large that typically only the first term, corresponding to the ground state energy, is important (see Equation 1.39).

$$q_{elec} = \sum_{i=0}^{\infty} g_i e^{-\frac{\varepsilon_i}{kT}} \approx g_0 e^{-\frac{\varepsilon_0}{kT}}$$

Equation 1.39 – The electronic partition function, q_{elec}. This is typically just dependent on the energy of the ground state due to the large spacing between energy levels.[1]

1.9. Solvation

A change in solvent can have an immense impact on a reaction, such as which product is preferentially formed along with reaction yields. A solvent is essential in a reaction as it dissolves the solutes, can act as a nucleophile, stabilise charge, act as an acid/base, stabilise the solute through hydrogen-bonding, and even change spectroscopic properties. Selecting the wrong type of solvent for a reaction can significantly influence the results.[15–20]

The inclusion of solvent in computational chemistry has been an on-going challenge. Solvent effects can be accounted for in two ways by including the solvent implicitly or explicitly in the calculation. A solvent will typically outnumber the solute, and thus most of the computational resources would be dedicated to the modelling of the bulk solvent. This is significant as most of the solvent molecules will not play a direct role in a reaction.

Determining the nature of solvent effects can be extremely difficult. Using robust experimental data, quantum chemical calculations can shed a light on these solvent effects. The synergy between experimental and computational work is crucial to be able to get a deep understanding of what could be occurring during a reaction.

1.10.1 Implicit Solvation Corrections

Solvation effects can be split into long- and short-range interactions. Long-range interactions include polarization and dipole orientation while short-range interactions include hydrogen-bonding, solvent-solute dynamics, and charge transfer effects. Continuum solvation models typically model the non-specific effects of solvation. Here a solute, S, is placed in a cavity inside the solvent which has a dielectric constant, ε (see Figure 1.2). Creating this cavity has a destabilizing effect but the system is typically then stabilized by solvent-solute interactions.

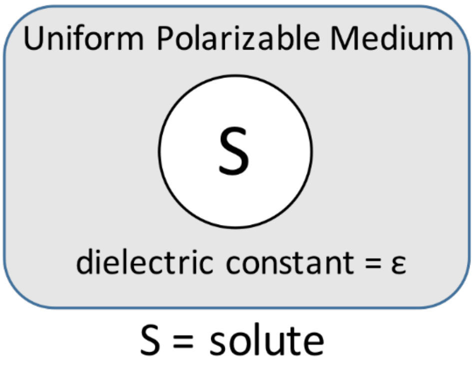

Figure 1.2 - Continuum solvation models treat the solvent as a uniform polarizable medium where only the dielectric constant ε determines the solvent that is used. A hole is made in this medium and the solute, S, is placed inside.

There are a variety of different continuum solvation models and typically differ in:

1) how the size and shape of the hole is defined
2) how the cavity and dispersion contribute to the solvation energy
3) the charge distribution of S
4) whether the solute is described by a force field or quantum mechanically
5) how the medium is described

For models that use only the dielectric constant to differentiate the solvent an issue arises in systems where hydrogen-bonding is known to stabilize a system or when the shape of the two solvents is vastly different. Models have been developed that include other parameters to differentiate between solvents.

With implicit solvent models the solvent is modelled as a continuous medium instead of individual explicit solvent molecules. These implicit models are most used as this does not greatly increase the computational cost, can be easily added at a later point as a correction, and the solvent can easily be altered. However, not all solvent effects are accounted for with this method and solvents with similar or identical dielectric constants will give the same results. For example, the hydrogen-bonding capability of 1-propanol (ε = 20.1) is quite different to that of acetone (ε = 20.7).

In general, implicit solvation models work well on a large range of systems but they do occasionally fail to replicate experimental data.[21–23] Most implicit models will not account for the entropic effects of the hydrophobic effect without a correction being applied.[24] Other effects in the first few solvation shells that are also difficult to describe using an implicit model are dispersion, hydrogen-bonding where structure distortions can occur resulting in wrongly predicted favoured structures, and the nonlinear response of the solvent with a highly charged solute.[23,25]

Implicit solvation methods such as the Polarizable Continuum Method (PCM), the Conductor-like Screening Model (COSMO), the Solvation Model based on Density (SMD), and many others are used extensively in the literature, with multiple reviews existing in the literature.[10,24,26–28]

1.9.1.1. Poisson-Boltzmann methods

The Poisson equation (see Equation 1.40) connects the electrostatic potential, the charge distribution, and the dielectric constant.[1]

$$\nabla^2\phi(\boldsymbol{r}) = -\frac{4\pi}{\varepsilon}\rho(\boldsymbol{r})$$

Equation 1.40 – The Poisson equation, linking the electrostatic potential (ϕ), the charge distribution (ρ), and the dielectric constant (ε).

This equation can be modified by including a thermal Boltzmann distribution of ions in the solvent. The negative ions in the solvent will be where there is a positive potential while the positive ions will accumulate where there is a negative potential. The addition of this Boltzmann distribution leads to the Poisson-Boltzmann equation (see Equation 1.41).

$$\nabla.\left(\varepsilon(\boldsymbol{r})\nabla\phi(\boldsymbol{r})\right) - \kappa^2\left(\frac{kT}{q}\right)\sinh\left(\frac{q\phi(\boldsymbol{r})}{kT}\right) = -4\pi\rho(\boldsymbol{r})$$

$$\kappa^2 = \frac{8\pi q^2 I}{kT}$$

Equation 1.41 – The Poisson-Boltzmann equation where I is the ion strength of the solution, ϕ the electrostatic potential, ρ the charge distribution, and ε the dielectric constant.

If the solute is not strongly charged the potential will be small and a Taylor expansion can be used to express sinh(x). Using just the first term from this Taylor expansion gives the Linearised Poisson-Boltzmann Equation. These differential equations, when solved, give the electrostatic potential at any given point in the solvent. This can then be used with the solute to determine where interactions with polar molecules are likely to occur.

1.9.1.2. PCM and COSMO

PCM and COSMO both use molecular shaped cavities and use the dielectric constant of the solvent in the calculations. PCM uses a van der Waals cavity, which is formed by using the van der Waals radii of the atoms, scaled by an empirical factor. It also uses a detailed description of the electron static potential based on the Poisson-Boltzmann equation. COSMO uses a scaled conductor boundary condition and can be considered to be the PCM method with the dielectric constant set to infinity. Both methods are used extensively in the literature and updates to the PCM method have been made to incorporate parts of the COSMO method, known as C-PCM. An improvement has been made to COSMO via statistical thermodynamics known as COSMO-RS.[29–32]

1.9.2. Explicit Solvation

Explicit solvation involves including solvent molecules in the calculation (see Figure 1.3). Hydrogen-bonding can therefore be directly included, and different solvent molecules will interact with the solute differently. However, the computational cost can be enormous, the number of possible conformations is greatly increased with each added solvent molecule, and all calculations must be redone when investigating a different solvent. Typically, solvent effects are investigated by adding a small number of solvent molecules first and then slowly increasing the number, ideally until no change in the property of interest is observed when another molecule is added. Examples of purely explicit solvation are much more limited, mainly due to the higher computational cost and the greater number of degrees of freedom.[33–35]

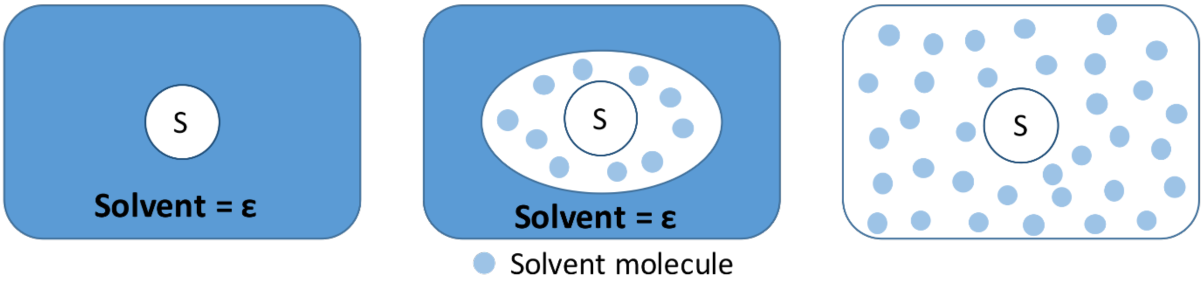

Implicit Solvation

Hybrid Implicit/Explicit Solvation

Explicit Solvation

Figure 1.3 - Solvation of a solute, S, can be dealt with computationally by including the solvent implicitly, explicitly, or by a combination of the two.

A hybrid explicit/implicit method is also possible where a few solvent molecules, typically the first solvation sphere, are included explicitly and the bulk is modelled implicitly (see Figure 1.3). Garcia-Rates *et al.* investigated the decomposition of methanol on metal surfaces.[36] To be able to reproduce experimental data an implicit/explicit method needed to be used where two water molecules were explicitly included.

Similarly Wong *et al.* determined that both an implicit model with an explicit methanol molecules needed to be used when modelling a nucleophilic addition reaction using Au(III).[36] The reaction between propyne and methanol, acting both as the solvent and nucleophile, using a $AuCl_3$ catalyst was modelled to determine the mechanism. It was found that explicit methanol molecules were needed to accurately model this system as it had been proven previously that the hydrogen-bonding network that is set up is crucial for locking the nucleophile, MeOH, in place for the reaction to occur (see Figure 1.4).

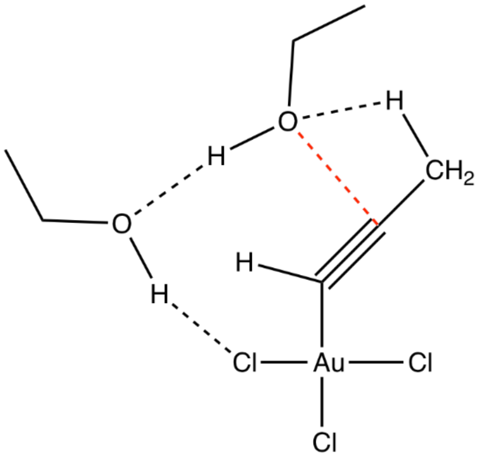

Figure 1.4 - A hydrogen-bonding network (black dashed lines) is set up to lock the methanol molecule in place for nucleophilic attack (red dashed line).

1.10. Aims

Quantum chemistry is able to provide great insight into reaction systems in a way that experimental investigations cannot. The barriers and states involved in a reaction can be obtained, however, accurate results depend on the availability of accurate and extensive experimental data. Access to experimental data means benchmarking of different methodologies must be carried out to test whether they are working for the chosen system. The degree of conformational space that needs to modelled can also be reduced as the experiments can cut down on the number of possibilities that need to be considered. With such experimental data, insights from the computational work can be used for further experimental work such as suggesting alternative ligands, metals, reactants, etc.

The aim of this work is to provide insight into reactions and to utilise more computationally demanding resources when the system requires it. In Chapter 2 the barriers for abstraction of hydrogen by F atoms in an ionic liquid will be investigated. With access to the barriers at each position on the ionic liquid, it will be possible to determine where the F atom is most likely to abstract a hydrogen. The experimental data was obtained at the gas-liquid interface, suggesting that gas-phase calculations would be sufficient to accurately model this system.

In Chapter 3 a phosphoramidation reaction between an alkyne and a Cp*Ir(III) phosphoramidate complex is examined to determine the origin of the regio- and stereoselectivity. This reaction was carried out in CH_2Cl_2, as such it is likely that implicit solvation corrections will be needed. The authors of the experimental study suggested that the solvent did not take an active role in the reaction, suggesting an explicit solvent model will not be needed.

Finally, in Chapter 4 two fluorinated solvents were found to greatly increase the rate of reaction in two reverse electron-demand Diels-Alder reactions. The occurrence of these solvent effects can be determined by generating the PES of both reactions with the solvent accounted for. The strong solvent effects seen in the reaction suggests that an implicit solvent model will not be enough to be able to predict the barriers of the reaction and determine the nature of the solvent effects.

All three chapters involve determining the ideal methodology to model the system accurately and shed light on the potential mechanism of the reaction. Each system requires a different solvent treatment, due to the different environments of the reactions. All three systems will make use of the available experimental data to increase the confidence in the computational results and the methodology chosen.

2. Investigating Hydrogen Abstraction from Ionic Liquids by F atoms

2.1. Introduction

Room-temperature ionic liquids (RTILs) are molten salts with a melting point below 100 °C. The research in this field has grown immensely over the last 20 years, due to their wide range of applications, including their potential as “green solvents”. Along with this, properties such as high thermal stability, high viscosity, and high ionic conductivity make them extremely desirable as solvents in synthesis but also applications where they act as lubricants, plasticisers, catalysts, and electrolytes.[47–50] Studies of mixtures have been carried out to determine whether the desired properties can be obtained through a mixture instead of needing to synthesise a pure single ionic liquid.[51,52]

A RTIL consists of an organic cation and a weakly coordinating anion. 1-alkyl-3-methylimidazolium cations (see Figure 2.1) are the most widely used in ionic liquids and are typically synthesised with a BF_4^-, NTf_2^-, NO_3^-, OTf^- or PF_6^- anion. By changing the alkyl chain length and the anion the chemical and/or physical properties of the ionic liquid can be adjusted.

The focus of the literature review below will be on research investigating the gas-liquid or vacuum-liquid surface of imidazolium based RTILs. First some of the commonly used techniques for surface investigations will be covered, followed by a more in-depth look at reactive-atom scattering methods.

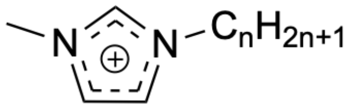

n = 1 1,3-dimethylimidazolium [mmim]
n = 2 1-ethyl-3-methylimidazolium [emim]
n = 3 1-propyl-3-methylimidazolium [pmim]
n = 4 1-butyl-3-methylimidazolium [bmim]

Figure 2.1 - General structure of 1-alkyl-3-methylimidazolium cation. Some of the most common chain lengths are given along with their abbreviations.

2.1.1. Surfaces of RTILs

The surface of RTILs are of great importance in applications such as CO_2 capture, nanoparticle and thin film preparation, and multiphase catalysis as these reactions are influenced by the groups present on the surface.[53] To understand how these applications work a deep understanding of the surface structure of the RTIL is needed, because the properties of the surfaces of RTILs have been found to be different to the bulk. Understanding properties such as the surface structure, charge distribution, the effect of impurities, etc. are continuing to be investigated in order to aid our understanding of how RTILs function in different applications and to aid in the optimisation of these and the development of new processes.[54,55]

Sum-frequency generation (SFG), angle-resolved X-ray photoelectron spectroscopy (ARXPS), low-energy ion scattering (LEIS), direct recoil spectroscopy (DRS), molecular dynamics simulations, and reactive-atom scattering (RAS) are some of the most widely used techniques to investigate the surfaces of RTILs. Some examples that utilise SFG, DRS, and MD simulations will be briefly discussed, followed by a more detailed look at RAS methods that use oxygen and fluorine atoms as the projectile.

SFG spectroscopy uses two laser beams that mix at an interface to generate an output beam that has a frequency equal to the sum of the frequencies of the two input beams. The output beam is then detected and indicates the resonant frequencies present on the surface of an RTIL, thus providing an idea of what functional groups are present. Iwahashi *et al.* used SFG spectroscopy to obtain a better understanding of how the triflate anion is oriented on the surface of [bmim][OTf] (see Figure 2.2).[56] They were able to determine that the CF_3 groups are oriented away from the bulk and the SO_3 groups point towards the bulk liquid.

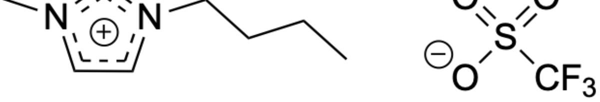

Figure 2.2 – Structure of $[bmim]^+$ and [OTf].

The effect on the surface of different chains lengths on the imidazolium ($[mmim]^+$, $[emim]^+$, and $[bmim]^+$) was investigated by Santos *et al.* using methylsulfate as the anion (see Figure 2.3).[57] For all three chain lengths they were able to show that the anion is present on the surface along with the alkyl chains of the imidazolium. Different anions were tested with $[bmim]^+$ by Baldelli and co-workers, which showed that the surface is not greatly altered by the choice of anion.[54] The imidazolium ring for all of these studies was found to lie flat on the surface with the butyl chains oriented up, away from the bulk liquid.

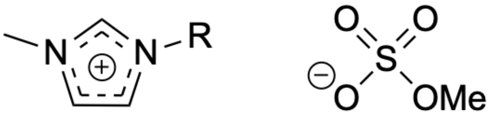

Figure 2.3 – Strucutre of [mmim]$^+$, [emim]$^+$, and [bmim]$^+$ (R= methyl, ethyl, and butyl) with methylsulfate RTILs.

DRS has also been used extensively in the literature to probe the surface of a variety of RTILs. Here the surface is bombarded with inert gas ions at a fixed incidence angle, which causes the ions to scatter and surface atoms to recoil. Time-of-flight determines the kinetic energy of the scattered atom, which is then used to determine the identity of the atom that it has collided with. The surface can thereby be probed by changing the incidence angle as only the top 2-4 Å of the liquid are affected, due to the shallow penetration depth of the gas ion projectiles.

Watson and co-workers have done extensive work probing the surface of different imidazolium ionic liquids using DRS.[51,58–61] In general their work has shown that the imidazolium ring is oriented perpendicular to the surface. This disagrees with the previous SFG spectroscopy studies that determined the ring to be parallel. DRS also showed that with short alkyl chains these did not protrude from the surface but as the length was increased the cation rotates and thus causes the alkyl chains to shift to the surface.

Molecular dynamic simulations have become increasingly prominent in the literature to investigate RTIL surfaces.[62–66] The difference in the surface structure that is observed between SFG and DRS is hoped to be determined through these simulations. Lynden-Bell *et al.* investigated the effect of different anions on [bmim]$^+$ at the ionic liquid/vacuum surface.[67] They found that the surface is typically composed of the butyl chains of the cation but that the anions ([PF$_6$]$^-$, [BF$_4$]$^-$, and Cl$^-$) are also present. Similarly Bhargava *et al.* showed that for [bmim][PF$_6$] the cations are arranged anisotropically with the imidazolium rings parallel to the surface when close to the vapour phase but is oriented perpendicularly in dense areas.[64] Their MD simulations also showed that the butyl chains were projecting out of the surface and into the vacuum. Even with a shorter chain length and a different anion this same structure was shown to be prominent.[63] These MD simulations provide insight into the discrepancy between the DRS and SFG results for the orientation of the imidazolium ring. Both the DRS and SFG results would appear to be valid and the differences are due to sampling denser areas with DRS compared to SFG.

2.1.2. Reactive-Atom Scattering

SFG and DRS can provide qualitative information on the surface but being able to quantitatively predict the surface structure of RTILs just from the ions used continues to remain a challenge. Reactive-atom scattering (RAS) has provided more quantitative answers through scattering of gas-phase atoms on the RTIL surface. Tesa-Serrate *et al.* utilised both laser-induced fluorescence (RAS-LIF) and mass spectrometry (RAS-MS) to detect the products formed through bombarding the surface of imidazolium RTILs with gas-phase $O(^3P)$ atoms.[53] OH and H_2O products are formed through this and provide information on the amount of abstractable hydrogen atoms on the surface of the RTIL (see Figure 2.4).

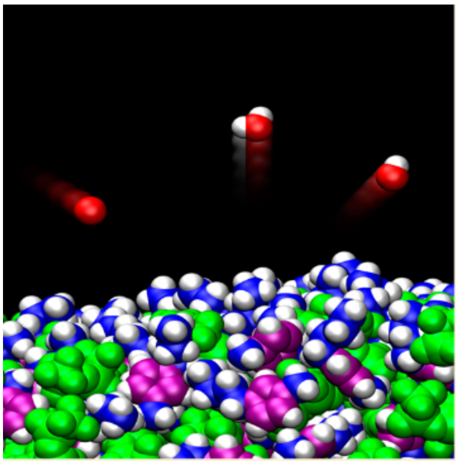

Figure 2.4 – Liquid-vacuum surface of RTILs using $O(^3P)$ atoms resulting in OH and H_2O products. (Reprinted with permission from the American Chemical Society[53])

RAS-LIF and RAS-MS were used in this study to be able to gain understanding from where hydrogen atoms were being abstracted. RAS-LIF only detects OH products and uses lower energy $O(^3P)$ atoms (15.8 kJ mol^{-1}). The lower energy atoms mean that this method is selective towards OH formation from the CH_2 groups of the alkyl chains in the RTIL, leaving the methyl group and ring hydrogen atoms on an imidazolium ion untouched, as the oxygen atoms do not have sufficient energy to abstract hydrogen from these positions. RAS-LIF can therefore provide information on the difference in the surface structure of different RTILs by detecting the presence of alkyl chains at the surface. For RAS-MS high-energy $O(^3P)$ atoms are used and both OH and H_2O products can be detected. The high-energy (504-511 kJ mol^{-1}) beam means that theoretically all hydrogen atoms can be abstracted, including the ring hydrogen atoms. RAS-MS is therefore able to provide information on the surface overall.

RAS-LIF results showed that as the alkyl chain length is increased the chains tend to dominate the surface of the RTIL. More hydrogen atoms were abstracted with the longer chain lengths that were not just due to the increasing number of CH_2 groups. RAS-MS showed that the hydrogen density remained almost identical as the chain length of the RTIL was increased. The authors therefore concluded that the alkyl chains, as shown by SFG and DRS, make up most of the surface of RTILs. Almost the same amount of hydrogen atoms were on the surface for the different RTILs but as the chain length increased RAS-LIF showed that a greater proportion of the abstractions were occurring on the alkyl chain. As the chain length therefore grows the alkyl chain extends towards the surface.

Both RAS-LIF and RAS-MS data showed that the surface is, however, not saturated with alkyl chains even with an octyl alkyl chain as a further increase in both OH and H_2O production was observed. Furthermore, saturation was still not reached with the dodecyl group. RAS-LIF experiments were able to show that the bulkier the anion the lower the alkyl coverage is on the surface.

Wu *et al.* carried out O(^{3}P) scattering on [emim][NTf_2] and [C_{12}mim][NTf_2].[65] RAS-MS was used to probe the surface and determine the changes to the surface structure as the alkyl chain length was increased. Once again, the longer alkyne chain showed greater reactivity than would be expected based on the increasing number of CH_2 groups. The scattering experiments in combination with MD simulations showed that RTILs with shorter alkyl chains tended to have stiffer surfaces with a higher surface density.

More recently Minton and co-workers used high energy F atoms, F• radicals, for the abstraction of hydrogen atoms on the surface of [bmim][Tf_2N].[68] Here the imidazolium cation was selectively deuterated to be able to determine where abstraction is taking place. Three different [bmim]$^+$ structures were prepared – d_6-[bmim]$^+$, d_3-im-[bmim]$^+$, and d_3-Me-[bmim]$^+$ where deuterium was present on the methyl and ring carbon atoms, the ring carbon atoms only, and the methyl carbon atoms only respectively (see Figure 2.5). This selective deuteration allowed for a better understanding of the surface since HF and DF could now be detected as products.

It was found that 86-95 % of the produced HF was originating from the butyl group, 4-12 % from the methyl group, and less than 3 % from the ring.[68] These amounts differ greatly from what would be expected based on stoichiometry alone and therefore indicates that the surface structure is not random. The authors concluded that the butyl group is therefore likely to be oriented away from the bulk liquid to allow for greater abstraction there. However, it is important to note that for some cations the methyl group is oriented away from the bulk instead of the butyl group.

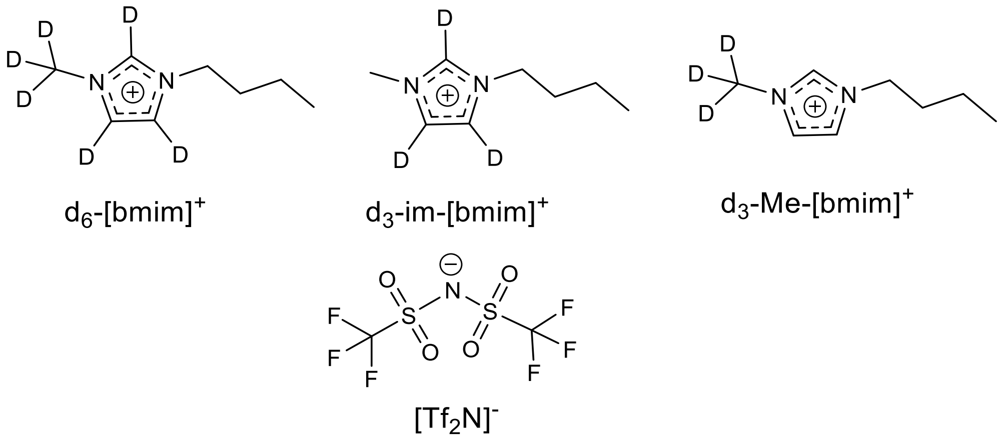

d_6-[bmim]$^+$ d_3-im-[bmim]$^+$ d_3-Me-[bmim]$^+$

[Tf_2N]$^-$

Figure 2.5 – Deuterated-[bmim]$^+$ ionic liquid ion structures along with [Tf_2N]$^-$, which were used to investigate the surface of [bmim][Tf_2N].

MD simulations showed that 17 % of the groups exposed on the surface are methyl groups and would therefore be predicted to be a small proportion of the positions that would be abstracted.[68] During these simulations it was assumed that abstraction at each of the carbon atoms would be equal in energy, which is known to not be true. The radical that is formed is better stabilised by a tertiary carbon than a secondary carbon, and the least stabilised by a primary carbon. Since the imidazolium is also positively charged abstraction of a ring hydrogen would result in a radical forming on the positively charged ring. This would theoretically result in a higher energy intermediate. While the simulations and RAS data show that the surface is composed of some methyl groups, these positions would be expected to require more energy for a hydrogen atom to be abstracted. The energy of the F atoms is 384 kJ mol^{-1}, which should allow for abstraction of any of the hydrogen atoms on the imidazolium. The actual energy for abstraction, however, has not yet been determined. The greater proportion of abstractions occurring on the butyl chain could be, in part, because less energy is required for abstraction of these hydrogen atoms and not just that they dominate the surface. Without an idea of the barriers involved for the different abstraction sites a key component to understanding the surface, and the abstractable hydrogen atoms present there, is still missing.

2.2. Aims

Minton and co-workers were able to show that the surface of [bmim][Tf_2N] is composed mostly of the butyl chains of the imidazolium cation through RAS experiments and MD simulations of the deuterated RTIL.[68] The actual energy required for the abstraction of a methyl hydrogen, an alkyl hydrogen, and a ring hydrogen have, however, not yet been obtained. The barrier heights for the abstraction of a hydrogen from each of the carbon atoms on 1-butyl-3-methylimidazolium (see Figure 2.6) by a fluorine atom were therefore determined.

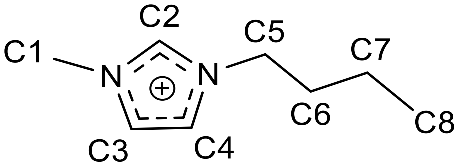

Figure 2.6 - Structure of 1-butyl-3-methylimidazolium cation showing the numbering scheme used for the investigation.

Abstraction of the ring hydrogen atoms was investigated *via* two mechanisms – a direct abstraction where the H-F bond is formed as the C-H bond is broken (see Figure 2.7) and through the formation of an F-C bond, leading to an intermediate C2-F-[bmim]$^+$, the F-H bond is then formed as the F-C bond is broken (see Figure 2.7). Both mechanisms were studied to try and determine if this alternative ring abstraction was energetically favourable for the ring hydrogen atoms.

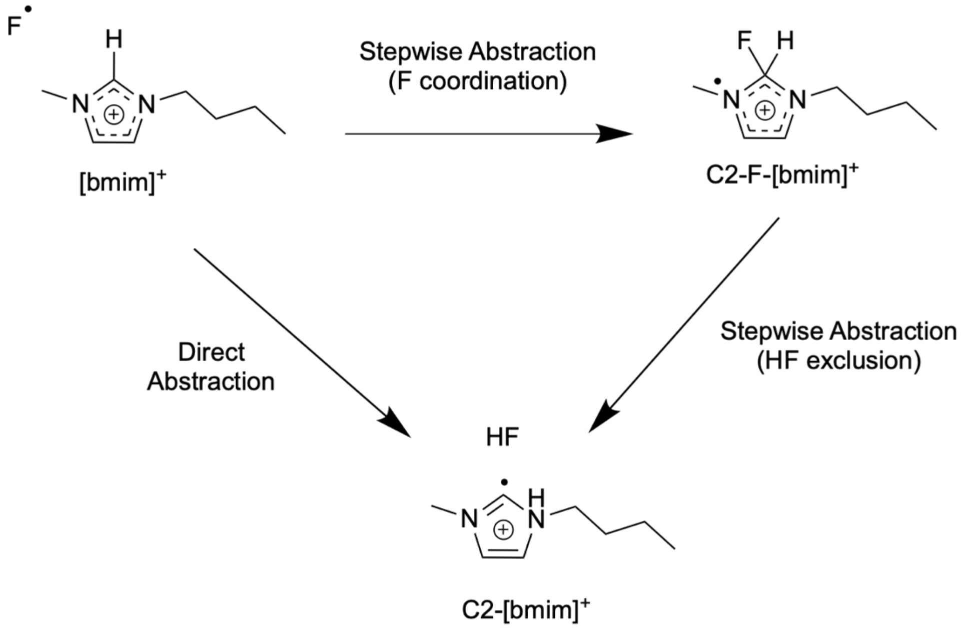

Figure 2.7 – Two mechanisms were explored for the abstraction of a ring hydrogen atom by an F atom: direct abstraction and an alternative stepwise abstraction mechanism. The intermediate is shown for the alternative abstraction mechanism along with the final product for both mechanisms for C2 abstraction.

With access to the abstraction barriers, it was possible to determine whether high energy F atoms have enough energy to abstract a hydrogen atom from any position on the ionic liquid, as was assumed in the original work. It was important to validate this assumption as it has an impact on the analysis that was carried out on the previous work. It also provided insight into which abstraction site is most favourable. To be able to predict this accurately, *ab initio* methods were employed to better describe the wave function and thereby calculate the barriers for abstraction with the highest accuracy possible, within the limits of the computational power available.

2.3. Computational Details

Geometry optimizations were carried out using the TURBOMOLE V6.40 package.[69,70] Calculations were carried out at the (RI)-MP2/def2-TZVPP//(RI)-MP2/def2-SV(P) and the (RI)-MP2/def2-QZVPP//(RI)-MP2/def2-SV(P) level of theory.[71–74] Geometry optimizations at the (RI)-MP2/def2-TZVPP level of theory were carried out for a few stationary points. No significant changes were seen in the geometry when a larger basis set was used for the optimisation, only significant changes in the electronic energy were seen and therefore optimization with a triple zeta basis set was not carried out routinely.

Vibrational frequency calculations were used to determine the nature of the stationary points and DRC calculations were used to connect transition states to their corresponding minima.[75–77] SCF energies were corrected by the addition of zero point energies. Gibbs energies and enthalpies were determined through the addition of thermodynamic corrections obtained from frequency calculations carried out at the (RI)-MP2/def2-SV(P) level of theory. PES scans were carried out using ORCA version 4.0.0.2 at the (RI)-MP2/def2-SV(P) level of theory.[78]

Single point calculations at the CCSD(T)-F12/cc-pVDZ level were also carried out using TURBOMOLE to determine the effects of using a more highly correlated post-Hartree Fock method.[79,80] Calculations using cc-pVTZ were attempted but the system proved to be too large for this basis set using the computational hardware available. In an attempt to overcome this limitation, a local coupled cluster approach (DLPNO-CCSD(T)) was explored using ORCA with the cc-pVDZ, cc-pVTZ, and cc-pVQZ basis sets.[78] Extrapolation to the complete basis set limit was carried out for the DLPNO-CCSD(T) results.[81,82]

2.4. Results

Two different abstraction mechanisms were investigated for the abstraction of a hydrogen atom on [bmim]$^+$ by an F atom and will be discussed separately below. The direct abstraction mechanism will be discussed first. The stepwise abstraction method that was explored for the ring hydrogen atoms (see Figure 2.7) was calculated for a simplified imidazolium, 1,3-dimethylimidazolium. Due to symmetry, calculations were only carried out on two of the three carbon atoms. This simplified imidazolium decreased the conformational flexibility of the system while still providing valuable insight into the potential barriers for this mechanism.

2.4.1. Direct Abstraction of Hydrogen Atoms

The energy required for abstraction of each of the hydrogen atoms in the 1-butyl-3-methylimidazolium cation by an F atom (see Figure 2.6) was determined. The barriers for the abstraction by a fluorine atom at these carbon atoms using MP2 theory is shown in Table 2.1. The barriers can be roughly grouped into three categories: 1) ring abstraction, 2) secondary carbon abstraction, and 3) primary carbon abstraction. The relative energies were calculated using the separate [bmim]$^+$ and F atom as the zero point.

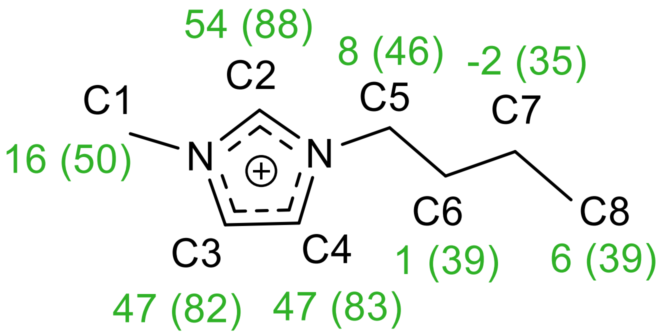

Figure 2.8 – Direct abstraction barriers of a hydrogen atom on [bmim]$^+$ by an F atom at the (RI)-MP2/def2-QZVPP//(RI)-MP2/def2-SV(P) level of theory. Enthalpies are stated in kJ mol^{-1} with Gibbs free energies in brackets.

The abstraction of ring hydrogen atoms at the (RI)-MP2/def2-QZVPP//(RI)-MP2/def2-SV(P) level of theory was found to proceed *via* the highest barrier requiring 45-55 kJ mol^{-1} at positions C2, C3, and C4. Abstraction at the secondary carbon atoms, C5, C6, and C7 was found to be low in energy at 0-8 kJ mol^{-1}, while the abstraction at the primary carbon atoms C1 and C8 resulted in barriers of 16 and 6 kJ mol^{-1} respectively. Figure 2.8 shows the exact enthalpies and Gibbs free energies for each of the abstraction sites at this level of theory.

Table 2.1 – Enthalpies and Gibbs free energies for the abstraction of a hydrogen atom at each of the abstraction sites on [bmim]$^+$ by a fluorine atom. All energies are with respect to the energy of an F atom and the imidazolium ion and are stated at the (RI)-MP2/def2-*VPP//(RI)-MP2/def2-SV(P) level of theory where * indicates the use of either a TZ or QZ basis set.

Abstraction Point	MP2 (TZ) ΔH (kJ mol^{-1})	MP2 (TZ) ΔG (kJ mol^{-1})	MP2 (QZ) ΔH (kJ mol^{-1})	MP2 (QZ) ΔG (kJ mol^{-1})
C1	19	53	16	50
C2	56	91	54	88
C3	51	85	47	82
C4	51	86	47	83
C5	10	48	8	46
C6	3	41	1	39
C7	0	37	-2	35
C8	8	41	6	39

The effects of using a more highly correlated post-Hartree Fock method was tested by carrying out both CCSD(T) and DLPNO-CCSD(T) calculations using a DZ, TZ, and QZ basis set. In general, the use of a larger basis set results in a lowering of the barriers by approximately 2-4 kJ mol^{-1} for both the entropy and the Gibbs free energy. CCSD(T) results with a triple zeta basis set were unsuccessful as too much memory was required for these calculations, these results have therefore been omitted. Table 2.2 shows the DLPNO-CCSD(T) determined energies for abstracting a hydrogen on each of the carbon atoms.

Table 2.2 – DLPNO-CCSD(T) barriers for the abstraction of a hydrogen on [bmim]$^+$ by an F atom with the cc-pVTZ and cc-pVQZ basis set are shown relative to the energy of an F atom and [bmim]$^+$.

Abstraction Point	DLPNO-CCSD(T) (TZ) **Δ**H (kJ mol^{-1})	DLPNO-CCSD(T) (QZ) **Δ**H (kJ mol^{-1})	Extrapolated DLPNO-CCSD(T) **Δ**H (kJ mol^{-1})
C1	6	3	-11
C2	71	69	72
C3	48	45	21
C4	45	42	17
C5	-3	-6	20
C6	-12	*	*
C7	-14	-18	-27
C8	-4	-8	-21

*The CCSD iterations for the abstraction at C6 with the QZ basis set did not converge even after attempting different geometries and changing the convergence threshold. The results are therefore not presented and extrapolation to the basis set limit was not possible either because of this.

The DLPNO-CCSD(T) results suggest that the barriers for the different abstraction points vary more than the MP2 results suggested. With a larger basis set the DLPNO-CCSD(T) and MP2 barriers were not significantly altered. For DLPNO-CCSD(T) a QZ basis set was able to be used due to the much quicker completion time with this methodology. Comparing the TZ to the QZ results shows that the barriers are not greatly affected when moving to the larger QZ basis set. For example, the largest barrier at C2 is predicted to proceed *via* barrier of 71 kJ mol^{-1} for the TZ basis set while for the QZ basis set this barrier is 69 kJ mol^{-1}. For C7 abstraction the QZ results predict a barrier that is 4 kJ mol^{-1} lower in energy than the TZ results. In general though, minimal changes are seen suggesting the results have already converged at the TZ level.

DLPNO-CCSD(T) results extrapolated to the basis set limit were obtained to try and correct for any potential BSSEs and are also shown in Table 2.2. Unfortunately, the results for some of the abstraction sites are quite different to the MP2 results and even the DLPNO-CCSD(T) results with a TZ and QZ basis set. It would be expected that with extrapolating to the basis set limit the energies of the transition state would tend towards a limiting value, which in turn would show the barriers converging on a certain value. This is seen, to some extent, for C7 and C8 where extrapolation to the basis set limit further reduces the energy for these barriers. For C1, C2, and C5 the extrapolated results have increased in energy, which would not be expected given the decrease in energy that was seen when using a QZ instead of a TZ basis set.

The same trends for the DLPNO-CCSD(T)/cc-pVQZ results are seen as for the MP2 results. Abstraction of the ring hydrogen atoms requires the most energy while abstraction at secondary carbon positions proceeds *via* the lowest barriers.

The trends seen here are exactly what would have been predicted based on radical stability. Abstraction at ring carbon atoms is high in energy due to the positive charge of the imidazole and the instability of the resulting radical that is forming during the TS. C2, C3, and C4 have the highest energy barriers due to the formation of aromatic radicals, which are less stable than aliphatic radicals. C6 and C7 have the lowest barriers since they are no longer adjacent to the imidazolium nitrogen atoms as the radical that is formed is a greater distance from the charged ring. C6 and C7 are also secondary carbon atoms and can stabilise the forming radical to a greater extent than the primary carbon atoms. The barrier for abstraction at C1 is higher compared to C5 even though they are in similar positions in the molecule because there are no neighbouring aliphatic carbon atoms. The adjacent nitrogen is part of a positively charged imidazole, and due to its greater electronegativity would make abstraction of a C1 hydrogen unfavourable. For C5, neighbouring carbon atoms can stabilize the product through inductive effects, but due to the close nitrogen the radical is destabilized resulting in a higher energy barrier than C6 and C7. C8 is a primary carbon, and the resulting radical is therefore not as greatly stabilized as for C6 and C7. The barrier for abstraction at C8 is, however, much lower than for C1 due to the neighbouring carbon atoms. Since there is no electronegative group adjacent to this carbon the barrier height is approximately the same as for C5.

Figure 2.9 shows the transition state structure for abstraction at C1 and C8 along with key bond lengths and the <F-H-C angle. The angle at which the F atom approaches is approximately 150 ° for both transition states. The F-H distance is shorter by 0.05 Å in **C1_TS** compared to **C8_TS**. This is due to the close C-N bond that is present in **C1_TS** since nitrogen is more electronegative the C-N bond is shorter in **C1_TS** than the C-C bond in **C8_TS** (1.45 vs 1.52 Å respectively). This shorter and stronger C-N bond in **C1_TS** slightly weakens the C-H bond, which in turn strengthens the interaction between hydrogen and fluorine resulting in a shorter distance.

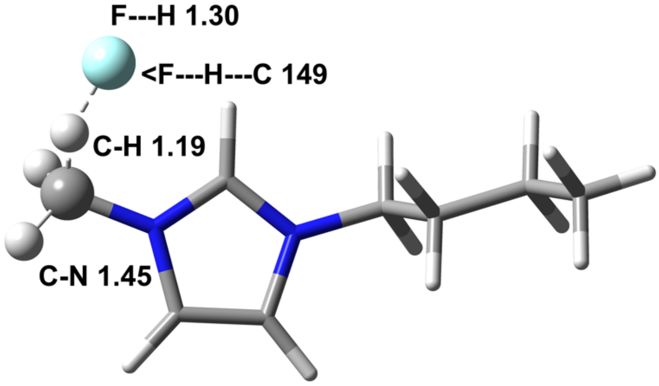

C1_TS

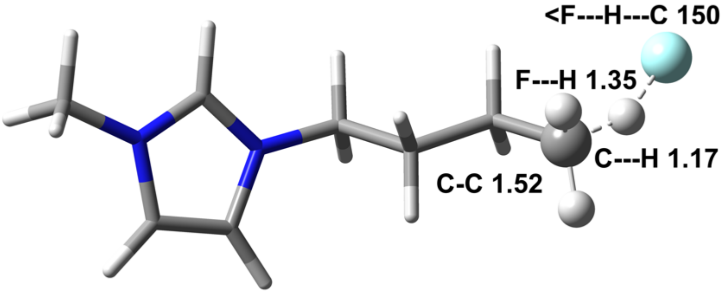

C8_TS

Figure 2.9 – (RI)-MP2/def2-TZVPP//(RI)-MP2/def2-SV(P) transition state structure for the abstraction of a hydrogen on C1 and C8 of $[bmim]^+$ by an F atom. Grey = carbon, blue = nitrogen, light blue = fluorine, and white = hydrogen. Distances are shown in Å and angles in °.

In Figure 2.10 the transition state structures for the abstraction at the ring carbon atoms is shown. The approach angle is close to identical for **C2_TS**, **C3_TS**, and **C4_TS** at approximately 130 °. The F-H and C-H distances are similar for all three transition states. The barrier for **C2_TS** was found to be higher in energy than the other two ring abstractions by approximately 25 kJ mol^{-1}. This larger barrier for **C2_TS** will be due to the presence of two nitrogen atoms on either side of the carbon. Both nitrogen atoms will be drawing electron density towards them, which would increase the energy required to then abstract a hydrogen. The carbon is already slightly electron deficient due to the greater electronegativity of the nitrogens and during the TS further electron density is being drawn from it resulting in a higher barrier.

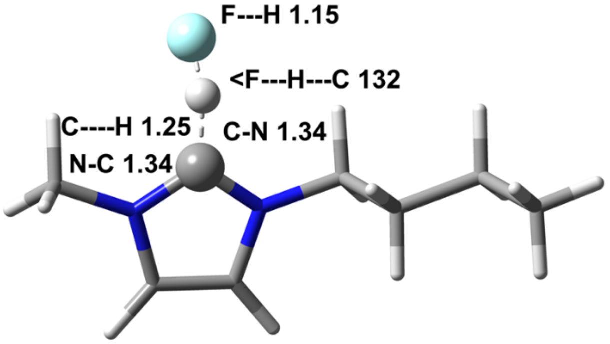

C2_TS

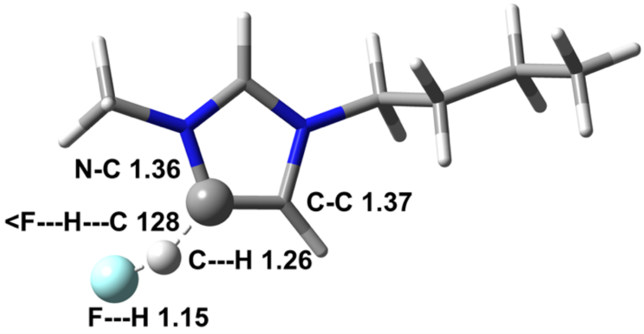

C3_TS

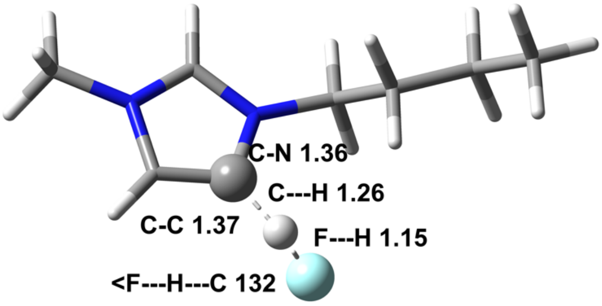

C4_TS

Figure 2.10 - (RI)-MP2/def2-TZVPP//(RI)-MP2/def2-SV(P) transition state structure for the abstraction of a hydrogen on C2, C3 and C4 of [bmim]$^+$ by an F atom. Grey = carbon, blue = nitrogen, light blue = fluorine, and white = hydrogen. Distances are shown in Å and angles in °.

The final group of transition states structures are **C5_TS**, **C6_TS**, and **C7_TS** (see Figure 2.11), which are the secondary carbon abstraction sites that were found to be the lowest in energy. The angle of approach in **C5_TS** is the same as for **C1_TS** and **C8_TS** at about 150 ° while for **C6_TS** and **C7_TS** the angle is smaller at about 147 °. The larger angle in **C5_TS** is due to less steric crowding at this carbon site since the neighbouring nitrogen has no hydrogen atoms and the carbon atoms in the ring have only a single hydrogen-bonded to them. The F-H and C-H distances in **C5_TS** are the same as in **C8_TS** at 1.35 Å and 1.17 Å respectively. These similarities are unsurprising since the barriers were almost identical. While the abstraction at **C8_TS** results in a radical forming on a primary carbon, the secondary carbon in **C5_TS** is bonded to a nitrogen, which results in a larger barrier due to the greater electronegativity of the neighbouring nitrogen. Electron density is being drawn from C5 and during the TS the abstraction of the hydrogen further decreases the electron density around C5. This can be seen by looking at the charge on C5, which is at -0.1201 in [bmim]$^+$ and at -0.1454 in **C5_TS**.

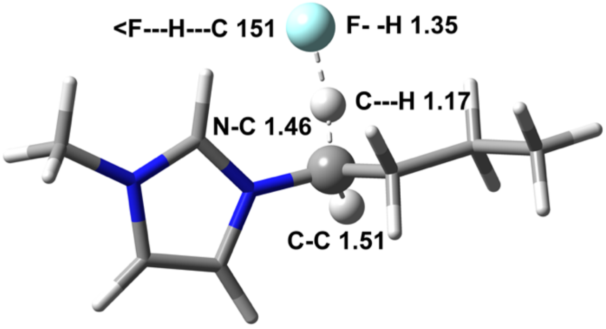

C5_TS

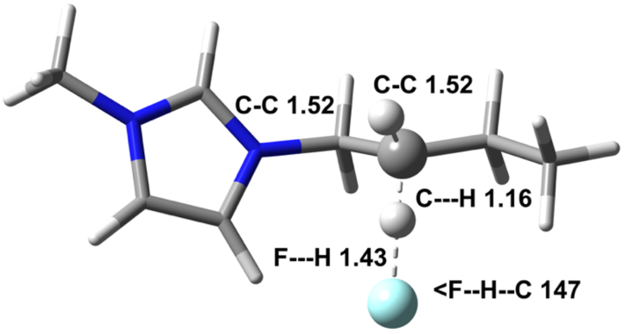

C6_TS

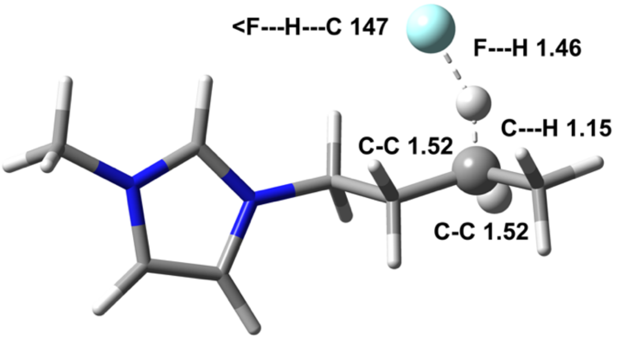

C7_TS

Figure 2.11 - (RI)-MP2/def2-TZVPP//(RI)-MP2/def2-SV(P) transition state structure for the abstraction of a hydrogen on C5, C6, and C7 of [bmim]$^+$ by an F atom. Grey = carbon, blue = nitrogen, light blue = fluorine, and white = hydrogen. Distances are shown in Å and angles in °.

The barriers for **C6_TS** and **C7_TS** are comparable, with the **C7_TS** barrier being slightly lower in energy by 2 kJ mol^{-1}. This small difference is due to C6 being closer to the ring and to the nitrogen atoms. Only small differences can be seen in the F-H and C-H distances, but these suggest that the hydrogen in **C7_TS** is being held more strongly than the hydrogen in **C6_TS**. In **C6_TS** the F-H distance is slightly shorter by 0.03 Å while no difference is seen in the C-H bond.

2.4.2. Stepwise Abstraction of Ring Hydrogen Atoms

An alternative mechanism to direct abstraction of the imidazolium ring hydrogen atoms was also investigated (see Figure 2.7), this mechanism involves the addition of the F atom to the imidazolium ring first resulting in the formation of a C-F bond. From this intermediate, **F-[mmim]$^+$** HF is then formed by concertedly breaking the C-H bond and forming the F-H bond to give the imidazolium radical. For this a simplified imidazolium, see Figure 2.12, was used to to be able to quickly determine whether this mechanism needed to be investigated further. The aim was to determine whether this alternative mechanism would be accessible and more likely to occur than direct abstraction. The PES for abstraction at C2 and C3 can be seen in Figure 2.13.

[mmim]$^+$

Figure 2.12 – Simplified imidazolium, [mmim]$^+$, used to study the stepwise abstraction mechanism.

Table 2.3 shows the energy of the stationary points for this mechanism calculated on both C2 and C3 of the imidazolium ion. The formation of the F-C bond, **ring_TS_CF**, proceeds *via* low barriers for both C2 and C3 at 10 and 11 kJ mol^{-1} respectively. The intermediate, **ring_min_CF**, is greatly stabilised compared to the starting material, lying 171 and 125 kJ mol^{-1} below the starting material for C2 and C3 respectively. **C2_ring_min_CF** is more stable than **C3_ring_min_CF**.

Table 2.3 – Electronic energies of stationary points for alternative abstraction at C2 and C3 of a simplified imidazolium with respect to an F atom and the imidazolium at the MP2/def2-TZVPP//MP2/def2-SV(P) level of theory. * Note that these barriers are approximate since they were obtained from scans at the DZ level.

Stationary Point	Relative Electronic Energy C2 (kJ mol^{-1})	Relative Electronic Energy C3 (kJ mol^{-1})
ring_TS_CF	10	11
ring_min_CF	-171	-125
ring_TS_HF	82*	95*
ring_min_HF	-33	-27

The barrier for the second transition state, **ring_TS_HF**, could not be determined accurately as no transition state could be located. The final minimum, **ring_min_HF**, however lies above **C2_ring_min_CF** and **C3_ring_min_CF** by 138 and 98 kJ mol^{-1} respectively. This indicates that the barrier for **ring_TS_HF** is too high, as loss of HF from **ring_min_CF** is a strongly exothermic process.

Forming the **ring_min_CF** intermediate involves breaking the C=N bond in the imidazolium cation. In turn a new C-F bond and a C-N bond is now also present. Comparing the bond enthalpies of the bonds formed and bonds broken gives approximately -175 kJ mol^{-1}, making the first transition state an exothermic process as seen.[83]

A relaxed PES scan was carried out where the F-H distance was varied in **ring_min_CF**. While this does not give an exact barrier as the transition state is not precisely determined, it does provide a good approximate value. It was found that the barrier for HF formation was 250 and 200 kJ mol^{-1} for **C2_ring_TS_HF** and **C3_ring_TS_HF** respectively. The formation of the stable intermediate **ring_min_CF** makes the formation *via* this stepwise abstraction mechanism unlikely since another lower energy pathway is available *via* direct abstraction. However, the high energy F atom beam that was used in the experiment (384 kJ mol^{-1}) would allow for formation of the final product, **ring_min_HF**, from this intermediate *via* this mechanism.

The final product, **ring_min_HF**, is formed by breaking the C-H and C-F bonds while forming a new H-F bond. A CN double bond is formed as in the starting material and the electron density in the imidazolium ring is delocalised again. Comparing the bonds formed and broken during **ring_TS_HF** gives an approximate enthalpy change of 21 kJ mol^{-1}.[83] This process is now endothermic as the PES in Figure 2.13 shows.

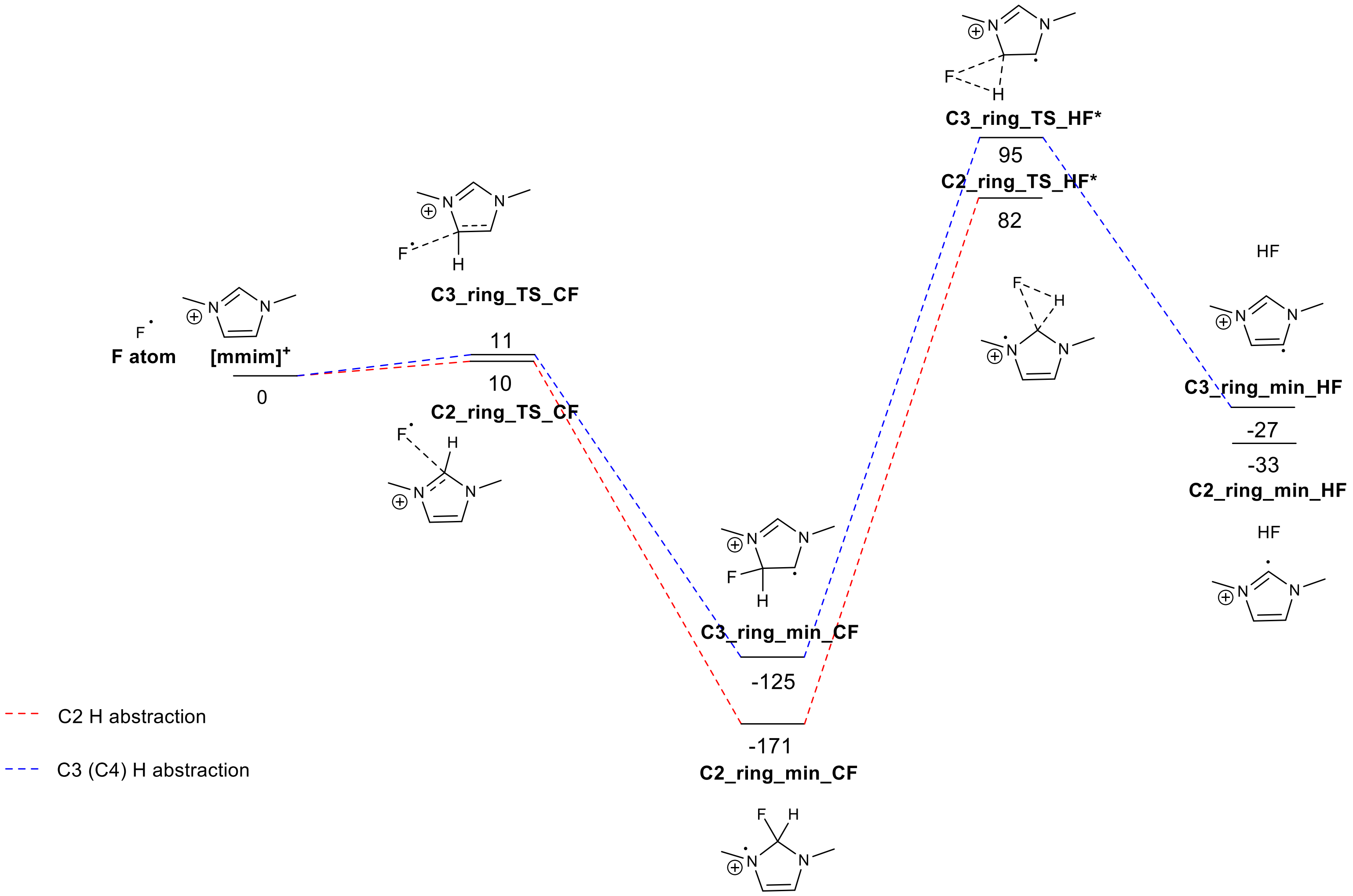

Figure 2.13 - PES for the stepwise abstraction of ring hydrogen atoms on C2 (red) and C3 (blue) on $[mmim]^+$. Relative electronic energies are shown in kJ mol^{-1} at the (RI)-MP2/def2-TZVPP//(RI)-MP2/def2-SV(P) level. Relative energies for **C2_ring_TS_HF** and **C3_ring_TS_HF** were determined through a relaxed scan.

2.5. Conclusions

The surface of RTILs has been studied in detail *via* techniques such as SFG spectroscopy, DRS, MD simulations, and RAS methods. Understanding the surface structure of RTILs is hoped to provide insight into applications such as multiphase catalysis where knowing the surface structure is of immense importance. Smoll *et al.* carried out RAS-LIF, RAS-MS, and MD simulations to investigate the surface of [bmim][Tf_2N] and found that the surface structure was mostly composed of the butyl chains of [bmim]$^+$.[68] This was determined through selective deuteration of the RTIL. The MD simulations were able to determine the proportion of different sites on the RTIL at the vacuum/liquid interface, which were in agreement with the experimental results.

The proportion of abstractions that were occurring on different sites (butyl, ring, and methyl) could not be determined with these experiments. The aim of this study was to provide an idea of the barriers involved for abstraction at each carbon atom and be able to determine whether abstraction of a hydrogen atom at every carbon atom is accessible under the experimental conditions.

Abstraction of a hydrogen from the imidazolium ring was found to proceed *via* the largest barrier, as would be expected. An aromatic radical is formed when abstraction occurs on the imidazolium ring, which is not as well stabilised as other positions. Abstraction at the two primary carbon atoms, along with the carbon next to the ring, C5, was found to proceed by lower barriers than ring abstraction. The positive charge of the imidazolium ring is now further from the abstraction site but the neighbouring nitrogen atoms to C1 and C5 make abstraction more difficult from these positions since nitrogen is more electronegative than carbon and is drawing electron density away from the neighbouring carbon. The radical is then formed on an already electron deficient carbon atom that is bound to a positively charged imidazolium ring.

For C8 the barrier was found to be surprisingly low considering it is a primary carbon atom. Abstraction at C6 and C7 was found to almost be barrierless due to the greater ability to stabilise the forming radical. C6 and C7 are secondary carbon atoms and are able to stabilise the radical that is formed during the TS to a greater extent due to inductive effects from the neighbouring carbon atoms. The charged ring and the nitrogen atoms are now also much further away, which aids in reducing the barrier.

The experiment that was carried out on this imidazolium salt was performed using a beam of high energy F atoms (384 kJ mol^{-1}). The stepwise hydrogen abstraction on the imidazolium ring does require more energy than the direct abstraction this process due to the formation of a very stable intermediate, **ring_min_CF**. Given the results presented here this alternative stepwise abstraction mechanism would still occur as the F atom beam is high enough in energy for this process. Hydrogen atoms present on the imidazolium ring do not form a large percentage of the RTIL surface, only approximately 3 % as determined using RAS-MS by Smoll *et al.*[68] Two possible mechanisms are theoretically possible for the imidazolium ring hydrogen atoms but the direct abstraction mechanism is a one-step process and proceeds *via* a barrier that is lower in energy than the stepwise mechanism by approximately 200 kJ mol^{-1}.

The majority of the RTIL surface was determined to be composed of the butyl chain with 86-95 % of the abstractions occurring from this site on the imidazolium cation. Given the barriers that were determined using MP2 theory abstraction would preferentially occur at C6 and C7 on the butyl chain due to the low barriers of 39 and 35 kJ mol^{-1} respectively. Abstraction of a hydrogen atom at all carbon atoms would occur due to the high energy of the F atom beam.

3. Phosphoramidate-Assisted Alkyne Activation

3.1 Introduction

The choice of metal and ligands in a transition metal complex are known to greatly affect reactivity. Fine-tuning is required to maximise the complex's reactivity while also maintaining the desired selectivity. The ligands typically take a supporting role to the metal but can take a more active part alongside the metal and thus facilitate the reaction. This metal-ligand cooperativity (MLC) has been observed extensively in the literature resulting in multiple reviews focused on this field.[13,84,85] MLC has played an important part in reactions ranging from electrochemical reduction of CO_2 using Fe,[86] water oxidation using Cu,[87] CO_2 hydrogenation to methanol using Ru,[88] and H_2 activation using Fe.[89] Examples of MLC are prominent in the literature and a few general examples focusing on C-H activation MLC reactions will be discussed below.

Fujita *et al.* carried out a dehydrogenation reaction of alcohols where MLC was shown to play a vital role.[90] The 2-hydroxypyridine ligand of an Cp*Ir catalyst (see Scheme 3.1) was found to be vital for the reaction. The catalytic cycle for the generic reaction can be seen in Scheme 3.2. The first step involves deprotonation of the incoming alcohol by the pyridine ligand and formation of an aloxo iridum species. Following this a hydrogen migration from the coordinated alcohol to the Ir causes the ketone to be released and forms the iridium hydride. Due to the hydroxypyridine ligand's ability to change dentisity by κ^2 binding *via* the nitrogen and oxygen, dihydrogen was then released. Another alcohol molecule can then coordinate to the complex. Without this flexible denticity of the 2-hydroxypyridine ligand the reaction would not proceed.

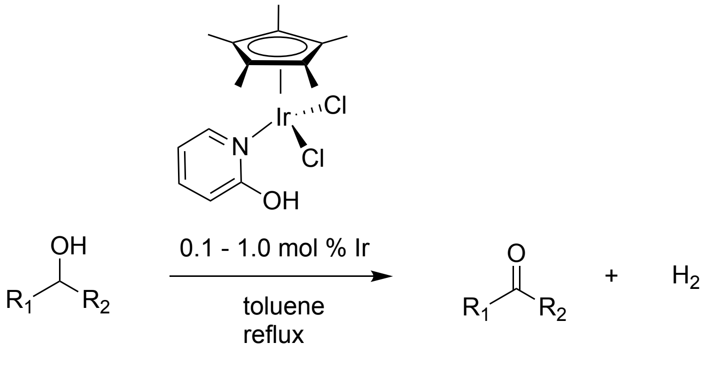

Scheme 3.1 - Cp*Ir catalyst with a 2-hydroxypyridine ligand was used to convert a secondary alcohol to a ketone and dihydrogen. The hydroxypyridine ligand was able to change denticity and thus aid in the formation of the product.[90]

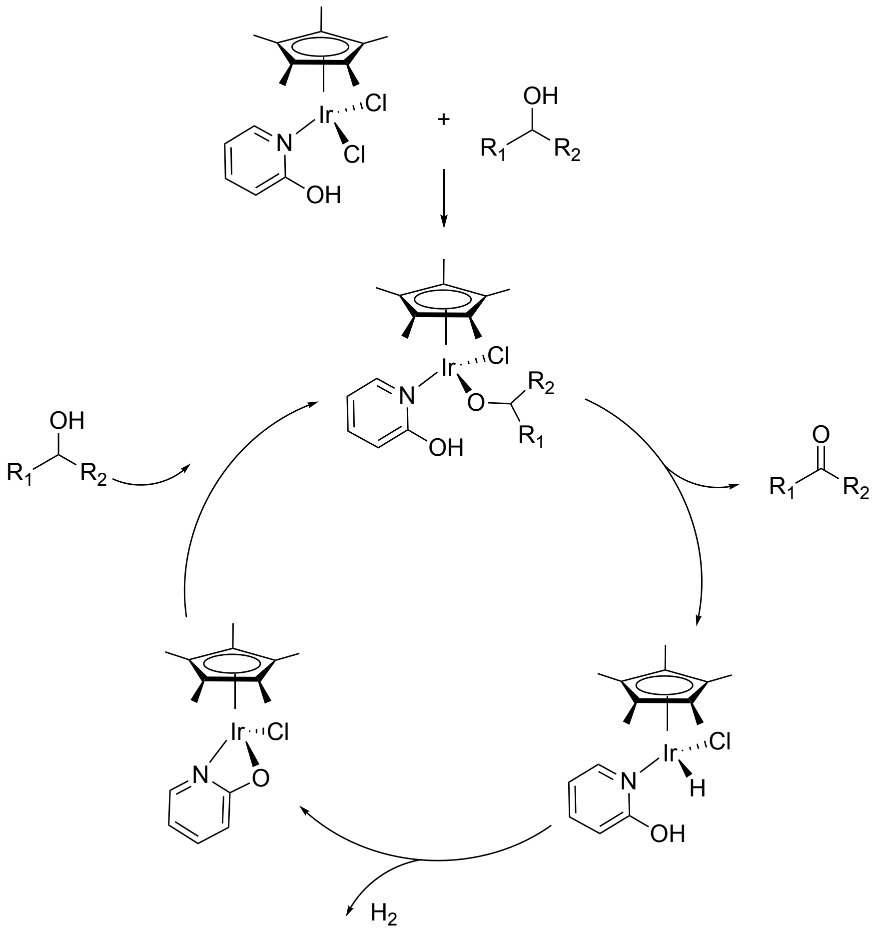

Scheme 3.2 – Proposed catalytic cycle for the reaction of secondary alcohols with an Cp*Ir complex with a 2-hydroxypyridine ligand.[90]

Computational studies in this area have also been carried out, such as the work carried out by Feller *et al.*, where DFT was used to predict that an MLC mechanism would be preferred for the activation and reductive splitting of CO_2 by an Ir-based catalyst.[91] A mixture of two Ir(I) hydrido pincer complexes was used, which can be seen in Figure 3.1.

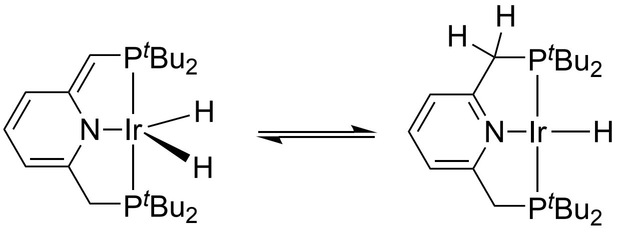

Figure 3.1 - Ir(I) complex used in the reductive splitting of CO_2. The pincer ligand was found to aid formation of the product because of the conversion between these two complexes.

Addition of CO_2 to the Ir(I) mixture resulted in the formation of an adduct, where CO_2 was found to coordinate both to the metal and the ligand, see Figure 3.2. Transfer of two hydrogen atoms, one from the metal and one from the ligand to CO_2 resulted in the formation of H_2O and CO. The DFT study allowed insight into the mechanism to show the importance of the ligand in this reaction.

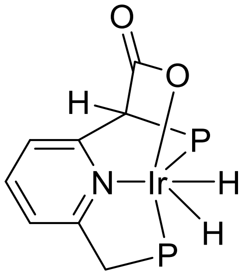

Figure 3.2 – Structure of the adduct formed upon the addition of CO_2 to the Ir(I) complex mixture. Formation of the adduct allowed for the release of H_2O and CO.

3.1.1 MLC and C-H Activation

MLC plays a very important role in C-H activation reactions. Mechanisms such as concerted metalation deprotonation (CMD), ambiphilic metal-ligand activation (AMLA), ligand-to-ligand hydrogen transfer (LLHT), and ligand-assisted proton shuttle (LAPS) all rely on the involvement of the ligand.

CMD and AMLA were originally coined by Lapointe *et al.* and Boutadla *et al.* respectively.[92,93] In both of these mechanisms the C-H bond of a substance is broken as a C-[M] bond is formed. Both intramolecular and intermolecular reactions have been carried out experimentally along with extensive computational studies, showing the scale of this field.[94] The first known example of CMD/AMLA is thought to be the work carried out by Winstein and Traylor in 1955.[95] Here acetolysis of dialkylmercury was carried out in acetic acid (see Scheme 3.3).

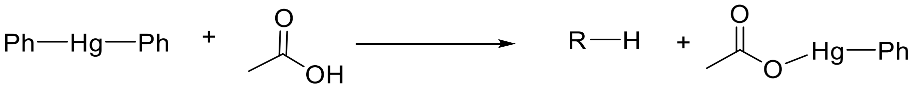

Scheme 3.3 - Acetolysis of dialkylmercury in acetic acid. This is the first known example of CMD/AMLA.

Combined with work published by Fung *et al.* and Olah *et al.* it was found that a π-complex is formed over the originally proposed σ-complex (see Figure 3.3).[96,97] Kinetic isotope effects (KIEs) showed that the C-H cleavage was rate limiting. In combination with further kinetic and thermodynamic data it was shown that the C-H bond was cleaved simultaneously as the C-Hg bond was formed making it a concerted metallation-deprotonation reaction.

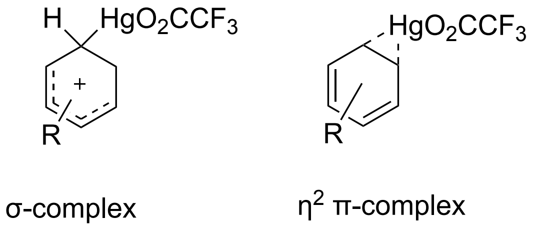

Figure 3.3 – σ- and π-complexes for the acetolysis of dialkylmercury in acetic acid.[96,97]

Computational studies have played an important role in CMD reactions as they are able to investigate the bonding and energetics of different potential mechanisms. In 2005 Davies *et al.* showed that in a palladium-promoted cyclometalation of (DMBA-H) the agostic C-H complex is energetically favourable over the originally proposed arenium ion (see Figure 3.4).[98] This agostic complex allows for an almost barrier-less H-transfer involving acetate *via* a six-membered transition state. The authors proposed that the acetate could also play a key role in stabilizing the agostic complex through hydrogen-bonding which is thought to also help orient the acetate and facilitate the C-H cleavage.

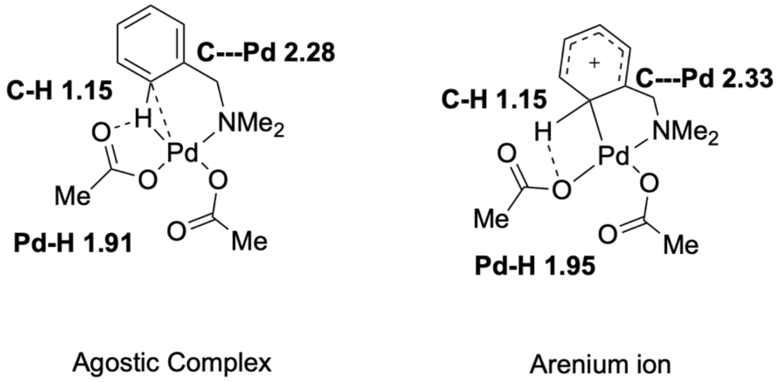

Figure 3.4 - Agostic complex and arenium ion for cyclometalation of DMBA-H. Bond distances for the agostic complex are given in Angstroms, as determined *via* DFT.[98]

DFT allowed for a deeper understanding of the interactions present in this reaction and has also been a key tool for investigating reactions where AMLA/CMD is thought to be important, which can be seen in the reviews written by Boutadla *et al.* and Lapointe *et al.*[92,93] A variety of computational studies have been carried out in this area including ones investigating the possibility of assisted intramolecular arylation using palladium,[99] Rh(I)-catalyzed arylation of indole,[100] and more recently an investigation into whether a concerted or non-concerted mechanism is preferred for the arylation of heterocycles,[101] showing the continuing importance of CMD reactions and C-H activation in general.

An alternative mechanism for C-H activation involving metal-ligand cooperativity is known as LLHT, where proton transfer between hydrocarbyl ligands occurs. This mechanism was proposed by Guihaumé *et al.* who carried out a theoretical mechanistic investigation on a nickel catalyzed hydrofluoroarylation reaction (see Figure 3.5).[102] DFT was used to study the mechanism along with the effect of different fluoroarenes on the reactivity. It was determined that traditional oxidative addition is not likely to occur as the computational results did not match the experimental observations. An alternative mechanism was suggested that involved coordination of the fluroarene to the Ni(alkyne) complex. From here a proton transfer occurs from the σ-coordinated arene to the alkyne. Notably this mechanism does not go via a metal hydride and NBO analysis suggests that this is a direct proton transfer between the two ligands. Changing the fluoroarene showed that C-H activation is improved by using arenes that are fluorinated at the *ortho* position.

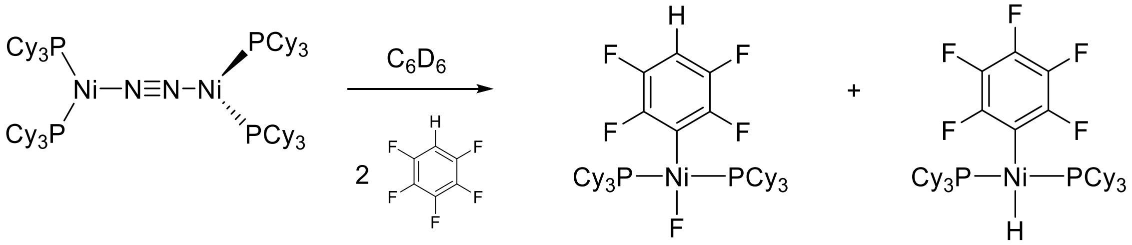

Figure 3.5 - Nickel catalysed hydrofluoroarylation reaction, which was found to proceed via a LLHT mechanism instead of a traditional oxidative addition mechanism.[102]

LLHT is therefore a standalone mechanism for C-H activation but still falls under MLC as the C-H activation barrier is directly linked to the bond energy of the Ni-aryl bond that is being formed. With CMD/AMLA the metal is directly involved in the reaction, while with LLHT the proton transfer occurrs directly between the two ligands.

3.1.2 Ligand-Assisted Proton Shuttle Mechanism

The LAPS mechanism is like CMD/AMLA, however the protonated ligand continues to react instead of dissociating. LAPS was proposed by Lynam and Slattery in 2010.[103] Experimental and theoretical investigations were carried out on the reaction between Ru(κ^2-OAc)$_2$(PPh$_3$)$_2$ and HC≡CPh to determine the mechanism for the formation of Ru(κ^1-OAc)(κ^2-OAc)(=C=CHPh)(PPh$_3$)$_2$ (see Scheme 3.4), which had previously been synthesized in 2009.[104]

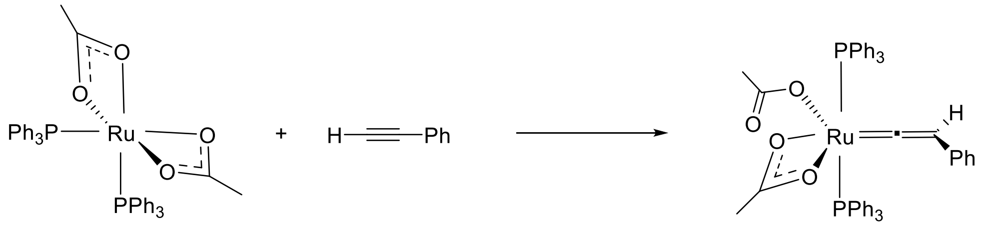

Scheme 3.4 – Reaction of Ru(κ^2-OAc)$_2$(PPh$_3$)$_2$ and HC≡CPh under mild conditions giving the resulting Ru(κ^1-OAc)(κ^2-OAc)(=C=CHPh)(PPh$_3$)$_2$ vinylidene.[104]

$H^{13}C\equiv CPh$ was used to investigate the vinylidene. $^{31}P\{^1H\}$ NMR using the ^{13}C labelled alkyne showed that the vinylidene was formed *via* hydrogen migration and not *via* phenyl migration due to a single doublet resonance. Low temperature ^{31}P NMR carried out at 205 K showed a major peak corresponding to the coordinated alkyne along with a minor peak corresponding to the vinylidene. The reaction mixture was warmed to 245 K and two new doublet resonances appeared corresponding to a new complex. Further warming to 255 K resulted in an increase of the vinylidene peaks and a decrease in the peaks corresponding to the new complex. Only the vinylidene was observed upon any further warming and the new complex was not observed when the mixture was cooled again. $H^{31}C\equiv CPh$ was used to gain insight into this new complex, this showed that hydrogen migration had already occurred but the vinylidene was no longer present. A new complex had formed through the attack of an acetate ligand by of the oxygen at the α-carbon position of the vinylidene (see Figure 3.6).

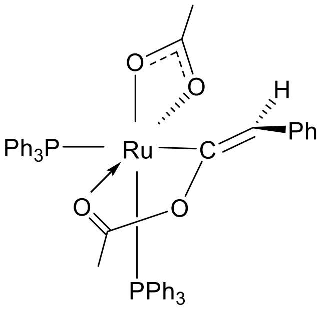

Figure 3.6 – NMR deduced structure of the complex formed after slow heating of the original reaction mixture to 245 K. Here the acetate ligand has attacked the α-carbon of the vinylidene. Upon further heating the original vinylidene was formed.[103]

DFT was used to determine the mechanism involved in the alkyne/vinylidene tautomerisation. Three different pathways were explored: 1,2-hydride shift, oxidative addition, and a pathway where an acetate ligand acts as a proton shuttle by deprotonating the alkyne and later protonating at the β position of the alkynyl complex (see Scheme 3.5). Two different models were investigated changing the ligand environment, PR'$_3$ when R'=H to Ph, and the alkyne, when R=Me or Ph.

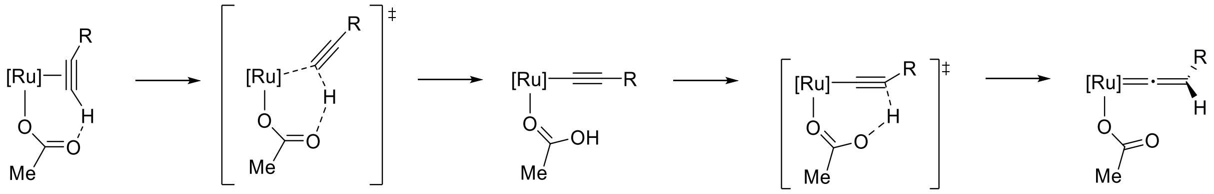

Scheme 3.5 - LAPS mechanism proposed by Lynam and Slattery for the reaction of $[Ru(OAc)_2(PR'_3)_2]$ with terminal alkynes (R = Me, or Ph and R' = H or Ph). [Ru] = [*trans*-$Ru(OAc)(PR'_3)_2$].[103]

The first step for all pathways involves a change in denticity of one of the acetate ligands from κ^2 to κ^1 to create a vacant site for the alkyne. Upon coordination of the alkyne, an alternative σ-complex was found that was determined to be higher in energy than the η^2-coordinated alkyne complex. It was found that the lowest energy pathway was *via* this acetate-mediated pathway, which was found to be almost barrier-less from the σ-complex (2-15 kJ mol^{-1}) and relatively accessible from the η^2-coordinated alkyne complex (52-80 kJ mol^{-1}). While the σ-complex is less stable than the η^2-coordinated alkyne complex it does lead to lower energy barriers, which was found to fit with the experimental observation of the reaction being facile at 255 K. The rate-determining step was found to be the creation of the vacant site on ruthenium but since solvent effects were not included it is very likely that the barriers are overestimated, as stated by the authors. The original computational model, where $PR'_3=PH_3$ and R=Me, showed that the vinylidene was not the thermodynamic product but the metallo-enolester, which did not match the experimental observations. The full system was therefore studied and correctly determined the vinylidene as the thermodynamic product without significantly changing the rest of the PES.

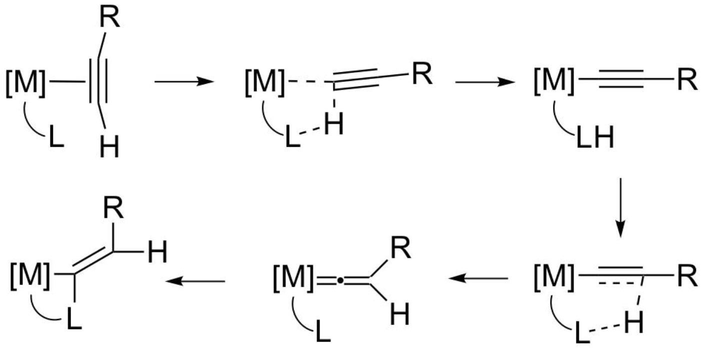

Figure 3.7 - General Ligand-Assisted Proton Shuttle proposed by Lynam and Slatter in 2010.[103] The ligand of a metal complex deprotonates the alkyne to give the acetylide. Subsequent protonation at the β carbon gives the vinylidene. Attack at α position results in the final product.

This work provided insight into an alternative C-H activation pathway compared to the traditional pathways of 1,2-hydride shift and oxidative addition. The first step of the LAPS mechanism is related to CMD/AMLA, but it is the second step of the LAPS mechanism that distinguishes it since the ligand does not dissociate and instead is further involved in the reaction. A general scheme for the LAPS mechanism can be seen in Figure 3.7. Here the ligand, L, deprotonates the hydrogen on the coordinated alkyne to give the acetylide complex. Then the same ligand protonates the acetylide at the β-position to give the vinylidene. The ligand is then able to attack the vinylidene at the α-positon.

This LAPS mechanism has been observed in a range of reactions containing ruthenium complexes.[105–107] In 2016, Drover *et al.* presented an Ir(III) system containing a hemilabile bidentate 1,2-N,O-phosphoramidate ligand that was used for anti-Markovnikov 1-alkyne O-phosphoramidation.[108] This phosphoramidation reaction gave access to an alternative method to synthesize vinyloxy organophosphates, which are commercial agrochemicals. The authors were able to show that C-O bond formation was selective, and that functionalization can be controlled through the choice of chelating ligand. The reaction was both regioselective and stereoselective as only the (*E*)-vinyloxyirida cycle was formed for a variety of alkynes (see Scheme 3.6).

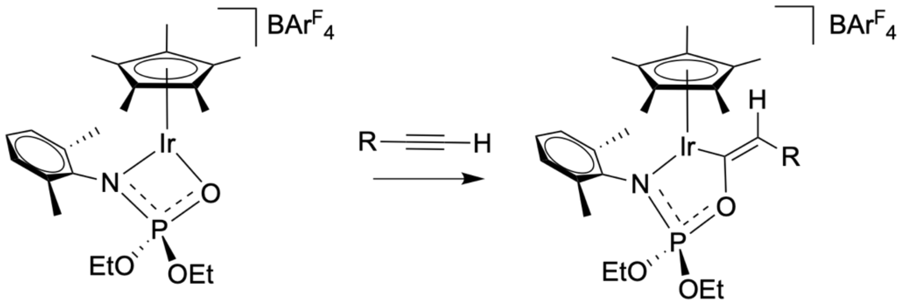

[**1**][BAr$^F_4$] [**2**][BAr$^F_4$]

R = Ph, *p*-*t*BuPh, Cy, *n*Bu, *t*Bu

Scheme 3.6 - The regio- and stereoselective *O*-phosphoramidation of 1-alkynes at Ir(III).

The formation of the O-phosphoramidation product was unexpected as this requires breaking the strong P=O bond to form the P-O-C linkage as seen in Scheme 3.6, which is typically thermodynamically disfavoured. In the N-phosphoramidation product this P=O bond is retained, yet it was not observed experimentally.

The reaction relies on the hemilability of the phosphoramidate ligand, which allows access to the κ^1-N species. While a κ^1-O species could theoretically be formed this was not observed. The authors proposed that a LAPS mechanism may be involved, which was tested *via* the addition of excess alkyne in the presence of a weak Lewis basic coordinating solvent, MeCN. This resulted in the formation of an equilibrium mixture of the κ^2-N,O mono and κ^1-N bis(acetonitrile) adducts. The five membered irida cycle was not observed and shows that a coordinating solvent such as MeCN can prevent vinylidene formation. This formation is prevented by the solvent coordinating to the vacant site created when the κ^1-N species is formed. MeCN coordinating to Ir(III) thereby stops the O-nucleophilic attack since the vinylidene is not able to be formed.

The initial experiments carried out provide great insight into the reaction and support the hypothesis of a LAPS mechanism. However, further study is needed to be able to confirm and explore all other potential competing pathways that could lead to the desired product. In addition, the origin of the observed regio- and stereoselectivity is not clear from this experimental work and would need to be investigated.

3.2 Aims

The work carried out by Schafer *et al.* provides interesting and reliable experimental data, making it an excellent reaction system to study computationally.[108] Along with this, a variety of mechanistic questions still remained unanswered for which a computational study was thought to be well suited to try and provide potential answers. More generally, further insight into MLC within the field of C-H bond activation can be achieved.

The experimental authors proposed that the reaction of [**1**][Bar$^F{}_4$] with an alkyne proceeds *via* a ligand-assisted proton shuttle (LAPS) mechanism to give [**2**][Bar$^F{}_4$]. One of the major aims is to determine all the possible mechanisms for the reaction and determine whether this reaction does proceed *via* a LAPS mechanism. The origins of the regio- and stereoselectivity was also investigated. A variety of different alkynes were used in the original work (R=Ph, *p*-*t*BuPh, Cy, *n*Bu, *t*Bu) and the effect these substituents have on the reaction was determined.

3.3 Computational Details

All calculations were performed using the TURBOMOLE V6.40 package.[69,70] Calculations were carried out at the (RI)-PBE0-D3BJ/def2-TZVPP//(RI)-BP86/def2-SV(P) level including COSMO solvation (in CH_2Cl_2, $\varepsilon = 8.93$ at 298 K) and DFT-D3BJ dispersion corrections.[33,109–116] Vibrational frequency calculations were used to determine the nature of the stationary points and (DRC) calculations to connect transition states to their corresponding minima. States connected by dashed lines in the potential energy surfaces show that DRC calculations confirmed that these states are connected.[75–77] Where no lines are present their connection has not been verified.

Gibbs energies and enthalpies were determined by correcting the SCF energies obtained at the (RI)-PBE0-D3BJ/def2-TZVPP level by adding thermodynamic corrections obtained from frequency calculations carried out at the (RI)-BP86/def2-SV(P) level of theory. Zero-point energies were also added to the SCF energies. Energies discussed are relative Gibbs energies including COSMO corrections in CH_2Cl_2 and DFT-D3BJ dispersion corrections. In the potential energy surfaces enthalpies are included in brackets. PES scans were carried out at the (RI)-BP86/def2-SV(P) level of theory using TURBOMOLE within ChemShell 3.7.0, where DL-FIND was used for the optimizations.[117,118]

A simplified system was used where the alkoxy groups of the phosphoramidate were shortened from ethyl groups to methyl groups. This reduction in the chain length greatly reduces the conformational freedom without greatly impacting the relative energies within the reaction.

In the original experimental study by Drover *et al.* various alkynes were used to determine the effect on the reaction.[108] For this mechanistic study a simplified model was used to reduce the conformational flexibility of the system. For the alkyne a methyl group was used for the R group compared to the much bulkier groups studied. Substitution effects were later investigated but only for the final products. The alkyl chains of the phosphoramidate were also shortened from ethyl groups to methyl groups. These changes, while decreasing the conformational flexibility and therefore the size of the PES needing to be studied, do not have a significant impact on the electronics of the system. Crystallographic data was compared to the calculated bond lengths and, at most, differed by 0.03 Å. The bond lengths of the final product, **5b_E**, obtained from these calculations and from the crystal structure of [**5**][BAr^F_4] can be seen in Table 3.1 and are in good agreement with each other giving confidence in the chosen methodology.

Table 3.1 – Key bond lengths in Å for **5a_*E*** at the (RI)-PBE0-D3BJ/def2-TZVPP//(RI)-BP86/def2-SV(P) level compared to bond lengths obtained from the crystal structure of [**2**][Bar$^F{}_4$].[108]

Complex	**C_α-C_β**	**P-O**	**P-N**	**Ir-N**	**Ir-C_α**
5a_*E*	1.36	1.60	1.63	2.06	2.03
[2][Bar$^F{}_4$]	1.334(3)	1.571(4)	1.633(9)	2.050(8)	1.999(2)

3.4 Results and Discussion

3.4.1 General Overview of the Reaction

An overview of the different pathways and corresponding intermediates that were studied is given in Scheme 3.7. The first step of the reaction involved coordination of the alkyne to the 16 electron κ^2-coordinated complex **1**, to give **2**, an 18-electron system with the alkyne coordinating in an η^2 fashion. From **2**, five different pathways were investigated that lead to the formation of the five-membered irida(III)cycle **5**:

1) O-Protonation – deprotonation of the terminal alkyne by the P=O oxygen of the phosphoramidate, consequently breaking the Ir-O bond
2) Cp*-Protonation – deprotonation of the terminal alkyne by the Cp* ligand
3) N-Protonation – deprotonation of the terminal alkyne by the nitrogen of the phosphoramidate, consequently breaking the Ir-N bond
4) Oxidative-Addition – a hydride is transferred onto the Ir causing a change in the oxidation state from Ir(III) to Ir(V)
5) 1,2-Hydride Shift – a hydride shift where the proton transfers from the alpha carbon of the alkyne to the beta carbon, thus proceeding directly to the vinylidene

O-Protonation, N-Protonation, and Cp*-Protonation are all examples of LAPS mechanisms (Scheme 3.7A). Here the ligand takes part in the reaction by deprotonating the alkyne to form the corresponding acetylide, **3a**, **3b**, and **3c** respectively. Subsequently a hydrogen transfer occurs to the β-carbon of the acetylide to give the vinylidene **4**. In the case of the N-Protonation pathway no vinylidene intermediate was found and instead protonation of the β-carbon directly leads to attack of the nitrogen and formation of **5b**. Attack of the oxygen onto the α-carbon of the vinylidene in **4** results in **5a**.

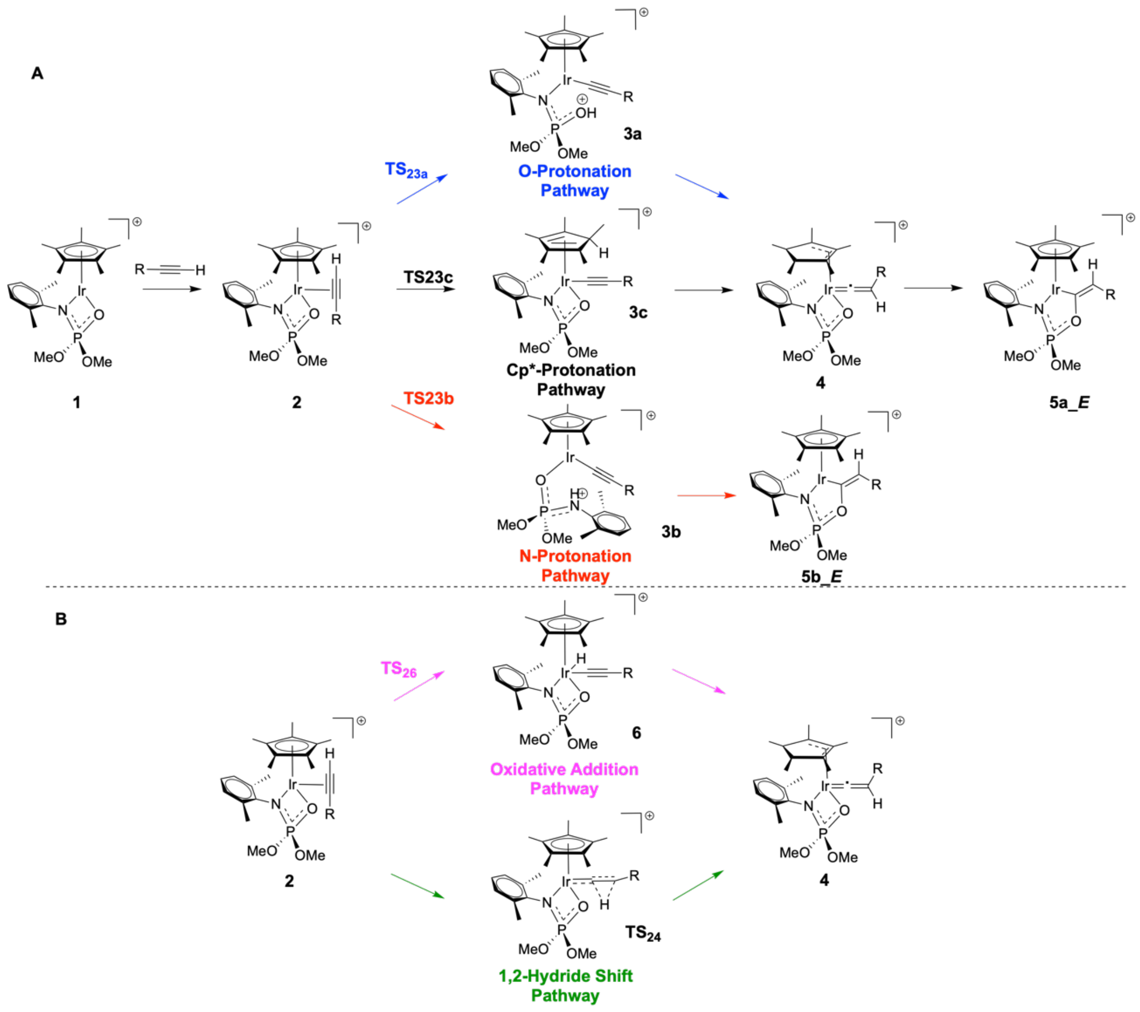

Scheme 3.7 – Reaction pathways investigated for the formation of **5** *via* the reaction of **1** with propyne. (A) LAPS pathways involving proton migration by a non-innocent ligand. (B) Traditional non-ligand assisted pathways by oxidative addition and 1,2-hydride shift. (Reprinted with permission from the American Chemical Society[119])

Scheme 3.7B shows the more traditional pathways oxidative addition and 1,2-hydride shift. In the Oxidative Addition pathway the alkyne adds to the Ir(III) complex resulting in an Ir(V) hydride complex, **6**. The hydride on the metal then transfers to the acetylide to give the vinylidene **4** as with the LAPS pathways. The 1,2-Hydride Shift pathway proceeds directly to the vinylidene **4** from the starting coordinated alkyne complex **2**. For both the oxidative-addition and 1,2-hydride shift the pathways converge with the O-protonation and Cp*-protonation pathways at complex **4**, where attack of the oxygen results in the product **5a**.

3.4.2 Potential Energy Surface

Figure 3.8 shows the Potential Energy Surface (PES) for three of the five pathways that were investigated: O-Protonation, N-Protonation, and 1,2-Hydride Shift. Oxidative Addition and Cp*-Protonation were determined to be inaccessible and part of the PES for those pathways is shown in Figure 3.9 for clarity. Overall, the reaction is downhill and results in a stabilization of between 50-75 kJ mol^{-1} for the two different regio- and stereoisomers of **5**, compared to the starting alkyne coordinated complex **2bi**.

3.4.3 O-Protonation Pathway

During the first transition state the P=O oxygen of the phosphoramidate deprotonates the terminal position of the alkyne as seen in Figure 3.8. A six-membered ring is formed during this transition state which can be seen in Figure 3.10. The orientation of the dimethylphenyl group on the nitrogen remains unchanged in **TS$_{23a}$** and **3a** along with the methoxy groups on the phosphorus. Only the orientation of the alkyne changes during this process. In **2b$_i$** the alkyne is coordinated in an η^2 fashion with the methyl group of the alkyne oriented away from the uncoordinated oxygen of the phosphoramidate ligand. During **TS$_{23a}$** the alkyne has already undergone most of the rotation to form the acetylide that is seen in **3a.**

The barrier for **TS$_{23a}$** was found to be 48 kJ mol^{-1}, a low energy process. The six-membered transition state and little change in the orientation of the ligands around the iridium centre explains this relatively low barrier.

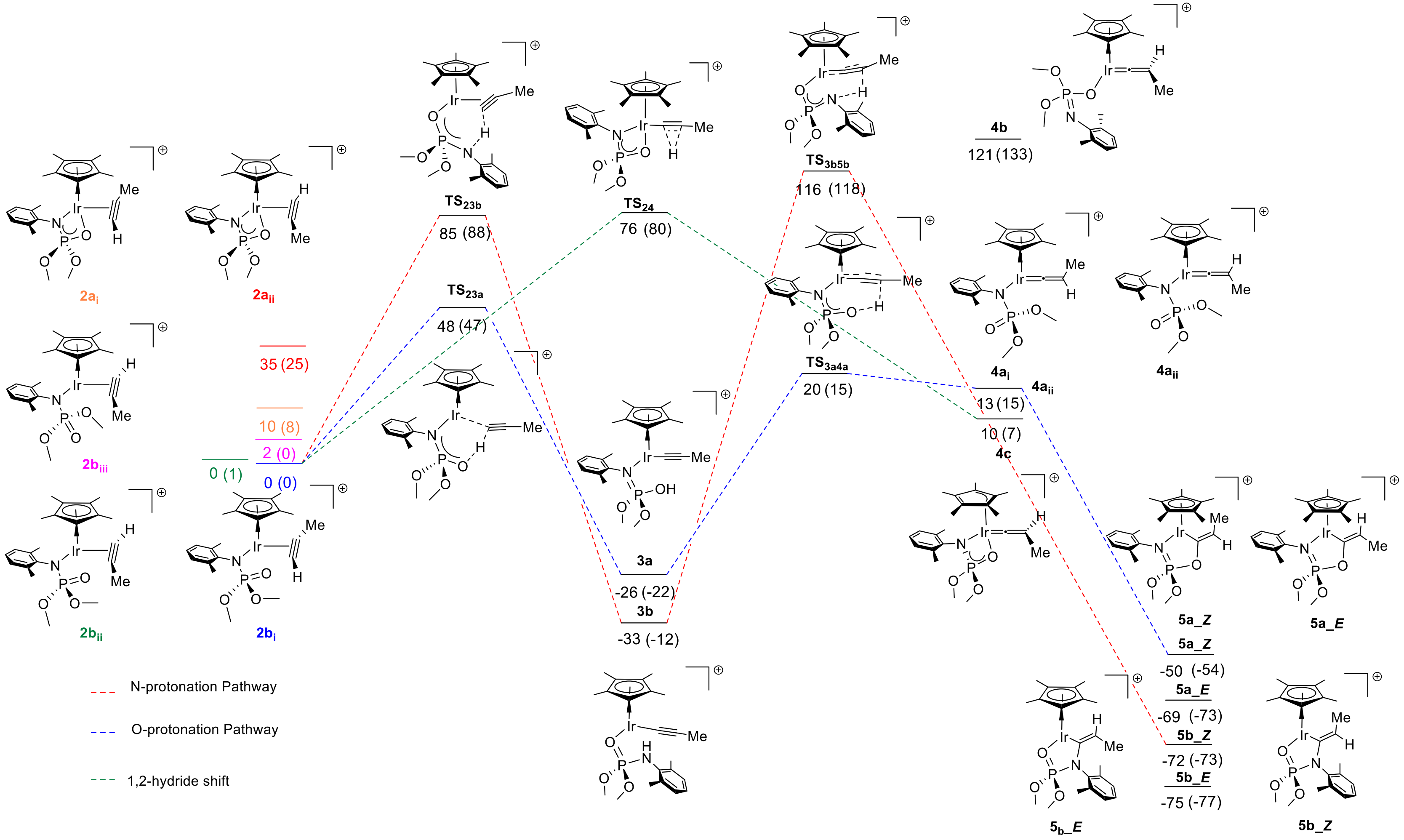

Figure 3.8 – PES for the N-protonation (red), O-protonation (blue), and 1,2-hydride shift (green) pathways for the formation of **5**. Relative Gibbs energies (and enthalpies in brackets) are shown in kJ mol^{-1} at the (RI)-PBE0-D3BJ/def2-TZVPP//(RI)-BP86/def2-SV(P) level in CH_2Cl_2 (COSMO). (Reprinted with permission from the American Chemical Society[119]).

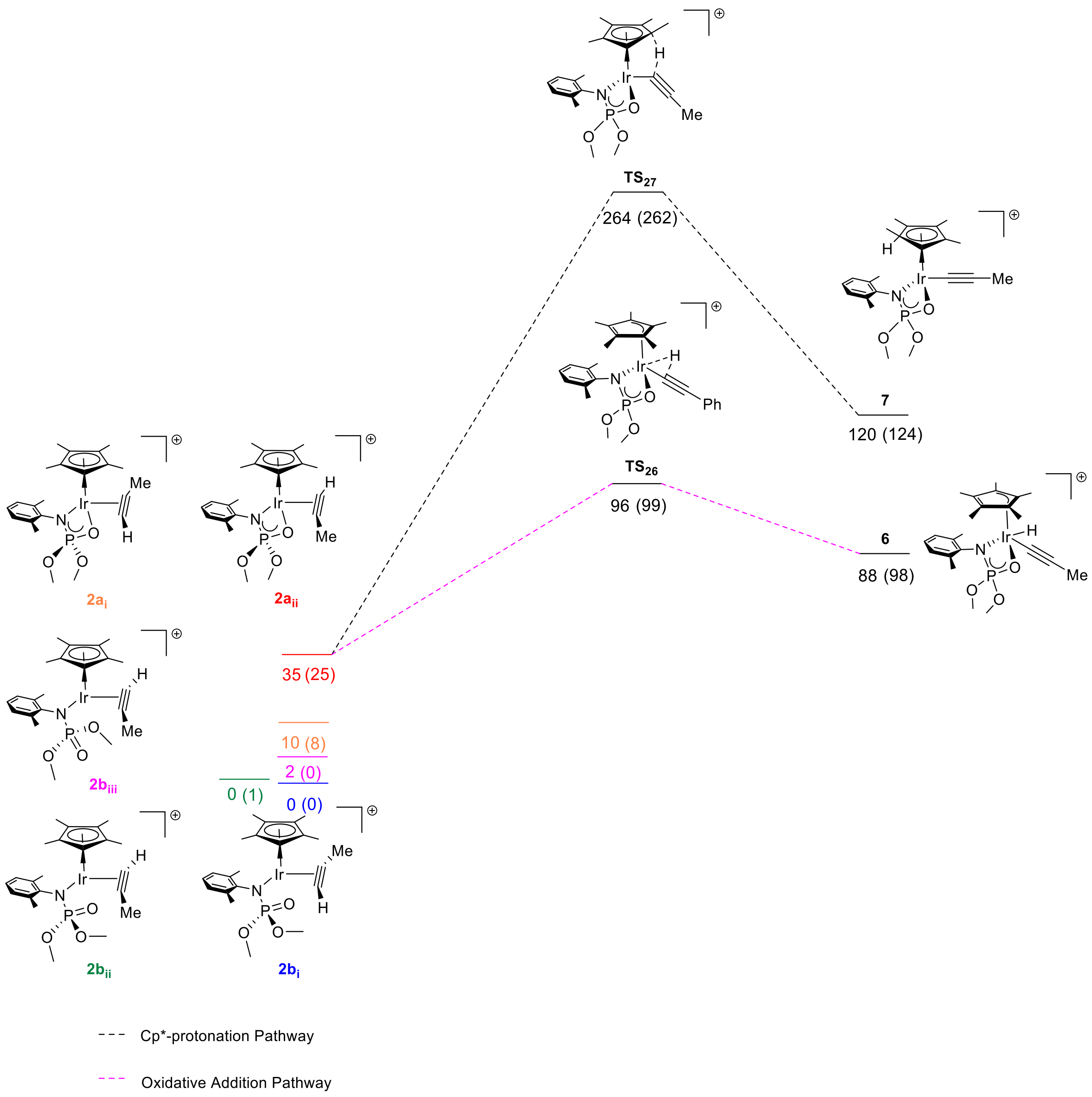

Figure 3.9 - PES for the first transition state for the oxidative-addition (purple) and Cp* protonation (black) pathway. Relative Gibbs energies (and enthalpies in brackets) are shown in kJ mol^{-1} at the (RI)-PBE0-D3BJ/def2-TZVPP//(RI)-BP86/def2-SV(P) level in CH_2Cl_2 (COSMO). (Reprinted with permission from the American Chemical Society[119]).

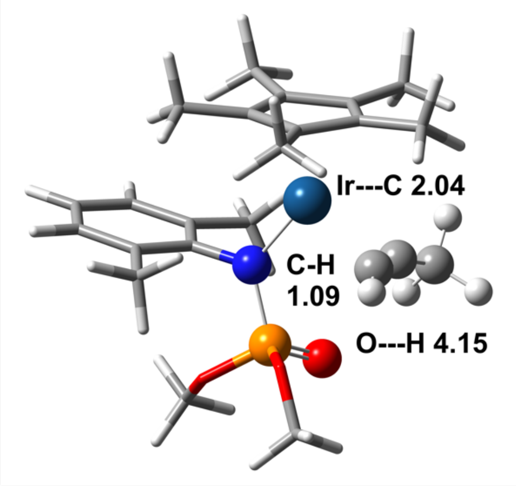

$2b_i$

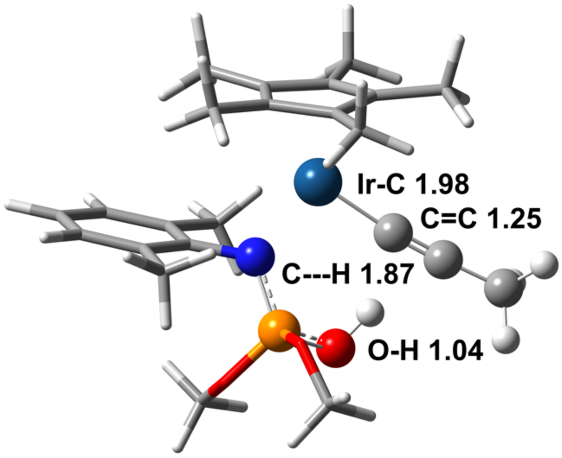

3a

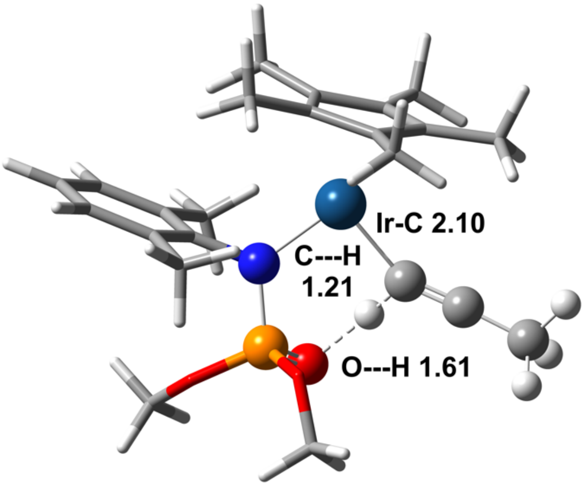

TS_{23a}

Figure 3.10 - (RI)-PBE0-D3BJ/def2-TZVPP//(RI)-BP86/def2-SV(P) level in CH_2Cl_2 (COSMO) transition state structure for **TS_{23a}** along with corresponding minima **$2b_i$** and **3a**. Selected distances are shown in Å. Dark blue = Ir, blue = N, orange = P, red = O, grey = C, and white = H.

The distance between iridium and the centroid of the η^2-C-C coordinated alkyne in **2bi** is approximately 2.04 Å. During the transition state, **TS_{23a}**, the coordinating of the alkyne changes to η^1 and a direct Ir-C bond is formed. In **TS_{23a}** this Ir-C distance increases to 2.10 Å, slightly longer than in the η^2 coordination in **2bi**. In **3a** this distance reduces to 1.98 Å. This change in coordination brings the hydrogen on the alkyne closer to the P=O oxygen in the phosphoramidate, 4.15 to 1.61 Å in **2bi** and **TS_{23a}** respectively. Meanwhile the C-H bond distance increases from 1.09 to 1.21 Å in **TS_{23a}**. This bond distance indicates that the transition state structure resembles the starting material rather than the product though the coordination of the alkyne has changed in the transition state.

Five isomers of **2** were determined and are shown in Figure 3.8. The alkyne in isomers can be oriented two ways in the complex, which can be seen when comparing isomers **2bi** and **2bii**. The P=O oxygen can be coordinated to the Ir centre such as in isomers of **2a**, while in **2b** the Ir-O bond is no longer present. To access **TS$_{23a}$**, a rearrangement from other isomers to **2b$_{i}$** would be needed as the oxygen needs to be uncoordinated and the alkyne must be oriented for deprotonation to occur.

In **2b$_{ii}$**, the methyl on the alkyne is oriented towards the P=O oxygen, but this isomer is similar in energy to **2b$_{i}$**. Re-coordinating to give **2b$_{i}$** then allows access to **3a** through **TS$_{23a}$**, which is 26 kJ mol^{-1} lower in energy and would be a driving force for re-coordination along with the overall stabilization of forming **5a_E**, which is 69 kJ mol^{-1} lower in free energy than the starting complex **2b$_{i}$**.

In **2a$_{i}$** and **2a$_{ii}$** the P=O oxygen is still coordinated to iridium, but since these minima are higher in energy, 10 and 35 kJ mol^{-1} respectively, compared to **2b$_{i}$**, it is energetically favourable for the oxygen to not be coordinated and then this allows for formation of **3a** and finally **5a_E**.

During the second transition state, **TS$_{3a4a}$**, the hydrogen migrates from the oxygen in **3a** to the β-carbon on the acetylide to give **4a$_{i}$**, which can be seen in detail in Figure 3.11. The barrier for this process was determined to be 46 kJ mol^{-1}, almost identical to the barrier for the first transition state, **TS$_{23a}$**. During the transition state the iridium-carbon distance decreases slightly to 1.91 Å from 1.98 Å in **3a**. This is coupled with only a negligible increase in the carbon-carbon bond distance of 0.03 Å.

The distance between the oxygen and the hydrogen in **TS$_{3a4a}$** increases to 1.43 Å from 1.04 Å in **3a**. As with **TS$_{23a}$** the orientation of the P-O group is relatively unchanged along with the dimethylphenyl group on the nitrogen and the methoxy groups on the phosphorus. This retention of the conformation seen in the minimum **3a** will play a role in the low barrier and is comparable to the barrier for **TS$_{23a}$**. The C-H distance decreases from 1.87 to 1.28 Å in **3a** and **TS$_{3a4a}$** respectively. Only the C-H and O-H distances undergo a significant change.

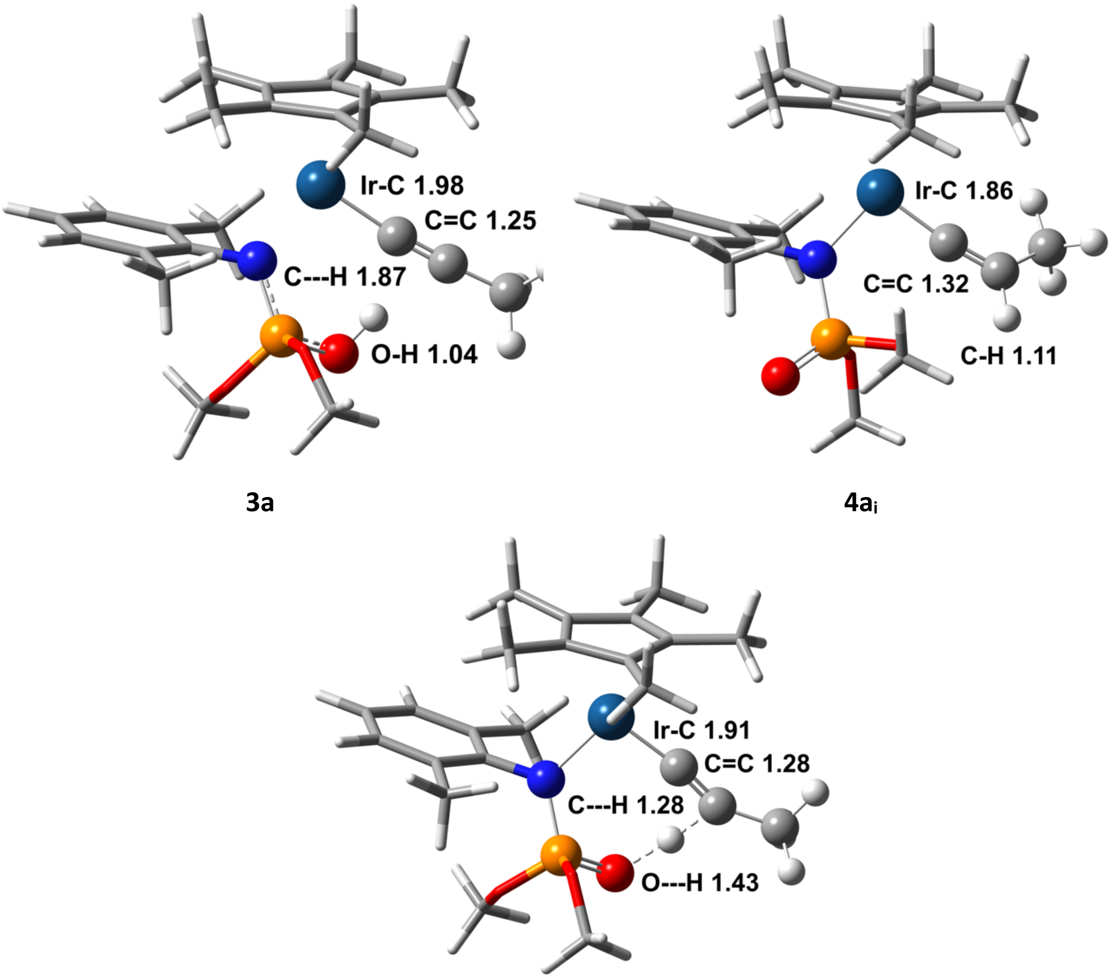

3a **4a$_i$**

TS$_{3a4a}$

Figure 3.11 - (RI)-PBE0-D3BJ/def2-TZVPP//(RI)-BP86/def2-SV(P) level in CH_2Cl_2 (COSMO) transition state structure for **TS$_{3a4a}$** with corresponding minima **3a** and **4a$_i$**. Selected distances are shown in Å. Dark blue = Ir, blue = N, orange = P, red = O, grey = C, and white = H.

The vinylidene that is formed, **4a$_i$**, has a much shorter Ir-C and longer C=C bond distance of 1.86 and 1.32 Å respectively compared to **3a** by 0.12 and 0.07 Å. This is to be expected as more electron density is now located between the iridium and carbon. Interestingly the P=O group is now oriented away from the vinylidene. This minimum is only 7 kJ mol^{-1} lower in energy than **TS$_{3a4a}$**. A more stable isomer of **4** was located where the oxygen is coordinated to the iridium. This however causes a shift in the coordination of the Cp* ligand from η^5 to η^3.

A DRC calculation was carried out and showed that **TS$_{3a4a}$** leads directly to **4a$_i$**. A change in the coordination can then occur to the more stable isomer of **4**, but this **4c** isomer was not found to be directly connected to **TS$_{3a4a}$**.

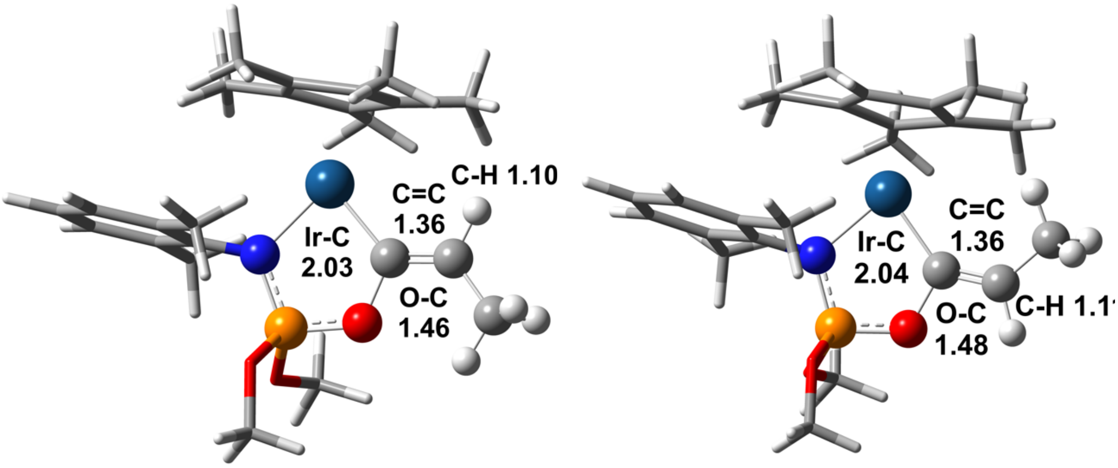

5a_E **5a_Z**

Figure 3.12 - (RI)-PBE0-D3BJ/def2-TZVPP//(RI)-BP86/def2-SV(P) level in CH_2Cl_2 (COSMO) structures of **5a_E** and **5a_Z**. Selected distances are shown in Å. Dark blue = Ir, blue = N, orange = P, red = O, grey = C, and white = H.

From **4a$_i$** the final 5-membered irida-cycle **5a** is formed, both stereoisomers are shown in Figure 3.12. No transition state was found for this process and was determined to proceed downhill with no barrier (See 3.4.9 Potential Energy Surface (PES) Scans). The key bond distances in both isomers are almost identical. The difference between these two isomers is the orientation of the methyl group in the alkene. **5a_E** is thermodynamically favoured by 19 kJ mol^{-1}, most likely due to a reduction in the steric interaction between the methyl group and the Cp* ligand.

In both isomers the <C-C-CH_3 and <C-C-H angles are roughly the same, 129 and 116 ° respectively. For both isomers this causes the methyl group to sit closer to surrounding groups however, there is a much more significant impact in **5a_Z** due to the proximity of the Cp* ligand.

3.4.4 N-Protonation Pathway

As with the O-protonation pathway, the first step in the N-protonation pathway involves deprotonation of the coordinated alkyne in **2b$_i$**. In this pathway the nitrogen of the phosphoramidate deprotonates the alkyne in the first transition state **TS$_{23b}$**, which can be seen in Figure 3.13. During this transition state the Ir-C distance has increased slightly from 2.04 to 2.08 Å in **2b$_i$** and **TS$_{23b}$** respectively. This slight increase is most likely to reduce steric clashing due to the bulk of the dimethylphenyl group on the nitrogen. The C-H distance is already much longer in **TS$_{23b}$** than in **2b$_i$** by 0.17 Å (1.26 and 1.09 Å respectively).

The C-C distance in the alkyne remains unchanged at approximately 1.25 Å in **2b$_i$, TS$_{23b}$,** and **3b**. The Ir-C distance does decrease in **3b** to 1.96 Å from 2.04 Å in **2b$_i$** due to a change in coordination to form the acetylide.

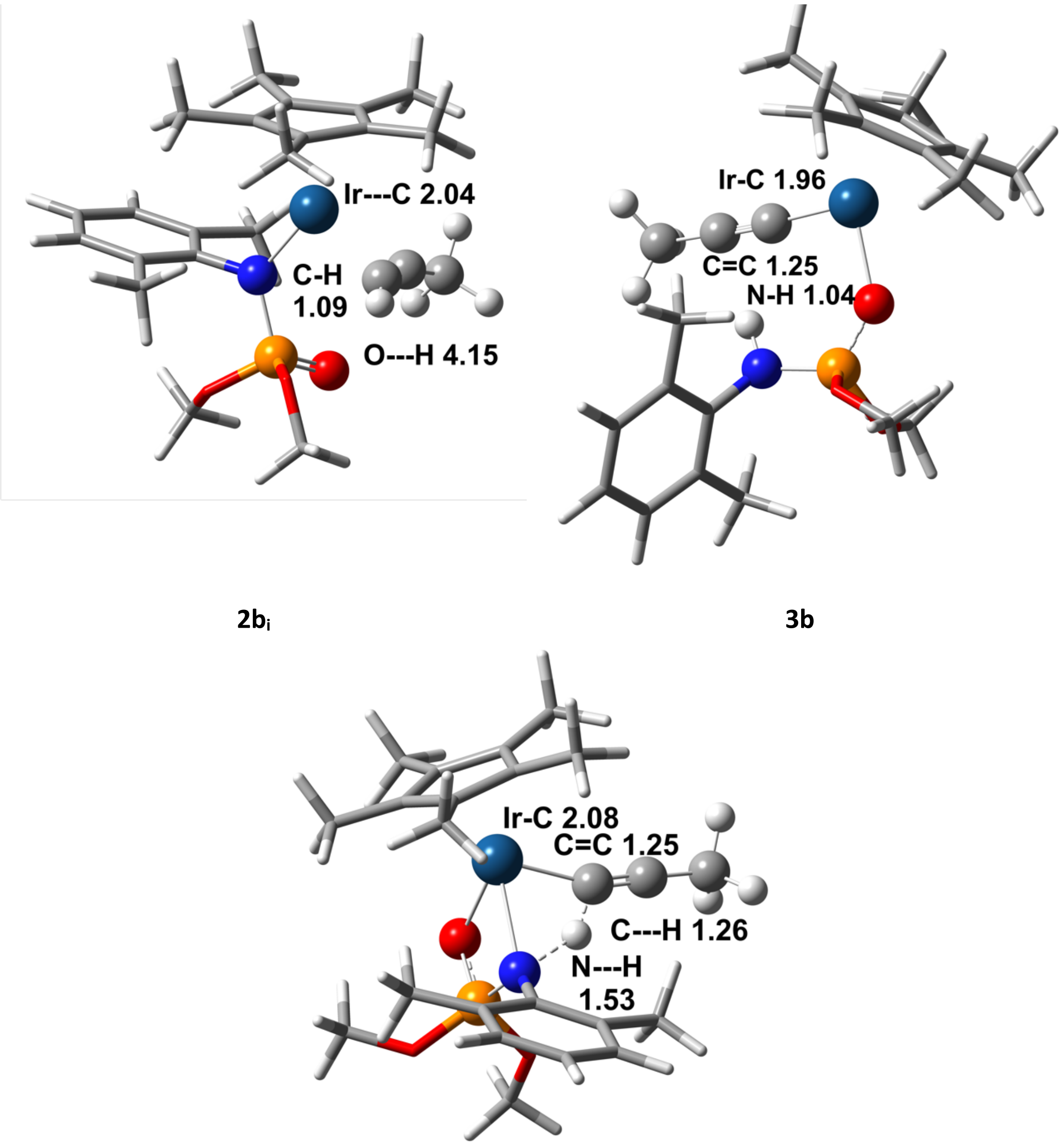

2b$_i$

3b

TS$_{23b}$

Figure 3.13 - (RI)-PBE0-D3BJ/def2-TZVPP//(RI)-BP86/def2-SV(P) level in CH_2Cl_2 (COSMO) transition state structure for **TS$_{23b}$** with corresponding minima **2b$_i$** and **3b**. Selected distances are shown in Å. Dark blue = Ir, blue = N, orange = P, red = O, grey = C, and white = H.

The barrier for formation of **3b** was determined to be 85 kJ mol^{-1} as seen in Figure 3.8. This is a much larger barrier than in the O-protonation pathway. There is increased steric clashing due to the dimethylphenyl group on the nitrogen that needs to reorient during this process. This bulkier group on the nitrogen does not allow for as much conformational freedom as is available in the O-protonation pathway. Furthermore, the larger barrier will be due to the energy penalty associated with breaking the Ir-N bond. No isomer of **2** could be found as the Ir—N always reforms. The strength of the Ir-N bond can also be seen later in isomer **4b**, where the vinylidene has formed. The Ir-N bond is broken in this isomer, but this is associated with an increase in free energy of 111 kJ mol^{-1} compared to **4a$_i$**.

The bond distances in **TS$_{23b}$** suggests that the nitrogen is still coordinated to the iridium while the N-H bond is formed. This results in a four-membered ring transition state which are known to be less favourable than six-membered transition states and could explain why this barrier is much larger than that for **TS$_{23a}$**. Further analysis on the bonding in this transition state would need to be done to determine whether this truly is a 4-membered ring transition state or 6-membered as with **TS$_{23a}$**.

The resulting minimum **3b** is more stable than **3a** by 7 kJ mol^{-1}. Since the Ir-N bond is now broken the dimethylphenyl group can orientate itself away from the rest of the complex, reduce any steric interaction and thereby lower the energy of the stationary point compared to the O-analogue **3a**. The more basic site on the ligand is also protonated, which will also be more stable.

During the second transition state the hydrogen on the nitrogen of the phosphoramidate transfers to the β-carbon in the acetylide. The barrier for this is very large at 149 kJ mol^{-1}, as seen in Figure 3.8. As with the O-protonation pathway this is a seven-membered ring transition state, but due to the dimethylphenyl group there is less flexibility. This lack in flexibility means that the acetylide and dimethylphenyl group are forced together to allow for protonation of the acetylide. The larger barrier is also due to the NH site being less acidic than the OH site and hence will not be as good a proton source.

The N-H distance in **TS$_{3b5b}$** is already elongated compared to **3b**, increasing to 1.91 Å from 1.04 Å, while the C=C distance has only slightly increased from 1.25 to 1.81 Å respectively, which can be seen in Figure 3.14. The orientation of the complex has only changed slightly with these minor changes in bond distances. The angles and orientation of groups remain unchanged, which indicates that the decreased distance between the phosphoramidate and the acetylide is causing this larger barrier.

Unlike with the O-protonation pathway, **TS$_{3b5b}$** leads directly to the final product **5b_E** by protonating the β-carbon of the acetylide while simultaneously forming a bond between the nitrogen and α-carbon of the acetylide. The C=C bond has increased slightly to 1.37 Å in **5b_E** from 1.31 Å in the transition state.

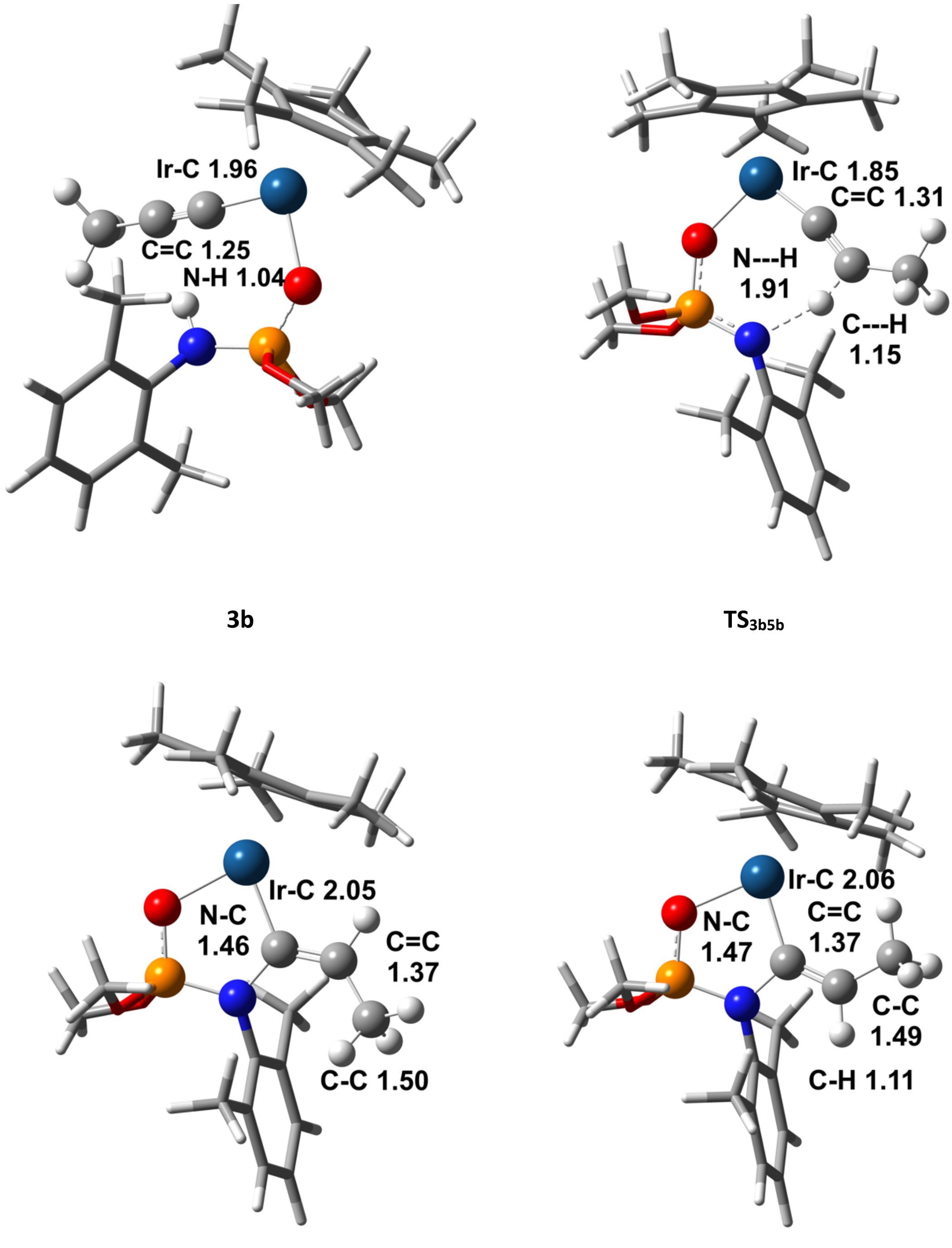

3b **TS$_{3b5b}$**

5b_E **5b_Z**

Figure 3.14 - (RI)-PBE0-D3BJ/def2-TZVPP//(RI)-BP86/def2-SV(P) level in CH_2Cl_2 (COSMO) transition state structure for **TS$_{3b5b}$** with corresponding minima **3b** and product **5b_E** and **5b_Z**. Selected distances are shown in Å. Dark blue = Ir, blue = N, orange = P, red = O, grey = C, and white = H.

3.4.5 Cp*-Protonation Pathway

As with the O-protonation and N-protonation pathways a transition state was found where the hydrogen of the alkyne is transferred to the Cp* ligand of the Ir(III) system. **TS$_{23c}$**, shown in Figure 3.15, was found to proceed *via* a barrier of 264 kJ mol^{-1}, see Figure 3.9. Cp* is known to be very stable spectator ligand, which is why it is used extensively in organometallic chemistry. While reactions involving the protonation of Cp* do exist the resulting C-H bond is relatively weak making the complexes very reactive.[120,121] Ligand-assisted behaviour like this is therefore going to be accompanied with a high energy barrier especially since protonating the ring breaks the conjugation present in Cp* resulting in a high energy barrier.

During **TS$_{23c}$** the Ir-C and C=C bond distance remains unchanged at 2.04 and 1.26 Å respectively. The C-H bond is elongated to 1.23 Å in the transition state from 1.09 Å in **2b$_i$**. In the resulting minimum **3c** the Ir-C distance has decreased slightly to 1.94 Å as with the other pathways where an acetylide is formed. The C=C bond length remains relatively unchanged, 0.03 Å elongation in **3c** is observed compared to **TS$_{23c}$**.

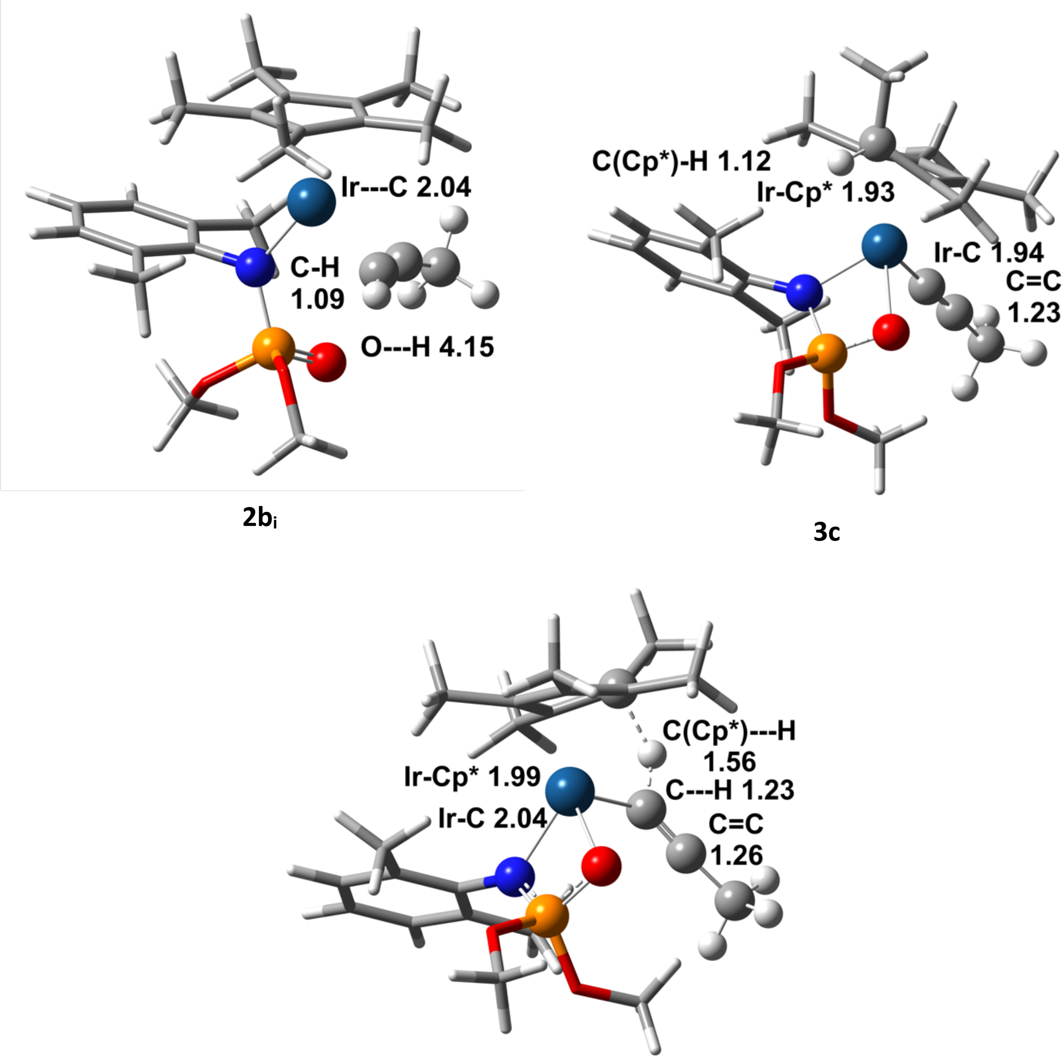

2b$_i$

3c

TS$_{23c}$

Figure 3.15 - (RI)-PBE0-D3BJ/def2-TZVPP//(RI)-BP86/def2-SV(P) level in CH_2Cl_2 (COSMO) transition state structure for **TS$_{23c}$** with corresponding minima **2b$_i$** and **3c**. Selected distances are shown in Å. Dark blue = Ir, blue = N, orange = P, red = O, grey = C, and white = H.

Since this barrier was much larger than the other LAPS mechanisms this pathway was not investigated any further. Protonation of the Cp* would not be accessible and highly unlikely, especially considering the other lower energy pathways that have already been located.

3.4.6 Oxidative-Addition Pathway

Oxidative addition is a reaction step that involves metal insertion between two atoms and an increase in oxidation state. For a C-H bond, insertion of a metal forms a hyride and an acetylide. In the reaction being studied the oxidation state of the iridium changes from Ir(III) to Ir(V). Iridium is known to be able to accommodate a variety of oxidation states ranging from 0 to +6 with +1 and +3 being the most common. Figure 3.9 shows the potential energy surface for this pathway which proceeds *via* a barrier of 96 kJ mol^{-1}. This is a higher energy pathway compared to the LAPS mechanisms involving oxygen and nitrogen protonation.

Figure 3.16 shows **TS$_{26}$** along with the corresponding minima **2b$_i$** and **6**. The acetylide in **6** is now angled down and away from the Cp* ligand compared to the acetylide in the other pathways. This is to accommodate the hydride, which sits closer to the Cp* ligand to reduce any steric interaction. During **TS$_{26}$**, the alkyne is oriented in a similar way as in **6**, which brings the methyl group on the alkyne and the phosphoramidate much closer together and thus raises the free energy of the system. The change in oxidation state of the iridium contributes to this larger barrier. Ir(III) is a common and stable oxidation state, while Ir(V) does exist it is not as common.

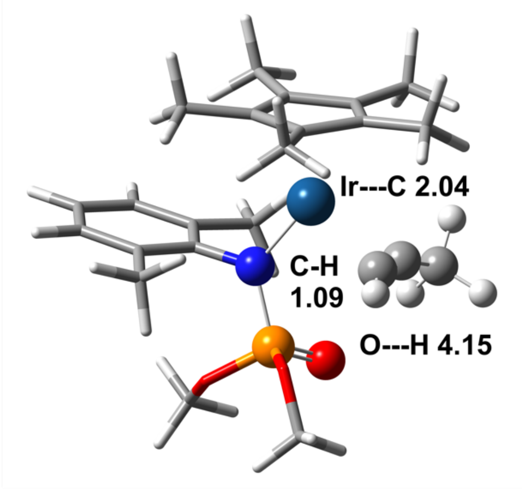

2b$_i$

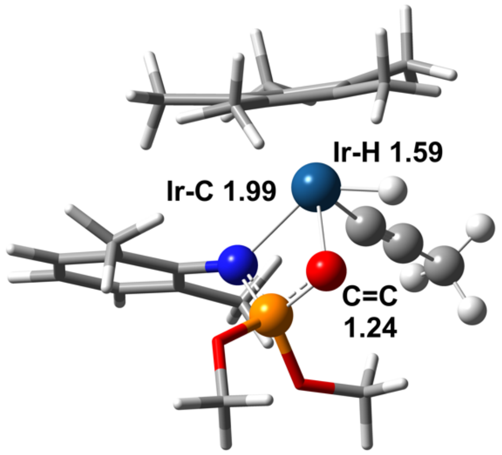

6

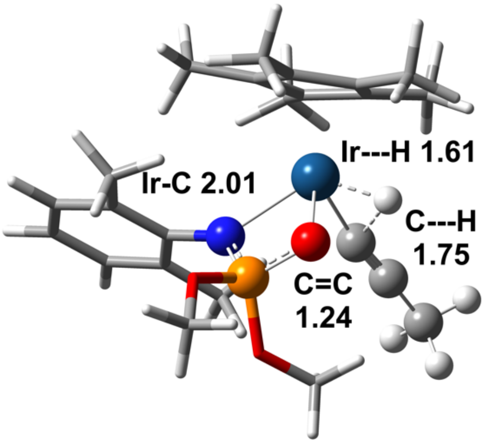

TS$_{26}$

Figure 3.16 - (RI)-PBE0-D3BJ/def2-TZVPP//(RI)-BP86/def2-SV(P) level in CH_2Cl_2 (COSMO) transition state structure for **TS$_{26}$** with corresponding minima **2bi** and **6**. Selected distances are shown in Å. Dark blue = Ir, blue = N, orange = P, red = O, grey = C, and white = H.

The Ir-H distance in **TS$_{26}$** is shorter than the C-H distance, 1.61 vs. 1.75 Å respectively, and lies close to the distance in the resulting minimum **6**, 1.61 and 1.59 Å respectively. The C=C bond length decreases slightly by 0.03 Å in **TS$_{26}$** and remains at this distance in **6**. The transition state therefore lies closer to **6**. This minimum sits 88 kJ mol^{-1} above **2b$_i$** which can be explained due to the need to accommodate an extra group at the iridium, which is now seven coordinate due to a ring slip of the Cp* ligand to η^3 from η^5. This ring slip is also seen in **TS$_{26}$**.

As with Cp*-Protonation, this pathway was not explored further due to the high free energy transition state. While this pathway is only 11 kJ mol^{-1} higher in free energy than the N-protonation pathway it would not be favourable, due to the ability to proceed *via* a lower energy pathway.

3.4.7 1,2-Hydride Shift Pathway

Along with oxidative addition, a hydride shift is a very common step in organometallic reactions, where the hydrogen of a hydrocarbon coordinated to the metal shifts position. For this reaction the terminal hydrogen on the alkyne shifts to the β-carbon classing it a 1,2-hydride shift. The barrier for this process was determined to be 76 kJ mol^{-1} as seen in Figure 3.8. The transition state, **TS$_{24}$**, can be seen in Figure 3.17 along with the corresponding minima **2b$_i$** and **4c**. In **TS$_{24}$** the alkyne is fully rotated from η^1 instead of the η^2 coordination seen in **2b$_i$**. The Ir-C distance decreases by 0.05 Å from **2b$_i$** to the transition state while in **4c** the distance has reduced further to 1.85 Å.

The C=C distance remains unchanged in **TS$_{24}$** but does increase slightly, by 0.05 Å, in **4c**. The Cp* and phosphoramidate ligands during this pathway remain almost unchanged which allows for maximised distance between to minimize any steric clash. The barrier for this process is comparable to that for the N-protonation pathway but is 28 kJ mol^{-1} higher in free energy than the O-protonation pathway. This is because the hydrogen migration is not facilitated by any of the ligands. Additionally, the O-protonation pathway involves an acidic hydrogen and a basic carbon site on the acetylide that is protonated.

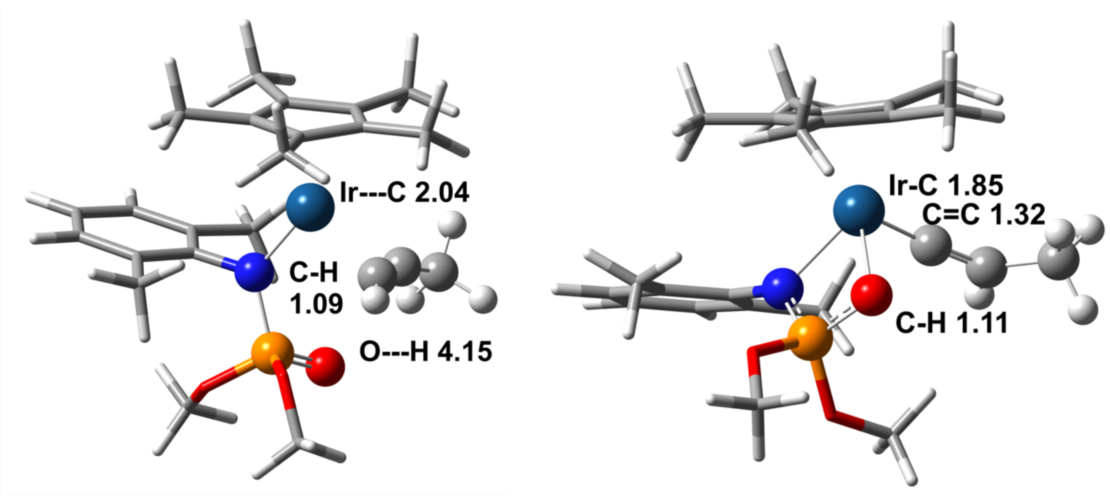

$2b_i$ **4c**

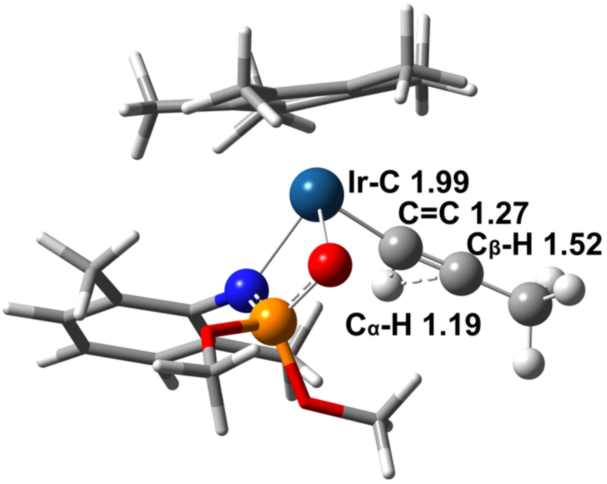

TS_{24}

Figure 3.17 - (RI)-PBE0-D3BJ/def2-TZVPP//(RI)-BP86/def2-SV(P) level in CH_2Cl_2 (COSMO) transition state structure for **TS_{24}** with corresponding minima **$2b_i$** and **4c**. Selected distances are shown in Å. Dark blue = Ir, blue = N, orange = P, red = O, grey = C, and white = H.

TS_{24} results in the formation of the vinylidene **4c**, where the Cp* ligand has slipped to η^3 coordination. This ring slip allows for coordination of both the nitrogen and the oxygen of the κ^2-phosphoramidate and a small stabilization of 3 kJ mol^{-1} compared to **$4a_i$** (see Figure 3.8). From **4c** the final product **5** can then be accessed. This 1,2-hydride shift pathway gives access to the final product *via* fewer intermediates, a lower barrier than in the N-protonation pathway, but larger than in the O-protonation pathway.

3.4.8 Alkyne Activation Mechanism

The initial investigation into different pathways showed that oxidative addition and Cp*-protonation proceed *via* high free energy barriers. These pathways were therefore not investigated further as they were determined not to be competitive. Further discussion of the remaining three pathways, O-protonation, N-protonation, and 1,2-Hydride Shift for the formation of **5** are necessary to determine the most likely pathway.

The first transition state for the O-protonation pathway was determined to be lower in energy than the N-protonation and 1,2-hydride shift pathways by 37 and 28 kJ mol^{-1} respectively. This lower energy barrier makes the O-protonation pathway the most accessible and likely. In the N-protonation pathway the intermediate **3b** is 13 kJ mol^{-1} lower in energy than **3a**, the O-protonation pathway analogue. This extra stabilisation, due to protonation of the more basic site, in the N-protonation pathway leads to a larger barrier for the second transition state **TS$_{3b5b}$** of 149 kJ mol^{-1} compared to 46 kJ mol^{-1} for **TS$_{3a4}$**. **TS$_{3b5b}$** does lead directly to the product instead of proceeding *via* a vinylidene intermediate but this large barrier makes the pathway unlikely.

The 1,2-hydride shift pathway proceeds *via* only one transition state, **TS$_{24}$**, which leads directly to intermediate **4c**. From here the isomer **4a$_i$** can be accessed, which was found to lie on the O-protonation pathway. Conversion from **4c** to **4a$_i$** requires breaking the Ir-O bond and changing the coordination of the Cp* ligand from η^3 to η^5. The isomer **4a$_i$** lies slightly higher on the PES than **4c** within an energy difference of 3 kJ mol^{-1}.

Theoretically, both **5a** and **5b** can be accessed from **4c** since both the Ir-N or the Ir-O bond can be broken and result in attack of the vinylidene. To test this a scan of **4c** was completed where the distance between the oxygen or nitrogen of the phosphoramidate and the α-carbon of the vinylidene was decreased (see section 3.4.9). This showed that there is a barrier of approximately 70 kJ mol^{-1} to reach **5a** and **5b** from **4c**.

5a could also be accessed from **4a$_i$**, since the Ir-O bond is already broken in this intermediate. A scan was once again carried out where the C-O distance was varied (see section 3.4.9). This PES scan showed that the product **5a_Z** is formed from **4a$_i$** and proceeds without a significant barrier. So, while both **5a** and **5b** can be formed from **4c**, a change in the coordination resulting in **4a$_i$** allows access to the product **5a_Z** directly, without overcoming a significant barrier.

5a_E does not result from **4a$_i$** since the methyl group on the vinylidene is oriented away from the oxygen. Vinylidene rotation was determined to be possible in this complex (see section 3.4.10) *via* a low energy barrier of 10 kJ mol^{-1}. The resulting isomer has the same energy and allows access to the thermodynamic product **5a_E**.

Overall the N-protonation pathway is not accessible. While the first transition state, **TS$_{23b}$**, proceeds through a barrier close in energy to the 1,2-hydride shift pathway the barrier of the second transition state, **TS$_{3b5b}$**, to reach **5b** is high in energy. While **3b** could be formed, this cannot react further and would require overcoming a barrier of 118 kJ mol^{-1} to reach the starting complex **2**. No such intermediate was seen experimentally and therefore it is likely that the N-protonation pathway does not proceed at all.

For the 1,2-hydride shift pathway, since this converges with the O-protonation pathway and proceeds *via* a barrier not much high in energy than those in the O-protonation pathway, it cannot be ruled out as a possible pathway. The N-protonation pathway is not likely to occur due to subsequent high energy barriers and since no side product, such as **3b**, was observed in the reaction it would be likely that the barrier for **TS_{24}** would also be too large. Thus, making the O-protonation pathway the most plausible for this reaction. As stated previously only the product **5a_E** was observed experimentally, which is consistent with the computational study carried out here. The regioselectivity seen in this reaction where the nitrogen product, **5b**, was not observed is due to a high barrier in the N-protonation pathway along with a high barrier for the formation of **5b** from **4c**. Only the *E*-isomer was observed experimentally, which is due to it being the thermodynamic product and the virtually barrierless rotation of the vinylidene in **4c** and **4a**. So, while **5a_Z** could be formed, since the DRC showed this to be the end product from **$4a_i$**, the thermodynamic product can be accessed by converting back to **$4a_i$** and undergoing rotation of the vinylidene *via* a barrier of 63 kJ mol^{-1}.

3.4.9 Potential Energy Surface (PES) Scans

Two scans were carried out to determine whether attack of the nitrogen or oxygen of the phosporamidate on the α-C of the vinylidene in **4c** takes place. For **$4a_{ii}$** a scan was carried out where the distance from the uncoordinated oxygen of the phosphoramidate and the α-carbon of the vinylidene was decreased. No transition state was located between **$4a_{ii}$** and **5a**, therefore the scan was used to determine whether there is a barrier for formation of the product. Figure 3.18 shows the N-C and O-C distances that were scanned in **4c** and **$4a_{ii}$**, from 3.12 to 1.22 Å and 2.84 and 1.34 Å respectively.

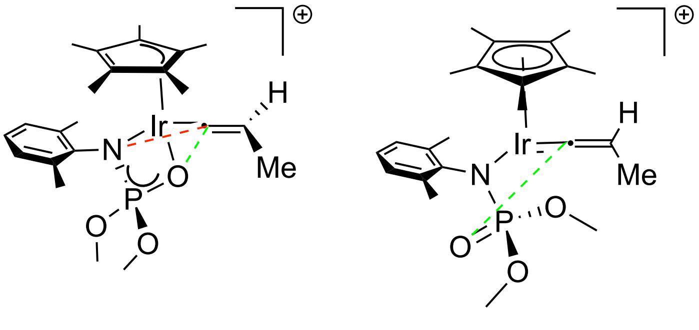

4c **$4a_{ii}$**

Figure 3.18 – Relaxed PES scans were carried out on **4c** and **$4a_{ii}$** to determine approximate barriers**.** Dashed bonds connect the two atoms involved in the scans, where the red line indicates the N-C scan and the green line the O-C scan.

Figure 3.19 shows the distances along with the relative energies of these states in kJ mol^{-1}. Both scans show that the barrier for formation of the corresponding product **5** is around 65 kJ mol^{-1}. This provides an alternative pathway for the formation of **5a** and **5b**. For the oxygen scan the relative electronic energy rises until 2.14 Å (see Figure 3.19). Here the relative energy is 67 kJ mol^{-1}, which gives an approximation of the barrier for the formation of **5a** from **4c**. A transition state could not be determined because the optimization continually converged to a minimum, even though attempts were made to alter step size, convergence threshold, functionals, and also which computational software used.

For **5a** the lowest energy pathway from **4c** would be tautomerisation to **4a**$_{ii}$ through the oxygen uncoordinating before proceeding to **5a** instead of attack of the oxygen directly from the iridium. As the distance between the iridium and oxygen increases this Ir-O bond will break as the Cp* ligand shifts from η^3 to η^5 and **4a**$_{ii}$ forms. If **4c** is formed during the reaction, this complex will tautomerise to complex **4a**$_{ii}$, followed by attack of the P=O oxygen on the vinylidene to give the final product **5a**.

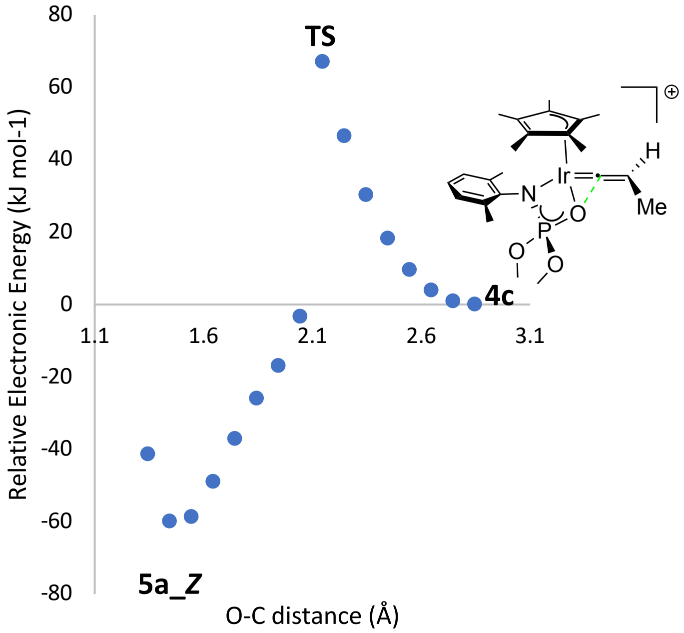

Figure 3.19 – Relative electronic energies of the relaxed scan of the O-C distance in **4c** varying from 2.84 to 1.34 Å at the (RI)-BP86/def2-SV(P) level.

For the Ir-N scan (see Figure 3.20) the energy change is much shallower. The relative energy rises until the distance between the nitrogen and α-carbon on the vinylidene reaches 2.22 Å. This gives a barrier of 63 kJ mol^{-1} for the formation of **5b** from **4c**. For **5b** this offers an alternative pathway that is lower in energy than proceeding from the N-protonation pathway or isomerising to isomer **4b**. However, since the O-protonation pathway has lower energy barriers, formation of **5b** *via* this pathway is not viable.

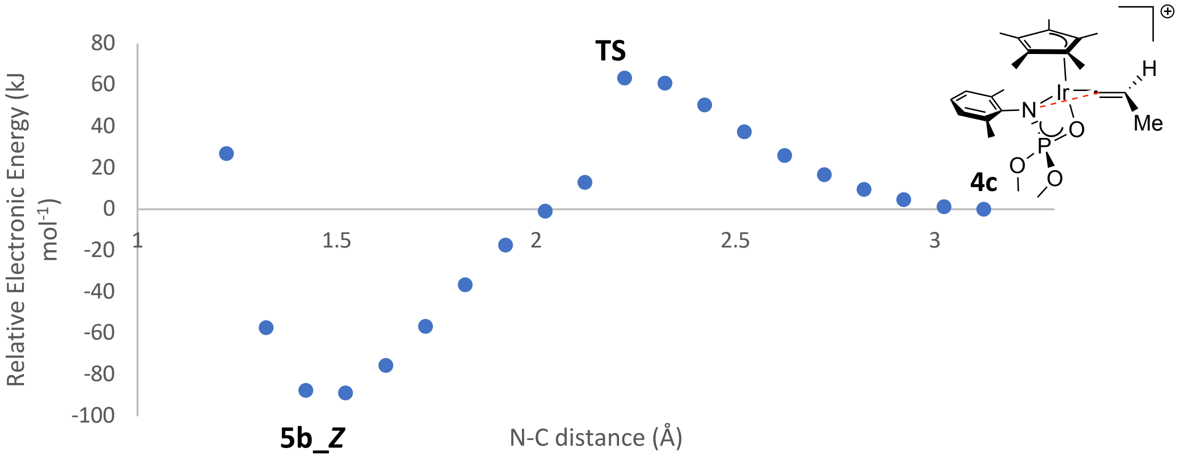

Figure 3.20 - Relative electronic energies of the relaxed scan of the N-C distance in **4c** varying from 3.12 to 1.22 Å at the (RI)-BP86/def2-SV(P) level.

Surprisingly the barrier for the formation of the N-C bond is slightly lower in energy than the barrier for the formation of **5a**. These results only provide an approximation of the barrier as these structures were not used to find a transition state at the same level of theory as the rest of the PES. Attempts at finding a transition state were made but were unsuccessful. Due to the absence of a transition state for both these processes no strong conclusion can be drawn about which is energetically preferred. Additionally, since alternative processes are possible from **4c** it is much more likely for tautomerisation of **4c** to **4a$_{ii}$** to occur to give **5a**.

Figure 3.21 shows the distances and relative energies for the scans of O-C carried out on **4a$_{ii}$**. As the distance between the oxygen to the vinylidene α-carbon is decreased the relative energy decreases. This shows that there is no barrier to formation of **5a** from **4a$_{ii}$**. **4a$_{ii}$**, which would therefore react very quickly to form **5a**.

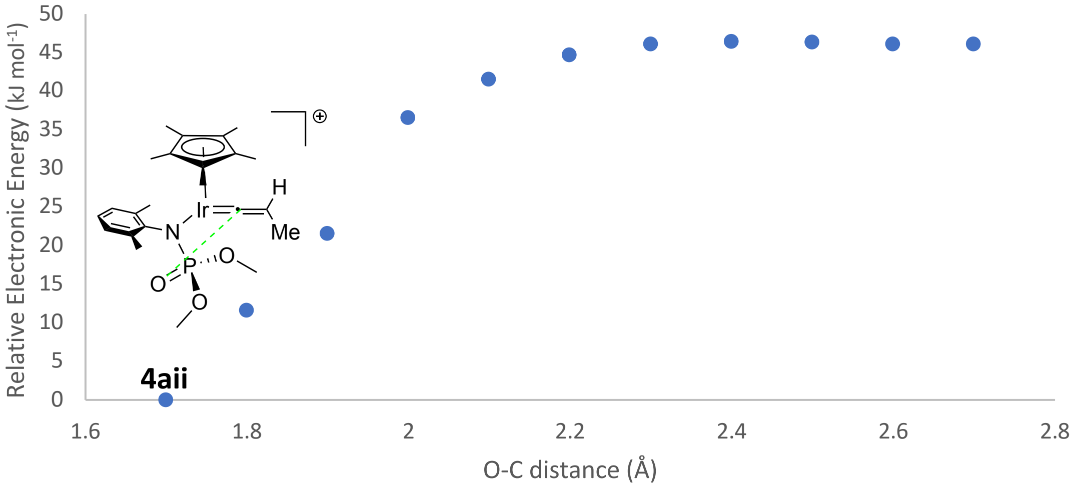

Figure 3.21 – Relative electronic energies of the relaxed scan of the O-C distance in **4a$_{ii}$** varying from 1.70 to 2.70 at the (RI)-BP86/def2-SV(P) level

A scan of O---C was also carried out to isolate the barrier to the formation of **5a** from the conformational isomer **4a$_{i}$**. In the conformational isomer **4a$_{i}$** (see Figure 3.22) the methyl group on the vinylidene is oriented up towards the Cp* ligand. Attack of the phosphoramidate oxygen on the vinylidene here would then lead to the **5a_Z** product. Just as with **4a$_{ii}$** the scan showed that there is no barrier to the formation of **5a_Z** (see Figure 3.23).

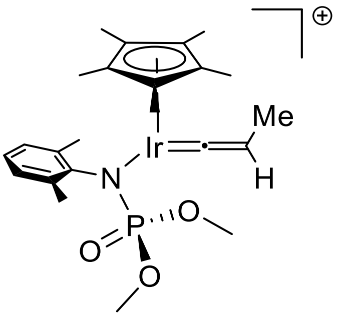

4a$_{i}$

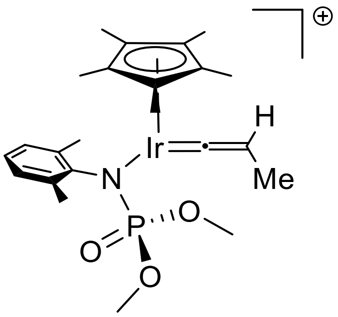

4a$_{ii}$

Figure 3.22 - Conformational isomers **4a$_{i}$** and **4a$_{ii}$**

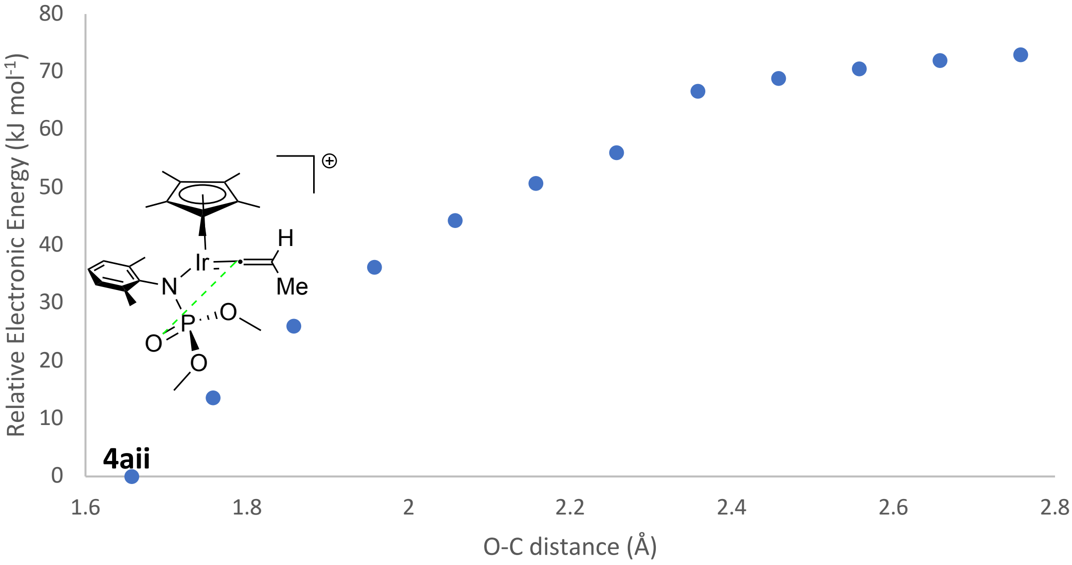

Figure 3.23 – Relative electronic energies of the relaxed scan of the O-C distance in **4ii** varying from 1.76 to 2.76 Å at the (RI)-BP86/def2-SV(P) level

3.4.10 Vinylidene Rotation Scan

As previously mentioned, vinylidene rotation is usually a low energy process. To confirm that this is the case here a scan of the dihedral angle of the vinylidene of **4c** was carried out. The scan was carried out in TURBOMOLE by freezing the dihedral angle of the four atoms involved (N, Ir, C, C(Me), see Figure 3.24) and optimizing the structure at each angle. Single point calculations were then carried out on these optimized structures to improve upon the electronic energy. A scan of 180 degrees was carried out where the Me group of the vinylidene passes the Me groups of Cp*. The rotation of an Me group of the vinylidene past the Cp* ligand would be higher in energy when compared to a H group. The greater bulk of the Me group of the vinylidene, compared to the H, would result in a greater steric clash and thereby increase the barrier for the rotation. Since the barrier for the Me group of the vinylidene was found to be 10 kJ mol^{-1} a full 360-degree scan was not carried out since it was assumed that the barrier for the H group rotating past the Cp* ligand would be lower in energy .

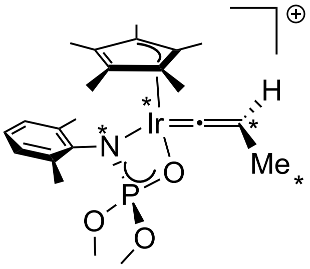

4c

Figure 3.24 – A relaxed PES scans were carried out on **4c** to determine the barrier of vinylidene rotation**.** Atoms included in the dihedral scan are indicated by *.

Figure 3.25 shows the dihedral angle and the relative energy for each of the angles. The barrier for rotation is only 10 kJ mol^{-1}, which occurs when the methyl group on the vinylidene is almost parallel to the N-C(dimethylphenyl) bond. At this point the empty p-orbital on the α-carbon is oriented in such a way that any backdonation from the metal to the ligand is no longer present.

With a barrier of 10 kJ mol^{-1} this rotation is easily accessible and explains why the thermodynamic product, **5b_E**, is formed in the reaction even though based on the structure of **4c** the Z-isomer would be expected.

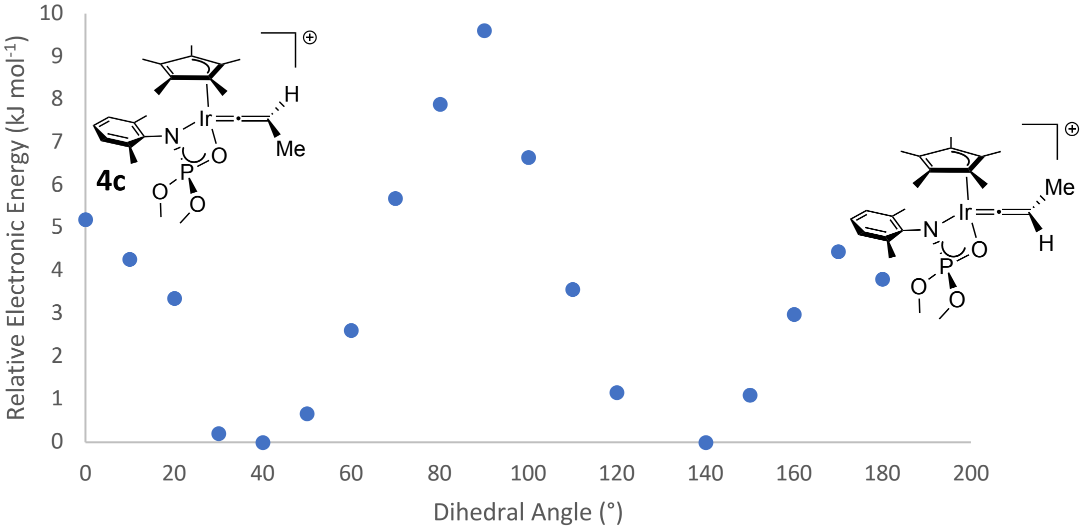

Figure 3.25 – Relaxed scan of the dihedral angle (N-Ir- C_β-C(Me)) in **4c** at the (RI)-PBE0/def2-SV(P) level

3.4.11 Origins of Regio- and Stereoselectivity

The two regio- and two stereo-isomers of **5** are shown in Figure 3.26. In the experiment carried out by Drover *et al.* only the **5a_*E*** isomer, the Ir-O product, was observed even when the R group on the alkyne was changed.[108] Not a trace of the alternative **5b** regioisomer nor the *Z*-isomer of either regioisomer was detected. Both the *E* and *Z* stereoisomer of **5b** are thermodynamically favoured over the **5a** isomer by 6 kJ mol^{-1} and 22 kJ mol^{-1} respectively as seen in Figure 3.8. The PES also shows that while **5b_*E*** is the thermodynamic product of the reaction, larger energy barriers for the N-protonation pathway make this product inaccessible *via* this pathway.

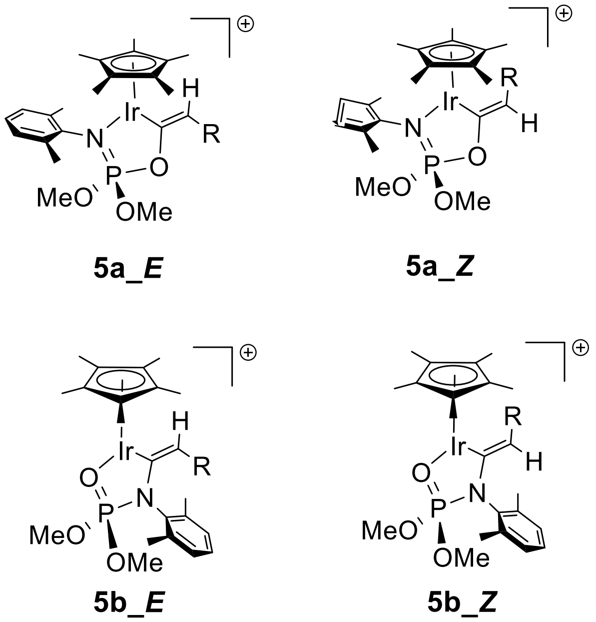

Figure 3.26 – Regio- and stereo-isomers of **5**.

5b could potentially be formed from the κ^2-*N,O* coordinated phosphoramidate vinylidene **4c** either by breaking the Ir-N bond followed by attack of the nitrogen or *via* direct attack of the nitrogen. Figure 3.8 shows that the **4b** isomer, which is formed by breaking the Ir-N bond, is 111 kJ mol^{-1} and 108 kJ mol^{-1} higher in energy than **4c** and **$4a_{ii}$** respectively. Formation of **5b** *via* an isomer of **4** was, therefore, determined to not be accessible due to the availability of a lower energy pathway *via* the O-protonation pathway. Direct attack of the nitrogen in **4c** was also determined not to be feasible as the scan in **Error! Reference source not found.** and Figure 3.19 showed this involved a barrier of around 60 kJ mol^{-1}. The combination of higher energy barriers for both the N-Protonation pathway and the reaction from the isomers of **4** give insight and possible reasons for why the thermodynamic regioisomer **5b** was not observed experimentally.

Regarding the stereoselectivity that was observed in the reaction the *E* isomer of both **5a** and **5b** is the thermodynamic product. The E isomer lies 19 and 3 kJ mol^{-1} lower in energy than the *Z* isomer of **5a** and **5b** respectively. The scan carried out on **4a$_{ii}$** leads to the *Z* isomer of **5a** due to the orientation of the vinylidene in **4a$_{ii}$**. The PES scan of **4a$_{i}$** showed that there was no barrier to the formation of **5a_*E***.

Vinylidene rotation was determined to be approximately 10 kJ mol^{-1} for **4c**. Rotation of the vinylidene through this low barrier, followed by attack of O at the α-carbon, allows access to the thermodynamic product. From **5a_*Z*** a barrier of 63 kJ mol^{-1} would need to be overcome to convert back to **4a$_{ii}$**. Vinylidene rotation can then occur and lead to a stabilization of 19 kJ mol^{-1} by formation of **5a_*E***. In the reaction carried out by Drover *et al.* the reaction was heated to 25 °C and allowed to react for 15 minutes. Under these conditions conversion to **4a$_{ii}$,** rotational of the vinylidene to give the other conformational isomer **4a$_{i}$**, and attack of the oxygen to give the thermodynamic product would be possible. For **5b** such a pathway is not possible since accessing the vinylidene **4b** would require overcoming a barrier of 193 kJ mol^{-1}. The stereoselectivity observed for this reaction is therefore due to a thermodynamic effect with **5a** and once again large energy barrier for **5b** preventing formation of this product.

3.4.12 Substituent Effects

The effect that the R group on the alkyne has on the thermodynamic preference of isomers **5a** and **5b** was tested. R= Me, Ph, *p*-^{t}BuPh, Cy, and ^{t}Bu (see Figure 3.27) were chosen as these groups exhibit different steric and electronic effects. Table 3.2 shows the relative Gibbs free energies of **5b** relative to **5a**. For R=Me, Ph, and *p*-^{t}BuPh the energy difference is negligible and within DFT error to suggest that there is no preference. R=Me is the smallest group and therefore sterics would not play a big part here. For R=Ph and *p*-^{t}BuPh there is the potential for steric clash with the Cp* ligand and the phosphoramidate. These potential clashes can be mitigated due to rotation since the phenyl group is planar. While *p*-^{t}BuPh is bulkier than Ph the bulk of this group is situated far from the rest of the ligands on the iridium and therefore does not result in a preference between the isomers.

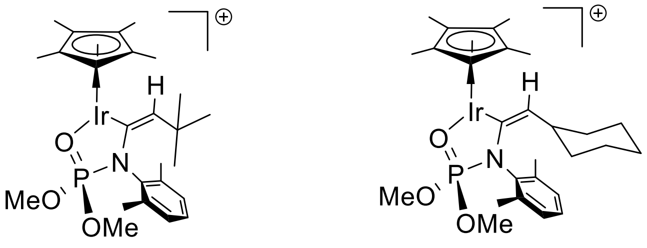

R=^{t}Bu R=Cy

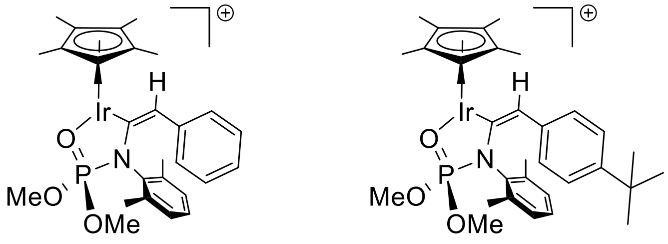

R=Ph R=*p*-^{t}BuPh

Figure 3.27 – The effect of the R group on the alkyne was tested on the isomers of **5b_E** with R=^{t}Bu, Cy, Ph, *p*-^{t}BuPh

For R=Cy and ^{t}Bu there is an isomer preference as the relative Gibbs free energies are now -14 and 15 kJ mol^{-1} respectively for isomer **5b**, relative to **5a**. The isomer **5b** is now preferred for the cyclohexyl group and **5a** for the *t*-butyl group.

Table 3.2: Free energies of isomer **5b**, relative to **5a**, with R=Me, Ph, *p*-^{t}BuPh, Cy, and ^{t}Bu at the (RI)-PBE0/def2-TZVPP//(RI)-BP86/def2-SV(P) level.

R	5b ΔG (5b-5a) (kJ mol^{-1})
Cy	-14
Me	-6
Ph	1
p-^{t}BuPh	3
^{t}Bu	15

In the case of R=^{t}Bu the **5a** isomer is thermodynamically favourable, which is consistent with the experimental results obtained by Drover *et al.*[108] The most likely explanation for this preference is due to the steric clash that would occur between the Cp* ligand and the *t*-butyl group in **5b**. In isomer **5b** the dimethylphenyl group on the nitrogen of the phosphoramidate is much closer to the R group of the reacted alkyne. Since this dimethylphenyl group is quite bulky it would be predicted that the R group on the alkyne that was used would be forced towards the Cp* ligand and thereby raise the energy of the system.

3.4.13 Functional Dependency

The functional dependence on the relative ordering of the isomers of the products **5a** and **5b** was tested. M06 and ωB97XD were chosen as M06 is known to work well with transition metal thermochemistry and organometallics in general[122] and ωB97XD includes longer range effects and deals well with dispersion.[123] Table 3.3 shows the relative energies of the isomers of **5** using PBE0, M06, and ωB97XD. For all three functionals the relative energies of the isomers are similar and are almost exactly the same when considering the errors associated with these calculations.

Table 3.3 - Relative electronic energies for the isomers of **5** at the PBE0-D3BJ/def2-TZVPP, M06/def2-TZVPP, and ωB97XD/def2-TZVPP level

	Rel. E (kJ mol^{-1})	Rel. E (kJ mol^{-1})	Rel. E (kJ mol^{-1})
5a_E	0	0	0
5b_E	-4	-1	-2
5a_Z	19	16	16
5b_Z	0	2	1

The small differences in the relative energies combined with the same ordering of the isomers for these three different functionals provides some confidence that there are no functional effects on the thermodynamic preference for these isomers and most likely for this reaction in general. Further work could be done by selecting a few stationary points to carry out a similar test to gain even more confidence in the methodology that was chosen.

3.5 Conclusions

A LAPS mechanism was proposed to occur when terminal alkynes were reacted with an Ir(III)Cp* complex containing a bidentate 1,3-N,O-phosphoramidate ligand to give a five-membered irida(III) cycle. Only the *E*-isomer of the O-phosphoramidate product was observed showing strong regio- and stereoselectivity. The occurrence of a LAPS mechanism was tested by carrying out the reaction in the presence of a weak Lewis base, MeCN. This hindered the formation of the irida(III) cycle and provided some evidence for a LAPS mechanism. A thorough computational investigation into the possible mechanisms that could be occurring had not yet been done.

Here, five different pathways for this reaction were investigated – O-Protonation, N-Protonation, Cp*-Protonation, Oxidative Addition, and 1,2-Hydride Shift. Access to the PESs for this reaction allowed insight into the reaction to understand the origins of the regio- and stereoselectivity that was observed. Two of these pathways, Cp*-Protonation and Oxidative Addition, were determined to proceed *via* high energy barrier and therefore would not be competitive in this reaction.

Out of the remaining three pathways two of these were LAPS pathways, O-Protonantion and N-Protonation, which showed very different reactivity. For the O-Protonation pathway the reaction proceeded *via* a vinylidene intermediate. Access to a vinylidene intermediate allows for the formation of the thermodynamically favoured product for this pathway, **5a_E**. The reaction proceeds *via* low energy barriers, 48 and 46 kJ mol^{-1} for $\mathbf{TS_{23a}}$ and $\mathbf{TS_{3a4a}}$ respectively, and the formation of the final product was determined to be barrierless through a PES scan.

For the N-Protonation pathway both $\mathbf{TS_{23b}}$ and $\mathbf{TS_{3b5b}}$ presented large barriers, 85 and 149 kJ mol^{-1} respectively. No vinylidene intermediate was found to be located along with PES as a DRC calculation showed the direct formation of **5b_Z** from $\mathbf{TS_{3b5b}}$. The large free energy barrier make this pathway unlikely.

The 1,2-Hydride Shift Pathway proceeds *via* only one transition state, $\mathbf{TS_{24}}$, with a barrier of 76 kJ mol^{-1}. This barrier is lower in energy than those for the N-Protonation pathway, but still larger than the barriers for the O-Protonation pathway. While it is likely that the reaction proceeds only *via* the O-Protonation pathway the energy of the 1,2-Hydride Shift pathway could be accessible. It is likely therefore that the reaction could proceed *via* more than just one pathway depending on the orientation of the alkyne and the phosphoramidate in the complex. $\mathbf{TS_{24}}$ leads to the intermediate **4c**, the κ-N,O Ir(III) complex. From **4c** it was determined that formation of either **5a** or **5b** would require overcoming a barrier of approximately 65 kJ mol^{-1}. A change in coordination, however, leads to $\mathbf{4a_{ii}}$, and consequently access to **5a**, as with the O-Protonation pathway, and thus a lower energy pathway.

Since no trace of **5b** was found experimentally it would be reasonable to assume that the barrier of approximately 65 kJ mol^{-1} from **4c** is high enough for this process not to occur. This would therefore suggest that the barrier of 76 kJ mol^{-1} for the 1,2-Hydride Shift pathway is also too high to occur. However, no definitive answer can be given on whether this pathway would occur without further experimental work being carried out.

The work presented here therefore suggests that the reaction investigated by Schafer *et al.* proceeds *via* a LAPS mechanism as was hypothesized in the original paper. The P=O oxygen of the phosphoramidate, therefore, acts as a proton shuttle where it aids in both the activation of the C-H bond in the alkyne, but also the formation of a new C-H bond to give the final irida(III) cycle.

While the N-phosphoramidation product, **5b**, is thermodynamically favoured only the O-phosphoramidation product was observed. This regioselectivity can be explained due to a high free energy barrier in the N-Protonation pathway combined with the significant barrier in the O-protonation and 1,2-Hydride Shift pathways for formation of **5b** from **4c**.

The final product, **5a_E**, is the thermodynamically favoured isomer of **5a** while **5a_Z** is the kinetic product. The O-protonation pathway proceeds *via* a vinylidene intermediate **4a$_{ii}$**. A scan was carried out that determined that vinylidene rotation is a low energy process as with many other vinylidene containing complexes. This lower energy barrier for rotation allows access to the other isomer of **4a$_{ii}$** and therefore the thermodynamic product **5a_E**.

The reaction between terminal alkynes and a phosphoramidate containing IrCp* complex is therefore most likely to proceed *via* a LAPS mechanism as originally proposed by the authors. Furthermore, the regioselectivity and stereoselectivity for this reaction are now understood since the N-protonation pathway is not competitive and even inaccessible given the experimental conditions.

4. Investigating the Strong Solvent Effects in Diels-Alder Reactions for the Synthesis of Methoxatin

4.1 Introduction

4.1.1 Catalysis

Homogeneous catalysis spans many areas such as transition metal catalysis, organocatalysis, and electrocatalysis. Here, the catalyst is in the same phase as the reactants, predominantely in a solvent medium. Catalysts are present in low concentration compared to the reactants and are not consumed during the reaction. Organocatalysts are small organic molecules used as catalysts for organic transformations. In 2021, Benjamin List and David MacMillian were awarded the Nobel Prize in Chemistry, because of their work involving organocatalysts back in 2000. List *et al.* showed that the amino acid *L*-proline (see Figure 4.1) successfully functioned as an asymmetric catalyst for an intermolecular aldol reaction between acetone and a selection of aldehydes.[124] Soon after, MacMillian and co-workers carried out a Diels-Alder reaction between α,ß-unsaturated aldehydes and various dienes, which was catalysed by a imidazolidinone (see Figure 4.1).[125]

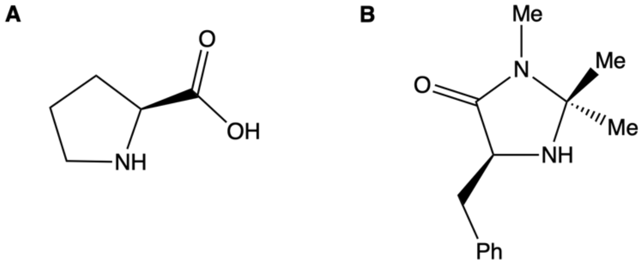

Figure 4.1 - *L*-proline (**A**) and an imidazolidinone (**B**) were shown to function as organocatalysts in an aldol reaction and Diels-Alder reaction respectively.

From 2000 the field of organocatalysis started growing in popularity due to their potential low cost, stability in air and water, and non-toxicity compared to transition metal catalysts.[126–128] Both transition metal complexes and organocatalysts are used extensively in asymmetric synthesis and C-H functionalisation.[84,102,129–132]

Michael additions, cycloadditions, alcohol acylation, Diels-Alder reactions, aldol reactions, and many more have all been carried out using organocatalysts and the field continues to grow.[3,35,138,139,84,124,125,133–137] In these reactions a catalytic amount is used, where the reactants greatly outnumber the catalyst. Solvents have been known to aid reactions and possess properties similar to catalysts. The solvent, however, greatly outnumbers the number of reactant molecules, but when acting "catalytically" it is not consumed or changed by the reaction it facilitates. Solvent catalysis, therefore, lies in a grey area of catalysis due to the large quantity present but the catalytic behaviour that is still seen. The following literature review will focus on recent examples of solvent catalysis.

4.1.2 Solvent catalysis

The effect of a solvent catalysing a reaction is often seen when very specific solvent effects occur in a reaction. A particular solvent will result in increased reactivity and not just due to hydrogen-bonding or charge stabilisation. Solvent effects in reactions are relatively common but can often be difficult to understand. A few examples of reactions where the solvent is thought to catalyse the reaction will be discussed followed by an in-depth look at a Diels-Alder reaction where the solvent could be acting catalytically.

Solvents are very important in reactions as they not only provide a medium but also have an impact on the reactivity and selectivity. Solvents can be categorized by their polarity and their proticity, which can make understanding solvent effects easier. A polar protic solvent can both stabilise charge and hydrogen bond. Examples include H_2O, ethanol, isopropanol, and pyrrolidine (see Figure 4.2).

Polar aprotic solvents contain a significant dipole due to unequal sharing of electrons in the molecule but have no hydrogens bonded to electronegative atoms such as O, N, or F, which would allow for hydrogen bonding. Examples include acetonitrile, acetone, pyridine, and tetrahydrofuran (THF) (see Figure 4.2). Non-polar solvents contain little to no dipole and can therefore not hydrogen bond or stabilise charge. Examples include benzene, cyclohexane, pentane, and toluene (see Figure 4.2). Solvents are therefore often grouped into these categories to try and understand what the effect of different solvents are on the reaction, which can then help provide information on the solvent effect observed.

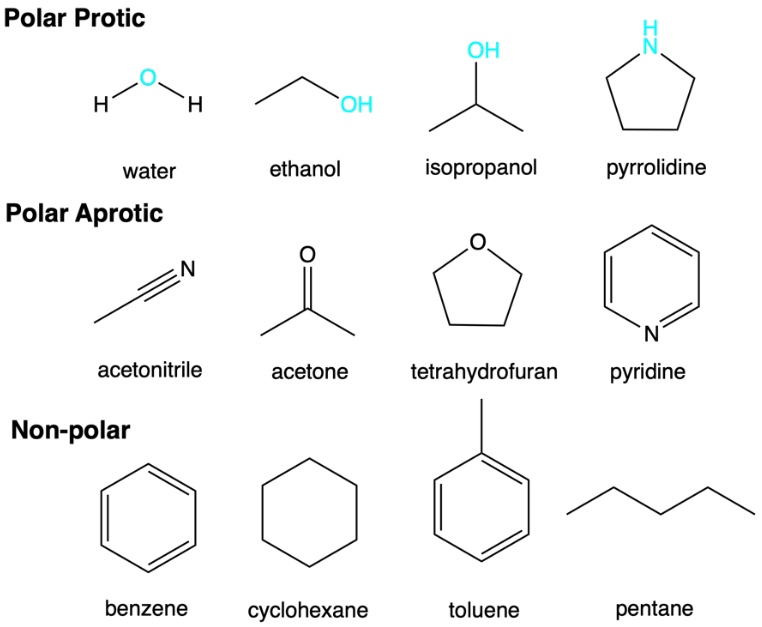

Figure 4.2 – Examples of polar protic, polar aprotic, and non-polar solvents. Atoms in blue indicate the hydrogen bond donors in the polar protic solvents.

The nature of these solvent effects has always been of great interest as the rate of a reaction can be greatly influenced depending on which solvent is used. In some cases, the solvent can directly catalyse the reaction, which is often referred to as "solvent catalysis" even though the solvent is not present in sub-stoichiometric amounts. Examples of solvent catalysis are limited but typically involve the solvent acting as an acid catalyst.[140–142] The lack of examples is likely due to the difficulty in determining the nature of solvent effects and whether the solvent truly can be thought of as a catalyst.

Diels-Alder reactions are an example of a pericyclic reaction, where a diene and a dienophile react to form a cyclic product. This concerted reaction proceeds via a single transition state where two new bonds are formed between the reactants.

The reaction is improved by using electron donating groups on the diene and electron withdrawing groups on the dienophile. Looking at the frontier molecular orbitals of the diene and dienophile in Figure 4.3, the HOMO-LUMO gap is decreased with these conditions. This is because electron donating groups raise the energy of the HOMO of the diene, which is donating into the LUMO of the dienophile, which in turn is lowered with electron withdrawing groups.

Inverse-electron demand Diels-Alder reactions use an electron poor diene and an electron rich dienophile. Here, the interaction between the LUMO of the diene and the HOMO of the dienophile are important (see Figure 4.3). Electron withdrawing groups on the diene lower the LUMO while electron donating groups on the dienophile raise the HOMO. The role of the diene and dienophile are now reversed compared to a traditional Diels-Alder reaction.

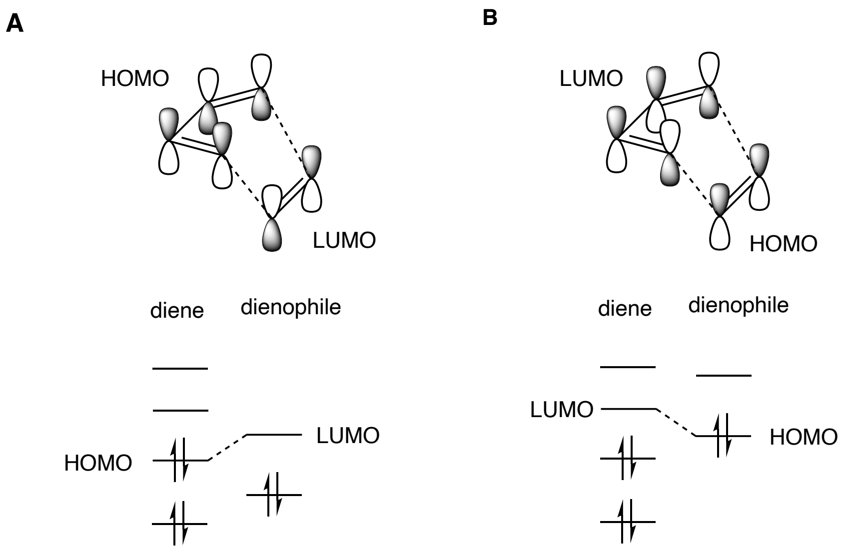

Figure 4.3 Frontier Molecule Orbitals for a traditional Diels-Alder reaction (A) and an Inverse-Electron Demand Diels-Alder reaction (B).

Two products can form during a Diels-Alder reaction: the endo and the exo product. Typically, the endo product is the major product, but this is dependent on the priority of the groups on the diene and dienophile. The endo orientation is when the highest priority group of the dienophile and highest priority group of the diene are on the same face of the resulting product (see Figure 4.4). The exo product is where the highest priority group of the dienophile is on the opposite face to the groups on the diene (see Figure 4.4).

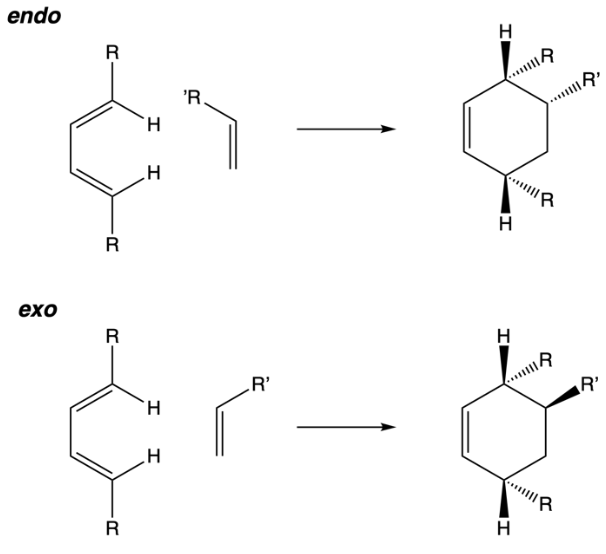

Figure 4.4 - *endo* and *exo* orientation in a Diels-Alder reaction are determined by the location of the highest priority groups of both the diene and dienophile on the resulting six-membered ring product.

Diels-Alder cycloadditions have been studied in detail due to strong solvent effects and the potential occurrence of solvent catalysis.[143,144] In 1980, Breslow *et al.* observed an increase in reactivity of the Diels-Alder reaction of cyclopentadiene and butanone when the reaction was carried out in water.[145] This unexpected acceleration was then investigated further by looking at two Diels-Alder reactions: 1) between nitrosobenzene and 1,3-cyclohexadiene and 2) between methyl vinyl ketone and 1,3-cyclopentadiene (see Scheme 4.1).[146] Both formamide and ethylene glycol showed an increase in reactivity compared to other organic solvents but, both solvents were unable to outperform water. The kinetic study suggested that solvophobic binding was occurring where the reactants are brought close together to minimise high energy interactions between the non-polar reactants and the polar solvent. Even though the authors suggest that formamide and ethylene glycol can be thought of as water-like solvents they were not able to increase the reactivity to the same extent as water.

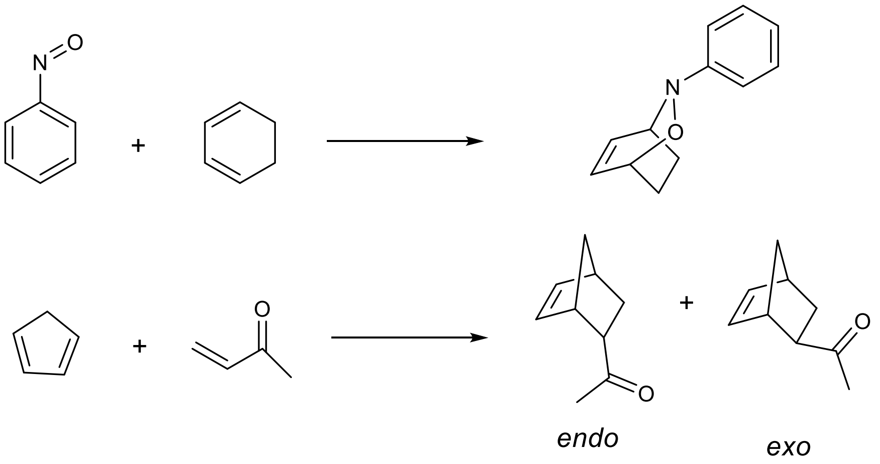

Scheme 4.1 – Diels-Alder reaction between nitrosobenzene and 1,3-cyclohexadiene (top) and methyl vinyl ketone and 1,3-cyclopentadiene (bottom). Both these reactions proceeded faster when carried out in water.

From these two experimental studies computational work started to emerge to try and further understand the solvent effects that were being seen in these Diels-Alder reactions. Jorgensen and co-workers have studied these water effects on Diels-Alder reactions extensively utilising a variety of computational techniques such as QM/MM, Monte Carlo simulations, and *ab initio* calculations with explicit solvent molecules.[6,147–150] They have been able to show that the transition state is stabilised to a greater extent by hydrogen-bonding than the reactants or the product and that hydrogen-bonding to the diene is favourable over hydrogen-bonding to the dienophile. The studies have also strengthened the idea that solvophobic binding is key for the acceleration that is seen along with the water hydrogen-bonding to the polar regions in the transition state. Depending on the substrate that is used hydrogen-bonding to an oxygen or nitrogen is seen where charge is built up during the transition state, which is stabilised through this hydrogen-bond.

Rate acceleration is seen in these Diels-Alder reactions due to hydrogen-bonding and to some degree charge stabilisation. Determining whether the water is acting as a catalyst is complex since in these examples the water is not acting as an acid catalyst. The reactions, however, proceed much slower when other solvents are used. The hydrogen-bonding seen and the solvophobic binding both contribute to the faster rates because the transition states are stabilised and the reactants are brought close together – something that also occurs during catalysis using transition metals and organocatalysts.

4.1.3 Solvent Catalysis in Inverse Electron Demand Diels-Alder Reaction

Surprising solvent effects, potentially due to solvent catalysis, were observed in 2016 by Glinkerman and Boger when investigating a Diels-Alder reaction as part of a total synthesis of methoxatin .[151] Methoxatin, pyrroloquinoline quinone (see Figure 4.5) is used by bacteria to convert methanol to formaldehyde to allow the bacteria to survive on single carbon units. In humans it is being used as a dietary supplement to reduce the damage suffered by a heart attack or stroke, which has resulted in greater interest in its total synthesis.

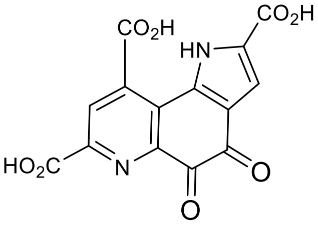

Figure 4.5 – Structure of methoxatin

The key step in the synthesis involved using an inverse electron demand Diels-Alder reaction (IEDDA) between an enamine and 1,2,3-triazine (see Scheme 4.2). Unlike a traditional Diels-Alder reaction in IEDDA reactions an electron-rich dienophile is used along with an electron-poor diene. The original reaction conditions only resulted in a yield of 8% for **7**. Subsequent optimization reactions showed that additives such as trifluoroacetic acid (TFA) and solvents such as hexafluoroisopropanol (HFIP) caused an increase in the observed yield at a standard reaction time and temperature.

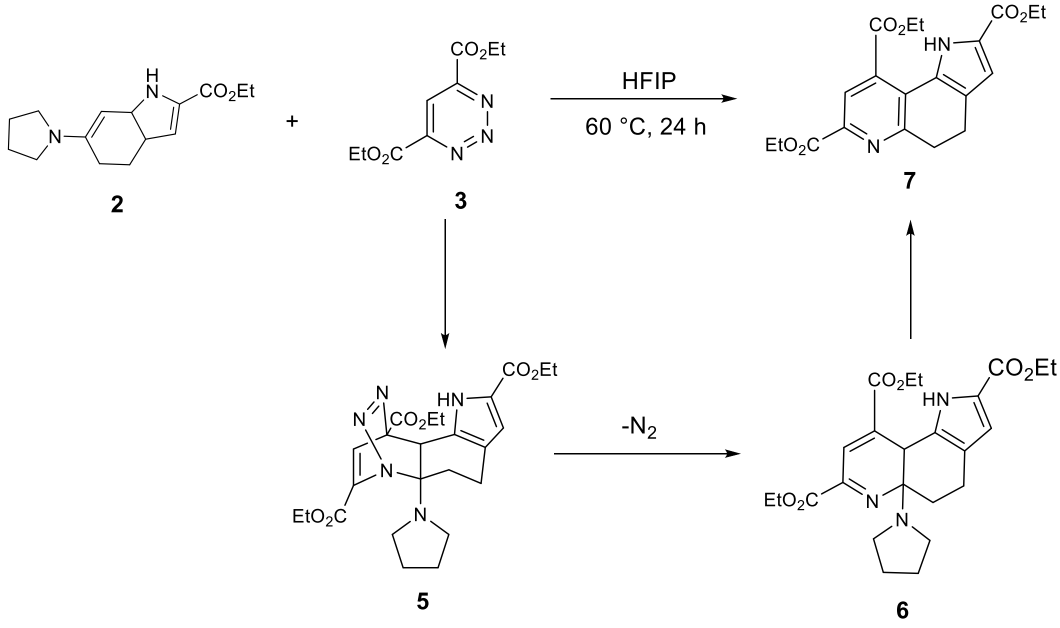

Scheme 4.2 - Reaction between **2** and **3** to give **7**, on the way to the synthesis of methoxatin . Two reaction intermediates **5** and **6** are shown.

Table 4.1 shows a selection of the reaction conditions that were tested. HFIP resulted in the highest yield at 95% when reacted for 24 hours at 60 °C, and trifluoroethanol (TFE) resulted in a significant yield of 36% at 23 °C when reacted for 24 hours. Interestingly the reaction in TFE was not carried out at 60 °C, like the reaction in HFIP. A higher temperature could therefore result in a higher yield with TFE. Chloroform, acetonitrile, dioxane, and toluene all showed very low yields ranging between 7% and 8% at 60 °C while ethanol showed no reactivity at all. The reaction in chloroform was significantly improved by the addition of 1.5 equivalents of TFA increasing the yield from 8% to 34%. The reaction temperature was also able to be decreased from 60 °C to 23 °C along with a reduction in the reaction time to 5 hours. While TFA did result in an increase in reactivity, the yields achieved with HFIP were much higher. After successful synthesis, **7** was oxidised and saponified to give the final product methoxatin, **1**, in 94% yield.

Table 4.1 - Optimization reaction conditions for the reaction between **2** and **3**. *this reaction was carried out with 1.5 equivalents of TFA.

Solvent	Temperature (°C)	Time (h)	Yield
$CHCl_3$	60	24	8 %
CH_3CN	60	24	7 %
Dioxane	60	24	8 %
Toluene	60	24	7 %
$CHCl_3$*	23	5	34 %
TFE	23	24	36 %
HFIP	60	24	95 %
EtOH	60	24	0 %

The authors hypothesised that using an additive such as TFA or a solvent such as HFIP and TFE (see Figure 4.6) resulted in higher yields due to hydrogen-bonding to the 1,2,3-triazine. Additionally, the solvent could aid in the aromatization of **6** by protonating the pyrrolidine. HFIP and TFE were also thought to be useful in this reaction since they would not act as nucleophiles and thus would not consume the starting triazine.

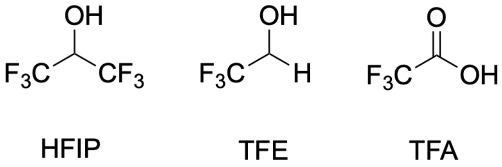

Figure 4.6 – Structures of HFIP, TFE, and TFA, which resulted in the greatest reactivity for the IEDDA reaction between 1,2,3-triazine and a variety of enamines.

The ability of HFIP to hydrogen-bond to the triazine was tested using ^{1}H NMR. Here 1,2,3-triazine was incrementally added to HFIP while the chemical shift of the HFIP alcohol proton was monitored. A downfield shift was seen (Δ1.36 ppm) along with a smaller shift of Δ0.19 ppm for the methane proton on HFIP. A shift to higher ppm is seen suggesting the proton is less shielded by the electrons of the oxygen in HFIP, which would occur due to an increase in the OH distance *via* hydrogen-bonding to the triazine. The shift of the aryl hydrogen on the triazine was much smaller (Δ0.03 ppm). Only small shifts in the methane proton on HFIP and the aryl hydrogen on triazine would be expected as these are further away from where hydrogen-bonding is occurring. The small change in chemical shift seen for the aryl hydrogen on the triazine is due to the proton being slightly deshielded since the electrons in the bond to the carbon are no longer as closely held to the nucleus and therefore do not shield the proton as well from the magnetic field.

The alcohol hydrogen on HFIP experiences a much larger shift since it is directly bonded to the oxygen that is hydrogen-bonding. As the electrons on the oxygen are shared with the hydrogen on the triazine the oxygen will draw the electrons in the bond to the alcohol hydrogen closer. This will cause the chemical shift to move downfield as the nucleus is no longer shielded as much. The small change in the chemical shift of the methine hydrogen of HFIP is to be expected, along with only the small change in the fluorine NMR due to the distance from the oxygen. Some deshielding is seen due to the oxygen now drawing more electron density to it by forming this hydrogen-bond. This will draw the electrons from the bonds between the carbon and hydrogen, and carbon and fluorine closer to the carbon and therefore deshield the hydrogen and fluorine causing a shift downfield.

A further reaction was studied in detail using β-tetralone (**8**) with 1,2,3-triazine (**3**) with a variety of solvents (see Scheme 4.3). As with the previous reaction only HFIP and TFE resulted in significant yields of 86% and 34% respectively. Leading on from this the authors tested a variety of azadienes to determine the effect HFIP had on the yields compared to chloroform. In general HFIP resulted in an increase in the reactivity, even resulting in reaction of some azadienes that were unreactive when chloroform was used.

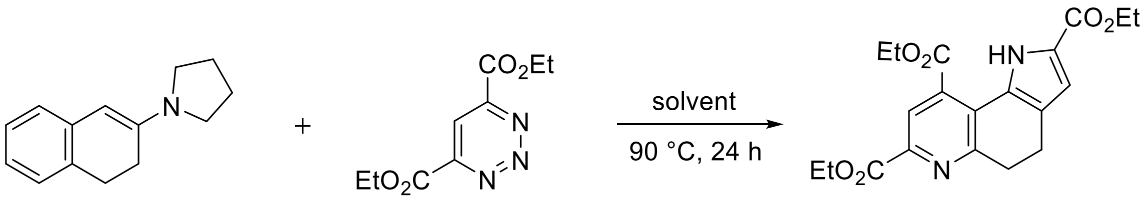

8 **3** **12**

C_6H_6 27%
Et_2O 10%
CH_2Cl_2 11%
THF 0%
CH_3CN 0%
$CHCl_3$ 17%
EtOH 0%
^{i}PrOH 0%
TFE 34%
HFIP 86%

Scheme 4.3 – Percentage yields for the reaction between enamine, **8**, and triazine, **3**, are shown for a variety of solvents studied by Glinkerman.[151]

Strong solvent effects were seen in both reactions shown above. Scheme 4.3 shows the observed yield for a few of the solvents that were tested. Polar aprotic solvents such as chloroform and dichloromethane showed low reactivity with a yield of 17% and 11% respectively, while THF and acetonitrile showed no reactivity. Benzene is a non-polar aprotic solvent and gave a surprisingly high yield of 27% while diethyl ether only gave a yield of 10%. Polar protic solvents such as EtOH and ^{i}PrOH showed no reactivity while HFIP and TFE gave the highest yields of 86% and 34% respectively. Figure 4.7 shows the solvents from Scheme 4.3 in the order of increasing polarity along with whether they are aprotic or protic. The highest yields were seen with polar protic solvents like TFE and HFIP with a yield of 34% and 86% respectively. Surprisingly, EtOH and ^{i}PrOH, protic solvents with lower polarity than HFIP and TFE, showed no reactivity at all.

Non-polar → **Polar**

Yield	C_6H_6	Et_2O	$CHCl_3$	CH_2Cl_2	THF	CH_3CN	*i*PrOH	EtOH	TFE	HFIP
	27 %	10 %	17 %	11 %	0 %	0 %	0 %	0 %	34 %	86 %
			Aprotic					**Protic**		

Figure 4.7 – Solvents investigated for the IEDDA reaction between **3** and **8** shown in the order of increasing polarity and grouped by their proticity, along with the corresponding yield.

Boger *et al.* were able to show that HFIP does hydrogen-bond to the triazine and that using a solvent that is capable of hydrogen-bonding vastly improves the reactivity.[151] Along with this the authors hypothesised that the solvent was necessary not just for hydrogen-bonding but also for protonating the pyrrolidine in **6** and thus aid in the aromatization to give **7**. The reaction therefore benefits from a solvent that can hydrogen-bond while also protonating the pyrrolidine in **7**. Nonpolar aprotic solvents therefore would be expected to not be effective, yet benzene still resulted in good reactivity. Polar aprotic solvents would also be expected to be unsuitable for the reaction which can be seen in the low yields or lack of reaction. For the polar protic solvents EtOH and ^{i}PrOH are likely to not show any reactivity because their conjugated bases are much better nucleophiles than the conjugated bases of HFIP and TFE. This means the starting triazine could be consumed and side reactions are more likely to occur because of the increase in nucleophilicity. The difference in the yields for HFIP and TFE are surprising since HFIP is a much bulkier solvent meaning hydrogen-bonding would be expected to not stabilise the system as much as TFE.

The strong solvent effects combined with robust experimental data make both reactions good candidates for a computational mechanistic study. As HFIP is not a nucleophile and no side reactions were seen for either of the reactions the yields observed are therefore very closely related to the kinetics of the reaction. A lower yield will be due to higher energy barriers since no product is being lost to competing reactions.

4.1.4 Computational Study on Solvent Effects

A computational study was published in 2017 by Houk *et al.*, who investigated the solvent effects seen in the reaction between **3** and **8**.[152] DFT was used to study the mechanism of two triazines with **8** utilising both implicit solvation corrections for the reaction in chloroform and HFIP (Scheme 4.4). The inclusion of a single HFIP molecule was also studied to determine the effect of including an explicit solvent molecule. The optimizations were carried out using M06-2X with the 6-31G(d) basis set followed by single point calculations using the 6-311+G(d,p) basis set to further improve the electronic energy. Solvent corrections were applied using the conductor-like polarizable continuum model (CPCM). Some of the stationary points were also optimized at this higher level of theory but since minimal changes were observed these were not carried out in full.

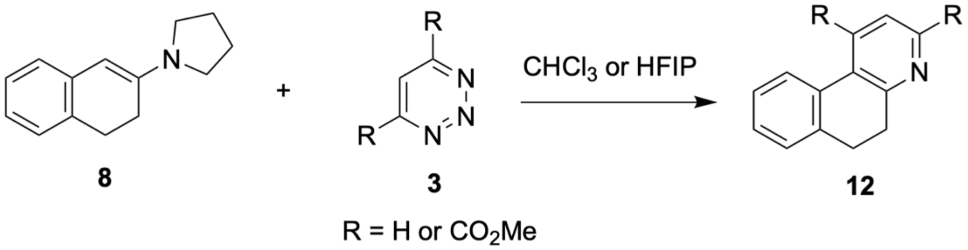

Scheme 4.4 – Reaction studied by Houk *et al.* investigating the effect that HFIP has on the reaction using two different triazines.[152]

Both the traditional concerted Diels-Alder mechanism along with a stepwise mechanism where the C-C and N-C bond are formed during different transition states for both the *endo* and *exo* orientation were studied. In the stepwise reaction the C-C bond was found to form leading to a zwitterionic intermediate, which would be expected to react quickly *via* a low barrier to form the N-C bond to give the Diels-Alder product. A very simple triazine along with the original triazine, but with Me intead of Et groups on the ester, were studied (see Scheme 4.4).

After the formation of the Diels-Alder product the concerted and stepwise reactions converge. The next step of the reaction is loss of N_2 followed by aromatization *via* the loss of pyrrolidine. For the implicit results, using chloroform as the solvent, the barriers for each step of the reaction are shown in Table 4.2. Unfortunately, the loss of pyrrolidine was only determine for the simpler triazine and not for the simplified triazine originally studied. The barrier for the loss of pyrrolidine with the simpler triazine was found to be 159 and 102 kJ mol^{-1} for the implicit and explicit results respectively.

The barriers for both the *endo* and *exo* orientation are almost identical and therefore only the *endo* results will be discussed here. The highest barrier is seen for the formation of the C-C bond at the start of the reaction with a barrier of 94 kJ mol^{-1}. Both the C-N formation transition state and the N_2 loss transition state proceed *via* low barriers of 24 and 15 kJ mol^{-1} respectively. These low barriers are to be expected since the zwitterionic intermediate would quickly react to form the C-N bond. For the N_2 loss this is both entropy driven since a stable molecule is released and results in a stabilisation of 312 kJ mol^{-1}.

Table 4.2 – Free energy barriers for implicit results in chloroform for *endo* and *exo* pathway as determined by Houk *et al.*[152]

Step	Barrier *endo* (kJ mol^{-1})	Barrier *exo* (kJ mol^{-1})
C-C formation	94	99
C-N formation	24	18
N_2 loss	15	9

When an HFIP molecule is included along with implicit solvent corrections there is a general decrease in the energy of the stationary points ranging from 10-40 kJ mol^{-1}. The barriers for the explicit results are shown in Table 4.3. As with the implicit results the barriers for the *endo* and *exo* pathway are almost identical. The inclusion of an HFIP molecule greatly reduces the barrier for C-C formation by 29 kJ mol^{-1} to 65 kJ mol^{-1}. The barrier for the C-N formation is, however, increased by 11 kJ mol^{-1} while the barrier for loss of N_2 remains the same.

Table 4.3 – Free energy barriers for explicit results in HFIP including a single HFIP molecule for both the *endo* and *exo* pathway as determined by Houk *et al.*[152]

Step	Barrier *endo* (kJ mol^{-1})	Barrier *exo* (kJ mol^{-1})
C-C formation	65	61
C-N formation	35	45
N_2 loss	14	15

The increase in the barrier of the C-N formation is most likely because the zwitterionic intermediate is now stabilised with the inclusion of an explicit HFIP molecule. HFIP is able to hydrogen-bond to the negatively charged nitrogen thus reducing the energy of this stationary point. While the C-N formation transition state is also stabilised by the inclusion of an HFIP molecule the stabilisation is not as great and leads to a larger barrier. The transition state for the C-N formation is likely to be less stabilised compared to the minimum due to the HFIP molecule and pyrrolidine of the enamine now being closer together.

The authors concluded from these results that it is the transition state where the C-N bond is formed that is rate-determining for the implicit model while it is the loss of N_2 for the explicit model. While these two stationary points are the highest energy points on the potential energy surface, they are not the rate-determining steps. The rate-determining step is determined by the largest barrier. No transition state for the pyrrolidine loss was included for the more complex triazine but this is the step that proceeded *via* the largest energy barrier for the simpler triazine. The inclusion of ester groups on the triazine is likely to have an impact on the barriers, as was already seen for the other barriers. Using the barriers for the simpler triazine as a rough approximation and would suggest that it is the pyrrolidine loss step that is rate-determining. The results from Boger *et al.*, however, suggest that it is the Diels-Alder step of the reaction that is rate-determining.[151]

The computational study provided detailed insight into one of the Diels-Alder reactions. The effect of including an explicit HFIP molecule greatly reduced the barrier for the formation of the C-C bond at the start of the reaction. This computational study however is not complete. To be able to determine why HFIP is able to facilitate this reaction so well other solvents also need to be studied. TFE showed good reactivity and therefore comparing the effect TFE has on the reaction with the results of HFIP would provide valuable insight. Along with this the current work carried out on this reaction does not match the experimental results available. The rate-determining step is the loss of pyrrolidine, which is not consistent with the work carried out by Boger *et al.*[151] The solvent effects present in these reactions is therefore still not fully understood.

4.2 Aims

The computational study by Houk *et al.* provided some insight into two of the reactions with **8** carried out by Boger *et al.* showing that both a concerted and stepwise mechanism are possible for the Diels-Alder step.[151,152] The stepwise mechanism was determined to be favourable over the concerted mechanism. Some insight into why HFIP resulted in higher yields was given. Through hydrogen-bonding HFIP lowers the energy of the stationary points causing the barrier for the C-C bond formation to decrease in energy. However, this work incorrectly determined the loss of N_2 as the rate-determining step when an explicit HFIP molecule was included. While the loss of N_2 is the stationary point with the highest energy it is the highest barrier that determines the rate-determining step. With the work currently presented by Houk *et al.* this would be the C-C bond formation but the pyrrolidine loss was never investigated for the more complex triazine.[152] For the simpler triazine it was the pyrrolidine loss that was the rate-determining step, which would suggest that it would also be the rate-determining step for the more complex triazine.

The work carried out here, therefore, was focused on expanding on the work of Houk *et al.* by studying the pyrrolidine loss step in detail utilising the available experimental results from Boger *et al.*[151,152] While the effect that HFIP had on the Diels-Alder step of the reaction has been studied in great detail a comparison to TFE is needed for a complete picture. Along with this the solvent effect on the Diels-Alder step of the reaction is only significant for understanding the difference in yield if it is the rate-determining step. Since the largest barrier is likely to be the loss of pyrrolidine, as indicated by the reaction using the simplier triazine, this step of the reaction was studied in detail along with the entire PES to determine the rate-determining step.

The potential energy surface was generated for both the concerted and stepwise reactions for both the *exo* and *endo* orientation for the reaction between **3** and **8**. The PES was first determined in the gas-phase followed by the addition of solvent corrections using COSMO to determine whether this would explain the observed solvent effects. This was then followed by the addition of an explicit solvent molecule to determine whether this replicated the experimental observations. 15 pathways were proposed to aid in the loss of pyrrolidine involving residual pyrrolidine, pyrrolidine and the solvent (HFIP or TFE), or just the solvent.

Following on from this the potential energy surface for the reaction between **2** and **3**, the original reaction studied by Boger *et al.*, was also studied to determine the effect of changing the enamine.[151] Once again the gas-phase PES was determined followed by the addition of implicit solvent corrections using COSMO. The results from the reaction between **3** and **8** were then used to selectively target key states to be optimised with explicit molecules.

Through this work it is hoped that a deeper understanding of the solvent effects observed by Boger *et al.* can be obtained.[151] This will provide insight into related reactions where solvent effects, in the form of potential solvent catalysis, play a crucial role. Determining the reason that HFIP and TFE result in such different reactivity when they are relatively similar in structure can help provide understanding into similar effects we see in related reactions.

4.3 Computational Details

All calculations were performed using the TURBOMOLE V6.40 package.[69,70] calculations were carried out at the (RI)-PBE0-D3BJ/def2-TZVPP//(RI)-PBE0/def2-SV(P) level including COSMO solvation (in MeCN, ε= 37.5 at 298 K, HFIP, ε= 16.7 at 298 K, and TFE, ε= 27.7 at 298 K) and DFT-D3BJ corrections.[33,109–116] Vibrational frequency calculations were used to determine the nature of the stationary points and (DRC) calculations to connect transition states to their corresponding minima.[75–77] States connected by dashed lines in the potential energy surfaces show that DRC calculations confirmed that these states are connected. Where no lines are present their connection has not been verified.

Gibbs energies and enthalpies were determined by correcting the SCF energies obtained at the (RI)-PBE0-D3BJ/def2-TZVPP level by adding thermodynamic corrections obtained from frequency calculations carried out at the (RI)-PBE0/def2-SV(P) level of theory. Zero-point energies were also added to the SCF energies. Energies discussed are relative Gibbs energies including COSMO corrections in CH_2Cl_2 and DFT-D3BJ dispersion corrections. In the potential energy surfaces enthalpies are included in brackets.

PES scans were carried out at the (RI)-PBE0/def2-SV(P) level of theory using TURBOMOLE within ChemShell 3.7.0, where DL-FIND was used for the optimizations.[117,118] Natural Bond Orbital (NBO) calculations were carried out by first performing a single point calculation using the Gaussian09 software package at the PBE0/def2-SV(P) level of theory.[83] The output was then used to run an NBO calculation using NBO 7.[133]

The reaction of **2** and **8** with **3** carried out by Boger *et al.* were carried out between 23 and 90 °C.[152] During this investigation the solvent corrections that were applied were calculated at 25 °C, which is the default temperature for thermodynamic corrections produced by TURBOMOLE. Carrying out the calculations at 25 °C also allowed for a more direct comparison to the work carried out by Houk *et al.*[152] Furthermore, it allowed the investigation to be focused on the different solvents and minimises the affect that the temperature could be having on the reaction.

4.4 Results and Discussion

The mechanism for the reaction between **3** and **8** is presented first and was studied in detail because of the smaller number of flexible groups on the enamine. Results from this study were then applied to the original reaction between **2** and **3**.

4.4.1 Triazine and Tetralone Reaction

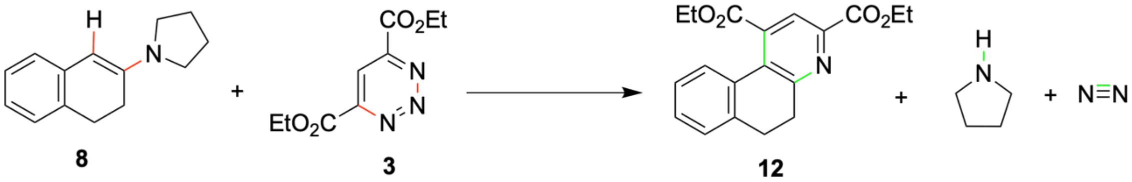

Scheme 4.5 – Reaction between triazine **3** and enamine **8** to give the product **12** was investigated to determine the effect of different solvents. The red and green bonds indicate the bonds that are broken and formed during the reaction respectively.

Scheme 4.5 shows the reaction studied by Boger *et al.* that utilised the much simpler enamine, **8**, which has fewer degrees of freedom than enamine **2**.[151] Firstly, the PES for this reaction was determined in the gas-phase. Access to the PES showed which steps of the reaction were likely to be rate-determining. With the gas-phase PES in hand implicit solvent corrections were then applied using COSMO in a variety of solvents which had been used in the experiment along with others that had not been studied experimentally. The gas-phase PES along with the solvation corrected did not explain the solvent effects but did show that the DA step and the pyrrolidine loss were the barriers with the highest energy. These were therefore then studied with explicit solvent molecules included.

As mentioned previously the computational study carried out by Houk *et al.* discovered that a stepwise Diels-Alder reaction can occur and proceeds *via* lower energy barriers than the traditional concerted mechanism.[152] To be able to make comparisons between the two mechanisms both were studied here. Following the Diels-Alder step of the reaction both mechanisms converge and proceed *via* the loss of N_2 followed by pyrrolidine loss to give the final product. Since the loss of pyrrolidine was determined to be the rate limiting step from the gas-phase calculations it was important to study the effect that different solvents have on this path of the reaction. Explicit solvent molecules were used to model specific solvent effects more accurately than using solely dielectric continuum models.

The pyrrolidine loss step of the reaction could be stabilised through the inclusion of a single solvent molecule by hydrogen-bonding to either the pyrrolidine or by breaking the C-H bond during this step directly. Since there are two ways in which the solvent could facilitate this pathway the inclusion of two solvent molecules was also studied.

4.4.1.1 Gas-phase results

The full PES was determined by studying both the concerted and stepwise Diels-Alder mechanism utilising the work by Houk *et al.*[152] Both the *endo* and *exo* orientation were studied. The stationary points located were then connected through DRC calculations to give the PESs seen in Figure 4.8 and Figure 4.10. The reaction proceeds *via* three crucial steps: 1) the Diels-Alder reaction to form a new C-C and N-C bond, 2) N_2 loss to relieve strain in the system, and 3) loss of pyrrolidine to form an alkene resulting in an aromatic system.

Houk *et al.* proposed that the Diels-Alder step of the reaction could either proceed *via* a traditional concerted method or *via* a stepwise pathway.[152] In the stepwise pathway the C-C bond is formed first, followed by N-C bond formation to give the identical product to the concerted pathway. Figure 4.8 shows the PES for the concerted and stepwise pathway for the *endo* orientation. There is a significant difference in energy between the first transition state for the concerted, ***endo*_TS$_{8\text{-}10}$**, and stepwise, ***endo*_TS$_{8\text{-}9}$**, pathways, 126 and 94 kJ mol^{-1} respectively. The stepwise reaction is therefore more favourable than the concerted pathway especially since the second step of the stepwise pathway where the N-C bond is formed only requires overcoming a barrier of 7 kJ mol^{-1}. The loss of N_2 is a very low energy process, 8 kJ mol^{-1}, and greatly stabilises the system. The loss of pyrrolidine is the rate-determining step for this reaction with a barrier of 159 kJ mol^{-1}.

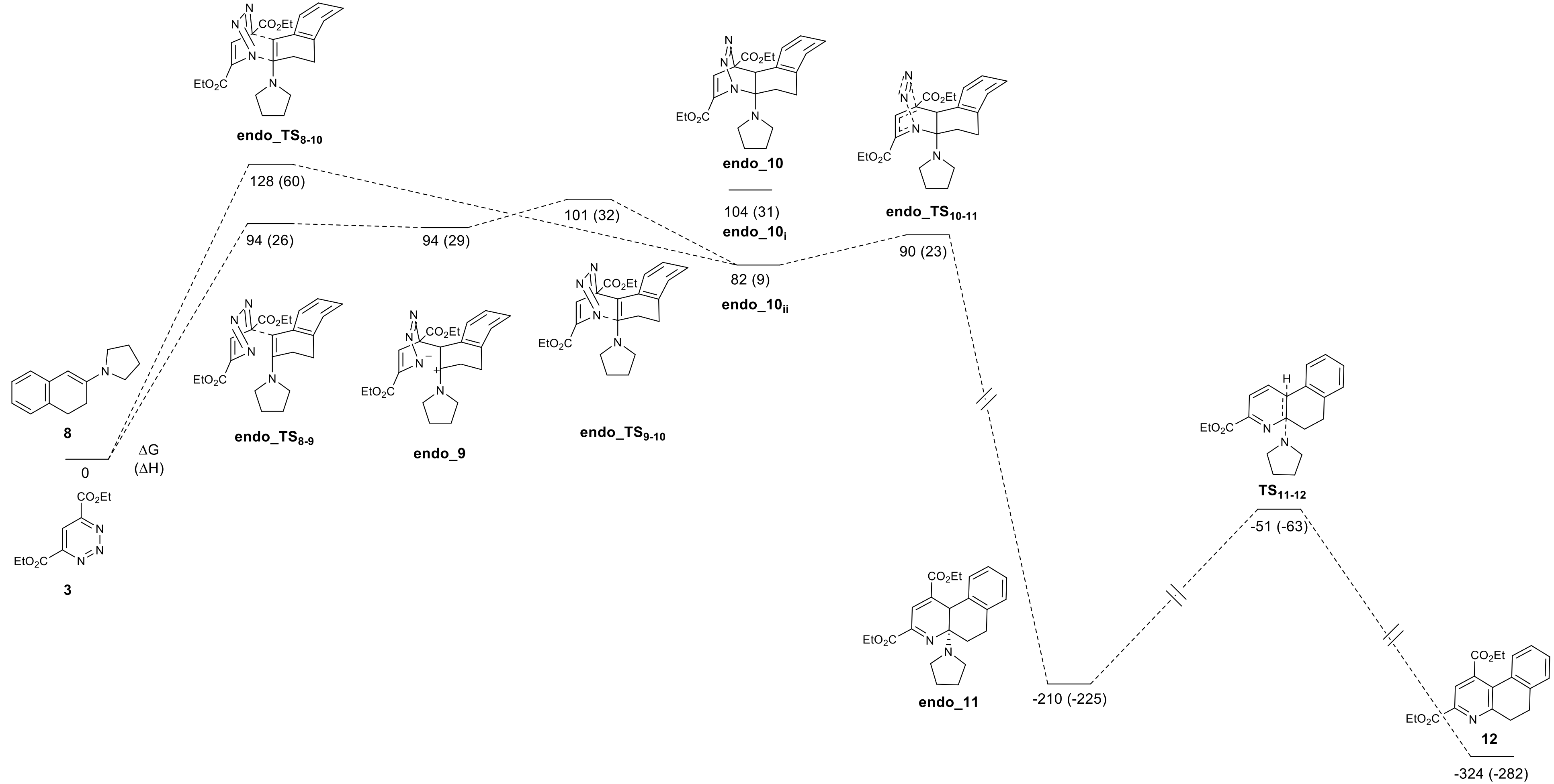

Figure 4.8- PES for the reaction between **3** and **8** for the concerted and stepwise pathways for the *endo* orientation in the gas-phase. Relative Gibbs energies (and enthalpies in brackets) are shown in kJ mol^{-1} at the (RI)-PBE0-D3BJ/def2-TZVPP//(RI)-PBE0/def2-SV(P) level.

The PES in Figure 4.8 is consistent with the data obtained by Houk *et al.* which also shows the stepwise pathway being favourable and with a large barrier for the loss of pyrrolidine.[152] Figure 4.10 shows the potential energy surface for the *endo* and *exo* orientation for the stepwise pathway. The first TS involves formation of the C-C bond between the enamine and the triazine. ***endo*_TS$_{8-9}$** is 5 kJ mol^{-1} lower in energy than **exo_TS$_{8-9}$**. The resulting zwitterionic minima, ***endo*_9** and **exo_9**, only differ by 1 kJ mol^{-1} and can therefore be considered to have the same energy. **endo_TS$_{9-10}$** proceeds *via* a barrier of 7 kJ mol^{-1} and 12 kJ mol^{-1} for **exo_TS$_{9-10}$**. **endo_10** and **exo_10** only differ by 4 kJ mol^{-1} with **exo_10** being lower in energy. The loss of N_2 is a lower energy process for both orientations (1 and 8 kJ mol^{-1} for **exo_TS$_{10-11}$** and ***endo*_TS$_{10-11}$** respectively). The resulting minima, ***endo*_11** and **exo_11**, are once again almost identical in energy (difference of 3 kJ mol^{-1} with ***endo*_11** lower in energy). The loss of pyrrolidine, **TS$_{11-12}$**, is the largest barrier for both orientations but ***endo*_TS$_{11-12}$**, has a slightly lower barrier than **exo_TS$_{11-12}$** (132 vs 159 kJ mol^{-1} respectively). With the loss of pyrrolidine both orientations give the same final product, **12**.

While the PES does show some difference in the energies of the two orientations the largest difference is only 14 kJ mol^{-1} in the pyrrolidine loss step, **TS$_{11-12}$**. This difference in energy does result in a lower barrier for pyrrolidine loss for the *exo* pathway compared to the *endo* pathway, 132 vs 159 kJ mol^{-1}. Due to the small energy differences and the errors usually associated with these calculations it is not possible to determine which orientation would be favoured. Since both orientations result in the same product, **12**, and the energy differences between the two orientations are negligible, it is likely that the reaction can proceed both *via* the *endo* and *exo* orientation.

The PESs in Figure 4.8 and Figure 4.10 clearly show that in the gas phase the rate-determining step of the reaction is pyrrolidine loss. This is not consistent with what was predicted by Boger *et al.* or by what was determined by Houk *et al.*, which both state that the Diels-Alder step of the reaction should be rate-determining.[151,152] Currently, nothing can be said about the solvent effects since no solvent has been introduced into these calculations. These gas-phase PESs allow for a better understanding of the reaction and where solvents are likely to interact with the substrate. A more detailed discussion of the stationary points for both orientations is given in the next section.

4.4.1.2 Endo Pathway

The first step for this concerted reaction involves a Diels-Alder reaction where the tetralone, **8**, and triazine, **3**, react to form two new bonds – a C-C bond and a N-C bond. Figure 4.9 shows detailed structures for ***endo*_TS$_{8-10}$** and ***endo*_10$_{ii}$** along with key bond lengths.

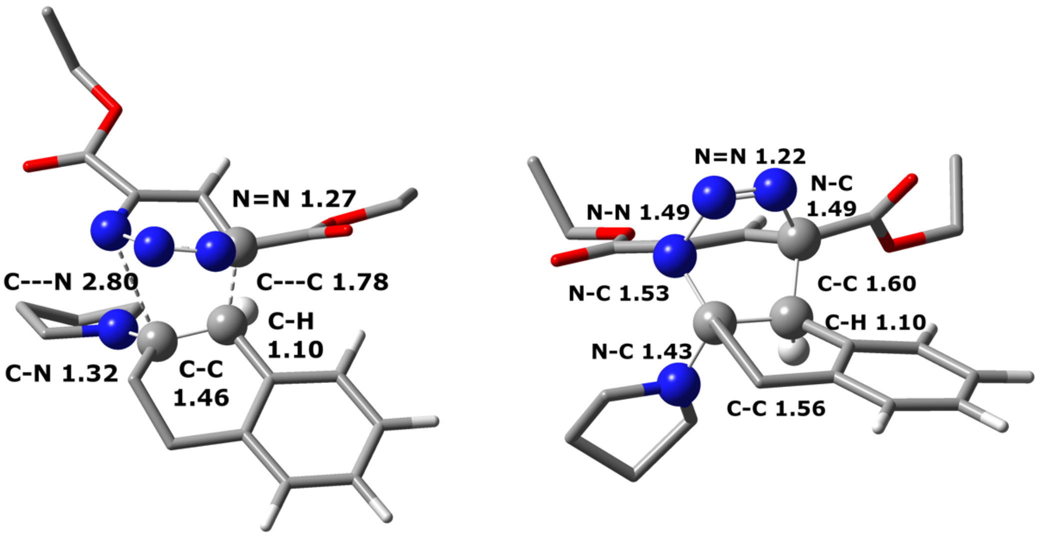

***endo*_TS**$_{8-10}$ ***endo*_10**$_{ii}$

Figure 4.9 – Structures for the stationary points ***endo*_TS**$_{8-10}$ and ***endo*_10**$_{ii}$. Selected distances are shown in Å. Blue = N, red = O, grey = C and white = H.

During ***endo*_TS**$_{8-10}$ the triazine, **3**, and tetralone, **8**, are brought together and a new C-C and N-C bond are formed between them. In ***endo*_10**$_{ii}$ the C-C bond distance of the alkene in **8** is only lengthened by 0.10 Å since the bond was already considerably lengthened during the transition state. The C-H bond distance remains unchanged while the C-N(pyrrolidine) bond length increased by 0.11 Å to accommodate for the loss of electron density. The N-C distance drastically decreases from 2.80 to 1.53 Å from ***endo*_TS**$_{8-10}$ to ***endo*_10**$_{ii}$ (a change of 1.27 Å) while the C-C distance only decreases by 0.18 Å. The pyrrolidine group now sits further below the plane of the rest of the molecule as the hybridisation on the carbon changes from sp^2 to sp^3. The barrier for ***endo*_TS**$_{8-10}$ was determined to be 128 kJ mol^{-1} while ***endo*_10**$_{ii}$ sits at 82 kJ mol^{-1} compared to the starting material – a relatively high energy but still accessible process that results in an intermediate that is quite high in energy.

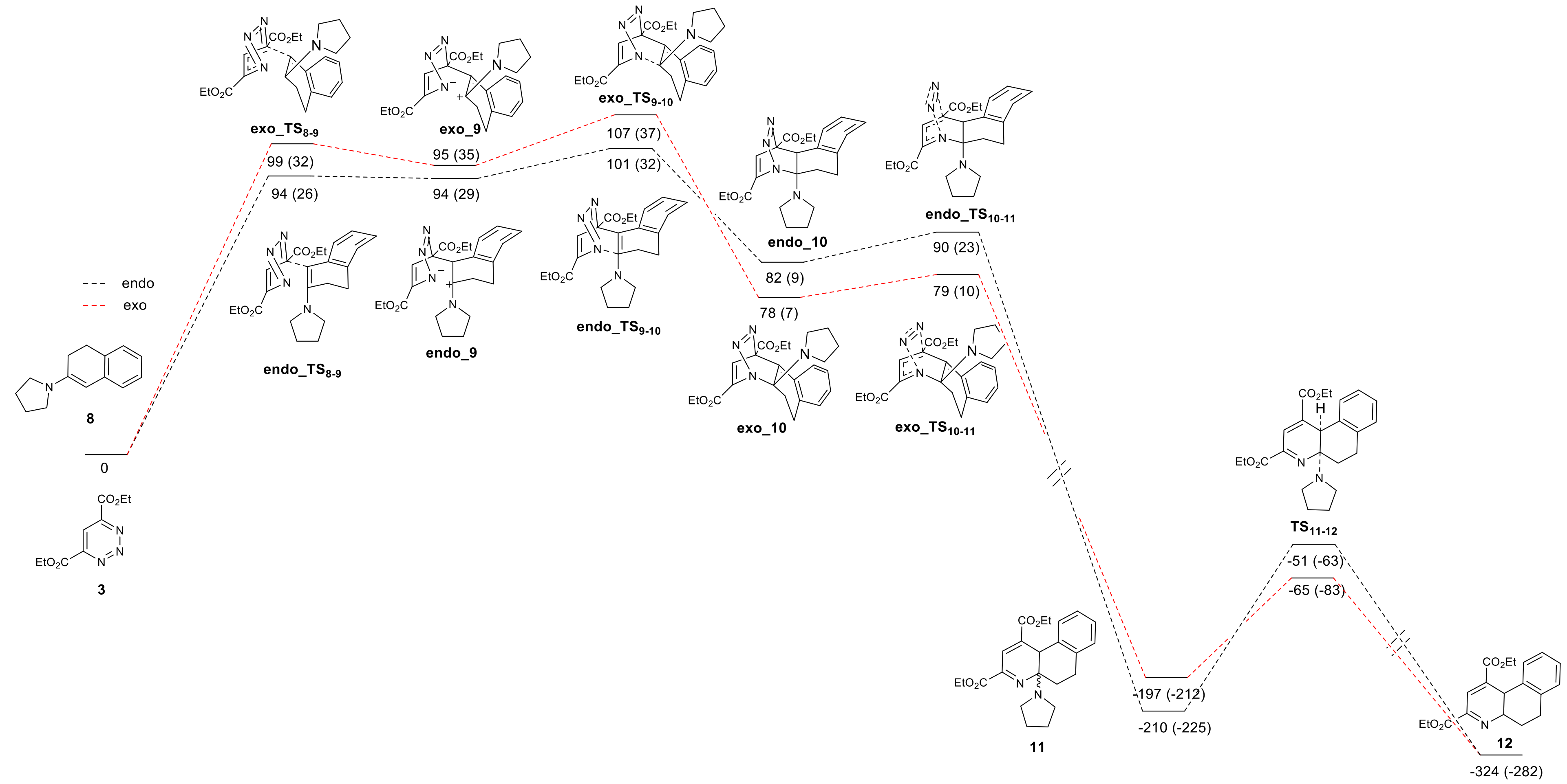

Figure 4.10- Potential energy surface for the reaction between **3** and **8** for the stepwise pathway for both the *endo* and *exo* orientation in the gas-phase. Relative Gibbs energies (and enthalpies in brackets) are shown in kJ mol^{-1} at the (RI)-PBE0-D3BJ/def2-TZVPP//(RI)-PBE0/def2-SV(P) level

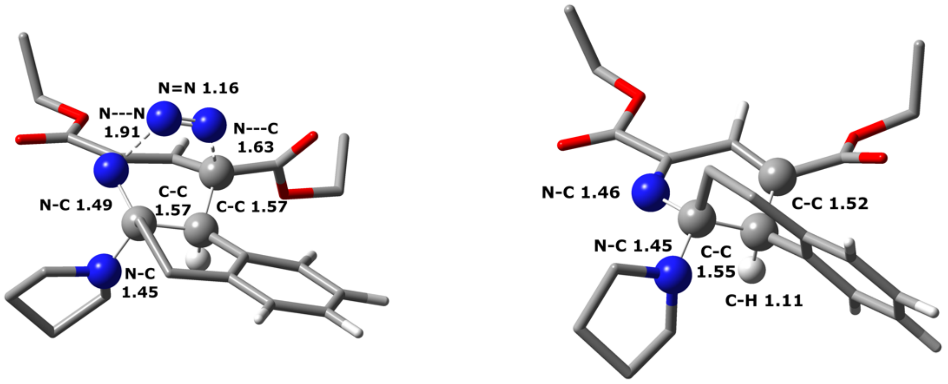

***endo*_TS$_{10-11}$** ***endo*_11**

Figure 4.11 – Structures for the stationary points ***endo*_TS$_{10-11}$** and ***endo*_11**. Selected distances are shown in Å. Blue = N, red = O, grey = C and white = H.

Figure 4.11 shows the structures of ***endo*_TS$_{10-11}$** and ***endo*_11** along with key bond length. During ***endo*_TS$_{10-11}$** as N_2 is being released the N-N and N-C distances increase as the N=N distance decreases. This results in a negligible shortening of the N(pyrr)-C distance (pyrr = pyrrolidine) along with the C-C distance. Notably the N-C and C-C bond lengths that were formed during ***endo*_TS$_{8-10}$** decrease by 0.04 and 0.03 Å respectively. The orientation of the ester groups and the pyrrolidine remain unchanged. The barrier for N_2 loss in ***endo*_TS$_{10-11}$**, is only 8 kJ mol^{-1}, a potentially barrier-less process when errors are considered. This low barrier is due to the release of a very stable molecule and will also be entropy driven.

***endo*_TS$_{10-11}$** results in an intermediate, ***endo*_11**, which sits at -210 kJ mol^{-1} compared to the starting material. The formation of ***endo*_11** is exergonic and results in a large release in energy (300 kJ mol^{-1}). It is therefore predicted that the intermediate ***endo*_10$_{ii}$** would be very short lived in the reaction and would very rapidly proceed *via* this lower energy transition state to give ***endo*_11**.

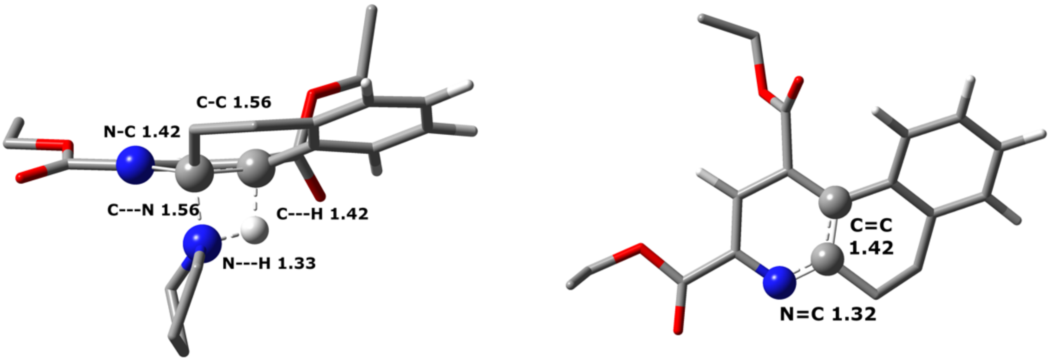

***endo*_TS**$_{11-12}$ **12**

Figure 4.12 – Structures for the stationary points ***endo*_TS**$_{11-12}$ and **12**, *endo* pathway. Selected distances are shown in Å. Blue = N, red = O, grey = C and white = H.

The final step of the reaction involves loss of pyrrolidine to form an alkene and give the product **12**. Figure 4.12 shows the structures of ***endo*_TS**$_{11-12}$ and **12** along with key bond lengths. The barrier for ***endo*_TS**$_{11-12}$ was found to be 159 kJ mol^{-1} and is the rate-determining step of this mechanism in the gas-phase. Figure 4.12 shows that in ***endo*_TS**$_{11-12}$ the C-N(pyrr) bond is broken along with the C-H bond. At the same time a new bond is formed between the nitrogen of the pyrrolidinium and the hydrogen. This is a four membered transition state, which are known to be high in energy due to the steric strain and poorer overlap of orbitals compared to six-membered transition states.

Both the C-N(pyrr) and C-H bond distances have significantly increased in ***endo*_TS**$_{11-12}$ from ***endo*_11**, 0.11 and 0.31 Å respectively. Interestingly, the C-C bond length remained unchanged along with the N-C bond length. It can also be seen that the entire molecule is already approaching a more planar structure, close to what is seen in **12**. In **12** the C-C bond distance has decreased to 1.42 Å and the N-C distance has decreased to 1.32 Å. Therefore, ***endo*_TS**$_{11-12}$, lies much closer to **11** than to **12**, and is an early TS. The final product **12** was found to result in a stabilisation of 324 kJ mol^{-1} compared to the starting material.

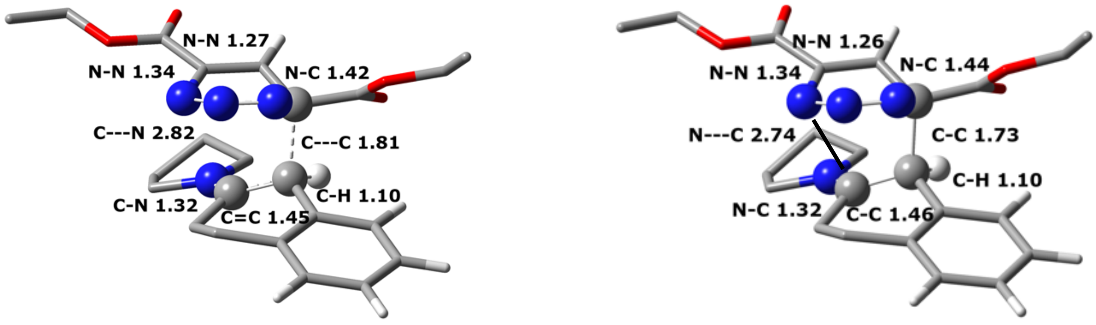

***endo*_TS**$_{8\text{-}9}$ ***endo*_9**

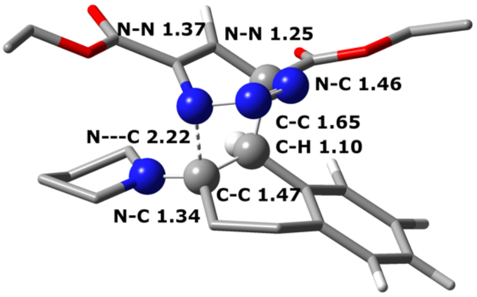

***endo*_TS**$_{9\text{-}10}$

Figure 4.13 - Structures for the stationary points ***endo*_TS**$_{8\text{-}9}$, ***endo*_9**, and ***endo*_TS**$_{9\text{-}10}$. Selected distances are shown in Å. Blue = N, red = O, grey = C and white = H.

Figure 4.13 shows the structures and key bond lengths for the three stationary points that are unique to the stepwise Diels-Alder pathway, ***endo*_TS**$_{8\text{-}9}$, ***endo*_9**, and ***endo*_TS**$_{9\text{-}10}$. In the stepwise pathway the C-C bond is formed first during ***endo*_TS**$_{8\text{-}9}$. The barrier for the formation of this C-C bond is 94 kJ mol^{-1}.

In ***endo*_9** a new C-C bond has formed but the N-C bond has not yet been formed. The C-C bond is now at 1.73 Å, a shortening of 0.08 Å from ***endo*_TS**$_{8\text{-}9}$. The N(triazine)-C(tetralone) distance has decreased slightly from 2.82 to 2.74 Å going from ***endo*_TS**$_{8\text{-}9}$ to ***endo*_9**. Negligible changes are seen in the surrounding bond lengths. Figure 4.8 shows that the intermediate ***endo*_9** has the same energy as ***endo*_TS**$_{8\text{-}9}$. The electronic energies of these two states show that the intermediate ***endo*_9** is just slightly higher in energy by approximately 0.5 kJ mol^{-1}, which is in line with the energy difference determined by Houk *et al.* where they observed a 0.1 kcal mol^{-1} energy difference.[151]

The orientation of the two starting materials remains almost entirely unchanged in ***endo*_TS**$_{8\text{-}9}$ and ***endo*_9** other than a decrease in the distance between the two molecules. The formation of this new C-C bond also means ***endo*_9** is zwitterionic since the N of the triazine now carries a negative charge while the C of the tetralone carries a positive charge.

The N-C bond is then formed during ***endo*_TS$_{9\text{-}10}$** *via* a barrier of 7 kJ mol^{-1}. This small energy barrier indicates that the zwitterionic intermediate ***endo*_9** is likely to be short-lived and quickly reacts to give ***endo*_10$_{ii}$**, as in the concerted pathway. During ***endo*_TS$_{9\text{-}10}$** the N-C distance is still quite long at 2.22 Å, but has decreased by 0.52 Å from ***endo*_9**. The C-C distance that was formed in ***endo*_TS$_{8\text{-}9}$** has decreased further to 1.65 Å. Interestingly the C-C distance of the previous alkene of the tetralone has not significantly increased even though the distance increases to 1.56 Å in ***endo*_10**. Once again the orientation of the ester groups on the triazine remains the same.

As was seen in Figure 4.8 the stepwise pathway for this reaction is favourable as it proceeds *via* a barrier that is 34 kJ mol^{-1} lower in energy. The zwitterionic nature of ***endo*_9** means that different solvents are likely to have an effect on reactivity and yield, due to the charge now present on N, which is avoided in the concerted mechanism.

4.4.1.3 Exo Pathway

As previously mentioned Diels-Alder reactions can occur with two different orientations. To be able to understand the reaction a thorough investigation into the PES needs to be carried out and therefore both the *endo* and *exo* orientation need to be studied. As with the *endo* pathway a detailed discussion of the different steps of the reaction are given below.

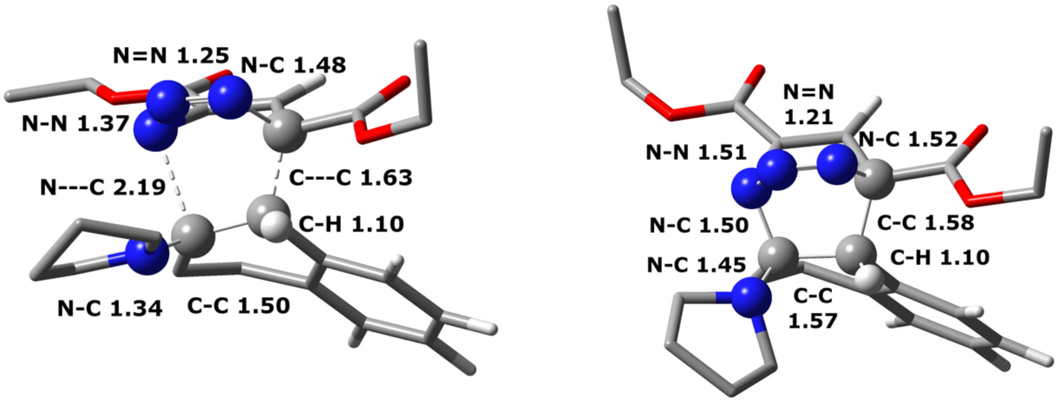

exo_TS$_{8\text{-}10}$ **exo_10**

Figure 4.14 – Structures for the stationary points **exo_TS$_{8\text{-}10}$** and **exo_10**. Selected distances are shown in Å. Blue = N, red = O, grey = C and white = H.

Figure 4.14 shows the structures of **exo_TS$_{8\text{-}10}$** and **exo_10**, the first transition state and intermediate in the exo pathway respectively. Here the new C-C and C-N bonds are formed on the other side of the tetralone, **8**.

In **exo_10** the C-C and N-C bond are fully formed and show a reduction by 0.05 and 0.69 Å respectively. As with the *endo* orientation, the N-C distance once again is much longer in the transition state compared to the C-C distance. A slight elongation of the previous alkene distance is seen by 0.07 Å and as with the *endo* orientation the C-N(pyrr) distance is elongated by 0.11 Å, while the C-H distance remains unchanged.

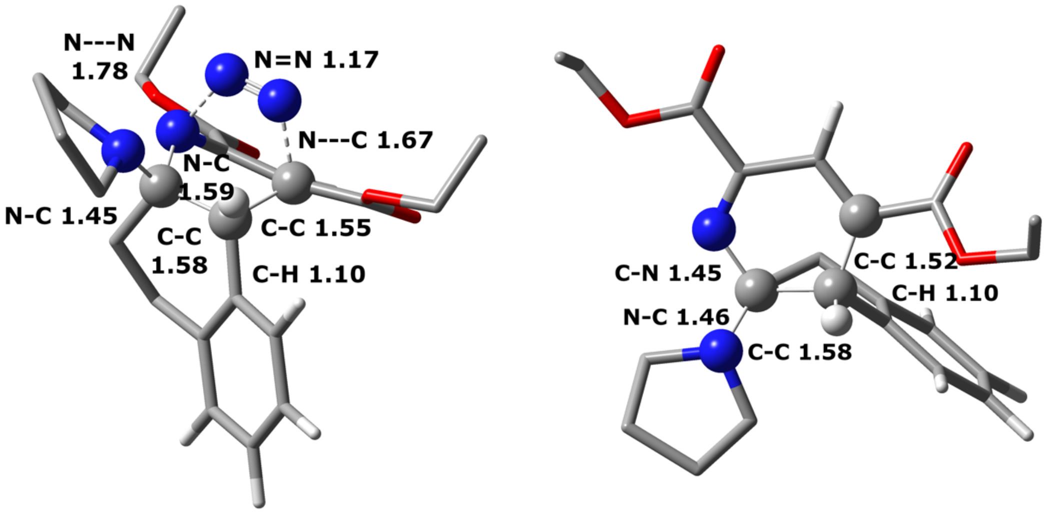

exo_TS$_{10-11}$

exo_11

Figure 4.15 – Structures for the stationary points **exo_TS$_{10-11}$** and **exo_11**. Selected distances are shown in Å. Blue = N, red = O, grey = C and white = H.

Figure 4.15 shows the structures and key bond lengths for **exo_TS$_{10-11}$** and **exo_11** where N_2 is lost. The only notable changes are the distances associated with the N_2 loss. The N=N distance has not significantly decreased only seeing a change of 0.04 Å, the N-N distance has lengthened by 0.27 Å and the N-C distance has increased by 0.09 Å compared to **exo_10**. The orientation of the ring structure from the original tetralone, **8**, is now oriented slightly further away from the ester groups from the original triazine, **3**. This orientation is possible due to the larger angle than can be achieved between these groups because the N-N and N-C bonds are being broken. The carbonyl groups of the ester are still oriented away from the nitrogen atoms.

In **exo_11** the C-N distance has decreased by 0.33 Å, while the C-C distance decreased by a negligible amount, 0.03 Å. As with ***endo*_11** the structure is already approaching planarity compared to the geometry of the transition state.

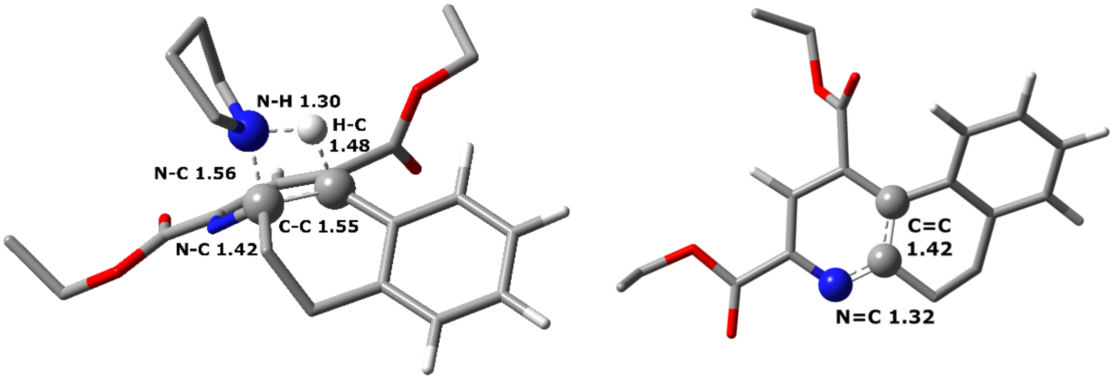

exo_TS$_{11-12}$ **12**

Figure 4.16 – Structures for the stationary points **exo_TS$_{11-12}$** and **12**. Selected distances are shown in Å. Blue = N, red = O, grey = C and white = H.

Figure 4.16 shows the final step of the reaction, **exo_TS$_{11-12}$**, and the product, **12**, along with key bond lengths. During **exo_TS$_{11-12}$**, pyrrolidine is lost to form a C=C bond and make the system aromatic. The C-N(pyrr) distance has increased by 0.11 Å while the C-C distance only increased by 0.03 Å. The C-H distance has increased from 1.10 to 1.48 Å from **exo_11** to **exo_TS$_{11-12}$**, which is the largest geometry change other than the decrease in the distance between the hydrogen and nitrogen of the pyrrolidine.

In the final product, **12**, the C-C distance has decreased to 1.42 Å (shortening of 0.13 Å from **exo_TS$_{11-12}$**). The N-C distance has also significantly decreased from 1.42 to 1.32 Å in **exo_TS$_{11-12}$** and **12** respectively. The final product is the same as for the *endo* orientation. Through the loss of pyrrolidine, a carbon-carbon double bond is formed, which allows for further conjugation and thereby stabilises the system compared to the starting material.

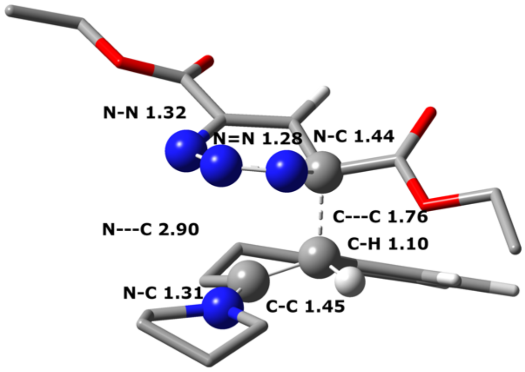

exo_TS$_{8-9}$

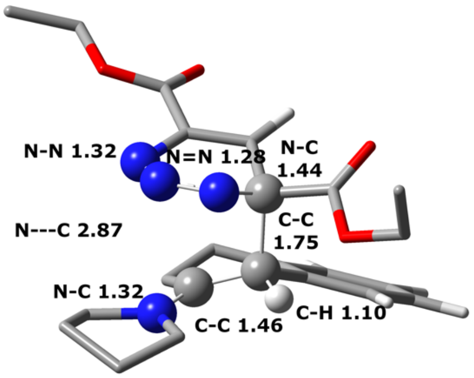

exo_9

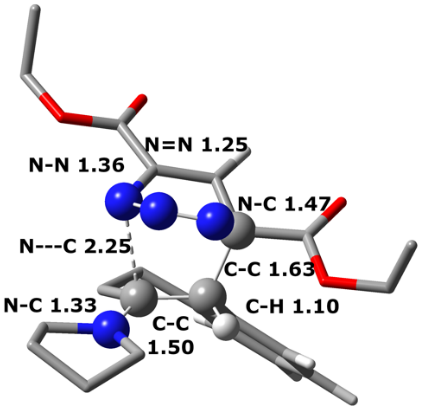

exo_TS$_{9-10}$

Figure 4.17 – Structures for the stationary points **exo_TS$_{8-9}$**, **exo_9**, **exo_TS$_{9-10}$**. Selected distances are shown in Å. Blue = N, red = O, grey = C and white = H.

Figure 4.17 shows the three structures that are unique to the stepwise Diels-Alder pathway for the *exo* orientation: **exo_TS$_{8-9}$**, **exo_9**, and **exo_TS$_{9-10}$**. In **exo_TS$_{8-9}$** the C-C bond between the tetralone, **8**, and the triazine, **3**, is being formed.

In **exo_9** the C-C bond has been formed while the N-C has not. The N-C distance has decreased marginally by 0.03 Å, but still sits far away at 2.87 Å. **Exo_9** shows that the transition state **exo_TS$_{8-9}$** is a late transition state as it lies close to the minimum since there is very minimal changes to the bond lengths and the orientation of any of the groups. The small barrier to proceed *via* **exo_TS$_{9-10}$** and the stabilisation of the system when proceeding to **exo_10** suggests that the minimum **exo_9** is short lived.

During **exo_TS$_{9-10}$** the C-C distance has decreased to 1.63 Å (shortening by 0.12 Å) combined with a significant decrease of the N-C distance to 2.25 Å, by 0.62 Å. As with **exo_TS$_{8-9}$** the orientation of the ester groups remains the same and negligible changes are seen in the surrounding bond lengths.

4.4.1.4 Summary

Through the mechanistic work that has been carried out a deeper understanding of the reaction has been obtained. The stepwise pathway seems most feasible for both the *exo* and *endo* conformation over the traditional concerted mechanism. While a few stationary points were more stable than others, the barrier for both the *exo* and *endo* orientation were found to be comparable. Both orientations are therefore likely to occur in this reaction since it is difficult to determine which pathway is favoured.

No insight has been gained on the solvent effects seen as no solvent has yet been introduced. The gas-phase PESs do provide insight into where possible differences could arise. The formation of a zwitterionic intermediate, ***endo*_9** and **exo_9**, means that the Diels-Alder transition states $\mathbf{TS_{8\text{-}9}}$ and $\mathbf{TS_{9\text{-}10}}$ are likely to be heavily influenced by the solvent used in the reaction. The build-up of charge during the transition state and the resulting charged minima would mean that solvents capable of hydrogen-bonding could stabilise these stationary points.

The small barrier for N_2 loss during $\mathbf{TS_{10\text{-}11}}$ is unlikely to be affected by different solvents. The pyrrolidine loss transition state, $\mathbf{TS_{11\text{-}12}}$, was found to be rate-determining due to it having the largest barrier for both orientations. The overall energetic span on the reaction was determined to be 159 kJ mol^{-1} for the *endo* orientation and 132 kJ mol^{-1} for the *exo* orientation. The energetic span was determined using **11** and $\mathbf{TS_{11\text{-}12}}$ as the turnover-determining intermediate and transition state respectively.[153] In the original work carried out by Boger *et al.* it was proposed that the Diels-Alder step of the reaction was rate-determining.[151] It was hypothesised in the paper that the solvent would play a role during this step. It is, therefore, not surprising that the loss of pyrrolidine is the rate-determining step here, as no solvent has been included yet. Given the large energy of the pyrrolidine loss step it is likely that the transition state $\mathbf{TS_{11\text{-}12}}$ would also be greatly affected when changing the solvent. The gas-phase results, therefore, show that the different observed reactivity is due to the chosen solvent.

4.4.1.5 Implicit Solvation

With a good understanding of the reaction and detailed PESs in hand the next focus was on introducing different solvents into the system to determine their effects on the reaction. This was done by adding solvent corrections using COSMO. A variety of solvents were chosen but the focus here will be on MeCN, HFIP, and TFE as these were the solvents that were of interest in the reaction carried out by Boger *et al.*[151] The implicit solvation correction was applied after the structure was optimised in the gas-phase. No optimisation in implicit solvent was carried out as this typically shows limited improvement while needing much more time and resources to converge.

Table 4.4 - – Lowest energy pathway and orientation along with largest ΔG barrier in the gas-phase, MeCN, HFIP, and TFE for the reaction between **3** and **8**.

	Gas-Phase	MeCN	HFIP	TFE
Pathway	stepwise	stepwise	stepwise	stepwise
Orientation	*exo/endo*	*exo/endo*	*exo/endo*	*exo/endo*
RDS	TS_{11-12}	TS_{11-12}	TS_{11-12}	TS_{11-12}
Barrier (kJ mol^{-1})	148	131	132	132
ε	N/A	37.5	16.7	27.7

Table 4.4 shows the lowest energy and pathway in the gas-phase and the three solvents of interest using COSMO solvent correction. The stepwise pathway was lower in energy for all of these models, but there was no preference for either orientation. Typically, the *endo* orientation is lower in energy and since no preference for either orientation was seen it will be the orientation discussed from here on out.

The rate-determining step for each is the loss of pyrrolidine where the barrier varies from 130-150 kJ mol^{-1}. While a decrease in the barrier for **TS_{11-12}** was seen when implicit solvent corrections were added the energy difference between the different solvents with COSMO corrections only varied by 1 kJ mol^{-1}. Applying implicit solvent corrections still does not provide answers into the solvent effects seen experimentally in this reaction.

Table 4.5 shows the barriers for the concerted mechanism for the *endo* orientation. As expected, ***endo*_TS_{8-10}** is stabilised through the inclusion of an implicit solvent compared to the gas-phase. MeCN and HFIP stabilise the structure by approximately 25 kJ mol^{-1} while TFE stabilised the structure by 34 kJ mol^{-1}. The resulting minimum, ***endo*_10**, is destabilised by all three solvents compared to the gas-phase. Once thermodynamic corrections are applied the minimum is higher in energy than the TS for all three of the solvents.

Table 4.5 – Relative enthalpies for the concerted *endo* pathway for the reaction **3** and **8** in the gas-phase and with implicit solvent corrections in MeCN, HFIP, and TFE.

	Gas-phase (kJ mol^{-1})	MeCN (kJ mol^{-1})	HFIP (kJ mol^{-1})	TFE (kJ mol^{-1})
*endo*_TS_{8-10}	128	103	105	94
*endo*_TS_{10-11}	8	10	10	9
*endo*_TS_{11-12}	159	141	142	141

***endo*_TS$_{10\text{-}11}$** occurs *via* a barrier of 8 kJ mol^{-1} in the gas-phase and increases to 12-13 kJ mol^{-1} for the three solvents. Even though ***endo*_10** is destabilised ***endo*_TS$_{10\text{-}11}$** is also destabilised when the solvent correction is applied which slightly increases the barrier compared to the gas-phase. The final transition state, ***endo*_TS$_{11\text{-}12}$**, has the largest barrier and is therefore the rate-determining step. The solvent corrections reduce the barrier for this by approximately 18 kJ mol^{-1} but no difference is seen between the three solvents.

Only in ***endo*_TS$_{8\text{-}10}$** is there a slight differentce between the three solvents, TFE reduces the barrier by a further 9 kJ mol^{-1} but this does not match the observations of the Glinkerman work.[151] COSMO solvation corrected values are not enough for this reaction to explain why HFIP results in a much higher yield compared to TFE and why MeCN shows no reactivity at all.

Table 4.6 - Relative enthalpies for the stepwise *endo* pathway in the gas-phase and with implicit solvent corrections in MeCN, HFIP, and TFE.

	Gas-phase (kJ mol^{-1})	MeCN (kJ mol^{-1})	HFIP (kJ mol^{-1})	TFE (kJ mol^{-1})
*endo*_TS$_{8\text{-}9}$	94	86	86	76
*endo*_TS$_{9\text{-}10}$	7	22	21	22
*endo*_TS$_{10\text{-}11}$	8	10	10	9
*endo*_TS$_{11\text{-}12}$	159	141	142	141

Table 4.6 shows the barriers for the stepwise mechanism for the *endo* orientation. The use of an implicit solvation model showed very little difference compared to the gas-phase results. The barrier for the first step, ***endo*_TS$_{8\text{-}9}$**, is slightly reduced to 86 kJ mol^{-1} for MeCN and HFIP and further reduced for TFE to 76 kJ mol^{-1}. For the second step of the DA reaction, ***endo*_TS$_{9\text{-}10}$**, the barriers are higher with the implicit correction compared to the gas-phase. The gas-phase barrier is 7 kJ mol^{-1} while for the three solvents the barrier is 21-22 kJ mol^{-1}. This is because ***endo*_TS$_{9\text{-}10}$** is destabilised compared to the gas-phase and ***endo*_9** is stabilised with the implicit correction thus giving a larger barrier. The stabilisation of the minimum is to be expected as this is a zwitterionic state and the inclusion of an implicit solvent would stabilise this charges state.

The loss of N_2, ***endo*_TS$_{10\text{-}11}$**, remained unchanged with the implicit solvent correction, showing only an increase of 1 to 2 kJ mol^{-1}. Some reduction in the barrier for the loss of pyrrolidine, ***endo*_TS$_{11\text{-}12}$**, is seen when an implicit solvent is used, by approximately 18 kJ mol^{-1}. Overall the use of an implicit solvent correction does not explain the trends seen by Boger *et al.*[151] The loss of pyrrolidine is still the rate-determining step and no major reduction in the barrier is seen for any of the solvents.

4.4.1.6 Combining Explicit and Implicit Solvent Models

As with the purely implicit solvation calculations the use of explicit solvent molecules in these calculations was focused on the *endo* orientation. ***endo*_TS$_{11-12}$** and **exo_TS$_{11-12}$** were both rate-determining in the gas-phase calculations with ***endo*_TS$_{11-12}$** proceeding *via* a slightly higher energy barrier. It can therefore be assumed that any reduction of the barrier in ***endo*_TS$_{11-12}$** would also reduce the barrier of **exo_TS$_{11-12}$**. Along with this assumption since no significant energy differences have been found between the *endo* and *exo* orientation both are likely to proceed and thus if **exo_TS$_{11-12}$** is not stabilised to the same extent as ***endo*_TS$_{11-12}$** the reaction would solely proceed with the *endo* pathway. This assumption was made as the scope of this reaction was already so large and this would make the work more manageable while not risking missing something important.

HFIP, TFE, and MeCN were chosen as the explicit solvent due to the impact they had on the reaction yields. HFIP resulted in a relatively high yield of 86 %, TFE a yield of 34 % and no product was seen with MeCN. The three solvents are also interesting as HFIP and TFE are both polar protic solvents with TFE being much smaller in size than HFIP. MeCN is a polar aprotic solvent and would, therefore, likely destabilise the TSs and zwitterionic intermediate of the stepwise DA reaction.

Since the addition of implicit solvent corrections did not provide answers to the observed solvent effects the next step was to include explicit solvent molecules in the calculations. Through the addition of explicit solvent molecules, the direct effect that the solvent has on the reaction is better modelled. The stepwise DA, **TS$_{8-9}$** and **TS$_{9-10}$**, and N_2 loss, **TS$_{10-11}$**, stationary points had already been studied by Houk *et al.* using HFIP.[151] The xyz coordinates for these stationary points were taken from the supplementary information and reoptimized. Since only the effect of HFIP was studied in this paper the single HFIP molecule used was then also replaced with a TFE molecule to see what effect this had. The focus here is to see whether addition of solvent molecules results in a decrease of the barrier of **TS$_{11-12}$** and therefore which step is rate-determining in this reaction.

The addition of explicit solvent molecules raises the issue of deciding on where these solvent molecules should be in relation to the solute. Many conformers exist and can greatly impact the stability of a stationary point and thus the relative energies. Since the previous computational study by Houk *et al.* already investigated this, their choice of solvent location was used.[152]

The reaction carried out by Glinkermann and co-workers involved the use of pyrrolidine at the start of the reaction which was then later removed. Some residual pyrrolidine will likely still be left in the reaction mixture and could therefore facilitate the loss of pyrrolidine. Once the reaction has started more pyrrolidine is formed and therefore it is more likely that pyrrolidine would aid in its loss from **endo_11**.

4.4.1.7 Explicit Solvation of the Diels-Alder and loss of N_2 Steps

As stated previously, the effect of explicit HFIP molecules on the Diels-Alder transition states (C-C bond formation and N-C bond formation) and N_2 loss was investigated by Houk *et al.*[152] They were able to determine that the addition of a single HFIP molecule lowered the barrier for the C-C forming transition states by 29 kJ mol^{-1} while the N-C forming transition state resulted in an increase of 12 kJ mol^{-1}. Calculations were carried out using an implicit solvent correction in chloroform, when no explicit solvent was present, and in HFIP, when an explicit HFIP was included. The effect of chloroform compared to HFIP (ε = 4.72 and 16.7 respectively) with regards to the implicit solvation is unlikely to cause a significant change in the energy, but it should be noted that the results are not directly comparable.

Table 4.7 shows a summary of the barriers that they obtained with and without the inclusion of an explicit HFIP molecule. The barriers for both the *endo* and *exo* orientation were once again comparable. The C-C bond formation transition state for both *endo* and *exo* orientations was greatly reduced, by approximately 30 kJ mol^{-1}, giving a barrier of 65 and 61 kJ mol^{-1} respectively. For the formation of the N-C bond the energy barrier increased by 10 kJ mol^{-1} for the *endo* pathway and by 27 kJ mol^{-1} for the *exo* pathway. This increase in energy is due to the zwitterionic intermediate being stabilised to a greater extent through hydrogen-bonding to the HFIP, which also stabilises the charge that is formed. This greater stabilisation of the intermediate leads to a larger barrier since the transition state is not stabilised to the same extent. The barrier for the loss of N_2 remains low with the addition of an HFIP molecule, with a barrier of 14 and 15 kJ mol^{-1} for the *endo* and *exo* pathways respectively.

Table 4.7 – ΔG barriers for C-C formation, N-C formation, and N_2 loss in $CHCl_3$ and in HFIP with an explicit solvent molecule. Results shown are from work carried out by Houk *et al.* for the reaction between $\mathbf{3_{Me}}$ and **8** at the M06-2X/6-311+G(d,p) level of theory.[152]

TS	$CHCl_3$ – endo (kJ mol^{-1})	HFIP – endo (kJ mol^{-1})	$CHCl_3$ – exo (kJ mol^{-1})	HFIP – exo (kJ mol^{-1})
C-C Formation	94	65	99	61
C-N Formation	24	35	18	45
N_2 Loss	15	14	9	15

To have a complete picture of the reaction and to compare our methodology to that carried out in the Houk study, the effect of a single HFIP molecule on the PES was also studied here. Our focus will be on the first three transition states (**TS$_{8-9}$**, **TS$_{9-10}$**, and **TS$_{10-11}$**) as it was found that the addition of a solvent molecule to **TS$_{11-12}$** was much more complex than for the other stationary points. The loss of pyrrolidine during **TS$_{11-12}$** will, therefore, be discussed in detail later. Both HFIP and TFE were studied to determine their impact on the reaction pathway and their role in the different steps.

Figure 4.18 shows the potential energy surface for the stepwise Diels-Alder reaction through to intermediate **11** with the addition of an explicit HFIP molecule for both the *endo* and *exo* orientation. The free energies are stated relative to the three starting species: **3**, **8**, and HFIP. Attempts at adding an HFIP molecule to either **3** or **8** raised an issue with where the solvent molecule should be placed. Minor changes in the position of the solvent molecule resulted in changing the relative energies of the stationary points. Since the solvent would surround both **3** and **8** in the actual reaction it was decided to set the relative zero as the energy of **3**, **8**, and a solvent molecule (HFIP or TFE). The aim was to try and reduce bias in the results.

Throughout the reaction the HFIP molecule was positioned to be able to hydrogen-bond to the nitrogen of the triazine that remains in the final product. The barriers for both the *endo* and *exo* orientation for this PES are shown in Table 4.8 along with the gas-phase and implicit solvation in HFIP with no explicit HFIP molecule results for both orientations for comparison. **TS$_{8-9}$** was found to be the highest in energy for both the *endo* and *exo* orientation with solvent corrections (Imp.) applied (86 and 92 kJ mol^{-1} respectively). The addition of an HFIP molecule (Imp./Exp.) significantly lowers the barrier by approximately 30 kJ mol^{-1}. The lowest energy barrier was for **TS$_{10-11}$** for all solvation models and both DA orientations.

Table 4.8 – ΔG barriers for *endo* and *exo* orientations in the gas-phase, in HFIP with COSMO solvent corrections with no explicit solvent molecules (Imp.) and in HFIP with COSMO solvent corrections and one HFIP solvent molecule (Imp./Exp.).

HFIP	Gas-phase – *endo* (kJ mol^{-1})	Imp. HFIP – *endo* (kJ mol^{-1})	Imp./Exp. HFIP – *endo* (kJ mol^{-1})	Gas-phase – *exo* (kJ mol^{-1})	Imp. HFIP – *exo* (kJ mol^{-1})	Imp./Exp. HFIP – *exo* (kJ mol^{-1})
TS$_{8-9}$	94	86	60	99	92	68
TS$_{9-10}$	7	11	48	12	23	45
TS$_{10-11}$	8	10	15	1	6	13

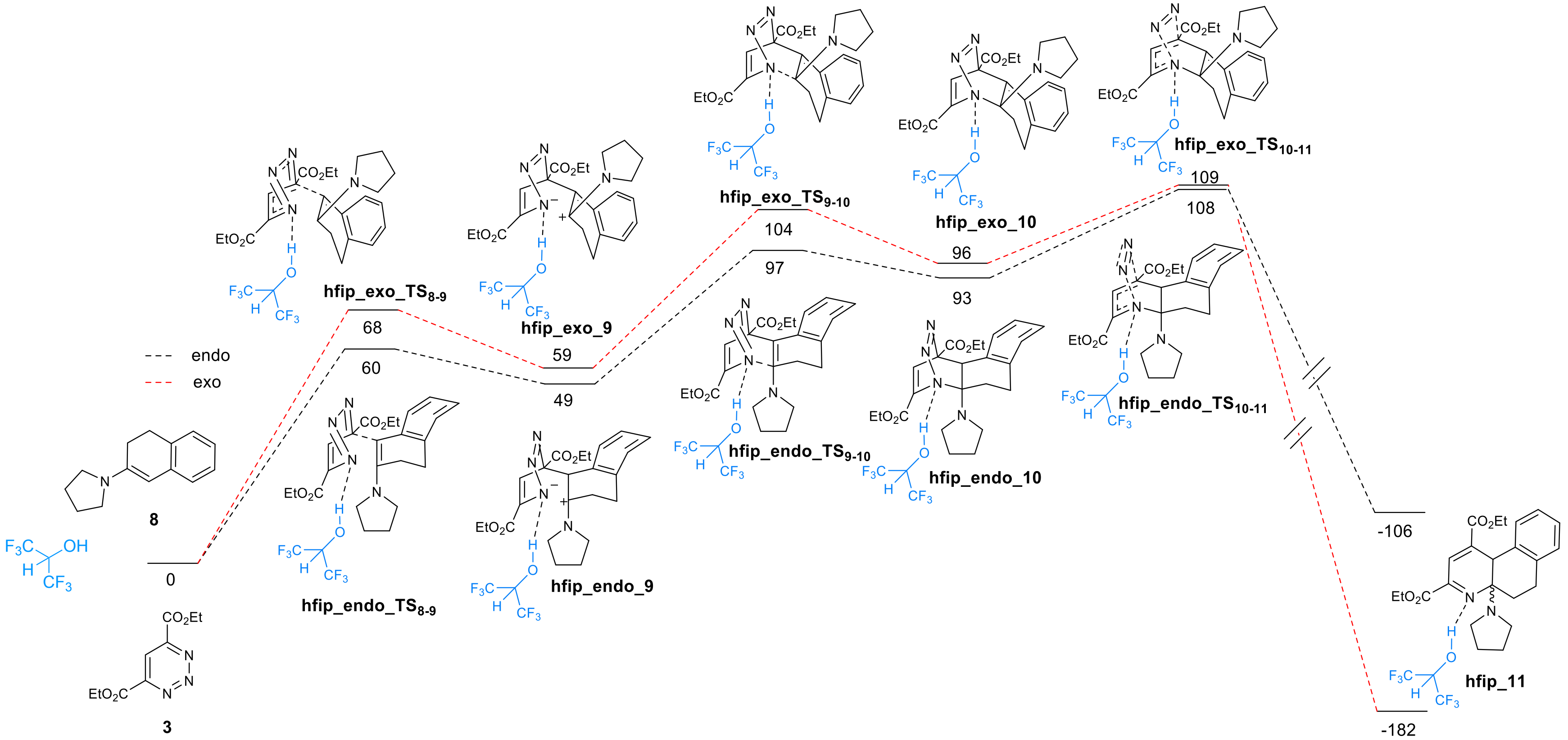

Figure 4.18 -PES for the start of the reaction between **3** and **8** until the formation of **11** including a single HFIP solvent molecule. Relative enthalpies are shown at the (RI)-PBE0-D3BJ/def2-TZVPP/(RI)-PBE0/def2-SV(P) level of theory in HFIP (COSMO).

While the barrier for $\mathbf{TS_{8\text{-}9}}$ is greatly reduced through the addition of HFIP, the second transition state, $\mathbf{TS_{9\text{-}10}}$, increases in energy by 41 and 33 kJ mol^{-1} for the *endo* and *exo* pathway respectively. As with the results presented by Houk, this increase in the C-N formation transition state occurs since the zwitterionic intermediate is now greatly stabilised by the HFIP compared to the transition state. Intermediates **hfip_*endo*_9** and **hfip_exo_9** are both greatly stabilised compared to the gas-phase results shown in Figure 4.10 (36 and 45 kJ mol^{-1} respectively). Transition states **hfip_*endo*_**$\mathbf{TS_{9\text{-}10}}$ and **hfip_exo_**$\mathbf{TS_{9\text{-}10}}$ are only stabilised by approximately 3 kJ mol^{-1} compared to the gas-phase results. The addition of implicit solvent corrections stabilised **9**, but destabilised $\mathbf{TS_{9\text{-}10}}$ giving a larger barrier compared to the gas-phase. However, **9** was not stabilised to a great extent, 11 and 7 kJ mol^{-1} for ***endo*_9** and **exo_9** compared to the gas-phase, which results in still quite a small barrier for $\mathbf{TS_{9\text{-}10}}$. The implicit corrections, therefore, stabilise $\mathbf{TS_{8\text{-}9}}$ and **9** but destabilise $\mathbf{TS_{9\text{-}10}}$. This is also seen with the addition of an explicit HFIP molecule, but to a greater extent. The intermediate **10** is destabilised through the implicit corrections and the addition of an HFIP molecule, but the explicit HFIP does stabilise this intermediate compared to the implicit corrections on their own. $\mathbf{TS_{10\text{-}11}}$ is also destabilised when HFIP is included and once again the explicit HFIP causes some stabilisation.

$\mathbf{TS_{8\text{-}9}}$ was found to be the highest in energy for both the *endo* and *exo* orientation with solvent corrections applied (86 and 92 kJ mol^{-1} respectively). The addition of an HFIP molecule significantly lowers the barrier by approximately 30 kJ mol^{-1}. The lowest energy barrier was for $\mathbf{TS_{10\text{-}11}}$ for all solvation models and both orientations. The stationary points that are stabilised, $\mathbf{TS_{8\text{-}9}}$ and **9**, involve charged species and therefore the addition of an HFIP will help stabilise this charge through hydrogen-bonding. The HFIP is able to hydrogen-bond to the pyrrolidine nitrogen where the charge would build up during the transition state. The other stationary points are destabilised through the implicit solvent correction because there is no charge build up in these states. With the addition of an HFIP molecule some stabilisation is seen due to the formation of a hydrogen-bond.

While the functional and basis set for our work was different the results in Table 4.8 show that the barriers are comparable to the work carried out by Houk *et al.*[152] The preference of one orientation over another is slightly different, most notably that the C-N formation barrier for the *endo* orientation is 13 kJ mol^{-1} higher in energy than predicted by Houk *et al.*[152] However, the energy differences are small and the largest barrier is still the formation of the C-C bond.

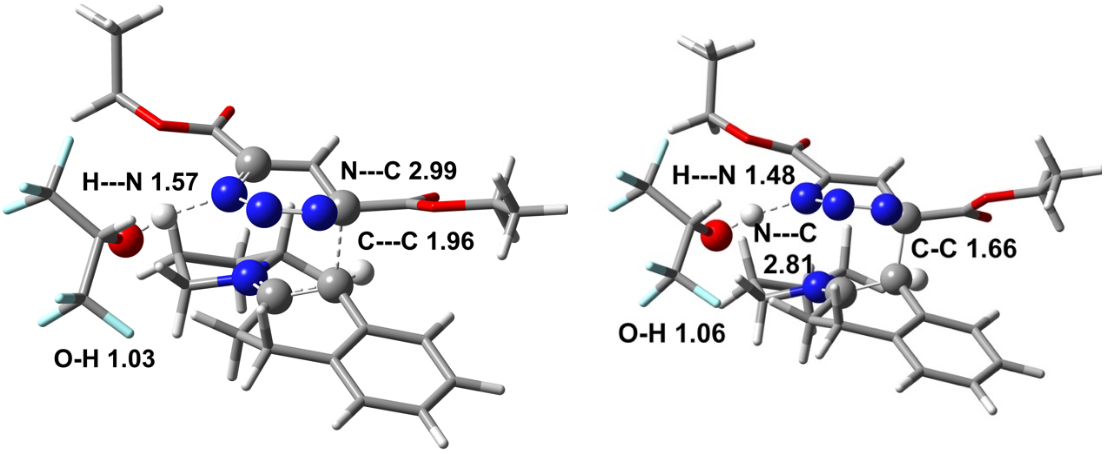

hfip_*endo*_TS$_{8\text{-}9}$ **hfip_*endo*_9**

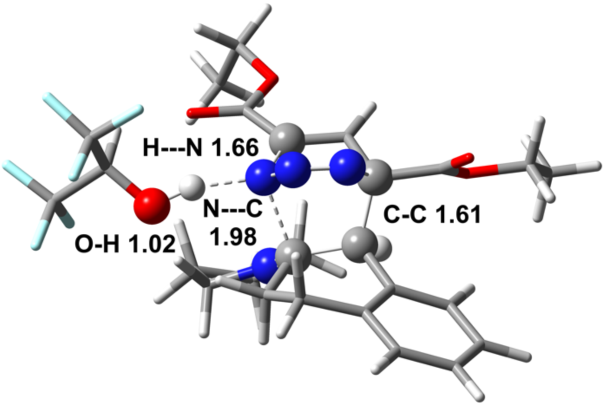

hfip_*endo*_TS$_{9\text{-}10}$

Figure 4.19 - Structures for the stationary points **hfip_*endo*_TS$_{8\text{-}9}$**, **hfip_*endo*_9**, **hfip_*endo*_TS$_{9\text{-}10}$**. Selected distances are shown in Å. Blue = N, red = O, grey = C and white = H.

The stationary points for the *endo* orientation are shown in Figure 4.19 and Figure 4.20 along with key bond lengths. The O-H distance in HFIP and the hydrogen-bond distance are shown in each figure, but only bond lengths with significant changes to the gas-phase geometry are shown alongside. In **hfip_*endo*_TS$_{8\text{-}9}$** the C-C bond that is formed is 0.15 Å longer with the addition of an HFIP compared to the gas-phase structure. The nitrogen and carbon that bond in the next transition state are also further apart by 0.17 Å. The distance between the nitrogen of the triazine and the hydrogen of HFIP is 1.57 Å indicating that there is an interaction present. Through this hydrogen-bond, electron density is pulled away from the neighbouring nitrogen atoms in the triazine, which makes the carbon where the bond is being formed less electron rich. The electrons from the C=C double bond will therefore be drawn more towards this electrophilic carbon, which could aid in the bond formation. In combination with the HFIP being able to stabilise the resulting charge that is built up the barrier for this transition state is decreased.

In **hfip_*endo*_9** the hydrogen-bond between HFIP and nitrogen is shortened by 0.09 Å, which would indicate a stronger interaction. The newly formed C-C bond is now shorter than in the gas-phase by 0.07 Å, while the distance between the nitrogen and carbon is still longer by 0.07 Å. In **hfip_TS**$_{\mathbf{9-10}}$ the hydrogen-bond is now longer by 0.16 Å since electron density from the nitrogen is now being drawn towards the carbon to form a bond. The C-C bond is slightly shorter with the addition of HFIP, but the distance between the nitrogen and carbon is significantly reduced by 0.24 Å compared to the gas-phase. As was mentioned above the addition of HFIP stabilises **9** to a greater extent than **TS**$_{\mathbf{9-10}}$, which can be seen by the shorter H(HFIP)---N interaction of 1.48 Å in **9** compared to 1.66 Å in **TS**$_{9-10}$.

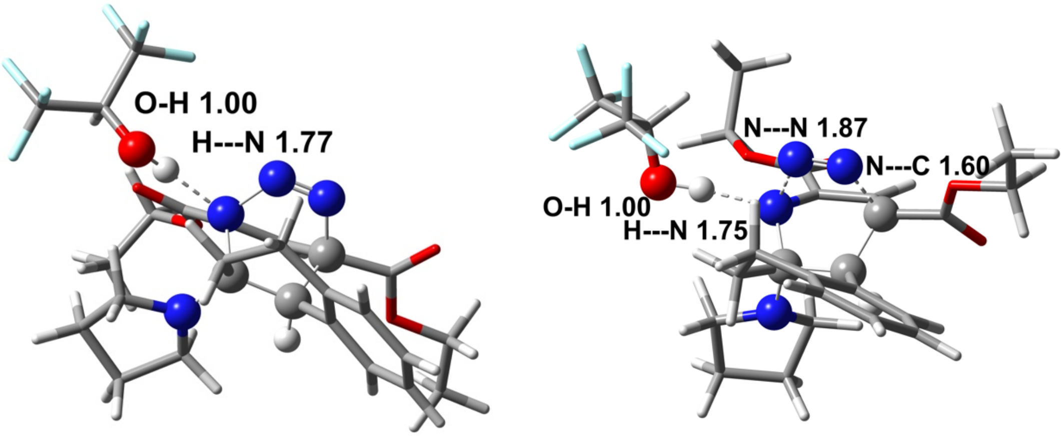

hfip_*endo*_10 **hfip_*endo*_TS**$_{\mathbf{10-11}}$

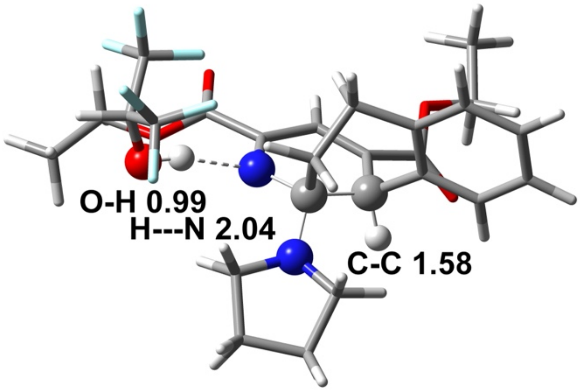

hfip_*endo*_11

Figure 4.20 - Structures for the stationary points **hfip_*endo*_10**, **hfip_*endo*_TS**$_{\mathbf{10-11}}$, **hfip_*endo*_11**. Selected distances are shown in Å. Blue = N, red = O, grey = C and white = H.

The hydrogen-bond further increases by 0.11 Å in **hfip_*endo*_10** and no significant changes to the gas-phase structure are seen. However, the free energy of **10** does increase significantly with the inclusion of HFIP, which is most likely due to the increased steric interaction that is not overcome by the hydrogen that is created. Since the N-C bond is now formed in **10** the nitrogen has less electron density which will weaken the hydrogen-bond, as can be seen by the longer distance. This hydrogen-bond slightly decreases in **hfip_*endo*_$\mathbf{TS_{10\text{-}11}}$** but only by 0.04 Å. The two bonds that are broken in **$\mathbf{TS_{10\text{-}11}}$** are both slightly shorter here than in the gas-phase by approximately 0.03 Å. In **hfip_*endo*_11** the hydrogen-bond distance is increased by 0.29 Å, once again indicating a weaker interaction. This weaker interaction will be due to the increased shared electron density between the nitrogen and carbon, which in turn decreases the interaction between the nitrogen and the hydrogen of the HFIP.

The PES containing the first three transition states where a TFE molecule is included is shown in Figure 4.21. As with the HFIP pathway the first transition state is stabilised along with **9**, while **$\mathbf{TS_{9\text{-}10}}$** and **10** are destabilised. This results in a lower barrier for **$\mathbf{TS_{8\text{-}9}}$**, which can be seen in Table 4.9. The implicit solvent correction lowered the energy of this barrier for the *endo* orientation to 76 kJ mol^{-1} from 94 kJ mol^{-1} in the gas-phase. Interestingly the addition of an explicit TFE molecule resulted in a minor increase in free energy, making the barrier 79 kJ mol^{-1}. For the *exo* orientation a further decrease is seen going from the implicit corrections to the mixed implicit/explicit approach, giving the same barrier as for the *endo* orientation.

Once again, the barrier for **$\mathbf{TS_{9\text{-}10}}$** is increased with the implicit approach and even further increased with the inclusion of explicit TFE. As with HFIP, the intermediate **9** will be greatly stabilised by TFE through hydrogen-bonding and stabilisation of the charge that was formed in **$\mathbf{TS_{8\text{-}9}}$**. The transition state **$\mathbf{TS_{9\text{-}10}}$**, however, would be stabilised to the same extent, which results in a higher barrier. **$\mathbf{TS_{10\text{-}11}}$** remains a low energy process, but it was found that the *exo* barrier is 15 kJ mol^{-1} higher in energy than the *endo* orientation.

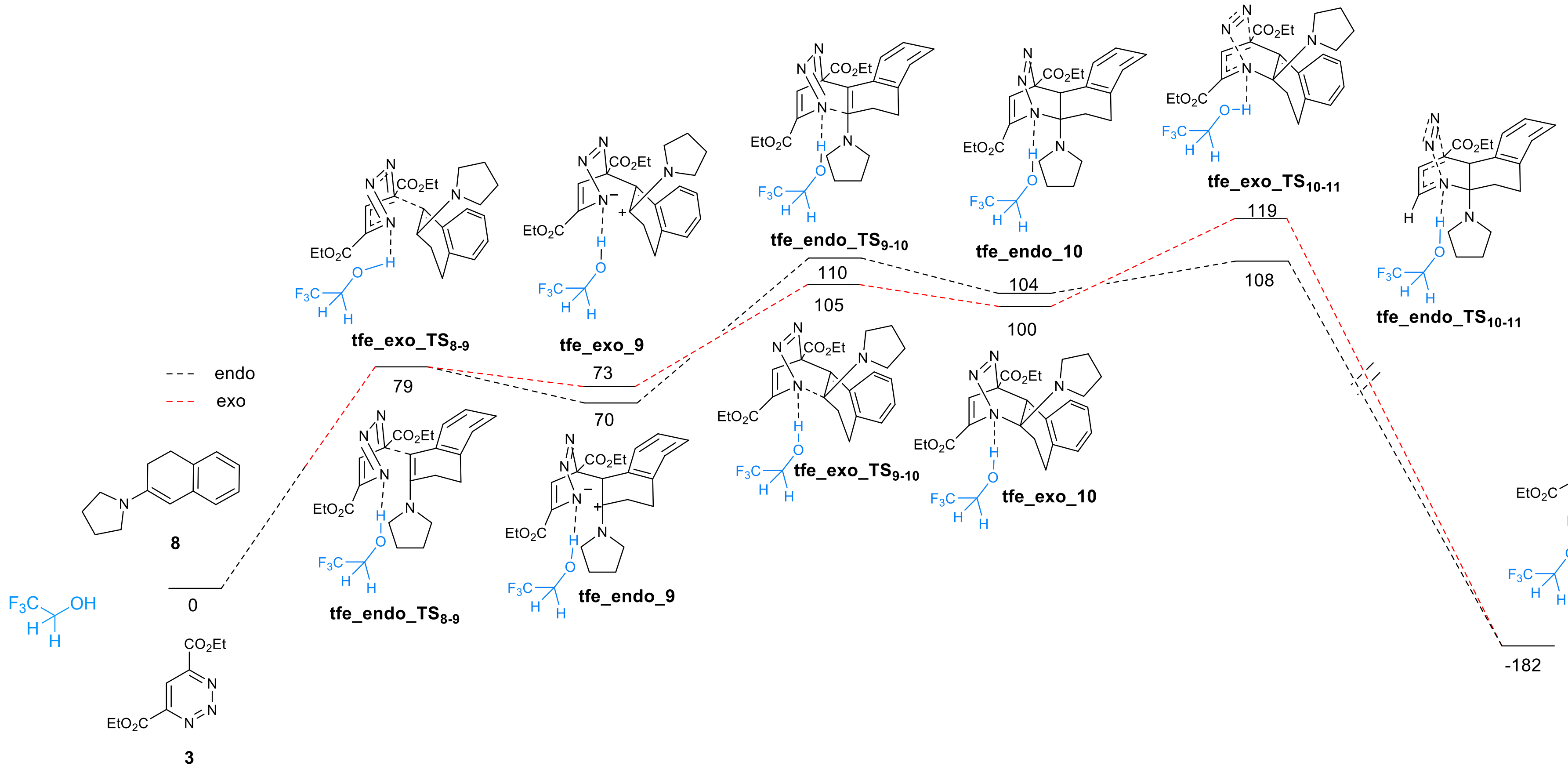

Figure 4.21 - PES for the start of the reaction between **3** and **8** until the formation of **11** including a single TFE solvent molecule. Relative enthalpies are shown at the (RI)-PBE0-D3BJ/def2-TZVPP/(RI)-PBE0/def2-SV(P) level of theory in TFE (COSMO).

Table 4.9 – ∆G barriers for *endo* and *exo* orientations in the gas-phase, in TFE with COSMO solvent corrections with no explicit solvent molecules (Imp.) and in TFE with COSMO solvent corrections and one TFE solvent molecule (Imp./Exp.) (ε = 8.55 for TFE).

TFE	Gas-phase – endo (kJ mol^{-1})	Imp. TFE – endo (kJ mol^{-1})	Imp./Exp. TFE – endo (kJ mol^{-1})	Gas-phase – exo (kJ mol^{-1})	Imp. TFE – exo (kJ mol^{-1})	Imp./Exp. TFE – exo (kJ mol^{-1})
TS$_{8-9}$	94	76	79	99	82	79
TS$_{9-10}$	7	22	41	12	23	32
TS$_{10-11}$	8	9	4	1	6	19

The structures of the *endo* stationary points are shown in Figure 4.22 and Figure 4.23 along with the O-H and hydrogen-bond distance. Further bond lengths are included where the value was found to be different compared to the gas-phase structures. In **tfe_*endo*_TS$_{8-9}$** the hydrogen-bond that is formed between TFE and the nitrogen of the triazine is slightly shorter than with HFIP by 0.07 Å. This longer distance suggests that the interaction is not as strong as with HFIP. While the barrier with an explicit TFE molecule is reduced compared to the gas-phase this is still 19 kJ mol^{-1} higher in energy compared to the barrier for HFIP. The C-C distance is also longer compared to the gas-phase, but it is shorter than with HFIP. The longer hydrogen-bond and the shorter C-C distance are both consistent with a larger barrier, since the transition state is now less stabilised with explicit TFE compared to HFIP.

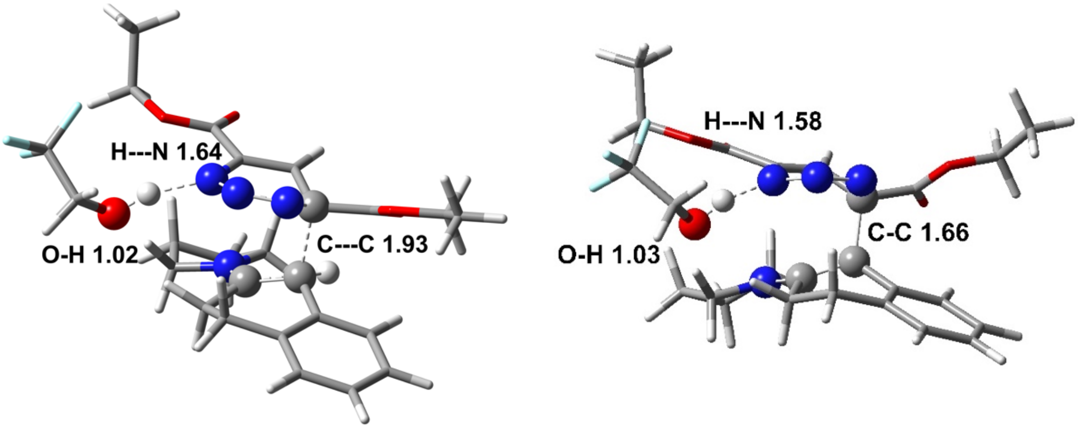

fe_*endo*_TS$_{8-9}$ **tfe_*endo*_9**

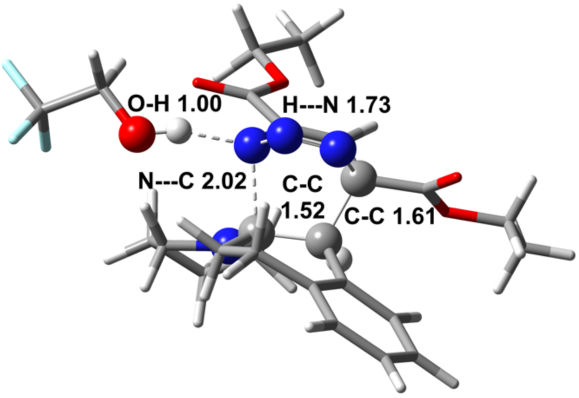

tfe_*endo*_TS$_{9-10}$

Figure 4.22 - Structures for the stationary points **tfe_*endo*_TS$_{8-9}$**, **tfe_*endo*_9**, **tfe_*endo*_TS$_{9-10}$**. Selected distances are shown in Å. Blue = N, red = O, grey = C and white = H.

In **tfe_*endo*_9** the C-C bond length is the same as in **hfip_*endo*_9** while the hydrogen-bond is once again longer with TFE than with HFIP by 0.1 Å. The barrier for **tfe_*endo*_TS$_{9-10}$** is roughly the same as for **hfip_*endo*_TS$_{9-10}$** at about 40 kJ mol^{-1}. The hydrogen-bond is still longer with TFE than HFIP, but the C-C bond that was formed in **TS$_{8-9}$** is the same yet the C=C bond that was broken in **TS$_{8-9}$** is now longer than in the gas-phase structures and the HFIP containing structures. The barriers for **TS$_{9-10}$** are similar for both solvents, because TFE does not stabilise **9** to the same extent as HFIP. The free energy of **9** with TFE is therefore higher compared to HFIP and **TS$_{9-10}$** is also not stabilised to the same extent with TFE than HFIP. This in combination leads to the barrier for **TS$_{9-10}$** having almost identical energies.

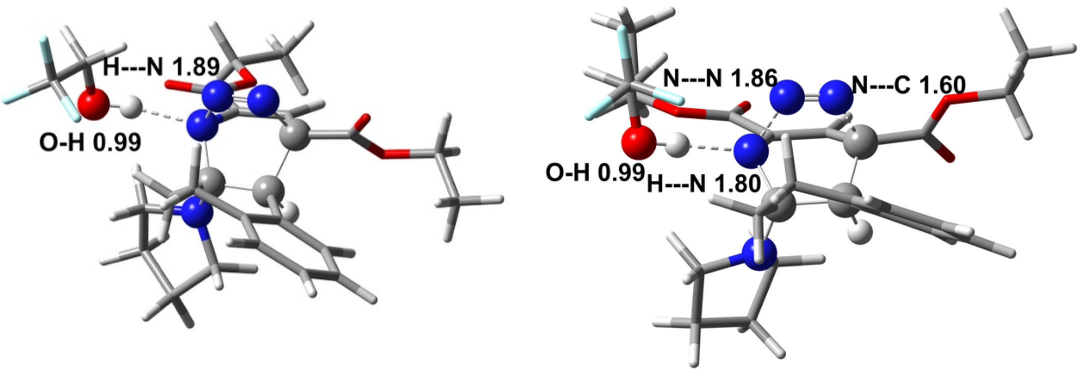

tfe_*endo*_10 **tfe_*endo*_TS_{10-11}**

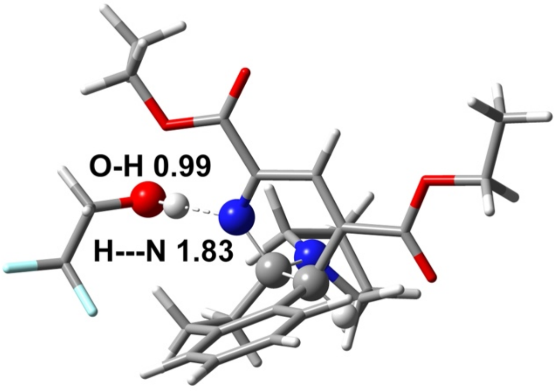

tfe_*endo*_11

Figure 4.23 - Structures for the stationary points **tfe_*endo*_10**, **tfe_*endo*_TS_{10-11}**, **tfe_*endo*_11**. Selected distances are shown in Å. Blue = N, red = O, grey = C and white = H.

The hydrogen-bond in **tfe_*endo*_10** is 0.12 Å longer than in **hfip_*endo*_10** while the rest of the bond lengths are almost identical. In **tfe_*endo*_TS_{10-11}** the hydrogen-bond distance decreases to a greater extent than in **hfip_*endo*_TS_{10-11}** (0.09 Å vs. 0.02 Å) but a stronger hydrogen-bond is still present with HFIP. For both HFIP and TFE the N-N and N-C bond that are being broken are shorter than in the gas-phase. The barrier for ***endo*_TS_{10-11}** is slightly lower for TFE than HFIP by approximately 10 kJ mol^{-1}, while the **tfe_exo_TS_{10-11}** barrier is roughly the same as for HFIP.

The inclusion of a single explicit solvent molecule and implicit solvent corrections, therefore, lowers the energy of the formation of the C-C bond while increasing the barrier for forming the N-C bond. This model more closely models the possible steps of the reaction. A difference between HFIP and TFE is now starting to be seen. Comparing the ***endo*_TS_{8-9}** results now shows that when the reaction is carried out in HFIP the barrier is 60 kJ mol^{-1} compared to 79 kJ mol^{-1} when done in TFE. This 19 kJ mol^{-1} difference in energy starts to provide insight into why the reaction with HFIP resulted in much higher yields than with TFE.

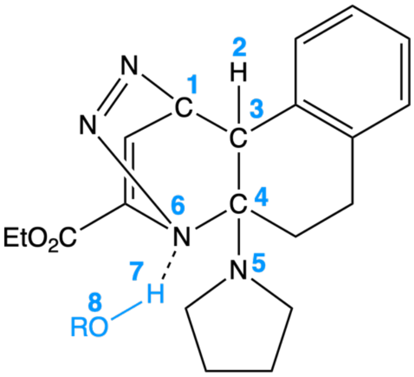

Figure 4.24 - Structure of **TS$_{8\text{-}9}$** for HFIP (R = C{CF$_3$}$_2$H)and TFE (R = C{CF$_3$}{H}$_2$)on which NBO calculations were carried out. Numbers indicate atoms that were focused on and will be referred to as XN throughout (X=atom, N=number).

To further understand the difference between HFIP and TFE in ***endo*_TS$_{8\text{-}9}$**, NBO calculations were carried out on both gas-phase geometries. Figure 4.24 shows the key atoms for which natural charges are presented in Table 4.10 for **hfip_*endo*_TS$_{8\text{-}9}$** and **tfe_*endo*_TS$_{8\text{-}9}$**. With TFE O8 is slightly more negatively charged, N6 is less negatively charged, and H7 is slightly more positively charged than with HFIP. This indicates that there is more electron density being pulled towards the oxygen in TFE than the nitrogen. With HFIP N6 is slightly more negatively charged than with TFE indicating there is more electron density on the nitrogen, with the electron density coming from the hydrogen in HFIP.

Table 4.10 - Natural charges from NBO 7 calculation for ***endo*_TS$_{8\text{-}9}$** including a single HFIP or TFE molecule for selected atoms.

Atom	hfip_*endo*_TS$_{8\text{-}9}$	tfe_*endo*_TS$_{8\text{-}9}$
C1	0.059	0.053
H2	0.262	0.263
C3	-0.349	-0.353
C4	0.426	0.433
N5	-0.315	-0.314
N6	-0.388	-0.386
H7	0.504	0.507
O8	-0.743	-0.761

In Table 4.11 the Wiberg bond indices are shown for the two transition states for a few key bond lengths. These bond indices further show that the hydrogen-bond with TFE is weaker than with HFIP since the bond index between H7 and O8 is higher for TFE than HFIP. The bond index for the hydrogen-bond (N6-H7) is also slightly higher for HFIP than TFE at 0.17 and 0.13 respectively. The other bonds are not greatly affected by the change in solvent.

Table 4.11 – Wiberg bond indices from NBO 7 calculations for ***endo*_TS$_{8\text{-}9}$** including a single HFIP or TFE molecule for selected atoms.

Bond	hfip_*endo*_TS$_{8\text{-}9}$	tfe_*endo*_TS$_{8\text{-}9}$
C1-C3	0.51	0.53
C3-C4	1.22	1.21
C4-N5	1.39	1.40
H2-C3	0.88	0.88
N6-H7	0.17	0.13
H7-O8	0.56	0.59

An idea of the strength of a hydrogen-bond can be determined through second bond order perturbation theory as shown in

Table 4.12. The largest interactions found for both solvents are shown. In all three cases it is the lone pair of N6 that is donating into an anti-bonding orbital. The largest stabilisation was for N6 donating into the anti-bonding orbital of the N-N bond, 282 kJ mol^{-1} for HFIP and 392 kJ mol^{-1} for TFE. Another large contribution was the donation into the anti-bonding orbital of the C=C double bond from the triazine, which was 274 kJ mol^{-1} for HFIP and 283 kJ mol^{-1} for TFE. For both TFE gave the bigger stabilisation. For the hydrogen-bond, which is donation into the H7-O8 anti-bonding orbital the contribution in HFIP was much larger than for TFE, 215 and 165 kJ mol^{-1}. The bond distances, natural charges, and Wiberg bond indices all suggest a stronger hydrogen-bond between HFIP and the triazine nitrogen and second order perturbation theory suggests that that this hydrogen-bond is 50 kJ mol^{-1} stronger than with TFE.

Table 4.12 - Second Bond Order Perturbation Theory from NBO calculation for ***endo*_TS$_{8\text{-}9}$** including a single HFIP or TFE molecule. Only large interactions are shown where a lone pair (LP) on N6 donates into an anti-bonding (BD*) orbital.

Donor	Acceptor	HFIP Energy (kJ mol^{-1})	TFE Energy (kJ mol^{-1})
LP N6	BD* N-N	382	392
LP N6	BD* C-C	274	283
LP N6	BD* H7-O8	215	165

4.4.1.8 Summary

The results presented by Houk showed that an explicit HFIP molecule was needed to understand why HFIP gave higher yields. However, no comparison between HFIP and any other solvent was made. By also studying the effect of TFE on the Diels-Alder reaction we can get a better understanding of the solvent effects in this reaction. While implicit solvent corrections do stabilise and destabilise certain stationary points, on their own they do not differentiate between HFIP and TFE. By using a mixed implicit/explicit solvation model it can be seen that the barrier for **TS$_{8\text{-}9}$** is greatly reduced due to hydrogen-bonding between the nitrogen in triazine and the hydrogen of HFIP or TFE.

Analysis of the transition state structures suggests that the hydrogen-bond between TFE and triazine is not as strong as with HFIP, which results in a higher barrier. NBO calculations provided further evidence for this through a more negatively charged oxygen in TFE compared to HFIP and a lower Wiberg bond index between TFE and triazine. Second Bond Order Perturbation Theory also showed that donation of electron density from the lone pair orbital of N6 into the anti-bonding orbital of the O-H bond stabilised the system by 50 kJ mol^{-1} more with HFIP than TFE.

4.4.1.9 Pyrrolidine Loss Pathways

The inclusion of an explicit solvent molecule for the loss of pyrrolidine needed to be considered in more depth than the previous steps of the reaction. The gas-phase and implicit results show that pyrrolidine loss, **TS$_{11\text{-}12}$**, is the rate-determining step of the reaction. Including an explicit solvent molecule raises the issue of deciding where this molecule should be placed. For the previous steps HFIP and TFE were able to hydrogen-bond to the same nitrogen in triazine throughout. This is also possible for pyrrolidine loss, but the solvent can also now take a more active role where it aids by hydrogen-bonding to the pyrrolidine and/or the hydrogen that are being lost during **TS$_{11\text{-}12}$**.

The loss of pyrrolidine was investigated by Houk using a single HFIP molecule, but only for the much smaller triazine. The barrier was reduced but remained high in energy at 102 kJ mol^{-1}, thus still making it the rate-determining step of the reaction. Once again, only HFIP was considered, which does not provide a complete picture of what effect the solvent is having on the reaction. During the reaction pyrrolidine is used and subsequently removed from the reaction, but it is likely that residual pyrrolidine will still be present. Combined with this pyrrolidine is continually being released during **TS$_{11\text{-}12}$**, which allows for pyrrolidine to aid in this transition state.

Fifteen pathways were proposed and explored for the loss of pyrrolidine. These pathways either involved two solvent molecules, one solvent molecule and one pyrrolidine molecule, or two pyrrolidine molecules. The solvent only pathways are likely to be the main pathway at the start of the reaction. As the reaction proceeds, however, pyrrolidine is released meaning the single and double pyrrolidine aided pathways would become accessible. From the original fifteen pathways, transition states and minima were only found for eleven of them, which are shown in Figure 4.25. Pathway 1, **P1**, is the original concerted pathway, but with implicit solvent corrections applied where no explicit solvent molecules are included. Pathways

2, **P2**, involves just two solvent molecules with the solvent molecule that is deprotonating the hydrogen being negatively charged and the solvent molecule that is stabilising the pyrrolidine being positively charged.

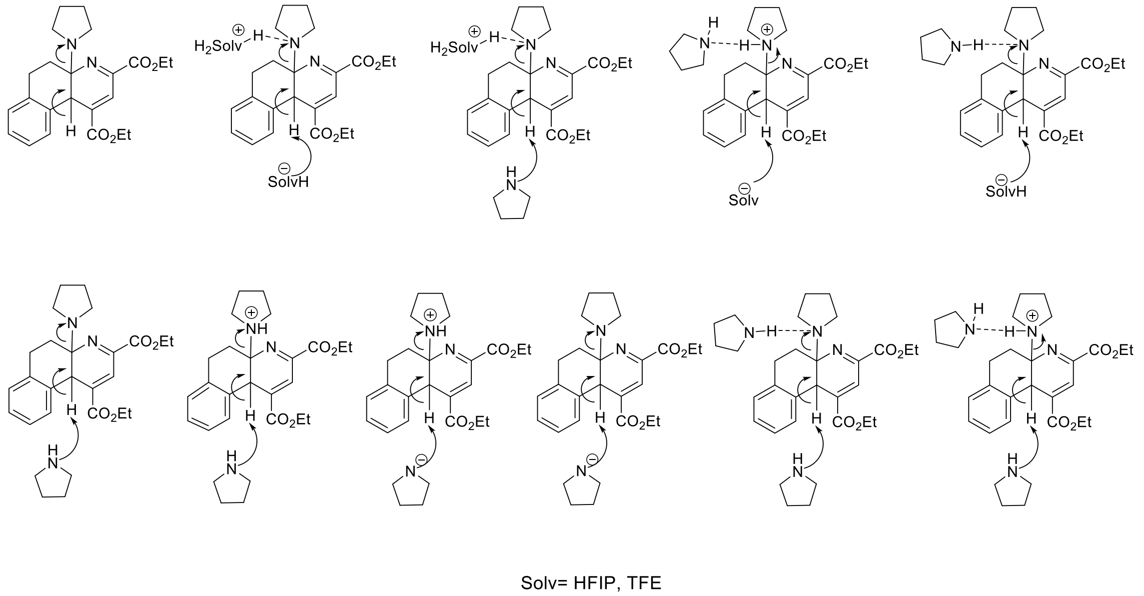

Figure 4.25 - Pathways for the loss of pyrrolidine, **TS$_{11\text{-}12}$**, for which a transition state was successfully found. Pathways are grouped into concerted (**P1**), solvent only (**P2**), solvent and pyrrolidine (**P3-5**), and pyrrolidine only (**P6-11**). Solv=HFIP or TFE.

Pathways 3-5, **P3**-**P5**, involve a single solvent molecule and a pyrrolidine molecule. In **P3** the solvent molecule is protonated and stabilising the pyrrolidine while the pyrrolidine solvent molecule is deprotonating the hydrogen. In **P4** the pyrrolidine that is being lost is already protonated and stabilised by a pyrrolidine molecule in solution with the solvent molecule acting as the base. In **P5** a pyrrolidine molecule in solution is stabilising the pyrrolidine that is being lost which is not protonated in this pathway while the solvent is again acting as the base.

Pathways 6-9, **P6**-**P9**, involves just one pyrrolidine molecule, which acts as the base with the pyrrolidine that is being lost already protonated in some of the pathways. In **P6** the dissociating pyrrolidine is not protonated and a pyrrolidine molecule in solution acts as the base. In **P7** the pyrrolidine that is being lost is protonated and a pyrrolidine molecule in solution acts as the base. In **P8** the dissociating pyrrolidine is also protonated but now a negatively charged pyrrolidine acts as the base. In **P9** the dissociating pyrrolidine is not protonated and once again a negatively charged pyrrolidine acts as the base.

Pathways 10 and 11, **P10** and **P11**, involve two pyrrolidine molecules. In **P10** a pyrrolidine molecule stabilises the going pyrrolidine and another pyrrolidine acts as the base. In **P11** the going pyrrolidine is protonated and stabilised by a pyrrolidine molecule while another pyrrolidine molecule acts as the base.

MeCN is a polar aprotic solvent meaning that it can aid in the reaction by stabilising any charges but is unable to hydrogen-bond. Including only one explicit solvent molecule would not simulate the role that MeCN would play very well. The proposed pyrrolidine loss pathways that involve only pyrrolidine, **P6**-**P11**, would therefore be the pathways that are accessible when MeCN is used as the solvent.

Figure 4.26 shows the four pathways that were proposed but were unsuccessful. While not locating a transition state does not mean these pathways are not possible close inspection of the proposed pathways can provide some insight into why these pathways are less likely to occur than others. In Pathway 12, **P12**, the pyrrolidine is stabilised by a protonated solvent molecule which would aid in the loss of pyrrolidine due to a stabilisation of the negatively charged pyrrolidine that is formed. Unlike **P2** the solvent molecule that is acting as a base is neutral and not negatively charged. For both HFIP and TFE this will decrease their effectiveness as a base and, therefore, is likely to increase the barrier for this pathway.

In Pathway 13, **P13**, the pyrrolidine is once again stabilised by a protonated solvent molecule while a negatively charged pyrrolidine acts as the base. While this pathway should be feasible it is likely that the negatively charged pyrrolidine acting as a base would not be as strong as HFIP and TFE. Pyrrolidine has a pKa of 11.27 meaning that it is more likely to exist as a pyrrolidinium ion in solution than pyrrolidine. The pathways that stabilise the dissociating pyrrolidine through hydrogen-bonding are therefore expected to be lower in energy than those that do not. This also means that any pathways relying on a negatively charged pyrrolidine are likely to have high barriers or not occur at all. In Pathways 14 and 15, **P14** and **P15**, a pyrrolidine and pyrrolidinium ion stabilise the pyrrolidine respectively, while a negatively charged pyrrolidine acts as the base. These two pathways are also not likely to be accessible since formation of this negatively charged pyrrolidine is unfeasible.

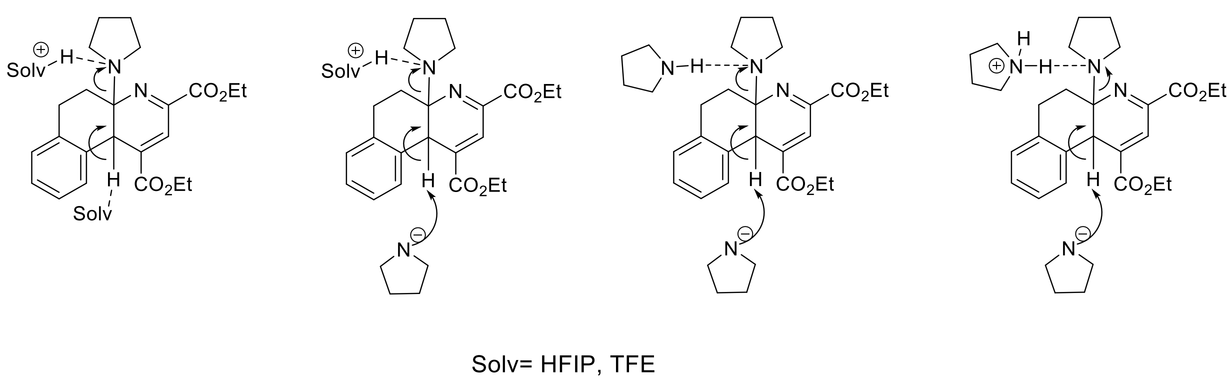

Figure 4.26 - Pathways for the loss of pyrrolidine, **TS$_{11-12}$**, for which no transition state was found. P12 is a solvent only pathway, P13 a mixed solvent/pyrrolidine pathway, and P14 and P15 are pyrrolidine only pathways. Solv=HFIP or TFE.

The barriers for the different pathways shown in Figure 4.25 for MeCN, HFIP, and TFE are shown in Table 4.13, Table 4.14, and Table 4.15 respectively. The barriers for the concerted pathway, **P1**, are shown as reference. Since MeCN is a polar aprotic solvent, it can only undergo the pathways that rely on pyrrolidine, which could already explain why such low yields were seen in acetonitrile. With both HFIP and TFE all eleven pathways should be accessible.

Table 4.13 – ΔG barriers for pyrrolidine loss pathways, **TS$_{8\text{-}9}$**, in implicit MeCN compared to gas-phase

Solvent	Pathway	Barrier (kJ mol^{-1})	Barrier Gas-Phase (kJ mol^{-1})
MeCN	**P1**	141	160
	P6	55	79
	P7	89	115
	P8	130	129
	P9	94	86
	P10	75	91
	P11	66	88

In general, the barriers for pyrrolidine loss are reduced when an implicit solvent correction for MeCN is included. The barrier for the concerted pathway, **P1**, is reduced by 19 kJ mol^{-1}, but remains a high energy barrier at 141 kJ mol^{-1}. **P6** and **P11** proceed *via* the lowest barriers of 55 and 66 kJ mol^{-1} respectively and are stabilised by over 20 kJ mol^{-1} through the inclusion of solvent effects. Surprisingly **P8** is not stabilised at all and **P9** is even destabilised compared to the gas-phase. Both **P8** and **P9** involve charged species so it is surprising that the inclusion of the implicit solvent correction would not stabilise these states. **P7** and **P10** proceed *via* barriers of 89 and 75 kJ mol^{-1}, where the barrier of **P7** is reduced by 26 kJ mol^{-1}.

All the pathways explored help to lower the energy of **TS$_{8\text{-}9}$**. Having a pyrrolidine molecule deprotonate helps to greatly reduce the barrier since a four-membered transition state is not formed. By protonating the pyrrolidine that is being lost, such as in **P7**, increases the barrier by 34 kJ mol^{-1}, compared to just using pyrrolidine to deprotonate as in **P6**. Comparing **P6** and **P9** the negative charge on pyrrolidine should make it a better base and thus reduce the barrier, however, the barrier for **P9** is 39 kJ mol^{-1} higher in energy than **P6**. In **P8** the pyrrolidine that is being lost is protonated and a negatively charged pyrrolidine is being used, which results in a much higher barrier of 130 kJ mol^{-1}, which is only 11 kJ mol^{-1} lower in energy than the concerted **P1** pathway. In **P10** the addition of a pyrrolidine molecule stabilising the pyrrolidine that is being lost also results in an increase in the barrier compared to **P6** by 20 kJ mol^{-1}. When a pyrrolidinium ion is used instead of pyrrolidine to stabilise the leaving pyrrolidine in **P11** the barrier is reduced by 9 kJ mol^{-1} compared to **P10**.

Many of the pathways that were investigated lowered the barrier for $\mathbf{TS_{8\text{-}9}}$ through the use of pyrrolidine to stabilise the system. Pathways **P6**, **P10**, and **P11** all have a barrier lower than that for $\mathbf{TS_{8\text{-}9}}$, which would then be the rate-determining step of the reaction. The barrier for these pathways rely on pyrrolidine being available in the reaction, which would explain the poor reactivity that was seen in MeCN. So, while $\mathbf{TS_{8\text{-}9}}$ is the rate-determining step, using MeCN as the solvent would only allow for the formation of the product if pyrrolidine is present in the reaction mixture. MeCN is not able to hydrogen-bond and aid in the loss of pyrrolidine. The low reactivity seen for MeCN is likely to be because of the small amount of pyrrolidine in the reaction that could lower the barrier for the loss of pyrrolidine.

Table 4.14 – ΔG barriers for pyrrolidine loss pathways, $\mathbf{TS_{8\text{-}9}}$, in implicit HFIP compared to gas-phase

Solvent	Pathway	Barrier (kJ mol^{-1})	Barrier Gas-Phase (kJ mol^{-1})
HFIP	**P1**	142	160
	P2	48	36
	P3	84	113
	P4	85	103
	P5	25	14
	P6	56	79
	P7	91	115
	P8	130	129
	P9	94	86
	P10	76	91
	P11	66	88

Table 4.14 shows the pathways that would be accessible in HFIP, the barriers of those pathways in implicit HFIP and the barriers in the gas-phase. All the barriers are accessible in HFIP and in general the addition of implicit solvent corrections lowers the barrier for the pathways. The barriers for **P2**, **P5**, **P9**, and **P10** are all higher with implicit solvent corrections than in the gas-phase. The lowest barriers are for **P2** and **P5** with a barrier of 48 and 25 kJ mol^{-1}.

Comparing **P2** and **P3**, the effect of using pyrrolidine to deprotonate instead of HFIP shows that this increases the barrier by 36 kJ mol^{-1}. However, using HFIP to deprotonate, but using pyrrolidine to stabilise the pyrrolidine that is being lost during $\mathbf{TS_{8\text{-}9}}$ reduces the barrier to 25 kJ mol^{-1} in **P5**. Protonating the stabilising pyrrolidine, however, increases the barrier by 60 kJ mol^{-1} in **P4** compared to **P5**. The lowest energy pathway is therefore a pathway that relies on both the solvent and pyrrolidine working together to greatly reduce the barrier for $\mathbf{TS_{8\text{-}9}}$.

In **P6** pyrrolidine is used to deprotonate which results in a moderate barrier of 56 kJ mol^{-1}. Protonating the pyrrolidine molecule that is being lost increases the barrier by 35 kJ mol^{-1} in **P7** and increases by a further 39 kJ mol^{-1} when a negatively charged pyrrolidine is used as the base in **P8**. In **P9** the same base is used, but the pyrrolidine that is being lost is not protonated, which lowers the barrier by 36 kJ mol^{-1}. Comparing the effect of using pyrrolidine to stabilise the pyrrolidine that is being lost shows that the barrier increases by 28 kJ mol^{-1} when pyrrolidine is used (**P10**) but only increases by 18 kJ mol^{-1} when a pyrrolidinium ion is used (**P11**).

Table 4.15 – ΔG barriers for pyrrolidine loss pathways, **TS$_{8\text{-}9}$**, in implicit TFE compared to gas-phase

Solvent	Pathway	Barrier (kJ mol^{-1})	Barrier Gas-Phase (kJ mol^{-1})
TFE	**P1**	142	160
	P2	6	-3
	P3	70	92
	P4	3	8
	P5	6	-5
	P6	55	79
	P7	90	115
	P8	130	129
	P9	94	86
	P10	76	91
	P11	66	88

Table 4.15 shows the barriers for the different pathways in implicit TFE along with the barriers in the gas-phase. For TFE the pathways **P2**, **P4**, and **P5** were found to be the lowest in energy, proceeding *via* a barrier of 6, 3, and 6 kJ mol^{-1}. Unlike with HFIP the pyrrolidinium ion stabilising the leaving pyrrolidine does not increase the barrier. Using pyrrolidine as the base in **P3** instead of TFE, however, greatly increased the barrier to 70 kJ mol^{-1}.

For **P6**-**P11** the same trends are seen as for HFIP. A negatively charged pyrrolidine molecule acting as the base increases the barrier along with protonating the pyrrolidine that is being lost. The barrier also increases when the leaving pyrrolidine is stabilised by a pyrrolidine molecule, but this barrier can be decreased by using pyrrolidinium.

The lowest energy pathways are therefore **P2** and **P5** for HFIP and TFE along with **P4** for TFE. Table 4.16 shows the lowest energy pathways with their corresponding barriers. The molecule that was utilised as a base and to stabilise the pyrrolidine through hydrogen-bonding is also shown, along with the barriers for the concerted pathway, **P1**, as reference.

The barriers involving MeCN were found to be higher in energy than **TS$_{8\text{-}9}$**. Only **P6**, **P10**, and **P11** were found to be lower in energy, thereby making **TS$_{8\text{-}9}$** the rate-determining step. However, all three of these pathways rely on the presence of pyrrolidine in the solution. At the start of the reaction the amount of pyrrolidine will be extremely low since this was removed earlier in the reaction. As the reaction progresses pyrrolidine is being released, which would then allow for the reaction to proceed. No reactivity was seen experimentally with MeCN suggesting that no pyrrolidine was present and, therefore, only the high energy barriers were available, which were not accessible.

For HFIP and TFE the solvent only pathway, **P2**, was found to be low in energy and easily accessible. The pathway that relies on both the solvent and pyrrolidine, **P5**, was found to be lower in energy for both HFIP and TFE. The low barrier for **P2** means that pyrrolidine is generated through this pathway, which then allows access to the lower pathway, **P5** (barrier of 25 and 6 kJ mol^{-1} for HFIP and TFE respectively) . These pathways have shown that both a base and a molecule capable of hydrogen-bonding to pyrrolidine are necessary for the reaction to proceed.

Table 4.16 - Lowest energy pathways with barriers for the loss of pyrrolidine, **TS$_{11-12}$**, in the gas-phase and with implicit solvation (MeCN, HFIP, and TFE). The molecule that acts as the base and the molecule that stabilises the pyrrolidine through hydrogen-bonding are also shown. The concerted pathway, **P1**, is shown for comparison. Free energies are shown in kJ mol^{-1}.

Pathway	P1	P9 – HFIP	P9 – TFE	P14 - TFE$^-$	P15 – HFIP	P15 – TFE
Base	N/A	HFIP$^-$	TFE	TFE$^-$	HFIP$^-$	TFE$^-$
H-Bond	N/A	HFIP	TFE	Pyrrolidine	Pyrrolidine	Pyrrolidine
Gas-Phase	160	36	-3	8	14	-5
HFIP	142	48	-	-	25	-
TFE	142	-	6	3	-	6

For HFIP and TFE the barriers are quite comparable but the barriers for TFE are lower than those for HFIP. The experimental data showed that the greatest yields were achieved in HFIP while some reactivity was seen in TFE. While the barriers here indicate that TFE results in lower barriers the barrier for pyrrolidine loss has been greatly reduced for both solvents. Pyrrolidine loss is no longer the rate-determining step of the reaction. The C-C forming transition state of the Diels-Alder step, **TS$_{8-9}$**, is now rate-determining and therefore what controls the final yield of the reaction.

TS$_{8-9}$ being the rate-determining step of the reaction is consistent with what was hypothesised by Boger and with the work carried out by Houk. The solvent was found to play a significant role in the loss of pyrrolidine, as predicted by Boger, but this crucial role of the solvent was not investigated by Houk. The full picture of what role the solvent plays in this reaction can only be obtained when the pyrrolidine loss during **TS$_{11-12}$** is also included.

A detailed discussion of **P2** and **P5** is given below for both HFIP and TFE as these two pathways were found to proceed *via* the lowest barrier. By looking into the bond lengths and carrying out NBO calculations, a better idea of the differences can be analysed between the two pathways and the two solvents.

4.4.1.10 Pathway 2 – HFIP

Pathway **P2_hfip** utilises both neutral HFIP and anionic HFIP$^-$ to stabilise the pyrrolidine and deprotonate the methoxatin analogue respectively. It was assumed that some HFIP$^-$ would be present in the solution due to the slight acidity of the solvent (pKa = 9.3).[154] Figure 4.27 shows the structure of the starting adduct, where the two solvent molecules are hydrogen-bonding to the main substrate, **P2_min1$_{\text{HFIP}}$**, the transition state where the substrate is deprotonated by HFIP$^-$, **P2_TS$_{\text{HFIP}}$**, and the resulting product minimum, **P2_min2$_{\text{HFIP}}$**.

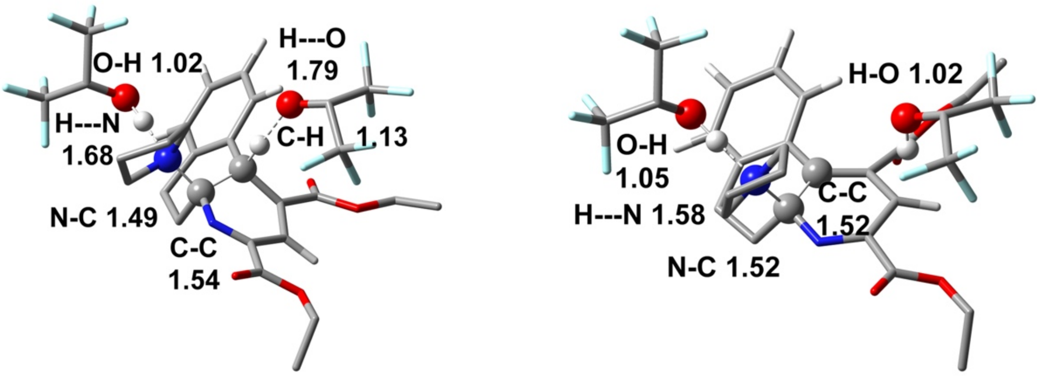

P2_min1$_{\text{HFIP}}$ **P2_min2$_{\text{HFIP}}$**

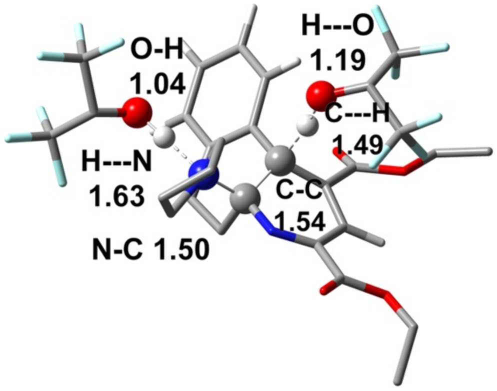

P2_TS$_{\text{HFIP}}$

Figure 4.27 – Structures for the stationary points **P2_min1$_{\text{HFIP}}$**, **P2_min2$_{\text{HFIP}}$**, and **P2_TS$_{\text{HFIP}}$**. Selected distances are shown in Å. Blue = N, red = O, green = F, grey = C and white = H. Hydrogens have been emitted for most of the backbone for clarity.

The C-H distance changes from 1.13 to 1.49 Å in **P2_min1$_{\text{HFIP}}$** to **P2_TS$_{\text{HFIP}}$** respectively and is then fully broken in **P2_min2$_{\text{HFIP}}$**. The O-H distance decreases from 1.79 to 1.19 and finally to 1.02 Å from **P2_min1$_{\text{HFIP}}$** through **P2_TS$_{\text{HFIP}}$** and then **P2_min2$_{\text{HFIP}}$**. The O-H distance in the HFIP molecule remains unperturbed during this process (1.02, 1.04 and 1.05 Å respectively). The slight lengthening of the O-H bond suggests some H-bonding. The C-C distance remains the same throughout **P2_min1$_{HFIP}$** and **P2_TS$_{HFIP}$** and slightly contracts in **P2_min2$_{HFIP}$** from 1.54 to 1.52 Å. The C-N bond length changes from 1.49 to 1.52 Å in **P2_min1$_{HFIP}$** to **P2_min2$_{HFIP}$**.

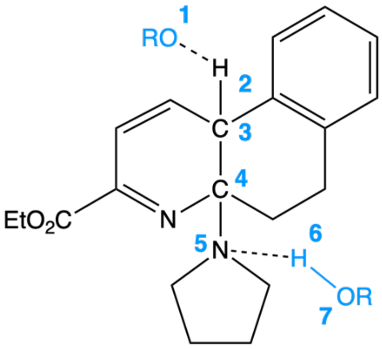

Figure 4.28 - Structure of **P2_TS** for HFIP (R = C{CF$_3$}$_2$H)and TFE (R = C{CF$_3$}{H}$_2$) on which NBO calculations were carried out. Numbers indicate atoms that were focused on and will be referred to as XN throughout (X=atom, N=number).

NBO analysis was carried out on all three of these **P2$_{HFIP}$** stationary points to gain more insight. The natural charges show that as the C-H, **H2**-**C3**, bond is broken the hydrogen and the carbon become more positively charged, while the neighbouring carbon, **C4,** becomes more negatively charged. This indicates that the electron density is moving from the C-H bond to the C-C bond, which is confirmed by the Wiberg bond indices that show the **H2**-**C3** bond breaking (0.7247 to 0.0087 in **P2_min1$_{HFIP}$** to **P2_min2$_{HFIP}$**) and the **C3**-**C4** bond is strengthened (0.9544 to 0.9736).

Table 4.17 - Natural charges from NBO calculation for **P2$_{HFIP}$** including a single HFIP molecule for selected atoms.

Atom	P2_min1$_{HFIP}$	P2_TS$_{HFIP}$	P2_min2$_{HFIP}$
O1	-0.869	-0.772	-0.711
H2	0.369	0.458	0.504
C3	-0.413	-0.392	-0.090
C4	0.319	0.323	0.280
N5	-0.480	-0.484	-0.487
H6	0.530	0.527	0.519
O7	-0.717	-0.721	-0.725

The charge on the oxygen of HFIP$^-$, **O1**, becomes more positive as the **O1**-**H2** bond is formed (-0.869 to -0.711 in **P2_min1$_{HFIP}$** to **P2_min2$_{HFIP}$**). The bond index increases from 0.0066 to 0.59 in **P2_min1$_{HFIP}$** to **P2_TS$_{HFIP}$**, showing the formation of the **O1**-**H2** bond. The bond index between **C4** and **N5** decreases slightly (0.95 to 0.88 in **P2_min1$_{HFIP}$** to **P2_min2$_{HFIP}$**), matching what is seen with the bond lengths.

Table 4.18 - Wiberg bond indices from NBO calculations for **P2$_{HFIP}$** including a single HFIP molecule for selected atoms.

Bond	P2_min1$_{HFIP}$	P2_TS$_{HFIP}$	P2_min2$_{HFIP}$
C3-C4	0.95	0.96	0.97
C4-N5	0.95	0.93	0.88
H2-C3	0.74	0.31	0.01
O1-H2	0.07	0.40	0.59
N5-H6	0.11	0.14	0.16
H6-O7	0.59	0.57	0.55

Second bond order perturbation theory shows the presence of a hydrogen-bond where a lone pair on **O1** is donating into the anti-bonding orbital of the **H2**-**C3** bond and stabilises the system by 51.1 kJ mol^{-1} in **P2_min1$_{HFIP}$**. This increases to 642 kJ mol^{-1} in **P2_TS$_{HFIP}$** and is no longer present in **P2_min2$_{HFIP}$** as a bond has now formed between **O1** and **H2**.

Further stabilisation occurs through the delocalisation of electron density in the CO_2Et groups of the molecule. The stabilisation seen through these interactions range from 153-210 kJ mol^{-1} and remains virtually unchanged in all three stationary points. Conjugation is seen along the N-C4-C3-C plane, stabilising the system by 457 and 311 kJ mol^{-1}.

An interaction between **N5** of the pyrrolidine and the anti-bonding orbital of **H6**-**O7** in HFIP stabilises the system by 139 kJ mol^{-1} in **P2_min1$_{HFIP}$**. This increases to 168 kJ mol^{-1} in **P2_TS$_{HFIP}$** and 296 kJ mol^{-1} in **P2_min2$_{HFIP}$**, this shows that the slight lengthening of the **H6**-**O7** bond of HFIP is due to the strengthening of this hydrogen-bond as the **H2**-**C3** bond is broken in the TS.

This increased interaction, which stabilises the TS by 168 kJ mol^{-1} will contribute to this pathway, **P2**, being lower in energy than the other options. This is especially important when comparing to the concerted pathway, where this interaction is not possible. Through the inclusion of just two solvent molecules the system is already described better and highlights how important individual solvent molecules are in this reaction.

4.4.1.11 Pathway 2 – TFE

In **P2_tfe** a neutral TFE and anionic TFE$^-$ solvent molecule are utilised just as with the HFIP analogue. It is assumed that some anionic, and cationic, TFE would be present in the reaction due to the slight acidity of the solvent (pKa = 12.4).[155] Figure 4.29 shows the three stationary points involved in this pathway. **P2_min1$_{TFE}$** is the starting minimum where the two solvent molecules hydrogen-bond to the system. An interaction is present between the TFE molecule and the nitrogen of the pyrrolidine, where the hydrogen to nitrogen distance is 1.77 Å. Another interaction is present between the anionic TFE molecule and the hydrogen that is involved in the transition state.

In **P2_TS$_{TFE}$** the hydrogen to nitrogen bond distance has remained relatively the same at 1.75 Å, while the C-H distance has increased from 1.18 to 1.29 Å in **P2_min1$_{TFE}$** and **P2_TS$_{TFE}$** respectively. The distance between the hydrogen and oxygen has increased by 0.24 Å in the transition state showing that the C-H bond is breaking, while an O-H bond is being formed. During this the C-C and C-N(pyrr) distance remain unchanged.

In the resulting minimum, **P2_min2$_{TFE}$**, a new O-H bond is formed at 0.96 Å but the C-C distance remains the same due to the C-N(pyrr) distance only increasing marginally by 0.02 Å. While the C-H bond has been broken the pyrrolidine molecule is still attached. This can also be seen in the minimal change in the distance between the hydrogen and the nitrogen, which has only decreased by 0.03 Å while the O-H distance remains unchanged.

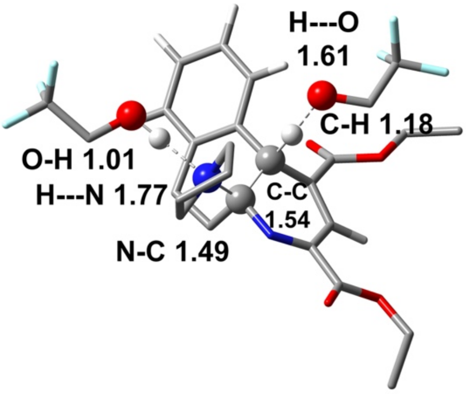

P2_min1$_{TFE}$

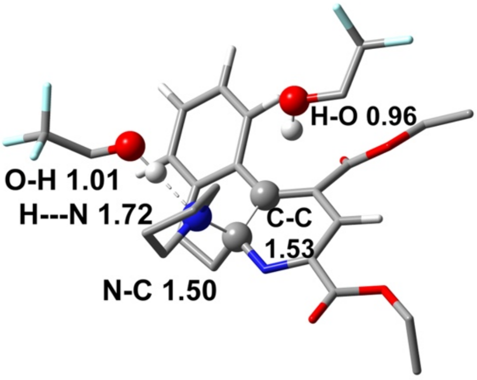

P2_min2$_{TFE}$

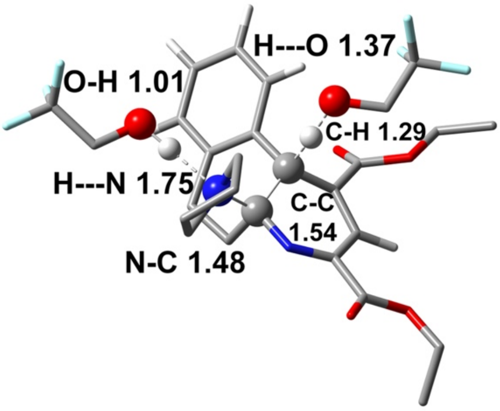

P2_TS$_{TFE}$

Figure 4.29- Structures for the stationary points **P2_min1$_{TFE}$**, **P2_min2$_{TFE}$**, and **P2_TS$_{TFE}$**. Selected distances are shown in Å. Blue = N, red = O, green = F, grey = C and white = H. Hydrogens have been emitted for the majority of the backbone for clarity.

Table 4.19 - Natural charges from NBO calculation for **P2$_{TFE}$** including a single HFIP molecule for selected atoms.

Atom	P2_min1$_{TFE}$	P2_TS$_{TFE}$	P2_min2$_{TFE}$
O1	-0.856	-0.810	-0.704
H2	0.384	0.408	0.510
C3	-0.425	-0.421	-0.085
C4	0.317	0.320	0.273
N5	-0.484	-0.485	-0.492
H6	0.522	0.522	0.520
O7	-0.724	-0.725	-0.739

The NBO natural charges show that **N5** becomes more negatively charged from **P2_min1** to **P2_min2** (-0.484 to -0.492) as the **C4**-**N5** bond is starting to weaken, which can be seen by the change in the Wiberg bond indices from Table 4.20 (0.63 to 0.62). Therefore, as the **H2**-**C3** bond is being broken the hydrogen-bond between pyrrolidine and HFIP is starting to strengthen. As with HFIP, **C3** becomes more positively charged and **C4** more negatively charged. Electron density is moving from the **H2-C3** bond to the **C3-C4** bond, which can be seen in the change in the Wiberg bond indices. The **H2-C3** bond breaks during the TS since the Wiberg bond index decreases to 0.01 from 0.64 going from **P2_min2$_{\mathbf{TFE}}$** to **P2_min1$_{\mathbf{TFE}}$**. Only a very small increase in the bond index is seen for **C3-C4** is seen of 0.02 going from min1 to min2 along with a small decrease in the **C4-C5** bond index (0.05). During **TS$_{\mathbf{11\text{-}12}}$** the C-N(pyrr) bond is therefore not fully broken.

Table 4.20 - Wiberg bond indices from NBO calculations for **P2$_{\mathbf{TFE}}$** including a single TFE molecule for selected atoms.

Bond	P2_min1$_{TFE}$	P2_TS$_{TFE}$	P2_min2$_{TFE}$
C3-C4	0.95	0.96	0.97
H2-C3	0.64	0.49	0.01
O1-H2	0.14	0.27	0.71
N5-H6	0.08	0.08	0.09
H6-O7	0.63	0.62	0.62
C4-N5	0.95	0.95	0.90

Second bond order perturbation theory shows a strong interaction of 151 kJ mol^{-1} between the lone pair orbital of **O1** into the anti-bonding orbital of **H2**-**C3** in **P2_min1**, which increases to 354 kJ mol^{-1} in the transition state. As with HFIP the CO_2Et groups show interactions that stabilise the system by 150-210 kJ mol^{-1}. Conjugation in **P2_min2** can be seen between N-C4-C3-C corresponding to 495 and 378 kJ mol^{-1}. An interaction is also present between **N5** of the pyrrolidine donating into the anti-bonding orbital of **H6**-**H7**. This interaction is 95 kJ mol^{-1} in **P2_min1**, which increases to 103 kJ mol^{-1} in the transition state, and finally to 112 kJ mol^{-1} in **P2_min2**.

4.4.1.12 Comparison of Pathway 2 for HFIP and TFE

The same trends for both solvents can be seen in these pathways. The distance between the solvent, acting as a base, and the hydrogen decreases as the reaction proceeds. The C-H bond is eventually broken and a new O-H bond is formed. The length of this hydrogen-bond was found to be longer in HFIP than in TFE by approximately 0.18 Å. In contrast, the length of the hydrogen-bond between the solvent and the nitrogen of pyrrolidine is shorter in HFIP than in TFE by 0.09 Å in **min1** and 0.14 Å in **min2**.

The same change in the charges is seen for all the atoms that were discussed, where **O1** and **H2** becomes more positively charged throughout this process, while **N5** and **H6** become more negatively charged. Both changes in combination with the change in bond lengths shows the presence of two hydrogen-bonds where the interaction is getting stronger.

Wiberg bond indices show that the **H2**-**C3** bond is broken while the **O1**-**H2** bond is formed. The **O1**-**H2** bond index in TFE was found to be larger than in HFIP suggesting a stronger bond, which is consistent with the shorter bond lengths seen in the three stationary points. Conversely, the bond index for **N5**-**H6** is higher in HFIP suggesting a stronger interaction, which was also seen in the shorter hydrogen-bond length.

Second bond order perturbation theory showed the presence of interactions that suggest hydrogen-bonding is occurring. The lone pair orbital on **O1** donates into the anti-bonding orbital of **H2**-**C3** during **P2_min1** and **P2_TS**. The interaction is much stronger with TFE than HFIP in **P2_min** by 100 kJ mol^{-1}, while in **P2_TS** the interaction with HFIP is stronger by 288 kJ mol^{-1}. In **min2** the hydrogen-bond between the solvent and the nitrogen of pyrrolidine is now much stronger in HFIP than TFE by 183 kJ mol^{-1}.

Both HFIP and TFE are therefore able to greatly stabilise the transition state and lower the barrier for pyrrolidine loss. The barrier for **P2_TS$_{\text{TFE}}$** is much lower than **P2_TS$_{\text{HFIP}}$**, which is likely because of the stronger interaction between TFE and the hydrogen. Even though TFE is not able to interact as strongly with pyrrolidine as HFIP, it is a better base, which lowers the barrier significantly compared to HFIP.

4.4.1.13 Pathway 5 – HFIP

In **P5**, HFIP$^-$ and pyrrolidine are involved in the reaction. HFIP$^-$ acts as the base while pyrrolidine stabilises the pyrrolidine that is being lost. During the transition state the C-H bond that is broken is elongated from 1.14 to 1.35 Å, while the distance between the oxygen of HFIP$^-$ and hydrogen is reduced from 1.78 to 1.30 Å as expected. The C-C distance is not altered during this step (1.55 to 1.54 Å from the minimum to the TS) and 1.53 Å in the product.

The explicit pyrrolidine hydrogen-bonding to the substrate pyrrolidine is also roughly the same in the minimum and TS (2.23 and 2.20 Å respectively), while the N-C distance of the substrate pyrrolidine is unchanged at 2.46 Å.

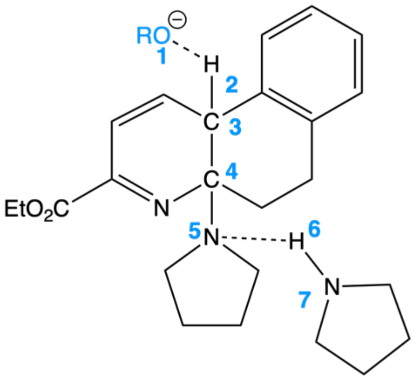

Figure 4.30 - Structure of **P5_TS** for HFIP (R = C{CF$_3$}$_2$H)and TFE (R = C{CF$_3$}{H}$_2$) on which NBO calculations were carried out. Numbers indicate atoms that were focused on and will be referred to as XN throughout (X=atom, N=number).

NBO analysis was carried out to investigate these stationary points further by looking into the strength of the hydrogen-bonding in the system along with the natural charges and Wiberg bond indices. Figure 4.30 shows the atoms that are key in **P5_TS** for both solvents along with the numbering scheme being used when referring to these atoms.

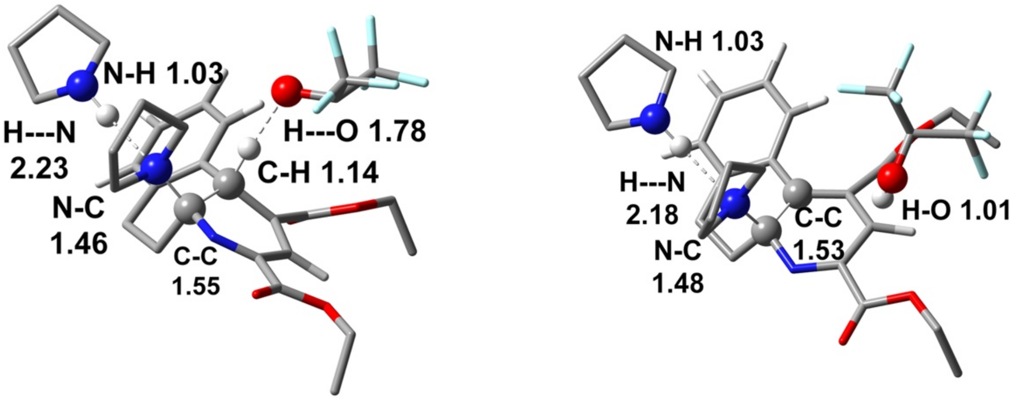

P5_min1$_{\text{HFIP}}$

P5_min2$_{\text{HFIP}}$

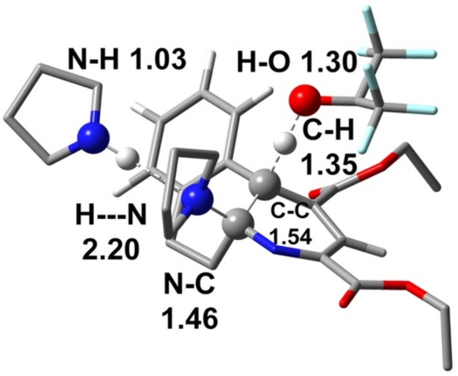

P5_TS$_{\text{HFIP}}$

Figure 4.31 - Structures for the stationary points **P5_min1$_{\text{HFIP}}$**, **P5_min2$_{\text{HFIP}}$**, and **P5_TS$_{\text{HFIP}}$**. Selected distances are shown in Å. Blue = N, red = O, green = F, grey = C and white = H. Hydrogens have been emitted for most of the backbone for clarity.

The natural charges of the key atoms involved changes as expected: **O1** becomes more positively charged as the hydrogen migration occurs, while **C3** becomes more negatively charged. This is also reflected in the Wiberg bond orders where a big increase is seen for the bond order between **O1** and **H2** (0.08 to 0.31 then 0.61 in **P5_min1**, **P5_TS$_{\text{HFIP}}$**, and **P5_min2** respectively) and **C3** and **H2** (0.71 to 0.43 then 0.01 in **P5_min1**, **P5_TS$_{\text{HFIP}}$**, and **P5_min2** respectively).

Table 4.21 - Natural charges from NBO calculation for **P5$_{HFIP}$** including a single HFIP molecule for selected atoms.

Atom	P5_min1$_{HFIP}$	P5_TS$_{HFIP}$	P5_min2$_{HFIP}$
O1	-0.860	-0.779	-0.712
H2	0.374	0.427	0.507
C3	-0.409	-0.419	-0.087
C4	0.303	0.310	0.265
N5	-0.465	-0.473	-0.475
H6	0.411	0.416	0.415
N7	-0.648	-0.650	-0.650

The second order perturbation theory showed a donation of a lone pair on oxygen into an anti-bonding orbital of the C-H bond, which stabilises the system by 70.7 kJ mol^{-1}. This interaction increases to 448.1 kJ mol^{-1} in the transition state and is no longer present in the product. Pyrrolidine allows hydrogen-bonding to occur and should stabilise the pyrrolidine leaving during this step. The lone pair on the nitrogen donates in the anti-bonding orbital of the N-H bond on the pyrrolidine, but only stabilises the molecule by 14.6 kJ mol^{-1} in the minimum, 16.7 kJ mol^{-1} in the TS and 19.2 kJ mol^{-1} in the product, showing this to be a much weaker hydrogen-bond than the interaction between HFIP$^-$ and the substrate.

Table 4.22 - Wiberg bond indices from NBO calculations for **P5$_{HFIP}$** including a single HFIP molecule for selected atoms.

Bond	P5_min1$_{HFIP}$	P5_TS$_{HFIP}$	P5_min2$_{HFIP}$
C3-C4	0.95	0.95	0.96
C4-N5	0.97	0.96	0.92
O1-H2	0.08	0.31	0.61
H2-C3	0.71	0.43	0.01
N5-H6	0.01	0.02	0.02
H6-N7	0.79	0.78	0.78

4.4.1.14 Pathway 5 – TFE

This pathway is the same as for HFIP but instead of HFIP$^-$ deprotonating TFE$^-$ is used instead. The C-H bond lengths from 1.1.17 to 1.30 Å while the O-H distance decreases from 1.66 to 1.36 Å. The C-C bond length remains unchanged (1.55 to 1.54 Å) along with the C-pyrr distance

(1.46 to 1.47 Å). The hydrogen-bond distance between pyrrolidine and the substrate is unchanged at 2.36 Å along with the N-H distance in pyrrolidine at 1.03 Å.

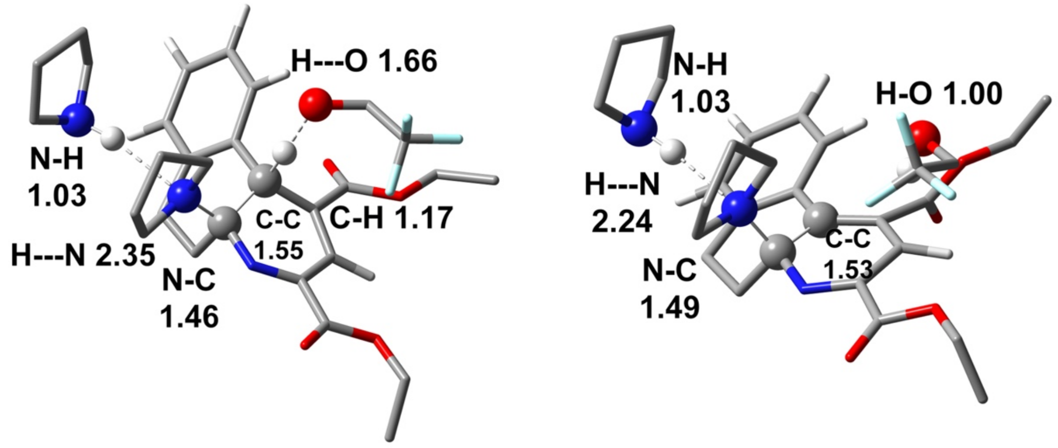

P5_min1$_{\mathrm{TFE}}$ **P5_min2**$_{\mathrm{TFE}}$

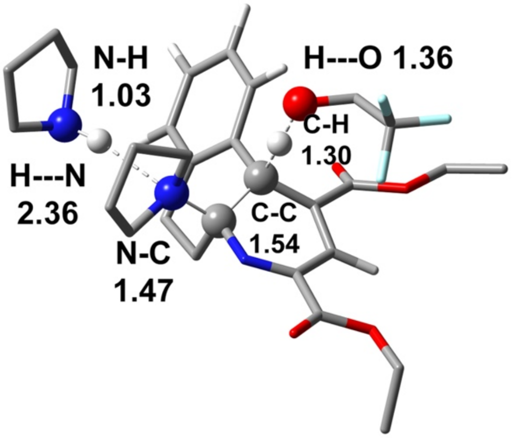

P5_TS$_{\mathrm{TFE}}$

Figure 4.32 - Structures for the stationary points **P5_min1**$_{\mathrm{TFE}}$, **P5_min2**$_{\mathrm{TFE}}$, and **P5_TS**$_{\mathrm{TFE}}$. Selected distances are shown in Å. Blue = N, red = O, green = F, grey = C and white = H. Hydrogens have been emitted for the majority of the backbone for clarity.

NBO analysis showed the oxygen of TFE$^-$ becoming more positively charged from **P5_min1**$_{\mathrm{TFE}}$ to **P5_min2**$_{\mathrm{TFE}}$ (-0.845 and -0.720 respectively).In turn the carbon of the substrate, **C3**, becoming more negatively charged changing from -0.421 to -0.0955 in **P5_min1**$_{\mathrm{TFE}}$ and **P5_min2**$_{\mathrm{TFE}}$ respectively. **H2** also becomes more positively charged, a change of 0.13 during the transition state. As before, **C4** becomes more negatively charged during this step of the reaction where the charge changes from 0.310 to 0.266. The Wiberg bond orders show that a bond is formed between **O1** and **H2** (0.13 in **P5_min1**$_{\mathrm{TFE}}$ and 0.65 in **P5_min2**$_{\mathrm{TFE}}$**).** At the same time the **H2-C3** bond is broken since the bond order decreases to 0.01 in **P5_min2**$_{\mathrm{TFE}}$ from 0.66 in **P5_min1**$_{\mathrm{TFE}}$. Small changes are also seen in the other bonds where the **C3-C4** bond is strengthened and the **C4-C5** bond is weakened.

Table 4.23 - Natural charges from NBO calculation for **P5$_{TFE}$** including a single TFE molecule for selected atoms.

Atom	P5_min1$_{TFE}$	P5_TS$_{TFE}$	P5_min2$_{TFE}$
O1	-0.845	-0.799	-0.720
H2	0.378	0.409	0.508
C3	-0.421	-0.418	-0.0955
C4	0.310	0.313	0.266
N5	-0.464	-0.467	-0.474
H6	0.399	0.401	0.406
N7	-0.635	-0.635	-0.639

Second order perturbation theory shows that the **O1-H2** hydrogen bond stabilises the system by 120.5 kJ mol^{-1} in **P5_min1$_{TFE}$** and by 371.1 kJ mol^{-1} in **P5_TS$_{TFE}$**. The **N5-H6** hydrogen bond stabilises the substrate by 10 kJ mol^{-1} in **P5_min1$_{TFE}$**, by 9.6 kJ mol^{-1} **in P5_$_{TSTFE}$** and by 16.7 kJ mol^{-1} in **P5_min2$_{TFE}$**. The smaller energies show that this hydrogen bond is weaker than that between **O1** and **H2**.

Table 4.24 - Wiberg bond indices from NBO calculations for **P5$_{TFE}$** including a single TFE molecule for selected atoms.

Bond	P5_min1$_{TFE}$	P5_TS$_{TFE}$	P5_min2$_{TFE}$
C3-C4	0.95	0.95	0.97
C4-N5	0.97	0.96	0.91
H2-C3	0.66	0.48	0.001
O1-H2	0.13	0.28	0.65
N5-H6	0.01	0.01	0.02
H6-N7	0.80	0.80	0.79

4.4.1.15 Comparison between HFIP and TFE – Pathway 5

The hydrogen bond between TFE and the substrate (**O1-H2**) is stronger than between HFIP and the substrate in **P5_min1** based on second order perturbation theory values (120.5 vs 70.7 kJ mol^{-1} respectively). This is expected since TFE is a stronger hydrogen bond “donor” than HFIP as HFIP is bulkier. During **P5_TS** the donation of the oxygen lone pair into the C-H bond is stronger for HFIP than TFE (448.1 vs 371.1 kJ mol^{-1}). This is also shown in the Wiberg bond indices, where the bond order between TFE and the substrate are higher in **P5_min1** with TFE than with HFIP (0.13 vs. 0.08 respectively) but during **P5_TS** this switches (0.28 vs. 0.31 for TFE and HFIP respectively). Pyrrolidine stabilises **P5_min1**, **P5_TS**, and **P5_min2** through hydrogen bonding by about 10-19 kJ mol^{-1} for both HFIP and TFE. This interaction occurs a long distance from the hydrogen migration, but could be greatly be effected if more solvent molecules were included and solvation of the whole molecule was computed.

4.4.1.16 Summary

The potential energy surface for the reaction between **1** and **3** was determined to understand why reaction in HFIP resulted in much higher yields compared to other solvents such as TFE and MeCN. The gas-phase PES for both the *endo* and *exo* orientation showed that two possible mechanisms for the Diels-Alder step of the reaction can occur, a concerted mechanism or a stepwise mechanism where the C-C bond is formed followed by the C-N bond. While both mechanisms proceed *via* relatively accessible barriers the stepwise mechanism is lower in energy for both the *endo* and *exo* orientation. The stepwise mechanism is therefore more likely to proceed, as was already predicted by Houk *et al.*[152]

Both the concerted and stepwise mechanisms converge *via* minimum **10**, which is followed by the loss of N_2, **TS$_{10\text{-}11}$**. This step of the reaction is highly exergonic and almost barrierless and results in **11**. The final step of the reaction is then loss of pyrrolidine *via* **TS$_{11\text{-}12}$** to give the final product **12**. Both the *endo* and *exo* orientation result in the same product when pyrrolidine is lost in **TS$_{11\text{-}12}$**. The gas-phase PES, while not providing insight into the solvent effects, shows that in the gas-phase the rate-determining step is **TS$_{11\text{-}12}$**, loss of pyrrolidine. The barrier for this reaction was determined to be 159 kJ mol^{-1} for the *endo* orientation.

With the gas-phase PES in hand, implicit solvent corrections were then applied to determine whether the difference between HFIP, TFE, and MeCN could be determined. While the PES did change (lower barrier for **TS$_{8\text{-}9}$**, higher barrier for **TS$_{9\text{-}10}$**, and a small decrease in the barrier for **TS$_{11\text{-}12}$**) nearly no differences were observed between the three implicit solvent corrections. The rate-determining step was still **TS$_{11\text{-}12}$** and this barrier was identical across all three solvents.

The addition of explicit solvent molecules of HFIP and TFE in the reaction was then attempted, which greatly changed the shape of the PES. **TS$_{8\text{-}9}$**, now differed by around 20 kJ mol^{-1}, with the pathway using HFIP being lower in energy. Minimal differences were observed for **TS$_{9\text{-}10}$** and **TS$_{10\text{-}11}$**. The loss of pyrrolidine was explored by investigating 15 different pathways, 11 of which were successfully optimised. **P2** and **P5** were found to significantly decrease the barrier for pyrrolidine loss to below 50 kJ mol^{-1} for HFIP and below 10 kJ mol^{-1} for TFE.

P2 involves two solvent molecules while **P5** utilises a pyrrolidine molecule along with a solvent molecule. Since no pyrrolidine is likely to be present at the start of the reaction it is proposed that the loss of pyrrolidine initially proceeds *via* **P2**. After the initial reaction process has equilibrised pyrrolidine is generated during **TS$_{11\text{-}12}$**, **P5** then becomes a feasible pathway.

TFE reduces the barrier for **TS$_{11\text{-}12}$** to a greater extent than HFIP even though the hydrogen bond that is formed between explicit solvent and the substrate is stronger with HFIP than TFE by 288 and 77 kJ mol^{-1} in **P2_TS** and **P5_TS** respectively. The low energy barrier for **TS$_{11-12}$** for both solvents now identifies that the rate-determining step of the reaction as **TS$_{8\text{-}9}$**, the C-C bond formation step of the Diels-Alder reaction. The barrier for **TS$_{8\text{-}9}$** was lower for explicit HFIP and for explicit TFE. The yields of the reaction, when carried out in HFIP, are therefore higher since the rate-determining step has a lower barrier than when the reaction is carried out in TFE.

The low yield with MeCN as the solvent medium can also be understood from these results. As MeCN is incapable of hydrogen bonding the low energy pathways **P2** and **P5** cannot be accessed. For the reaction to occur only the higher energy pathways for the loss of pyrrolidine during **TS$_{11\text{-}12}$** are accessed, which results in significantly lower yields.

4.4.2 Triazine and Enamine Reaction

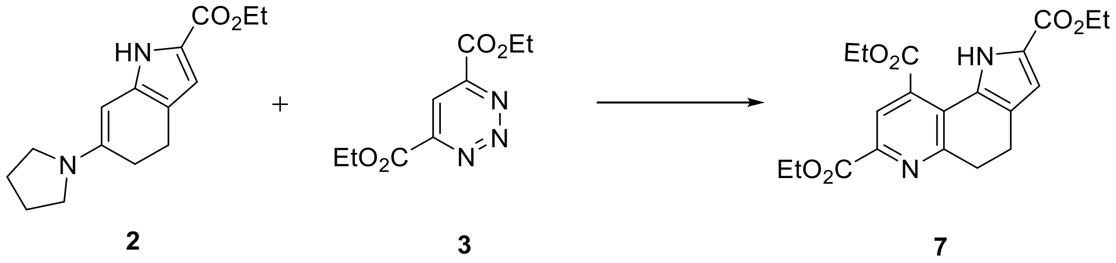

Scheme 4.6 - Reaction between enamine **2** and triazine **3** to give the product **7** was investigated to determine the effect of HFIP and TFE.

For the reaction shown in Scheme 4.6 only gas-phase and implicit solvation calculations were carried out in full. Enamine **2** has more conformational isomers than **8** due to the ester group, which could make it more difficult to study computationally. Changes in the orientation of the ester group leads to a difference in the stability of the enamine and in turn can affect the relative energy of stationary points.

The mechanism for the reaction between **2** and **3** was thought to not greatly differ from the reaction between **8** and **3**. It was thought that it was still worth investigating this reaction to determine the impact that the enamine has on the PES and the reactivity.

4.4.2.1 Gas-phase results

As with the first reaction between **3** and **8**, both a concerted and stepwise mechanism were computed. The potential energy surface for these two pathways for the *endo* orientation can be seen in Figure 4.33. The concerted pathway proceeds *via* one barrier, ***endo*_TS$_{2\text{-}5}$**, at 123 kJ mol^{-1} to give the intermediate ***endo*_5**. The free energy barriers for the stepwise mechanism are 121 and 8 kJ mol^{-1} for ***endo*_TS$_{2\text{-}4}$** and ***endo*_TS$_{4\text{-}5}$** respectively. For this reaction the stepwise mechanism is only 2 kJ mol^{-1} lower in energy than the concerted mechanism, therefore, both mechanisms would be competitive for this reaction.

During ***endo*_TS$_{5\text{-}6}$** N_2 is released and is a barrierless process (1 kJ mol^{-1}) giving ***endo*_6**,which lies 222 kJ mol^{-1} below the starting material. The final step of the reaction is the loss of pyrrolidine in ***endo*_TS$_{6\text{-}7}$**, which proceeds *via* a barrier of 150 kJ mol^{-1}. ***endo*_TS$_{6\text{-}7}$** has the largest barrier and based on the gas-phase results would be the rate-determining step of the reaction.

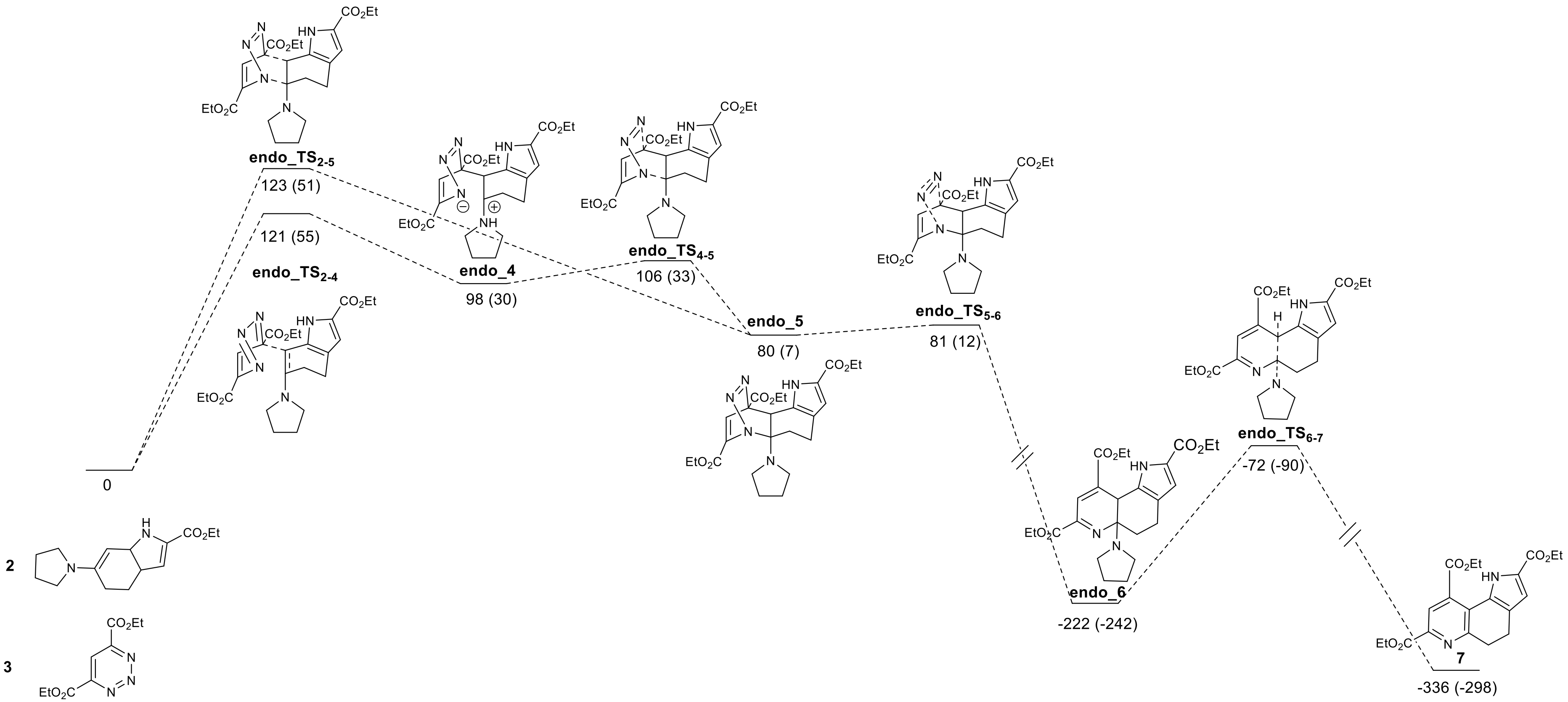

Figure 4.33 - PES for the reaction between **2** and **3** for the concerted and stepwise pathways for the endo orientation in the gas-phase. Relative Gibbs energies (and enthalpies in brackets) are shown in kJ mol^{-1} at the (RI)-PBE0-D3BJ/def2-TZVPP//(RI)-PBE0/def2-SV(P) level.

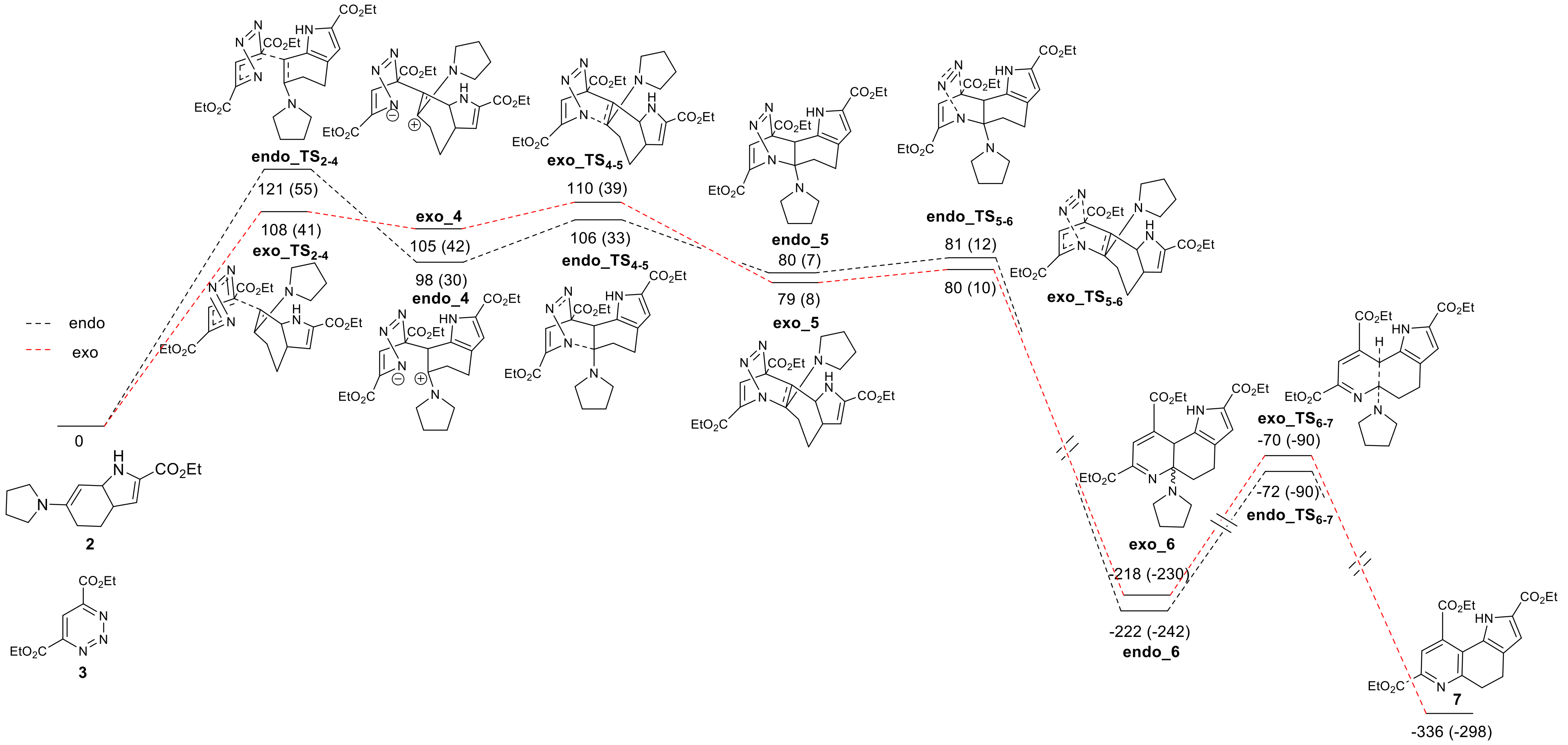

Figure 4.34 - PES for the reaction between **2** and **3** for the stepwise pathways for the *endo* and *exo* orientations in the gas-phase. Relative Gibbs energies (and enthalpies in brackets) are shown in kJ mol^{-1} at the (RI)-PBE0-D3BJ/def2-TZVPP//(RI)-PBE0/def2-SV(P) level.

Figure 4.34 shows the stepwise mechanism for the *endo* and *exo* orientation. While it was found that the concerted pathway would also be competitive for both orientations the focus was on the stepwise pathway to be able to compare the results to the previous reaction. Only minor energy differences are seen between the two conformers with the largest difference seen in **TS$_{2-4}$** where **exo_TS$_{2-4}$** is 18 kJ mol^{-1} lower in energy than ***endo*_TS$_{2-4}$**. In general, the energy difference is only approximately 4 kJ mol^{-1} indicating very little difference in the two orientations. Since the same product is formed from both orientations this has no impact on the observed yield.

As with the first reaction the loss of pyrrolidine during **TS$_{6-7}$** is rate-determining for both the *endo* and *exo* orientations, proceeding *via* a barrier of 150 and 148 kJ mol^{-1} respectively. The gas-phase calculations provide a starting point for determining the reason for the observed solvent effects. This reaction is likely to proceed *via* both the concerted and stepwise Diels-Alder reaction unlike the first reaction, which has much lower barriers for the stepwise mechanism. For both reactions the energy difference between the *endo* and *exo* stationary points was minimal suggesting that both orientations would occur in the reactions.

4.4.2.2 Implicit Solvation

As with the previous reaction a variety of different solvents were investigated but the focus was on HFIP, TFE, and MeCN. Table 4.25 shows the free energy barriers for the concerted *endo* pathway in the gas-phase and with implicit solvent corrections for MeCN, HFIP, and TFE. The barrier for ***endo*_TS$_{2-5}$** was decreased through the solvent corrections for all three pathways. MeCN and HFIP stabilised the transition state structure by 9 kJ mol^{-1} while TFE showed a greater stabilisation of 25 kJ mol^{-1}. The barrier for ***endo*_TS$_{5-6}$** was found to be slightly higher at 4-5 kJ mol^{-1}, but still classed as a barrierless process. The loss of pyrrolidine during ***endo*_TS$_{6-7}$** decreased by approximately 20 kJ mol^{-1} for all three solvents.

Table 4.25 - Relative enthalpies for the concerted *endo* pathway for the reaction between **2** and **3** in the gas-phase and with implicit solvent corrections in MeCN, HFIP, and TFE.

	Gas-phase (kJ mol^{-1})	MeCN (kJ mol^{-1})	HFIP (kJ mol^{-1})	TFE (kJ mol^{-1})
***endo*_TS$_{2-5}$**	123	114	114	98
***endo*_TS$_{5-6}$**	1	4	4	5
***endo*_TS$_{6-7}$**	153	132	133	131

For the concerted mechanism the rate-determining step was pyrrolidine loss even though the barrier was reduced through the inclusion of solvent corrections. For the stepwise pathway the barrier for ***endo*_TS$_{2\text{-}4}$** was stabilised to the same extent as ***endo*_TS$_{2\text{-}5}$**, lowering the barrier to a greater extent for TFE (see Table 4.26). The barrier for ***endo*_TS$_{4\text{-}5}$** was found to increase in energy with the inclusion of implicit solvent corrections. The barrier increased by about 16 kJ mol^{-1} for all three solvents. As with the first reaction this is because the intermediate, ***endo*_4**, is stabilised to a greater extent than ***endo*_TS$_{4\text{-}5}$**, thereby increasing the barrier.

Table 4.26 - Relative enthalpies for the stepwise *endo* pathway for the reaction between **2** and **3** in the gas-phase and with implicit solvent corrections in MeCN, HFIP, and TFE.

	Gas-phase (kJ mol^{-1})	MeCN (kJ mol^{-1})	HFIP (kJ mol^{-1})	TFE (kJ mol^{-1})
***endo*_TS$_{2\text{-}4}$**	121	111	112	95
***endo*_TS$_{4\text{-}5}$**	8	24	23	24
***endo*_TS$_{5\text{-}6}$**	1	4	4	5
***endo*_TS$_{6\text{-}7}$**	153	132	133	131

While the implicit solvent corrections do have an impact on the barriers compared to the gas-phase results no major difference can be seen between MeCN, HFIP, and TFE that would explain the observed solvent effects. While the barrier for both ***endo*_TS$_{2\text{-}5}$** and ***endo*_TS$_{2\text{-}4}$** were lower in energy in TFE compared to MeCN and HFIP this step is not rate-determining and therefore does not explain the difference in reactivity.

4.4.2.3 Summary

Implicit solvent corrections help to lower the energy of stationary points, such as **TS$_{2\text{-}4}$**, **TS$_{2\text{-}5}$**, and **4**, by stabilising the charge imbalance that is present in these states. This in turn lowers the barrier for both **TS$_{2\text{-}4}$**and **TS$_{2\text{-}5}$**, but increases the barrier for **TS$_{4\text{-}5}$** due to a greater stabilisation of **4** compared to the transition state. The addition of these corrections, therefore, does start to show some of the impact of the solvent used, however, MeCN is a polar aprotic solvent and therefore should not stabilise the stationary points to the same extent as a polar protic solvent such as HFIP does.

The rate-determining step of the reaction is still the loss of pyrrolidine during **TS$_{6\text{-}7}$**, which is inconsistent with what Glinkermann and co-workers have predicted.[151] While it could be the rate-determining step of the reaction, it is likely that just as with the reaction involving **8** and **3**, the solvent needs to be included explicitly. Inclusion of explicit solvent along with the implicit solvent corrections would allow for direct hydrogen-bonding, which would stabilise the transition states **TS$_{2\text{-}4}$** and **TS$_{4\text{-}5}$** but also the zwitterionic intermediate **4**. It would also allow for alternative pathways for the loss of pyrrolidine during **TS$_{6\text{-}7}$**.

4.4.2.4 Combining Explicit and Implicit Solvation Models

The results for the previous reaction were used to determine what the likely key states were going to be for this reaction. The effect of both HFIP and TFE being included explicitly in the calculations was carried out for **TS$_{2\text{-}4}$** and **TS$_{6\text{-}7}$** *via* **P2**. Only **P2** was chosen to be investigated for this reaction as this pathway is more strongly dependent on the solvent than **P5**.

Table 4.27 – Free energy barriers for **TS$_{2\text{-}4}$** and **TS$_{6\text{-}7}$** for the reaction between **2** and **3** in the gas-phase, with HFIP implicit solvent correction with no explicit solvent, and in HFIP with two explicit HFIP molecules.

HFIP	Gas-phase – endo (kJ mol^{-1})	Imp. HFIP – endo (kJ mol^{-1})	Imp./Exp. HFIP – endo (kJ mol^{-1})
TS$_{2\text{-}4}$	121	112	106
TS$_{6\text{-}7}$	150	133	24

Table 4.27 shows the barriers for **TS$_{2\text{-}4}$** and **TS$_{6\text{-}7}$** in the gas-phase, with implicit HFIP, and the combined explicit/implicit method used in the reaction between **8** and **3**. The barrier for the Diels-Alder step of the reaction, **TS$_{2\text{-}4}$,** was not significantly altered through the inclusion of explicit HFIP. A decrease of only 6 kJ mol^{-1} to 106 kJ mol^{-1} was seen. As with the reaction between **8** and **3**, the inclusion of explicit HFIP significantly decreased the barrier for **TS$_{6\text{-}7}$** from 133 to 24 kJ mol^{-1} for the implicit and explicit/implicit results respectively. This large decrease in the free energy, 109 kJ mol^{-1}, now makes the Diels-Alder step, **TS$_{2\text{-}4}$,** the rate-determining step of the reaction.

Table 4.28 – Free energy barriers for **TS$_{2\text{-}4}$** and **TS$_{6\text{-}7}$** for the reaction between **2** and **3** in the gas-phase, with TFE implicit correction solvent, TFE with no explicit solvent, and in TFE with two explicit TFE molecules.

TFE	Gas-phase – endo (kJ mol^{-1})	Imp. TFE – endo (kJ mol^{-1})	Imp./Exp. TFE – endo (kJ mol^{-1})
TS$_{2\text{-}4}$	121	95	120
TS$_{6\text{-}7}$	150	132	15

Table 4.28 shows the barriers for **TS$_{2\text{-}4}$** and **TS$_{6\text{-}7}$** in the gas-phase, with implicit TFE, and the combined explicit/implicit method. Unlike with HFIP, an increase in the barrier for **TS$_{2\text{-}4}$** is computed of 25 kJ mol^{-1} when an implicit/explicit method is used. The barrier for **TS$_{6\text{-}7}$** is also significantly lowered with the inclusion of explicit TFE molecules, reducing the barrier by 117 kJ mol^{-1}.

4.4.2.5 Summary

As with the reaction between **8** and **3**, the inclusion of explicit solvent molecules in the computational model, is crucial to understand the role that the solvent plays in this reaction. HFIP results in higher yields as it stabilises **TS$_{2-4}$** to a greater extent than TFE. The barrier for **TS$_{2-4}$** is comparable in the two solvents as it only differs by 14 kJ mol^{-1}. The yield in HFIP for this reaction was 41 % compared to 36 % in TFE. The small difference in yield is not explained by this small energy difference but it does indicate that HFIP interacts with the substrate differently and enough to proceed *via* a lower energy barrier than TFE.

Explicit solvent molecules are especially important for the loss of pyrrolidine step, **TS$_{6-7}$**. The gas-phase and implicit solvation results indicate that this is the rate-determining step of the reaction as it proceeds *via* barrier that is higher than 100 kJ mol^{-1} for both orientations and in both solvents. The addition of two solvent molecules, as in **P2**, decreased the barrier of **TS$_{6-7}$** in HFIP to 24 kJ mol^{-1} and just 15 kJ mol^{-1} in TFE. This reduction in the barrier for **TS$_{6-7}$** changes the rate-determining step to the Diels-Alder step, **TS$_{2-4}$**, of the reaction, which is consistent with the hypothesis stated by Glinkerman and co-workers.[151] Explicit solvent molecules with implicit solvent corrections are therefore needed to understand the solvent effects seen in the reaction between **2** and **3**.

The addition of explicit solvent molecules is crucial for determining the rate-determining step and understanding the difference in yield when HFIP and TFE are used as the solvent. More significantly, the explicit solvent molecules show that without the presence of a solvent that can act as a catalyst, the reaction does not proceed with high yields. The barrier for the loss of pyrrolidine during **TS$_{6-7}$** is significantly reduced in the presence of HFIP and TFE. When MeCN is used as the solvent some reactivity is seen but results in very low yields. The low yields are because MeCN is not able to hydrogen-bond and thereby catalyse the reaction like HFIP and TFE. Only the higher energy pathways are therefore accessible for MeCN.

4.5 Conclusions and Future Work

Glinkerman and co-workers determined a method for synthesising methoxatin using an inverse electron demand Diels-Alder reaction. A variety of enamines were tested but for each reaction the authors noticed a strong solvent effect. HFIP resulted in the greatest reactivity while a related solvent, TFE, was found not to be as effective. Solvents such as MeCN, ^{i}PrOH, and EtOH showed no reactivity at all. The authors hypothesised that the solvent was needed to stabilise the Diels-Alder reaction, but also to facilitate the loss of pyrrolidine later in the reaction.

This investigation into the mechanism of two of the original reactions aimed to understand the nature of these solvent effects and to test these predictions made by the authors. The reaction between the much simpler enamine, **8**, was studied first focusing on HFIP, TFE, and MeCN solvents. Work carried out by Houk *et al.* was drawn upon as they had shown that a stepwise mechanism for the Diels-Alder reaction was energetically favourable, which was also found here. The authors had concluded that the formation of the C-C bond during the Diels-Alder reaction was rate-determining, but both the gas-phase and implicit results shown here identify that it is the loss of pyrrolidine, $\mathbf{TS_{11\text{-}12}}$, which is rate-determining for both the *endo* and *exo* orientation.

While the implicit solvation corrections changed the potential energy surface through stabilising $\mathbf{TS_{8\text{-}9}}$ and **9**, and destabilising $\mathbf{TS_{9\text{-}10}}$, which more accurately reflects the reaction environment, no difference between the three solvents was found. HFIP, TFE, and MeCN stabilised and destabilised the same states to roughly the same extent. The rate-determining step remained unchanged, even though the barrier was reduced slightly. As the energy differences between the *endo* and *exo* orientation were almost identical for both the gas-phase and implicit solvation corrections, only the *endo* orientation was considered further.

Explicit HFIP and TFE molecules were then used to try and determine if these would explain why there was a different outcome with these solvents. First the effect of HFIP and TFE were investigated for $\mathbf{TS_{8\text{-}9}}$, **9**, $\mathbf{TS_{9\text{-}10}}$, **10**, and $\mathbf{TS_{10\text{-}11}}$. The same trends were seen here as for the inclusion of implicit solvent corrections, but to a greater extent. The barrier for $\mathbf{TS_{8\text{-}9}}$ was reduced due to the transition state being stabilised through hydrogen-bonding to the solvent. HFIP formed a much stronger hydrogen-bond to the substrate than TFE and stabilised the transition state to a greater extent. Thus, the barrier for $\mathbf{hfip\_TS_{8\text{-}9}}$ was lower than for $\mathbf{tfe\_TS_{8\text{-}9}}$. $\mathbf{TS_{9\text{-}10}}$ was destabilised with the addition of explicit solvent molecules due to **9** being greatly stabilised through hydrogen-bonding. The barrier for $\mathbf{TS_{10\text{-}11}}$ remained virtually unchanged, as with the implicit solvent correction.

15 different pathways were investigated for **TS$_{11\text{-}12}$** and it was found that **P2** and **P5** were the lowest energy pathways. **P2** involved two HFIP molecules while **P5** utilised an HFIP molecule with a pyrrolidine molecule. While the barrier for **P5** was found to be lower than **P2**, both pathways are likely to occur during the reaction. At the start no pyrrolidine would be presented in the reaction meaning only **P2** would be accessible. After pyrrolidine is released as a by-product, **P5** becomes an accessible pathway. It was found that **P2** and **P5** with TFE proceeded *via* lower barriers than HFIP due to stronger hydrogen-bonds. The inclusion of explicit solvent molecules greatly reduced the barrier for pyrrolidine loss, to the extent that the rate-determining step was found to now be **TS$_{8\text{-}9}$**.

With **TS$_{8\text{-}9}$** now being the rate-determining step of the reaction the difference in reactivity between HFIP and TFE can be understood. HFIP stabilises the rate-determining step to a greater extent than TFE, lowering the barrier for the reaction significantly. The barrier for TFE is also reduced and is accessible, which explains why reactivity was observed in TFE. As MeCN cannot hydrogen-bond only high energy pathways for **TS$_{11\text{-}12}$** are available in this solvent. The rate-determining step therefore remains **TS$_{11\text{-}12}$** for MeCN and the large barrier for this step means that little to no reactivity is seen. The solvent is therefore key as a catalyst and is needed in the reaction to aid in the loss of pyrrolidine.

With the knowledge of the two key steps of the reaction, **TS$_{8\text{-}9}$** and **TS$_{11\text{-}12}$**, the findings were applied to a reaction with a more complex enamine, **2**. The gas-phase and implicit solvent corrected results showed the same trends as the model reaction. The stepwise pathway was once again favourable and very little difference was seen in the *endo* and *exo* orientation for this reaction. The implicit solvent corrections helped stabilise **TS$_{2\text{-}4}$** and **4** while destabilising **TS$_{4\text{-}5}$**, but no difference between HFIP, TFE, and MeCN was noted. For the gas-phase and all three solvents **TS$_{6\text{-}7}$** was still the rate-determining step.

The addition of explicit HFIP and TFE molecules in **TS2$_{2\text{-}4}$**, **4**, **TS$_{4\text{-}5}$**, **5**, and **TS$_{5\text{-}6}$** showed a further decrease in the barrier of **TS$_{2\text{-}4}$** while the barrier for **TS$_{4\text{-}5}$** increased slightly. **P2** was computed for this reaction and showed a significant decrease in the barrier for **TS$_{6\text{-}7}$**. In HFIP the barrier was reduced to 24 kJ mol^{-1} while in TFE the barrier was reduced even further to 15 kJ mol^{-1}. Once again, this significant reduction makes the Diels-Alder step of the reaction, **TS$_{6\text{-}7}$**, rate-determining.

The solvent, therefore, plays a crucial role in this reaction by stabilising the rate-determining step, C-C formation, but also takes a more active role by facilitating the loss of pyrrolidine later in the reaction. The solvent acts as catalyst in **P2** and **P5**, providing a lower energy pathway, and results in higher yields. A solvent that can hydrogen-bond, but also acts as a base, is therefore required for this reaction to be successful. The results suggest that HFIP stabilises the Diels-Alder step to a greater extent by forming a stronger hydrogen-bond with the substrate. TFE, however, was found to form a stronger hydrogen-bond during the loss of pyrrolidine as it is a smaller solvent and is therefore not as greatly affected by the steric bulk present in this step. Reactivity could theoretically be improved further by using a solvent that forms strong hydrogen-bonds to the starting material but is smaller than HFIP, so that the loss of pyrrolidine step is not negatively impacted. Solvents such as MeOH and EtOH have high dielectric constants and can hydrogen-bond, while also being small in size. However, these solvents showed no reactivity even though they can hydrogen-bond like HFIP and TFE. It is likely that these solvents are too nucleophilic, but these solvents were not investigated in this study. The effect of these two solvents could be tested by first looking at their effect on the C-C bond formation step of the reaction, **TS_{8-9}** and **TS_{2-4}**. The loss of pyrrolidine can then be investigated if answers are not found in this first step.

The loss of pyrrolidine has been presented as a single step process here but it likely to involve two steps: 1) breaking the C-H bond followed by 2) breaking the C-N(pyrr) bond. DRC calculations and optimization of the end points did not conclusively show that the C-N(pyrr) bond is broken at the end of **TS_{11-12}** and **TS_{6-7}**. Calculations have already been undertaken to determine whether a one-step or two-step process is more likely. Preliminary data suggests that for some pathways a two-step process could be feasible and is potentially even preferable. Further work to confirm the connectivity from **TS_{11-12}** to **12** and **TS_{6-7}** to **7** still needs to be investigated.

5. Conclusions

The role of a solvent in a reaction can vary greatly. The solvent can be a reaction medium, stabilise charged reactants, intermediates or products, hydrogen bond to stabilise the species present, or aid in the reactivity by actively taking part in the reaction. Within computational chemistry studying a reaction done in the gas phase is simple. The reactants, intermediates, and products can all be optimised by considering the general methodology needed i.e. *ab-initio* methods, empirical methods, DFT functionals, basis sets, etc. Since no solvent is present no computational resources are needed to account for it.

When computationally studying a reaction that occurs in a solvent extra thought does need to be given to how to account for it. Quite often a simple implicit solvent correction such as COSMO can be applied and does an excellent job of modelling the effect of the solvent. When it is known that a solvent effect is present in the reaction much more care needs to be given to model the reaction accurately. QM/MM methodologies have been employed but present a challenge due to the time required to set up the system, along with the difficulty in accurately modelling solvents.

A hybrid method can be applied where some explicit solvent molecules are included in combination with an implicit solvent correction. A hybrid approach allows for including solvent molecules in very specific locations where it is thought that hydrogen bonding is important or where charge is likely to build up, which can be stabilised by the solvent. This approach does require more time and effort than just using an implicit solvent correction, but it provides better results in less time than QM/MM calculations.

This general approach when studying a reaction computationally is therefore to start with studying the reaction in the gas-phase first. Results are obtained quickly and provide a better understanding of the reaction. After this, an implicit solvent correction can be applied if the reaction is carried out in solution. A more intense approach using explicit solvent molecules can be used for systems where strong solvent effects are observed that are not explained with an implicit model. This approach was used here by first calculating gas-phase structures, followed by the addition of an implicit model, and finally an explicit model was used by adding solvent molecules to strategic areas.

The first system studied the reaction mechanism involved with the abstraction of a hydrogen atom from an imidazolium ion, $[bmim]^+$, using a high energy F atom beam. Since the surface of the ionic liquid was being studied it was decided that no solvent corrections would be needed. Abstraction from the ring, the methyl group, and the butyl group were determined and showed that abstraction from the ring required the most energy. The high free energy barriers for the ring carbons, approximately 80 kJ mol^{-1}, arose because the transition state is destabilised due to the formation of a radical on a carbon that is already part of a positively charged ring. The barriers for the abstraction of a hydrogen from the alkyl carbons follow the typical trend for radical stability where the barrier at tertiary carbons proceeds *via* the lowest barrier (**C6** and **C7** with a barrier of 39 and 35 kJ mol^{-1}) and primary carbons *via* the highest (**C1** with a barrier of 50 kJ mol^{-1}).

An alternative stepwise mechanism for abstraction of a hydrogen from the ring carbons was determined for a simplified imidazolium, [mmim]$^+$, but this process was found to be higher in energy than the direct abstraction. The large barrier occurs due to the formation of a stable fluorinated intermediate, **ring_min_CF**. While a transition state for the alternative ring abstraction mechanism was not determined for [bmim]$^+$, the [mmim]$^+$ results suggest that the alternative ring abstraction mechanism would be accessible with an approximate barrier of 253 and 220 kJ mol^{-1} for abstraction at **C2** and **C3** respectively. Given the large amount of energy present in the F atom beam, 384 kJ mol^{-1}, abstraction at all positions on the imidazolium would be possible even if the stable fluorinated intermediate, **ring_min_CF**, was formed.

Previous computational work studying the surface of [bmim]$^+$ for the abstraction by a fluorine atom beam suggested that the surface was almost entirely composed of the butyl chain of the ionic liquid. Abstraction at any of the positions on the butyl chain would be possible due to the high energy of the F atom beam. If a small fraction of the surface contained the ring or methyl group, these could also be abstracted by the beam. This was already proposed in previous studies, but this work shows that the barriers for hydrogen abstraction are significantly lower than the energy of the F atom beam. Using gas-phase calculations it was possible to determine this quantitatively. Accurate results were obtained with these gas-phase calculations because no solvent medium was used in the reaction that needed to be modelled computationally.

In the second system a phosphoramidation reaction was studied that utilised an Ir(III) complex containing a hemilabile bidentate 1,2-N,O-phosphoramidate ligand. Only the O-phosphoramidate product was formed, even though the N-phosphoramidate product was thought to be favourable since the strong P=O bond is retained. Questions regarding the regio- and stereoselectivity of the reaction were raised and answered by modelling the reaction using COSMO to simulate the role of the solvent, CH_2Cl_2. A solvent model was used for this system since interactions between the substrate and the CH_2Cl_2 solvent molecules needed to be investigated.

Oxidative addition and a 1,2-hydride shift pathway were determined along with three LAPS pathways: N-protonation, O-protonation, and Cp*-protonation. Oxidative addition and Cp*-protonation were found to proceed *via* larger barriers (96 and 264 kJ mol^{-1}) compared to the other mechanisms and were therefore determined not to be competitive. The O-protonation pathway proceeded *via* the lowest barriers and due to the hemilability of the phosphoramidate ligand and the low energy rotation of the vinylidene in **4c** the thermodynamic product, **5b_E**, could be formed. The N-product was found to not be formed due to the high energy barrier of **TS_{3b5b}**, 149 kJ mol^{-1}, and the high energy of the intermediate **4b** at 121 kJ mol^{-1}. The 1,2-hydride shift pathway lead to **4c** *via* a barrier of 76 kJ mol^{-1}, which would then proceed to the O-product and thus provide an alternative pathway.

No explicit solvent effects were present in this reaction. CH_2Cl_2 is a polar aprotic solvent and would thereby impact the reaction by stabilising and destabilising charged and neutral species respectively. Robust experimental data allowed for comparison of the final product to the computational structure to determine that the addition of a polarisable continuum model solvent correction was sufficient at approximating the reaction conditions. This can be seen in the bond lengths obtained of **5a_E** at the (RI)-PBE0-D3BJ/def2-TZVPP//(RI)-BP86/def2-SV(P) level when compared to the bond lengths obtained from the crystal structure of [**2**][BAr^F_4]. The calculated bond lengths varied by less than 0.03 Å, even for the vinylidene and the phosphoramidate ligand, which are part of the reaction centre. Therefore, the addition of explicit solvent molecules is unlikely to greatly increase the accuracy of the results, but the methodology would greatly increase the computational cost in terms of resources and time.

The hypothesis proposed by the authors that the reaction proceeds *via* a LAPS mechanism were confirmed through this investigation. Furthermore, the reason for the absence of the N-phosphoramidate product was determined along with why the thermodynamically stable **5b_E** isomer is the sole product formed in the reaction.

Finally, two inverse electron demand diels-alder reactions were modelled that had been used during the synthesis of methoxatin that showed strong dependencies on the solvent used. A stepwise mechanism was found to be lower in energy by 34 kJ mol^{-1} than the traditional concerted mechanism, which was in agreement with the previous study by Houk *et al.*[152] Gas-phase calculations provided insight into the reaction overall. Implicit solvent corrections were next applied using COSMO. For all three solvents studied the inclusion of an implicit correction reduced the barrier of **$TS_{8\text{-}10}$** by 25, 23, and 34 kJ mol^{-1} for MeCN, HFIP, and TFE respectively. A small increase by 1-2 kJ mol^{-1} occurred for **$TS_{10\text{-}11}$**, while for **$TS_{11\text{-}12}$** a decrease of 17-18 kJ mol^{-1} was observed. While changes in the PES were observed with an implicit solvent model, they were not able to account for the solvent effects seen in the reaction. HFIP and TFE are both polar protic solvents and are therefore able to hydrogen bond to the reactants, which cannot be accounted for by an implicit solvent model. A hybrid implicit-explicit model was therefore used by including explicit solvent molecules in strategic positions. The previous work by Houk *et al.* was utilised when determining the position of the solvent molecules.[152]

HFIP and TFE were investigated due to their ability to hydrogen bond and because the largest yields were obtained with these solvents. It was determined that through the addition of two solvent molecules differences between HFIP and TFE could now be seen. Both solvents were able to hydrogen bond to the structures and thus lower the barriers for the reaction. HFIP was found to lower the energy of the rate-determining step, **TS$_{8-9}$**, to a greater extent than TFE, 30 kJ mol^{-1} vs. 15-20 kJ mol^{-1} respectively, which agreed with the experimental results. A yield of 86 % was achieved for the reaction between **3** and **8** when carried out in HFIP compared to 34 % in TFE.

The crucial step when modelling this reaction was found to be the loss of pyrrolidine during **TS$_{11-12}$**. This step was found to proceed *via* the largest barrier when no solvent was accounted for explicitly, 150-160 kJ mol^{-1} for both reactions. Only through the addition of two solvent molecules during this step were the barriers significantly lowered. Pathways involving pyrrolidine were also determined, since these become accessible as the reaction proceeds and pyrrolidine is released. TFE was found to lower the barrier of **TS$_{11-12}$** to a greater extent than HFIP because of its smaller size. The barriers in TFE were found to be virtually barrierless at 6 kJ mol^{-1}, while in HFIP they varied between 25-48 kJ mol^{-1}.

The key to understanding the solvent effects present in this reaction is role that the solvent plays in both **TS$_{8-9}$** and **TS$_{11-12}$**. Without a solvent that can lower the barrier for **TS$_{11-12}$**, this becomes the rate-determining step and due to the large barrier the reaction cannot occur. This is why no reactivity was observed in MeCN for the reaction between **3** and **5**. MeCN is a polar aprotic solvent and cannot stabilise **TS$_{11-12}$** through hydrogen bonding. Solvents such as HFIP and TFE that can hydrogen bond aid in the loss of pyrrolidine and consequently **TS$_{8-9}$** becomes the rate-determining step. Since HFIP is able to stabilise **TS$_{8-9}$** to a greater degree than TFE, the yield is higher.

Three very different systems were studied, and the approach needed was adapted to fit the system. Starting with gas-phase calculations provides a simplified view of the reaction and comparison with experimental data allows us to determine whether a more demanding methodology is needed. The abstraction of hydrogen by an F atom beam was carried out without a solvent medium and therefore gas phase calculations were able to model the reaction system effectively. The phosphoramidation reaction was carried out in CH_2Cl_2 and an implicit solvent model was utilised to model the effect of the polar aprotic solvent. Comparison between experimentally and computationally determined bond lengths showed these to vary by less than 0.03 Å, confirming that an implicit model is sufficient for this system. Finally, the diels-alder reactions showed increased reactivity when carried out in polar protic solvents such as HFIP and TFE. Implicit solvent calculations were not able to account for the difference in reactivity between these two solvents and MeCN. The inclusion of explicit solvent molecules was needed to determine that HFIP reduces the barrier of the rate-determining step to a greater extent than TFE. This vigorous hybrid approach was needed for this investigation but would have provided no extra insights for the other two systems.

Quantum chemistry allows us to investigate a reaction in great detail and shed light on the crucial steps of a reaction. Systematically building on the methodology used allows for the best use of resources such as computational time. Insights from these are then able to feed into future experimental work and lead to smarter and more efficient research.

List of abbreviations

5Z – quintuple zeta
AM1 – Austin model 1
AMLA - ambiphilic metal ligand activation
ARXPS – angle resolved X-ray photoelectron spectroscopy
BSSE – basis set superposition error
cc – correlation consistent
CC – coupled cluster
CCD – CC doubles
CCSD – CC single doubles
CCSD(T) – CC single doubles with perturbated triples
CI – configuration interaction
CID – CI doubles
CIS – CI singles
CISD – CI single doubles
CMD – concerted metalation deprotonation
COSMO – conductor-like screening model
CPCM – conductor-like polarizable continuum model
DFT – density functional theory
DLPNO – domain-based pair natural orbital
DRC – dynamic reaction coordinate
DRS – diffuse reflectance spectroscopy
DZ – double zeta
ECP – electron core potential
GGA – generalised gradient approximation
GTO – Gaussian type orbital
HFIP – hexafluoro-2-propanol
IEDDA – inverse electron demand Diels-Alder reaction
IRC – intrinsic reaction coordinate
KS-DFT – Kohn-Sham DFT
LAPS – ligand-assisted proton shuttle
LDA – local density approximation
LEIS – low-energy ion scattering
LLHT – ligand-to-ligand hydrogen transfer

MBPT – many-body perturbation theory

MD – molecular dynamics

MLC – metal ligand cooperativity

MM – molecular mechanics

MNDO – modified neglect of diatomic overlap

MO – molecular orbital

PBC – periodic boundary conditions

PCM – polarizable continuum model

PES – potential energy surface

PM3 – parametric method 3

PP – pseudopotential

pyrr = pyrrolidine

QM – quantum mechanics

QM/MM – quantum mechanics/molecular mechanics

QZ – quadruple zeta

RAS – reactive atom scattering

RTIL – room temperature ionic liquid

SCF – self-consistent field

SFG – sum frequency generation spectroscopy

SMD – solvation model based on density

STO – Slater type orbital

TFA – trifluroacetic acid

TFE – 2,2,2-trifluoroethanol

TS – transition state

TST – Transition-State Theory

TZ – triple zeta

References

1. Jensen, F. *Introduction to Computational Chemistry*. (John Wiley & Sons, 2017).
2. Szabo, A. & Ostlund, N. S. *Modern Quantum Chemistry: Introduction to Advanced Electronic Structure Theory*. (Courier Corporation, 2012).
3. Andris, E. *et al.* Aurophilic Interactions in [(L)AuCl]⋯[(L′)AuCl] Dimers: Calibration by Experiment and Theory. *J. Am. Chem. Soc.* **140**, 2316–2325 (2018).
4. Forni, A., Pieraccini, S., Rendine, S., Gabas, F. & Sironi, M. Halogen-bonding interactions with π systems: CCSD(T), MP2, and DFT calculations. *ChemPhysChem* **13**, 4224–4234 (2012).
5. Lu, N. *et al.* Neutron Diffraction Study of Significant sp3and sp2C-H Bond Shortening in a Fluorinated Pyridinium Saccharinate. *J. Am. Chem. Soc.* **143**, 5550–5557 (2021).
6. Acevedo, O. & Jorgensen, W. L. Understanding rate accelerations for Diels-Alder reactions in solution using enhanced QM/MM methodology. *J. Chem. Theory Comput.* **3**, 1412–1419 (2007).
7. Zheng, J., Xu, X. & Truhlar, D. G. Minimally augmented Karlsruhe basis sets. *Theor. Chem. Acc.* **128**, 295–305 (2011).
8. Weigend, F. & Ahlrichs, R. Balanced basis sets of split valence, triple zeta valence and quadruple zeta valence quality for H to Rn: Design and assessment of accuracy. *Phys. Chem. Chem. Phys.* **7**, 3297–3305 (2005).
9. Senn, H. M. & Thiel, W. QM/MM methods for biomolecular systems. *Angew. Chemie - Int. Ed.* **48**, 1198–1229 (2009).
10. Tomasi, J., Mennucci, B. & Cammi, R. Quantum mechanical continuum solvation models. *Chem. Rev.* **105**, 2999–3093 (2005).
11. Riahi, S. & Rowley, C. N. The CHARMM-TURBOMOLE interface for efficient and accurate QM/MM molecular dynamics, free energies, and excited state properties. *J. Comput. Chem.* **35**, 2076–2086 (2014).
12. Keane, A. J., Farrell, W. S., Yonke, B. L., Zavalij, P. Y. & Sita, L. R. Metal-Mediated Production of Isocyanates, R 3 EN=C=O from Dinitrogen, Carbon Dioxide, and R 3 ECl. *Angew. Chemie* **127**, 10358–10362 (2015).
13. Khusnutdinova, J. R. & Milstein, D. Metal-Ligand Cooperation. *Angew. Chemie - Int. Ed.* **54**, 12236–12273 (2015).
14. Pérez-Jiménez, A. J. & Sancho-García, J. C. Extracting dimer structures from simulations of organic-based materials using QM/MM methods. *Chem. Phys.* **459**, 112–124 (2015).
15. Li, L., Zhao, S., Joshi-Pangu, A., Diane, M. & Biscoe, M. R. Stereospecific Pd-catalyzed

cross-coupling reactions of secondary alkylboron nucleophiles and aryl chlorides. *J. Am. Chem. Soc.* **136**, 14027–14030 (2014).

16. Lennox, A. J. J. & Lloyd-Jones, G. C. Selection of boron reagents for Suzuki-Miyaura coupling. *Chem. Soc. Rev.* **43**, 412–443 (2014).
17. Alexander, J. S. & Ruhlandt-Senge, K. Not just heavy 'Grignards': Recent advances in the organometallic chemistry of the alkaline earth metals calcium, strontium and barium. *Eur. J. Inorg. Chem.* 2761–2774 (2002) doi:10.1002/1099-0682(200211)2002:11<2761::AID-EJIC2761>3.0.CO;2-2.
18. Cook, J. L., Hunter, C. A., Low, C. M. R., Perez-Velasco, A. & Vinter, J. G. Solvent effects on hydrogen bonding. *Angew. Chemie - Int. Ed.* **46**, 3706–3709 (2007).
19. Cotugno, P. *et al.* Suzuki coupling of iodo and bromoarenes catalyzed by chitosan-supported Pd-nanoparticles in ionic liquids. *J. Organomet. Chem.* **752**, 1–5 (2014).
20. Fustero, S., Simón-Fuentes, A., Barrio, P. & Haufe, G. Olefin metathesis reactions with fluorinated substrates, catalysts, and solvents. *Chem. Rev.* **115**, 871–930 (2015).
21. Gieseking, R. L., Ratner, M. A. & Schatz, G. C. Implementation of INDO/SCI with COSMO implicit solvation and benchmarking for solvatochromic shifts. *J. Phys. Chem. A* **120**, 9878–9885 (2016).
22. Chen, W. L. & Lin, S. T. Explicit consideration of spatial hydrogen bonding direction for activity coefficient prediction based on implicit solvation calculations. *Phys. Chem. Chem. Phys.* **19**, 20367–20376 (2017).
23. Lee, M. S., Salsbury, F. R. & Olson, M. A. An efficient hybrid explicit/implicit solvent method for biomolecular simulations. *J. Comput. Chem.* **25**, 1967–1978 (2004).
24. Cramer, C. J. & Truhlar, D. G. Implicit Solvation Models: Equilibria, Structure, Spectra, and Dynamics - Chemical Reviews (ACS Publications). *Chem. Rev.* (1999).
25. Cui, Q. Combining implicit solvation models with hybrid quantum mechanical/molecular mechanical methods: A critical test with glycine. *J. Chem. Phys.* **117**, 4720–4728 (2002).
26. Tomasi, J. & Persico, M. Molecular Interactions in Solution: An Overview of Methods Based on Continuous Distributions of the Solvent. *Chem. Rev.* **94**, 2027–2094 (1994).
27. Orozco, M. & Luque, F. J. Theoretical methods for the description of the solvent effect in biomolecular systems. *Chem. Rev.* **100**, 4187–4225 (2000).
28. Bernales, V. S., Marenich, A. V., Contreras, R., Cramer, C. J. & Truhlar, D. G. Quantum mechanical continuum solvation models for ionic liquids. *J. Phys. Chem. B* **116**, 9122–9129 (2012).
29. Tomasi, J. E. scrocco. **55**, 117–129 (1981).
30. Mennucci, B. Polarizable continuum model. *Wiley Interdiscip. Rev. Comput. Mol. Sci.* **2**, 386–404 (2012).

31. Klamt, A. The COSMO and COSMO-RS solvation models. *Wiley Interdiscip. Rev. Comput. Mol. Sci.* **8**, 1–11 (2018).

32. Klamt, A. & Schüürmann, G. COSMO: A new approach to dielectric screening in solvents with explicit expressions for the screening energy and its gradient. *J. Chem. Soc. Perkin Trans. 2* 799–805 (1993) doi:10.1039/P29930000799.

33. Allouche, A. Software News and Updates Gabedit — A Graphical User Interface for Computational Chemistry Softwares. *J. Comput. Chem.* **32**, 174–182 (2012).

34. Joung, I. S. & Cheatham, T. E. Determination of alkali and halide monovalent ion parameters for use in explicitly solvated biomolecular simulations. *J. Phys. Chem. B* **112**, 9020–9041 (2008).

35. Demille, R. C., Cheatham, T. E. & Molinero, V. A coarse-grained model of DNA with explicit solvation by water and ions. *J. Phys. Chem. B* **115**, 132–142 (2011).

36. Garcia-Ratés, M., García-Muelas, R. & López, N. Solvation Effects on Methanol Decomposition on Pd(111), Pt(111), and Ru(0001). *J. Phys. Chem. C* **121**, 13803–13809 (2017).

37. Senn, H. M., Thiel, S. & Thiel, W. Enzymatic hydroxylation in p-hydroxybenzoate hydroxylase: A case study for QM/MM molecular dynamics. *J. Chem. Theory Comput.* **1**, 494–505 (2005).

38. Wu, Q., Deng, C., Peng, Q., Niu, Y. & Shuai, Z. Quantum chemical insights into the aggregation induced emission phenomena: A QM/MM study for pyrazine derivatives. *J. Comput. Chem.* **33**, 1862–1869 (2012).

39. Chang, X. P., Xie, X. Y., Lin, S. Y. & Cui, G. QM/MM Study on Mechanistic Photophysics of Alloxazine Chromophore in Aqueous Solution. *J. Phys. Chem. A* **120**, 6129–6136 (2016).

40. Martínez-Fernández, L. *et al.* Computing the Absorption and Emission Spectra of 5-Methylcytidine in Different Solvents: A Test-Case for Different Solvation Models. *J. Chem. Theory Comput.* **12**, 4430–4439 (2016).

41. Faheem, M. & Heyden, A. Hybrid quantum mechanics/molecular mechanics solvation scheme for computing free energies of reactions at metal-water interfaces. *J. Chem. Theory Comput.* **10**, 3354–3368 (2014).

42. Tongraar, A. & Michael Rode, B. The hydration structures of F??? and Cl??? investigated by ab initio QM/MM molecular dynamics simulations. *Phys. Chem. Chem. Phys.* **5**, 357–362 (2003).

43. Takahashi, H., Matubayasi, N., Nakahara, M. & Nitta, T. A quantum chemical approach to the free energy calculations in condensed systems: The QM/MM method combined with the theory of energy representation. *J. Chem. Phys.* **121**, 3989–3999 (2004).

44. Lev, B., Roux, B. & Noskov, S. Y. Relative free energies for hydration of monovalent ions

from QM and QM/MM simulations. *J. Chem. Theory Comput.* **9**, 4165–4175 (2013).

45. Dybeck, E. C., König, G., Brooks, B. R. & Shirts, M. R. Comparison of Methods to Reweight from Classical Molecular Simulations to QM/MM Potentials. *J. Chem. Theory Comput.* **12**, 1466–1480 (2016).
46. Steffen, C. *et al.* TmoleX--a graphical user interface for TURBOMOLE. *J. Comput. Chem.* **31**, 2967–2970 (2010).
47. Yan, X., Anguille, S., Bendahan, M. & Moulin, P. Ionic liquids combined with membrane separation processes: A review. *Sep. Purif. Technol.* **222**, 230–253 (2019).
48. Keskin, S., Kayrak-Talay, D., Akman, U. & Hortaçsu, Ö. A review of ionic liquids towards supercritical fluid applications. *J. Supercrit. Fluids* **43**, 150–180 (2007).
49. Ghandi, K. A Review of Ionic Liquids, Their Limits and Applications. *Green Sustain. Chem.* **04**, 44–53 (2014).
50. Aghaie, M., Rezaei, N. & Zendehboudi, S. A systematic review on CO2 capture with ionic liquids: Current status and future prospects. *Renew. Sustain. Energy Rev.* **96**, 502–525 (2018).
51. Smoll, E. J. *et al.* Determining the composition of the vacuum-liquid interface in ionic-liquid mixtures. *Faraday Discuss.* **206**, 497–522 (2018).
52. Bruce, D. W. *et al.* Nanosegregation and Structuring in the Bulk and at the Surface of Ionic-Liquid Mixtures. *J. Phys. Chem. B* **121**, 6002–6020 (2017).
53. Tesa-Serrate, M. A. *et al.* Ionic liquid-vacuum interfaces probed by reactive atom scattering: Influence of alkyl chain length and anion volume. *J. Phys. Chem. C* **119**, 5491–5505 (2015).
54. Rivera-Rubero, S. & Baldelli, S. Surface characterization of 1-butyl-3-methylimidazolium Br-, I-, PF6-, BF4-,(CF3SO2) 2N-, SCN-, CH3SO3-, CH3SO4-, and (CN) 2N-ionic liquids by sum frequency generation. *J. Phys. Chem. B* **110**, 4756–4765 (2006).
55. Rivera-Rubero, S. & Baldelli, S. Influence of water on the surface of hydrophilic and hydrophobic room-temperature ionic liquids. *J. Am. Chem. Soc.* **126**, 11788–11789 (2004).
56. Hallett, J. P. & Welton, T. Room-temperature ionic liquids: Solvents for synthesis and catalysis. 2. *Chem. Rev.* **111**, 3508–3576 (2011).
57. Santos, C. S. & Baldelli, S. Surface orientation of 1-methyl-, 1-ethyl-, and 1-butyl-3-methylimidazolium methyl sulfate as probed by sum-frequency generation vibrational spectroscopy. *J. Phys. Chem. B* **111**, 4715–4723 (2007).
58. Iwahashi, T. *et al.* Anion configuration at the air/liquid interface of ionic liquid [bmim]OTf studied by sum-frequency generation spectroscopy. *J. Phys. Chem. B* **112**, 11936–11941 (2008).

59. Gannon, T. J., Law, G., Watson, P. R., Carmichael, A. J. & Seddon, K. R. First observation of molecular composition and orientation at the surface of a room-temperature ionic liquid. *Langmuir* **15**, 8429–8434 (1999).

60. Law, G., Watson, P. R., Carmichael, A. J. & Seddon, K. R. Molecular composition and orientation at the surface of room-temperature ionic liquids: Effect of molecular structure. *Phys. Chem. Chem. Phys.* **3**, 2879–2885 (2001).

61. Law, G. & Watson, P. R. Surface orientation in ionic liquids. *Chem. Phys. Lett.* **345**, 1–4 (2001).

62. Katakura, S., Nishi, N., Kobayashi, K., Amano, K. I. & Sakka, T. Surface Structure of Quaternary Ammonium-Based Ionic Liquids Studied Using Molecular Dynamics Simulation: Effect of Switching the Length of Alkyl Chains. *J. Phys. Chem. C* **123**, 7246–7258 (2019).

63. Yan, T. *et al.* Structure of the liquid-vacuum interface of room-temperature ionic liquids: A molecular dynamics study. *J. Phys. Chem. B* **110**, 1800–1806 (2006).

64. Bhargava, B. L. & Balasubramanian, S. Layering at an ionic liquid-vapor interface: A molecular dynamics simulation study of [bmim][PF6]. *J. Am. Chem. Soc.* **128**, 10073–10078 (2006).

65. Wu, B. *et al.* Inelastic and reactive scattering dynamics of hyperthermal oxygen atoms on ionic liquid surfaces: [emim][NTf2] and [C12mim][NTf 2]. *J. Phys. Chem. C* **114**, 4015–4027 (2010).

66. Yockel, S. & Schatz, G. C. Modeling O(3P) and Ar scattering from the ionic liquid [emim] [NO3] at 5 eV with hybrid QM/MM molecular dynamics. *J. Phys. Chem. B* **114**, 14241–14248 (2010).

67. Lynden-Bell, R. M. & Del Pópolo, M. Simulation of the surface structure of butylmethylimidazolium ionic liquids. *Phys. Chem. Chem. Phys.* **8**, 949–954 (2006).

68. Smoll, E. J. *et al.* Probing Conformational Heterogeneity at the Ionic Liquid-Vacuum Interface by Reactive-Atom Scattering. *J. Phys. Chem. Lett.* **10**, 156–163 (2019).

69. Ahlrichs, R., Bär, M., Häser, M., Horn, H. & Kölmel, C. Electronic structure calculations on workstation computers: The program system turbomole. *Chem. Phys. Lett.* **162**, 165–169 (1989).

70. Furche, F. *et al.* Turbomole. *Wiley Interdiscip. Rev. Comput. Mol. Sci.* **4**, 91–100 (2014).

71. Vahtras, O., Almlöf, J. & Feyereisen, M. W. Integral approximations for LCAO-SCF calculations. *Chem. Phys. Lett.* **213**, 514–518 (1993).

72. Feyereisen, M., Fitzgerald, G. & Komornicki, A. Use of approximate integrals in ab initio theory. An application in MP2 energy calculations. *Chem. Phys. Lett.* **208**, 359–363 (1993).

73. Kendall, R. A. & Früchtl, H. A. The impact of the resolution of the identity approximate integral method on modern ab initio algorithm development. *Theor. Chem. Acc.* **97**, 158–163 (1997).

74. Bernholdt, D. E. & Harrison, R. J. Large-scale correlated electronic structure calculations: The RI-MP2 method on parallel computers. *Chem. Phys. Lett.* **250**, 477–484 (1996).

75. Deglmann, P., May, K., Furche, F. & Ahlrichs, R. Nuclear second analytical derivative calculations using auxiliary basis set expansions. *Chem. Phys. Lett.* **384**, 103–107 (2004).

76. Deglmann, P., Furche, F. & Ahlrichs, R. An efficient implementation of second analytical derivatives for density functional methods. *Chem. Phys. Lett.* **362**, 511–518 (2002).

77. Maluendes, S. A. & Dupuis, M. A dynamic reaction coordinate approach to ab initio reaction pathways: Application to the 1,5 hexadiene Cope rearrangement. *J. Chem. Phys.* **93**, 5902–5911 (1990).

78. Neese, F. The ORCA program system. *Wiley Interdiscip. Rev. Comput. Mol. Sci.* **2**, 73–78 (2012).

79. Dunning, T. H. A road map for the calculation of molecular binding energies. *J. Phys. Chem. A* **104**, 9062–9080 (2000).

80. Fast, P. L., Corchado, J. C., Sánchez, M. L. & Truhlar, D. G. Multi-Coefficient Correlation Method for Quantum Chemistry. *J. Phys. Chem. A* **103**, 5129–5136 (1999).

81. Truhlar, D. G. Basis-set extrapolation. *Chem. Phys. Lett.* **294**, 45–48 (1998).

82. Varandas, A. J. C. Basis-set extrapolation of the correlation energy. *J. Chem. Phys.* **113**, 8880–8887 (2000).

83. Frisch, M. J. *et al.* Petersson., GA et al. Gaussian09, Rev. C. 01; Gaussian. *Inc. Wallingford, CT* (2010).

84. Elsby, M. R. & Baker, R. T. Strategies and mechanisms of metal-ligand cooperativity in first-row transition metal complex catalysts. *Chem. Soc. Rev.* **49**, 8933–8987 (2020).

85. Higashi, T., Kusumoto, S. & Nozaki, K. Cleavage of Si-H, B-H, and C-H Bonds by Metal-Ligand Cooperation. *Chem. Rev.* **119**, 10393–10402 (2019).

86. Derrick, J. S. *et al.* Metal-Ligand Cooperativity via Exchange Coupling Promotes Iron-Catalyzed Electrochemical CO2Reduction at Low Overpotentials. *J. Am. Chem. Soc.* **142**, 20489–20501 (2020).

87. Garrido-Barros, P. *et al.* Redox Metal-Ligand Cooperativity Enables Robust and Efficient Water Oxidation Catalysis at Neutral pH with Macrocyclic Copper Complexes. *J. Am. Chem. Soc.* **142**, 17434–17446 (2020).

88. Mathis, C. L. *et al.* Thermodynamic Analysis of Metal-Ligand Cooperativity of PNP Ru Complexes: Implications for CO2 Hydrogenation to Methanol and Catalyst Inhibition. *J. Am. Chem. Soc.* **141**, 14317–14328 (2019).

89. Rauch, M. *et al.* Metal-Ligand Cooperation Facilitates Bond Activation and Catalytic Hydrogenation with Zinc Pincer Complexes. *J. Am. Chem. Soc.* **142**, 14513–14521 (2020).
90. Fujita, K., Tanino, N. & Yamaguchi, R. Ligand-Promoted Dehydrogenation of Alcohols Catalyzed by Cp * Ir Complexes . A New Catalytic System for Oxidant-Free Oxidation of Alcohols. *Org. Lett.* 2006–2008 (2007).
91. Feller, M., Gellrich, U., Anaby, A., Diskin-Posner, Y. & Milstein, D. Reductive Cleavage of CO2 by Metal-Ligand-Cooperation Mediated by an Iridium Pincer Complex. *J. Am. Chem. Soc.* **138**, 6445–6454 (2016).
92. Lapointe, D. & Fagnou, K. Overview of the Mechanistic Work on the Concerted Metallation–Deprotonation Pathway. *Chem. Lett.* **39**, 1118–1126 (2010).
93. Boutadla, Y., Davies, D. L., Macgregor, S. A. & Poblador-Bahamonde, A. I. Mechanisms of C-H bond activation: rich synergy between computation and experiment. *Dalton Trans.* 5820–5831 (2009) doi:10.1039/b904967c.
94. Davies, D. L., Macgregor, S. A. & McMullin, C. L. Computational Studies of Carboxylate-Assisted C-H Activation and Functionalization at Group 8-10 Transition Metal Centers. *Chem. Rev.* **117**, 8649–8709 (2017).
95. Winstein, S. & Traylor, T. G. Mechanisms of Reaction of Organomercurials. II. Electrophilic Substitution on Saturated Carbon. Acetolysis of Dialkylmercury Compounds. *J. Am. Chem. Soc.* **77**, 3747–3752 (1955).
96. Fung, C. W., Khorramdel-vahed, M., Ranson, R. J., Roberts, R. M. G. & Park, W. Kinetics and Mechanism of Mercuriation of Aromatic Compounds by Mercury Trifluoroacetate in Trifluoroacetic Acid. *J. Chem. Soc., Perkin Trans. 2* 267 (1980).
97. Olah, G. A., Yu, S. H. & Parker, D. G. Organometallic Chemistry. 12: Proton and Carbon-13 Nuclear Magnetic Resonance Study of Arenemercurinium Ions, the Intermediate Complexes of Aromatic Mercuration. **4834**, 1064–1067 (2003).
98. Davies, D. L., Donald, S. M. A. & Macgregor, S. A. Computational study of the mechanism of cyclometalation by palladium acetate. *J. Am. Chem. Soc.* **127**, 13754–13755 (2005).
99. García-Cuadrado, D., De Mendoza, P., Braga, A. A. C., Maseras, F. & Echavarren, A. M. Proton-abstraction mechanism in the palladium-catalyzed intramolecular arylation: Substituent effects. *J. Am. Chem. Soc.* **129**, 6880–6886 (2007).
100. Wang, Y., Shi, Y., Shao, J. & Deng, C. Theoretical insights into the mechanism of rhodium-catalyzed, PIII-directed regioselective C-H arylation of indole with anhydride. *Int. J. Quantum Chem.* **121**, 1–7 (2021).
101. Gandon, V. & Hoarau, C. Concerted vs Nonconcerted Metalation-Deprotonation in Orthogonal Direct C-H Arylation of Heterocycles with Halides: A Computational Study. *J. Org. Chem.* **86**, 1769–1778 (2021).

102. Guihaumé, J., Halbert, S., Eisenstein, O. & Perutz, R. N. Hydrofluoroarylation of alkynes with Ni catalysts. C-H activation via ligand-to-ligand hydrogen transfer, an alternative to oxidative addition. *Organometallics* **31**, 1300–1314 (2012).

103. Johnson, D. G., Lynam, J. M., Slattery, J. M. & Welby, C. E. Insights into the intramolecular acetat-mediated formation of ruthenium vinylidene complexes: a ligand-assisted proton shuttle (LAPS) mechanism. *Dalton Trans.* **39**, 10432–10441 (2010).

104. Lynam, J. M., Welby, C. E. & Whitwood, A. C. Exploitation of a chemically non-innocent acetate ligand in thesynthesis and reactivity of ruthenium vinylidene complexes. *Organometallics* **28**, 1320–1328 (2009).

105. Arita, A. J., Cantada, J., Grotjahn, D. B. & Cooksy, A. L. Computational study of the extensive role of heterocyclic ligands in acetylene hydration by a bifunctional organometallic catalyst. *Organometallics* **32**, 6867–6870 (2013).

106. Jiménez-Tenorio, M. *et al.* Counteranion and solvent assistance in ruthenium-mediated alkyne to vinylidene isomerizations. *Inorg. Chem.* **52**, 8919–8932 (2013).

107. Breit, B. *et al.* Mechanistic insight into the ruthenium-catalysed anti-Markovnikov hydration of alkynes using a self-assembled complex: A crucial role for ligand-assisted proton shuttle processes. *Dalt. Trans.* **43**, 11277–11285 (2014).

108. Drover, M. W., Love, J. A. & Schafer, L. L. Toward anti-Markovnikov 1-Alkyne O-Phosphoramidation: Exploiting Metal-Ligand Cooperativity in a 1,3-N,O-Chelated Cp???Ir(III) Complex. *J. Am. Chem. Soc.* **138**, 8396–8399 (2016).

109. Eichkorn, K., Weigend, F., Treutler, O. & Ahlrichs, R. Auxiliary basis sets for main row atoms and transition metals and their use to approximate Coulomb potentials. *Theor. Chem. Acc.* **97**, 119–124 (1997).

110. Császár, P. & Pulay, P. Geometry optimization by direct inversion in the iterative subspace. *J. Mol. Struct.* **114**, 31–34 (1984).

111. Eichkorn, K., Treutler, O., Öhm, H., Häser, M. & Ahlrichs, R. Auxiliary basis sets to approximate Coulomb potentials (Chem. Phys. Letters 240 (1995) 283) (PII:0009-2614(95)00621-4). *Chem. Phys. Lett.* **242**, 652–660 (1995).

112. Grimme, S., Antony, J., Ehrlich, S. & Krieg, H. A consistent and accurate ab initio parametrization of density functional dispersion correction (DFT-D) for the 94 elements H-Pu. *J. Chem. Phys.* **132**, (2010).

113. Schäfer, A., Klamt, A., Sattel, D., Lohrenz, J. C. W. & Eckert, F. COSMO implementation in TURBOMOLE: Extension of an efficient quantum chemical code towards liquid systems. *Phys. Chem. Chem. Phys.* **2**, 2187–2193 (2000).

114. Klamt, A. & Schüürmann, G. COSMO: a new approach to dielectric screening in solvents with explicit expressions for the screening energy and its gradient. *J. Chem. Soc., Perkin*

Trans. 2 799–805 (1993) doi:10.1039/P29930000799.

115. Baldes, A. & Weigend, F. Efficient two-component self-consistent field procedures and gradients: Implementation in Turbomole and application to Au-20. *Mol. Phys.* **111**, 2617–2624 (2013).
116. Von Arnim, M. & Ahlrichs, R. Geometry optimization in generalized natural internal coordinates. *J. Chem. Phys.* **111**, 9183–9190 (1999).
117. Metz, S., Kästner, J., Sokol, A. A., Keal, T. W. & Sherwood, P. ChemShell-a modular software package for QM/MM simulations. *Wiley Interdiscip. Rev. Comput. Mol. Sci.* **4**, 101–110 (2014).
118. Kästner, J. *et al.* DL-FIND: An open-source geometry optimizer for atomistic simulations*. *J. Phys. Chem. A* **113**, 11856–11865 (2009).
119. Leeb, N. M., Drover, M. W., Love, J. A., Schafer, L. L. & Slattery, J. M. Phosphoramidate-Assisted Alkyne Activation: Probing the Mechanism of Proton Shuttling in a N,O-Chelated Cp∗Ir(III) Complex. *Organometallics* **37**, 4630–4638 (2018).
120. Peng, Y., Ramos-Garcés, M. V., Lionetti, D. & Blakemore, J. D. Structural and Electrochemical Consequences of [Cp∗] Ligand Protonation. *Inorg. Chem.* **56**, 10824–10831 (2017).
121. Chalkley, M. J., Oyala, P. H. & Peters, J. C. Cp∗ Noninnocence Leads to a Remarkably Weak C-H Bond via Metallocene Protonation. *J. Am. Chem. Soc.* (2019) doi:10.1021/jacs.9b00193.
122. Zhao, Y. & Truhlar, D. G. The M06 suite of density functionals for main group thermochemistry, thermochemical kinetics, noncovalent interactions, excited states, and transition elements: Two new functionals and systematic testing of four M06-class functionals and 12 other function. *Theor. Chem. Acc.* **120**, 215–241 (2008).
123. Minenkov, Y., Singstad, Å., Occhipinti, G. & Jensen, V. R. The accuracy of DFT-optimized geometries of functional transition metal compounds: A validation study of catalysts for olefin metathesis and other reactions in the homogeneous phase. *Dalt. Trans.* **41**, 5526–5541 (2012).
124. List, B. *et al.* Proline-Catalyzed Direct Asymmetric Aldol Reactions Most enzymatic transformations have a synthetic counterpart . Often though , the mechanisms by which natural and synthetic catalysts operate differ markedly . The catalytic asymmetric aldol reaction as a. *J. Am. Chem. Soc.* **122**, 2395–2396 (2000).
125. Ahrendt, K. A., Borths, C. J. & MacMillan, D. W. C. New strategies for organic catalysis: The first highly enantioselective organocatalytic diels - Alder reaction [16]. *Journal of the American Chemical Society* vol. 122 4243–4244 (2000).
126. Jacobsena, E. N. & MacMillanb, D. W. C. Organocatalysis. *Proc Natl. Acad. Sci. U. S. A.*

107, 20618–20619 (2010).

127. Qin, Y., Zhu, L. & Luo, S. Organocatalysis in Inert C-H Bond Functionalization. *Chem. Rev.* **117**, 9433–9520 (2017).

128. Methot, J. L. & Roush, W. R. Nucleophilic Phosphine Organocatalysis. *Adv. Synth. Catal.* **346**, 1035–1050 (2004).

129. Chen, J. & Lu, Z. Asymmetric hydrofunctionalization of minimally functionalized alkenes via earth abundant transition metal catalysis. *Org. Chem. Front.* **5**, 260–272 (2018).

130. Liang, Q. & Song, D. Iron N-heterocyclic carbene complexes in homogeneous catalysis. *Chem. Soc. Rev.* **49**, 1209–1232 (2020).

131. Ghislieri, D. & Turner, N. J. Biocatalytic approaches to the synthesis of enantiomerically pure chiral amines. *Top. Catal.* **57**, 284–300 (2014).

132. Ma, C., Fang, P. & Mei, T. S. Recent Advances in C-H Functionalization Using Electrochemical Transition Metal Catalysis. *ACS Catal.* **8**, 7179–7189 (2018).

133. Glendening, E. D. *et al.* Natural Bond Order 7.0, Theoretical Chemistry Institute. *Univ. Wisconsin Madison, WI* (2018).

134. Laury, M. L. & Wilson, A. K. Performance of Density Functional Theory for Second Row (4 d) Transition Metal Thermochemistry. *J. Chem. Theory Comput.* **9**, 3939–3946 (2013).

135. Hong, B. *et al.* Synthesis of planar chiral imidazo[1,5-a]pyridinium salts based on [2.2]paracyclophane for asymmetric β-borylation of enones. *Tetrahedron Asymmetry* **22**, 1055–1062 (2011).

136. Kästner, J. Umbrella sampling. *Wiley Interdiscip. Rev. Comput. Mol. Sci.* **1**, 932–942 (2011).

137. Wu, B. *et al.* Inelastic and reactive scattering dynamics of hyperthermal oxygen atoms on ionic liquid surfaces: [emim][NTf2] and [C12mim][NTf 2]. *AIP Conf. Proc.* **1333**, 516–521 (2011).

138. Clément, S. *et al.* Ethynyl[2.2]paracyclophanes and 4-isocyano[2.2]paracyclophane as ligands in organometallic chemistry. *J. Organomet. Chem.* **692**, 839–850 (2007).

139. List, B. The ying and yang of asymmetric aminocatalysis. *Chem. Commun.* 819–824 (2006) doi:10.1039/b514296m.

140. Zaharani, L., Khaligh, N. G., Mihankhah, T. & Johan, M. R. Synthesis of a series of novel dihydro- solvent-catalyst activity of a low viscous and acid- functionalized ionic liquid. *Synth. Commun.* **50**, 1633–1640 (2020).

141. Nomura, K. & Terwilliger, P. Self-dual Leonard pairs Use of deep eutectic solvents as catalyst : a. 355–372 (2019).

142. Su, C. *et al.* International Journal of Biological Macromolecules Enhancement of the antioxidant abilities of lignin and lignin-carbohydrate complex from wheat straw by

moderate depolymerization via LiCl / DMSO solvent catalysis. *Int. J. Biol. Macromol.* **184**, 369–379 (2021).

143. Furlani, T. R. & Gao, J. Hydrophobic and hydrogen-bonding effects on the rate of diels-alder reactions in aqueous solution. *J. Org. Chem.* **61**, 5492–5497 (1996).

144. Liu, F., Yang, Z., Mei, Y. & Houk, K. N. QM/QM′ Direct Molecular Dynamics of Water-Accelerated Diels-Alder Reaction. *J. Phys. Chem. B* **120**, 6250–6254 (2016).

145. Breslow, R. & Rideout, D. C. Hydrophobic Acceleration of Diels-Alder Reactions. *J. Am. Chem. Soc.* **102**, 7816–7817 (1980).

146. Breslow, R. & Guo, T. Diels-Alder reactions in nonaqueous polar solvents. Kinetic effects of chaotropic and antichaotropic agents and of β-cyclodextrin. *J. Am. Chem. Soc.* **110**, 5613–5617 (1988).

147. Blake, J. F. & Jorgensen, W. L. Solvent Effects on a Diels-Alder Reaction from Computer Simulations. *J. Am. Chem. Soc.* **113**, 7430–7432 (1991).

148. Jorgensen, W. L., Blake, J. F., Lim, D. & Severance, D. L. Investigation of solvent effects on pericyclic reactions by computer simulations. *J. Chem. Soc. Faraday Trans.* **90**, 1727–1732 (1994).

149. Acevedo, O., Jorgensen, W. L. & Evanseck, J. D. Elucidation of rate variations for a diels-alder reaction in ionic liquids from QM/MM simulations. *J. Chem. Theory Comput.* **3**, 132–138 (2007).

150. Chandrasekhar, J., Shariffskul, S. & Jorgensen, W. L. QM/MM simulations for Diels-Alder reactions in water: Contribution of enhanced hydrogen bonding at the transition state to the solvent effect. *J. Phys. Chem. B* **106**, 8078–8085 (2002).

151. Glinkerman, C. M. & Boger, D. L. Catalysis of Heterocyclic Azadiene Cycloaddition Reactions by Solvent Hydrogen Bonding: Concise Total Synthesis of Methoxatin. *J. Am. Chem. Soc.* **138**, 12408–12413 (2016).

152. Yang, Y. F., Yu, P. & Houk, K. N. Computational Exploration of Concerted and Zwitterionic Mechanisms of Diels-Alder Reactions between 1,2,3-Triazines and Enamines and Acceleration by Hydrogen-Bonding Solvents. *J. Am. Chem. Soc.* **139**, 18213–18221 (2017).

153. Kozuch, S. & Shaik, S. How to conceptualize catalytic cycles? the energetic Span model. *Acc. Chem. Res.* **44**, 101–110 (2011).

154. Pozhydaiev, V., Power, M., Gandon, V., Moran, J. & Lebœuf, D. Exploiting hexafluoroisopropanol (HFIP) in Lewis and Brønsted acid-catalyzed reactions. *Chem. Commun.* **56**, 11548–11564 (2020).

155. Roberts, C. W., McBee, E. T. & Hathaway, C. E. The Potentiometric Titration of Fluorinated Alcohols in Aqueous and Non-Aqueous Systems. *J. Org. Chem.* **21**, 1369–1370 (1956).